3-D Photopolymer Disks for Correlation and Data Storage, and Cross-talk in Volume Holographic Memories

Thesis by
Kevin Curtis
In Partial Fulfillment of the Requirements
for the Degree of
Doctor of Philosophy

California Institute of Technology
Pasadena, California
1994
(Submitted March 9, 1994)

0.1 ACKNOWLEDGMENTS

A very heartfelt thank you is due to Professor Psaltis. He is a wonderful advisor who never led me astray and a patient and understanding teacher. Best of all, the Professor is a friend with a great sense of humor that makes working with him fun. I have enjoyed the time I spent in his group. Professor has succeeded in making the group into a wonderful family. If I have produced anything of worth, Professor and my professional family have had a lot to do with it. I can only say thank you.

This thesis is the result of collaboration and discussions with many people. Dr. Sidney Li has always been willing to help in any problem. During my first year, Sid provided me with something of a role model in how get things done. Thanks to Dr. Fai "Fay" Mok for some really good advice over the years. In addition, Geoffrey Burr assisted me many times, and provided much needed comic relief. Thanks for friendship and assistance to Annette Grot, Robert Denkewalter, David Marx, Ernest Chuang, Jean-Jacques Drolet, Xin An, Jeffrey Davis, George Barbastathis, Michael Levene, Allen Pu, Jiafu Luo, Min Lu, Ya-yun Liu, Dr. Yong Qiao, Dr. Mark Neifeld, Dr. Alan Yamamura, Dr. Chaunyi Ji, Seiji Kobayashi, Subrata Rakshit, and Dr. Steven Lin. You have all been good friends and have contributed to my understanding of many topics. Thanks to Su McKinley, Lucinda Acosta, and Helen Carrier for providing good will and very efficient administrative support.

My first three years at Caltech were supported by the Northrop Fellowship Program. I would like to thank all involved with the program for the help and support that they provided. In particular, Margaret Paulin has always been available to answer questions. In addition, I would like to thank Hugh Logan, Wes Massenton, Jim Reis, and Hal Stoll for their help and encouragement. I deeply appreciate all the support that the entire Northrop Corporation has given me.

I also thank Jay Calio and Dr. Steven Zager of DuPont for their help in understanding photopolymers and for providing the material that was used in many of my experiments. In addition, I would like to thank Dr. Grubbs of Caltech's Chemistry Department for interesting discussions that furthered my understanding of photopolymers.

I am deeply indebted to my parents Dick and Marilyn Curtis who have supported me with love and understanding for many years. They have provided me with the encouragement and support that is a big part of why I have been successful. I also thank my loving wife Barb, whose support has made this possible. I will not say that I did it for her, since she would have probably preferred that I had spent more time with her, but I thank her for her understanding.

0.2 ABSTRACT

This thesis considers the optical storage and processing of data using volume holography. First, cross-talk noise due to geometrical considerations is calculated for volume holographic memories. Cross-talk is due to energy diffracted from non-Bragg matched gratings. The SNR (signal-to-noise-ratio) of holographic memories due to cross-talk noise is calculated for Fourier transform holograms stored by angle, wavelength, phase-coded, and rotational multiplexing methods. Considerations include page size, geometry, angular bandwidth of the optical system, wavelength of the light used, material size, spatial light modulator (SLM) contrast, and the phase of the image plane. The SNR for angle multiplexed image plane holograms is also calculated and compared to the results for Fourier transformed angle multiplexed holograms. A comparison of the various multiplexing methods based on cross-talk is presented, and then the effect of geometry and material dynamic range is included to determine when cross-talk will be the dominant noise source. The use of photopolymers as a holographic element is then presented. The recording characteristics of the DuPont photopolymer are described and a method of multiplexing multiple holograms in the photopolymer is given. A new method for multiplexing holograms (called peristrophic multiplexing) is described. This method significantly increases the storage capacity of thin films. After this, a 3-D disk-based correlator and storage device using the photopolymer is described and demonstrated. In this device, holograms are multiplexed at a given spot and then disk rotation/head motion are used to access multiple spots on the disk. Theoretical correlation speed, read-out rates, and the storage capacity of the 3-D disk as limited by geometry and laser power are given.

Advisor: Professor Demetri Psaltis.

Contents

List of Figures

Chapter 1

Introduction

1.1 Holography

In 1948, Dennis Gabor proposed [1] a wavefront reconstruction method of imaging, and holography was born. When a coherent reference beam is interfered with an object beam, the intensity of the interference pattern contains both the amplitude and phase information of the beams. Since materials such as film record the intensity of the light, this method allows for the total information of the object beam to be recorded in the film. Gabor called the interference pattern a hologram, meaning "total recording."

Through out the fifties, Gabor [2, 3] and a few others [4, 5, 6] expanded the principles laid out in his original paper. During this time, holograms were recorded on-axis. This meant that both real and virtual images were reconstructed at the same time and in the same direction, and therefore the quality of the reconstruction was seriously limited. It was not until Leith and Upatnieks [7] developed off-axis holography that the quality of holographic reconstructions significantly improved. In off-axis holography, the reference beam is incident on the film at an angle while the object is incident to the medium at a different angle. This allows the virtual and real images, as well as the undiffracted light, to be separated. With this breakthrough in recording technique came new applications besides the original application of imaging.

For example, 3-D image reconstruction [8], information storage [9] – [13], filtering [14, 15], aberration correction in imaging systems [16, 17], and synthetic-aperture radar processing [18, 19] were all proposed and to some extent demonstrated during the 1960's and early 1970's.

During the 1960's, the material used in most experimental work was photographic film. A lot of work was done on evaluating the holographic quality [20, 21, 22] and the linearity of these films [23, 24]. The film was typically a thin, two dimensional (2–D) layer of recording material. Thin holograms lack sensitivity to changes in angle of the reconstruction beam. This property allows for the construction of shift invariant filters for correlation, but also restricts the capacity to approximately one hologram per spatial location on the film.

1.2 Volume Holography

The limited storage density of 2–D holograms can be overcome by using volume holography. In volume holography, the recording medium is a three dimensional (3–D) solid. Due to the fact that the interference pattern is recorded throughout the material, thick holograms are sensitive to changes in angle or wavelength of the reconstructing beam. This effect was first noticed in X-ray diffraction from crystals by Bragg in 1942 [25]. In 1969, Kogelnik [26] analyzed the diffraction of light from a hologram written in a volume by interfering two plane waves. Kogelnik's result showed how Bragg selectivity applied to thick, optical, volume holograms. Later analysis [27, 28, 29, 30] discussed Bragg selectivity and diffraction from materials whose thickness is between the thick and thin holographic regimes. Using the Bragg selectivity inherent to volume holography, multiple holograms can be stored in the same volume by changing either the angle or wavelength of the recording beams. Since Bragg selectivity allows for many holograms to be superimposed inside the same volume, it significantly increases the storage density of the medium.

Historically, the most important type of material for volume holography is photorefractive crystals. In photorefractives, light excites electrons out of traps in the material and into the conduction band. Once in the conduction band, the electrons either diffuse out of the illuminated regions or are forced out of these regions by built in or applied electric fields. Once in the dark regions, they are retrapped. Therefore, in the illuminated regions there are uncompensated positive charges while in the dark regions there are uncompensated negative (trapped electrons) charges. This separation of charge has an associated electric field with it, which in turn generates a change in index of refraction of the material by the electro-optic effect. Thus the sinusoidal interference pattern due to two coherent plane waves is recorded by a sinusoidal perturbation in the index of refraction of the material called a phase grating. Phase gratings can have high diffraction efficiency (up to 100 percent). The theoretical details of this recording process in photorefractives were worked out by several authors [31]–[36] including Kukhtarev [37].

Holographic storage in photorefractives was demonstrated in the late 1960's and early 1970's by several authors [38]–[41]. Particularly impressive was the work of Amodei, Philips, and Staebler in iron doped $LiNbO_3$. They demonstrated storage of several hundred holograms in $LiNbO_3$:Fe [42]. Recently, several thousand holograms have been stored in iron doped $LiNbO_3$ [43, 44] and recalled with good signal-to-noise ratio.

Although photorefractives are inherently dynamic materials, there are a few methods of "fixing" the holograms – making the holograms permanent. Thermal fixing (heating the crystals to several hundred degrees Celsius) has been demonstrated in several photorefractives [45]–[49]. In thermal fixing, the electronic gratings established by the optical fields are compensated by ionic gratings. Since the ions are only mobile at very high temperatures, these ionic gratings are effectively permanent at room temperature. In Strontium Barium Niobate (SBN), electrical fixing [51]–[56] is accomplished by electric domain reversal in the ferroelectric crystal. In this method, the electronic gratings set up by the optical field are partially compensated by electric domain reversal after a depoling electric field is applied to the crystal. Another method of preventing hologram decay is the continual refreshing of the holograms (copying), and this method has been experimentally demonstrated [57, 58, 59]. Reading out the holograms with a wavelength that is non-destructive has also been shown [60, 61, 62, 63, 64]. Thus, in photorefractives, volume holographic storage has been extensively studied.

Other, less common materials for volume holography are organic polymers. Recently, polymers have been used in several holographic and non-holographic storage techniques. Examples of non-holographic storage include Rentzepis's 3-D storage [65, 66, 67], electron trapping materials [68, 69], and for spectral hole burning applications [70, 71, 72, 73]. In addition, there have been several recent ideas for dynamic holographic photopolymer materials. These include liquid crystal doped polymers [74]–[79], and the development of photorefractive polymers [80]–[99]. In photorefractive polymers, the recording mechanism is similar to the mechanism in inorganic crystals except that the mobile charges are holes, and strong electric fields have to be applied to enable charge migration and to enhance the electro-optic effect. Fixed gratings have yet to be demonstrated in these photorefractive polymers. With this new emphasis on polymers in recent years, there has been renewed interest in the original type of photopolymer. In this type of photopolymer light induces polymerization of monomers inside a polymer host.

In the early 1970's, while photorefractives were initially being developed, photopolymers were also pursued for the purpose of holographic storage [100]–[110].

These photopolymers consist of monomers and a light sensitive dye inside a polymer matrix. The light excites the dye and initiates a free radical reaction. This locally polymerizes the monomers in the illuminated regions and sets up a gradient in monomer concentration. The monomers then diffuse into these regions and are polymerized, which increases the density of the film in the illuminated regions. This density change directly relates to a change in the index of refraction. Thus, like photorefractives, these polymers record phase gratings. Unlike photorefractives, these films inherently record permanent gratings since the polymerization reaction is strongly irreversible. After the holograms are stored, the film is uniformly exposed to ensure complete polymerization of the film. In 1976, Bartolini et al. [111] angle multiplexed 550 holograms in one centimeter thick photopolymer film. Using similar material, DuPont had a holographic photopolymer that was commercially available in the 1970's. Recently, DuPont, Polaroid, and others have photopolymer films [112]–[117] that have good sensitivity, resolution, and relatively large index changes. These films have been used for filters [118, 119, 120], holographic storage [121, 122], and the verification of drivers licenses and credit cards (although, the holograms on these cards are mechanically, not holographically reproduced). In addition, the theory of polymerization and monomer diffusion in photopolymer films has been investigated [123, 124].

1.3 Volume Holographic Storage – Then and Now

The advantages of holographic storage are high storage density and the parallel access capability. These features were recognized in the 1960's and 1970's [9, 39, 111] and serious efforts were made to take advantage of the technology. Unfortunately, this work did not lead to a commercial product. Lately, holographic storage has again received attention as a possible technology for high density data storage. A valid question is, what has changed in the last 20 years to make holographic storage a commercially viable technology ?

Some of the more important factors that have changed in the last 20 years are listed below.

- **Need:** The emergence of applications that require storage on the order of terabytes is a very important factor. As computers transform from stand alone units to large networks with graphical/oral interfaces, and the emergence of multimedia (the fusion of text, video, and audio information), the storage requirements and data readout rates for storage devices have dramatically increased. In addition to these memory applications, new applications that require high storage density and parallel access have arisen such as neural networks, image processing, and large data bases. Clearly, the need for data storage on the terabyte level has changed significantly since the 1970's.

- **Evolution of CCD and SLM technology:** In the 1970's, presenting digital data and quickly reading out digital data from an optical system was impeded by the lack of input and output devices. The choice for input devices was limited to 1–D modulators such as acoustic-optical modulators or electro-optical modulators. With the advent of projection televisions, spatial light modulators (SLMs) based on liquid crystal technology have become commercially available. These SLMs provide an easy way to present digital data in a 2–D form to an optical system [125]–[137]. SLMs can have large transfer rates and some types support gray level encoding of the data. In addition, the dramatic changes in VLSI (very large scale integrated) technology, have made available large, fast CCD (charge coupled device) arrays [138, 139, 140, 141]for detecting and reading out the data in parallel. Thus, using both SLMs and CCD arrays, large amounts of digital data can be stored and accessed in parallel.

- **Light Sources:** Commercially viable optical memories need reasonably compact, reliable, and efficient light sources. Since most holographic materials are sensitive in the visible, these light sources have to operate in the visible to near infrared region of the spectrum. Using these criteria, there was not an acceptable light source available in the 1970's. Recently, tremendous advancements have been made in solid state lasers [142, 143, 144, 145] and even short wavelength (blue) semiconductor lasers [146, 147, 148, 149]. Currently, solid state lasers are commercially available at 532 nanometers with the high power necessary for holographic storage.

- **Holographic Storage Techniques:** Very significant advancement has occurred in holographic storage techniques. These include understanding the scaling of diffraction efficiency with the number of holograms stored , recording schedules for storing large numbers of holograms with equal diffraction efficiency, understanding cross-talk, increased stability of recording setup, optimization and characterization of storage materials, and most importantly computer control of the storage process. The advancement in computer control was an enabling technology that made the repeated recording of a large number of holograms technically feasible.

- **Optical Components:** The manufacture and design of optical systems has made dramatic improvements in the last 20 years. The development of diffractive optics to make diffusers and lenses has significantly increased the flexibility of holographic storage system design. Computers themselves have changed how optical systems can be designed and manufactured to decrease both the cost and the volume of the systems.

- **Storage Materials:** The availability of storage materials has been significantly improved, and now several materials for volume holographic storage are commercially available in quantity. Also, procedures for the optimization and characterization of photorefractive crystals have been developed. Materials are still critical for improved recording rates and for the future extension of holographic memories from the current write once and read many times (WORM) or read only memories (ROM) memory architectures to dynamic read/write memories.

Clearly, there have been many important advances since the 1970's. Essentially, the holographic storage effort of the 1970's did not have the supporting technology needed to have a chance of making a commercially viable memory. Whether or not holographic storage has a future now is still an open question. Currently, there is no technical impediment to making holographic memory systems, but cost and market niche are certainly important factors to consider when faced with competition from mature storage technologies such as magnetic, semiconductor, and conventional optical memories.

1.4 Outline of Thesis

The major sections of this thesis involve cross-talk calculations, photopolymer storage, and a 3–D holographic disk for data storage and correlation. Cross-talk is presented first, since it is inherent in any volume holographic memory or processor. Next DuPont's photopolymer is investigated as an example of a particular storage medium Then the holographic photopolymer disk is presented as a new holographic storage and processing architecture.

Chapter 2 details the cross-talk calculations. Cross-talk due to purely geometrical factors is calculated for Fourier plane holograms stored by angle, wavelength, phase codes, and rotation multiplexing. This is extended to image plane angle multiplexed holograms, and the effect of finite image contrast is also analyzed.

Chapter 3 compares the various multiplexing methods on the basis of cross-talk. The best geometrical arrangements to minimize the cross-talk noise are discussed. Then, the circumstances where cross-talk is the dominant noise source are determined.

Holographic recording characteristics of DuPont's HRF-150 photopolymer are investigated in Chapter 4. The modulation transfer function is determined and explained. The effect of intensity, fringe visibility, grating period, and grating tilt on diffraction efficiency is determined. The lateral spread of the polymerizing reaction is also investigated. A method for recording multiple holograms in DuPont photopolymer films is then explained. A new method for multiplexing holograms (peristrophic multiplexing) is then explained and demonstrated. This new technique significantly increases the storage capacity of thin films.

The details of a 3–D holographic disk-based correlator and storage device is introduced in Chapter 5. The experimental correlator generates full 2–D correlations using disk motion, and was experimentally validated using photopolymer film. The possible use of this architecture as a data storage system is examined. The geometrically limited storage capacity of such a system is determined as well as the power limited read-out rate.

Chapter 2

Cross-talk in Volume Holographic Memories

2.1 Introduction

Volume holography achieves high storage density by superimposing many holograms inside the same volume, but as the old adage says, "you don't get something for (sic) nothing." Part of the price for this increase in storage capacity is the amount of noise that the other non-Bragg matched holograms add to the desired reconstruction. Figure 2.1 shows a volume with two gratings inside of it. The reference beam, incident from the left, has the correct wavelength and angle to be Bragg matched to one of the gratings. This Bragg matched grating diffracts a strong signal beam, but the other grating, even though it is not Bragged matched, still diffracts some light. Therefore, in a holographic memory, the non-Bragg matched holograms in the volume are also reconstructed with lower efficiency and with distortions due to Bragg mismatch. This diffraction of light from non-Bragg matched gratings is called cross-talk noise. Cross-talk noise places an upper limit on the signal-to noise ratio (SNR) of the system, and therefore the storage capacity of the memory.

The original efforts to calculate cross-talk [150, 151, 152, 153, 154] were hindered by the lack of understanding about how to space the holograms in angle. Bragg selectivity applies to a change of angle in only one direction. The superposition of

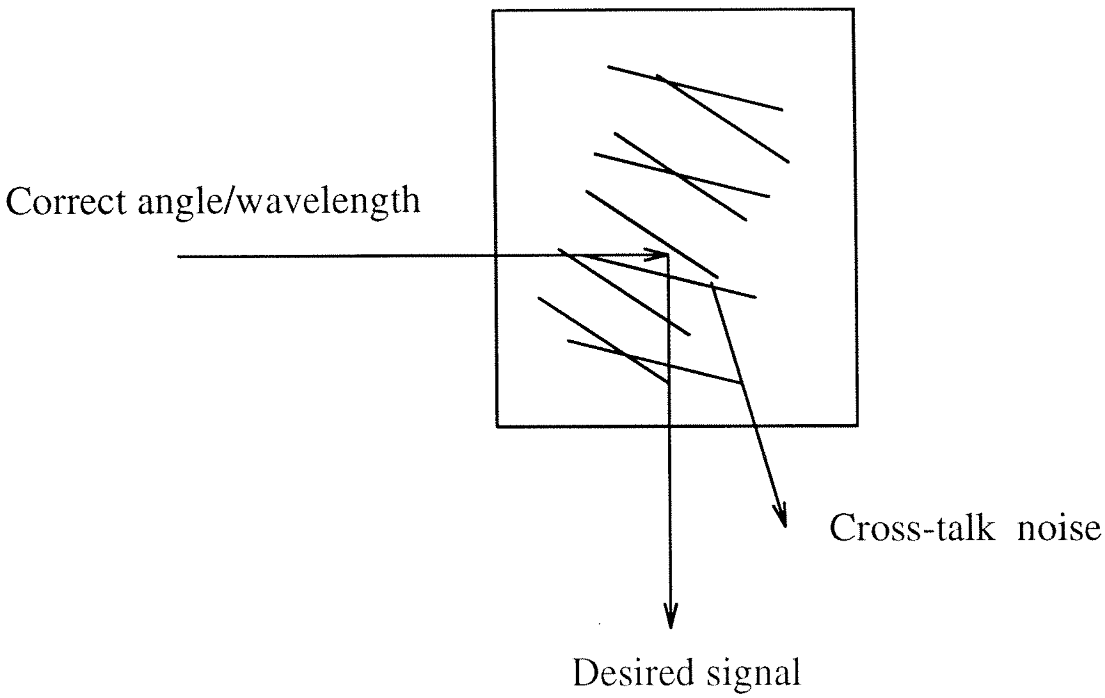

Figure 2.1: Cross-talk from non-Bragg matched gratings.

holograms can only (ignoring fractal sampling grids for the moment) be done by changing the reference beam angle in the plane of intersection. In the other direction, the gratings are very insensitive to changes in angle. This effect is called grating degeneracy. Grating degeneracy means that certain sets of angles in the reference and object beams are connected by a single grating. Most of the early calculations of cross-talk were dominated by this "first order" cross-talk noise. Schemes for eliminating cross-talk due to grating degeneracy, called fractal sampling grids, were derived and demonstrated by Psaltis et al. [155] and others [156, 157].

Other work focused on the effects of two-wave mixing, and using coupled-wave analysis to determine cross-talk for a small number of gratings [158] – [167]. Recently, it was shown that for low (less than 1%) throughput holograms, the cross-talk due to angular sidelobe overlap is the dominant cross-talk effect [168, 169]. Since for holographic memories, a large number of holograms means low diffraction efficiency, this geometrical cross-talk is the relevant cross-talk source.

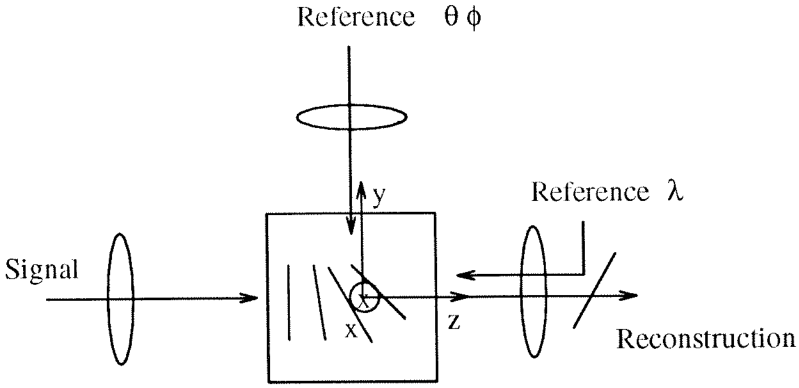

Figure 2.2: Geometry for wavelength, phase coded, and angle multiplexing.

The information storage capacity of volume holographic memories is limited by geometry and material dynamic range. The SNR is a convenient metric that we use to assess the storage capability of holographic memories. In this chapter we calculate the SNR due to cross-talk between holograms purely due to geometrical constraints. The derivation of the cross-talk for the various multiplexing methods we present here is analogous to the method used to by Gu et al. [170] for angle multiplexing and Curtis et al. [171, 172, 173, 174] for the other multiplexing methods.

2.1.1 Multiplexing Methods

Multiple holograms can be recorded in a material by changing either the reference beam angle [42, 43] (angle multiplexing), the recording wavelength [176, 175] (wavelength multiplexing), or by phase coding the reference beam [177, 178, 179]. These volume holographic memories have potentially high storage capacity and fast – page at a time – readout. The geometries used for recording are shown in Figure 2.2. In all geometries shown in Figure 2.2, the input data is presented on a spatial light modulator (SLM) from the left and detected on the right. For angle multiplexing, the reference is a plane wave input at a given angle (shown as 90° in Figure 2.2). Multiple holograms are recorded by changing the angle of the reference beam. Wavelength multiplexing is done in reflection geometry for maximum capacity. Multiplexing is accomplished by changing the wavelength of the recording beams. In phase-code multiplexing, the reference beam consists of a set of plane waves each with an individual phase. The set of phases is called a phase-code. Multiple holograms are recorded by changing the phase-code of the reference beam.

2.2 Wavelength Multiplexing

2.2.1 Introduction

In the past, most of the work has concentrated on angle multiplexing, primarily because convenient frequency-tunable light sources have not been available. With the advent of semiconductor and solid-state tunable lasers, there has been renewed interest in wavelength multiplexing. Rakuljic et al. [175] have argued that wavelength multiplexed memories have low cross-talk noise. The section contains two main results. First, we show that for the optimum counter-propagating reflection geometry, the SNR for wavelength multiplexed holograms saturates for a large number of holograms [181]. Second, we derive a closed-form expression for the SNR for a large number of holograms (more than several hundred) in a general reflection geometry which shows that, for a given SNR, cross-talk limits the size of the stored images.

2.2.2 Theory for Wavelength Multiplexing

Fourier-transform holograms are wavelength multiplexed in a volume holographic medium using the setup shown in Figure 2.3. A plane wave R_m is generated at a wavelength λ_m and at an angle θ with respect to the z axis by collimating light from a point source. This interferes inside the holographic medium with S_m – the Fourier-transform of the mth object image also of wavelength λ_m. By labeling the holograms $m = -M, -(M-1), ..., 0, ..., M$, the presence of these $N = 2M + 1$ holograms modulates the permittivity of the material such that the change in the permittivity

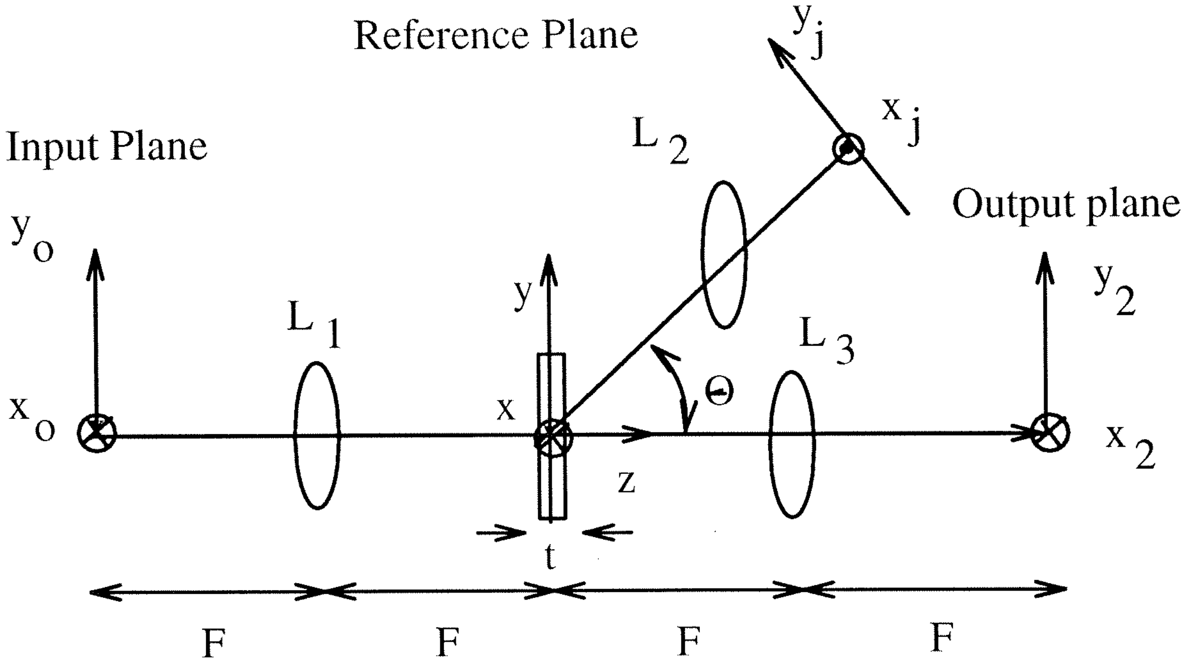

Figure 2.3: Recording and readout geometry for λ multiplexing.

of the medium can be written as

$$\Delta\epsilon \sim \sum_{m=-M}^{M} R_m^* S_m + c.c. \tag{2.1}$$

where *c.c.* is the complex conjugate term. The reference wave is given by

$$R_m = e^{ik_m \cdot r}, \tag{2.2}$$

where k_m is the wave vector coming from the reference point source with wavelength λ_m. In addition, using standard Fourier-optics analysis [182], the mth signal beam can be expressed as

$$S_m(r) \approx e^{i\frac{2\pi}{\lambda_m}z} \iint dx_o\, dy_o f_m(x_o, y_o) e^{-i\frac{2\pi}{\lambda_m F}(xx_o+yy_o)} e^{-i\frac{\pi z}{\lambda_m F^2}(x_o^2+y_o^2)}. \tag{2.3}$$

In the expression above, $f_m(x_o, y_o)$ is the m-th object image, x, y, z are the coordinates at the back focal plane of lens L_1, and F is the focal length of all three lenses L_1, L_2, L_3. By substituting Equations 2.2 and 2.3 into Equation 2.1, $\Delta\epsilon$ can be written out explicitly.

2.2.3 Calculation of Cross-talk

The recorded medium is illuminated with one of the reference plane waves. Ideally, this reconstructs the hologram associated with that particular reference. In what follows we will calculate the deviations of the reconstructed wave from the desired image. The diffracted plane wave component, $E(\vec{k_d})$, with wave vector $\vec{k}_{d,j}$ and wavelength λ_j, can be derived from standard scalar diffraction theory [183] (see Appendix 2.0 for details). The following expression assumes that the Born and paraxial approximations are valid.

$$E(\vec{k_d}) \approx \int d\vec{r'} e^{-i\vec{K}\cdot\vec{r'}} \Delta\epsilon(\vec{r'}), \tag{2.4}$$

where $\vec{K} = \vec{k}_{d,j} - \vec{k}_j$ and $\vec{k}_j$ is the illuminating reference beam with wavelength λ_j. The stored perturbation $\Delta\epsilon$ contains a grating vector component $\vec{K}$ that will give the desired response as a strong contribution to the integral in Equation 2.4. However, the finite volume over which the integration is carried out causes frequency components other than $\vec{K}$ to also yield non-zero contributions to the above integral. Therefore, Equation 2.4 describes both the diffracted light due to the desired S_j plus the noise due to the diffracted light from the other holograms.

Using Equations 2.1 – 2.4, the diffracted light due to the presence of the permittivity perturbation can be explicitly stated. This result can then be related to the detected pattern by using the paraxial approximation to describe how lens L_3 maps $k_{d,j}$ to a point x_2, y_2 at the output plane:

$$k_{d,j} = \Big(\frac{2\pi x_2}{\lambda_j F}, \frac{2\pi y_2}{\lambda_j F}, \frac{2\pi}{\lambda_j}(1 - \frac{x_2^2}{2F^2} - \frac{y_2^2}{2F^2})\Big). \tag{2.5}$$

Carrying out the integration over the volume of the medium, the electric field at the output plane can be written as

$$E(x_2, y_2) \approx \sum_{m=-M}^{M} \iint dx_o\, dy_o f_m(x_o, y_o)\ \mathrm{sinc}\Big(\frac{a}{2\pi}(\Delta K_{mjx} + \frac{2\pi}{F}(\frac{x_2}{\lambda_j} + \frac{x_o}{\lambda_m}))\Big)$$

$$\times \ \mathrm{sinc}\Big(\frac{b}{2\pi}(\Delta K_{mjy} + \frac{2\pi}{F}(\frac{y_2}{\lambda_j} + \frac{y_o}{\lambda_m}))\Big)$$
$$\times \ \mathrm{sinc}\Big(\frac{t}{2\pi}\Big(\Delta K_{mjz} + (\frac{2\pi}{\lambda_j} - \frac{2\pi}{\lambda_m}) + \frac{2\pi}{F^2}(\frac{x_o^2 + y_o^2}{\lambda_m} - \frac{x_2^2 + y_2^2}{\lambda_j})\Big)\Big). \quad (2.6)$$

Making use of the assumption that the transverse dimensions of the medium (a and b in Eq. 2.6) are much larger than the spatial bandwidth of the images so that the transverse sinc functions can be approximated as delta functions, the electric field at the output plane can be written as

$$\begin{aligned} E(x_2, y_2) \approx & \sum_{m=-M}^{M} f_m(\frac{-\lambda_m}{\lambda_j}x_2 - \frac{F\lambda_m}{2\pi}\Delta K_{mjx}, \frac{-\lambda_m}{\lambda_j}y_2 - \frac{F\lambda_m}{2\pi}\Delta K_{mjy}) \\ & \times \ \mathrm{sinc}\Big(\frac{t}{2\pi}\Big(\Delta K_{mjz} + (\frac{2\pi}{\lambda_j} - \frac{2\pi}{\lambda_m}) + \frac{\pi(x_2^2 + y_2^2)}{F^2}(\frac{\lambda_m}{\lambda_j^2} - \frac{1}{\lambda_j}) + \\ & \frac{\lambda_m}{\lambda_j F}(\Delta K_{mjx}x_2 + \Delta K_{myj}y_2) + \frac{\lambda_m}{4\pi}(\Delta K_{mjx}^2 + \Delta K_{mjy}^2)\Big)\Big), \end{aligned} \quad (2.7)$$

where $\Delta K_{mj} = k_m - k_j$ is the difference between the mth reference wave vector k_m, and the illuminating beam's wave vector k_j and $\Delta K_{mj\alpha}$ is the component of ΔK_{mj} in the α direction. In Equation 2.7, t is the thickness of the material in the z direction. Notice that when $k_m = k_j$, $E_j(x_2, y_2) = f_j(-x_2, -y_2)$ which is just the mirror-image of the desired stored image.

The cross-talk noise arises from the $m \neq j$ terms in Equation 2.7. We first write explicit expressions for the Bragg-mismatch terms:

$$\begin{aligned} \Delta K_{mjx} &= 0 \\ \Delta K_{mjy} &= -\left(\frac{2\pi}{\lambda_m} - \frac{2\pi}{\lambda_j}\right)\sin\theta \\ \Delta K_{mjz} &= -\left(\frac{2\pi}{\lambda_m} - \frac{2\pi}{\lambda_j}\right)\cos\theta \end{aligned} \quad (2.8)$$

where θ is the angle between the reference beam and the optical axis of the output plane. To estimate the noise-to-signal ratio (NSR) we divide the total average noise power by the magnitude squared of the signal. We assume that each pixel of the stored images is an independent random variable taking the values minus one and one with equal probability. In this case, the NSR is given by

$$\mathrm{NSR} = \sum_{m \neq j} \mathrm{sinc}^2 \Big(-t(\frac{1}{\lambda_m} - \frac{1}{\lambda_j}) \cos\theta - t(\frac{1}{\lambda_m} - \frac{1}{\lambda_j}) + \frac{t(x_2^2 + y_2^2)}{2F^2}(\frac{\lambda_m}{\lambda_j^2} - \frac{1}{\lambda_j}) - \frac{t\lambda_m y_2}{F\lambda_j}(\frac{1}{\lambda_m} - \frac{1}{\lambda_j}) \sin\theta + \frac{t\lambda_m}{2}(\frac{1}{\lambda_m} - \frac{1}{\lambda_j})^2 \sin^2\theta \Big). \quad (2.9)$$

In order to minimize the NSR, the spacing between the holograms in frequency (or wavelength) is chosen to place the center pixel of each hologram at the zero of the sinc function of the two adjacent holograms: $\Delta\nu = c/[t(1 + \cos\theta)] \equiv \Delta$.

2.2.4 SNR Results

In order to calculate the NSR using this frequency schedule, we assume that the individual frequencies are given in terms of $\nu_m = m\Delta + \nu_o$. Rewriting Equation 2.9 in terms of frequency and substituting in the expression for the individual frequencies results in

$$\mathrm{NSR} = \sum_{m \neq j} \mathrm{sinc}^2 \Big(-(m - j) - \frac{(x_2^2 + y_2^2)(j\Delta + \nu_o)}{2F^2(1 + \cos\theta)(m\Delta + \nu_o)}(m - j) - (\frac{j\Delta + v_o}{m\Delta + \nu_o}) \frac{y_2(m - j)}{F(1 + \cos\theta)} \sin\theta + \frac{c(m - j)^2}{2t(m\Delta + \nu_o)(1 + \cos\theta)^2} \sin^2\theta \Big). \quad (2.10)$$

The NSR is a function of the hologram number j (or equivalently the reconstructing λ_j) and the location at the output plane (x_2, y_2). Given t, ν_o, F, θ, and N, the above expression can be numerically evaluated . The NSR on the output plane for the hologram stored at the center frequency ($j = 0$) was calculated by numerically evaluating Equation 2.10 with $F = 30$ cm, $t = 1$ cm, $x_{2max} = y_{2max} = 1.5$ cm, $\nu_o = 6 \times 10^{14}$ Hertz, and $N = 401$ holograms. Figure 2.4 shows the output plane for $\theta = 0.0°$ while Figure 2.5 shows the output plane for $\theta = 15.0°$.

In both cases, the maximum NSR is at the edges of the output plane. Setting x_2 and y_2 to their maximum values, we can plot the worst case SNR vs hologram

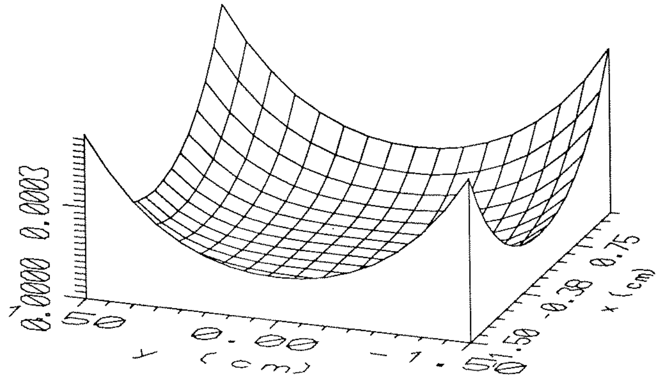

Figure 2.4: NSR at the output plane for the $j = 0$ hologram with $\theta = 0.0°$.

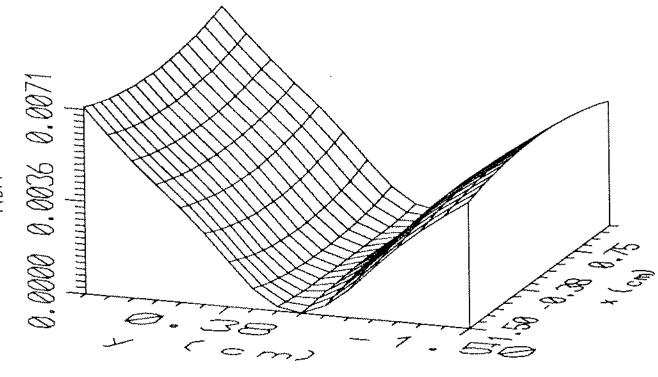

Figure 2.5: NSR at the output plane for the $j = 0$ hologram with $\theta = 15.0°$.

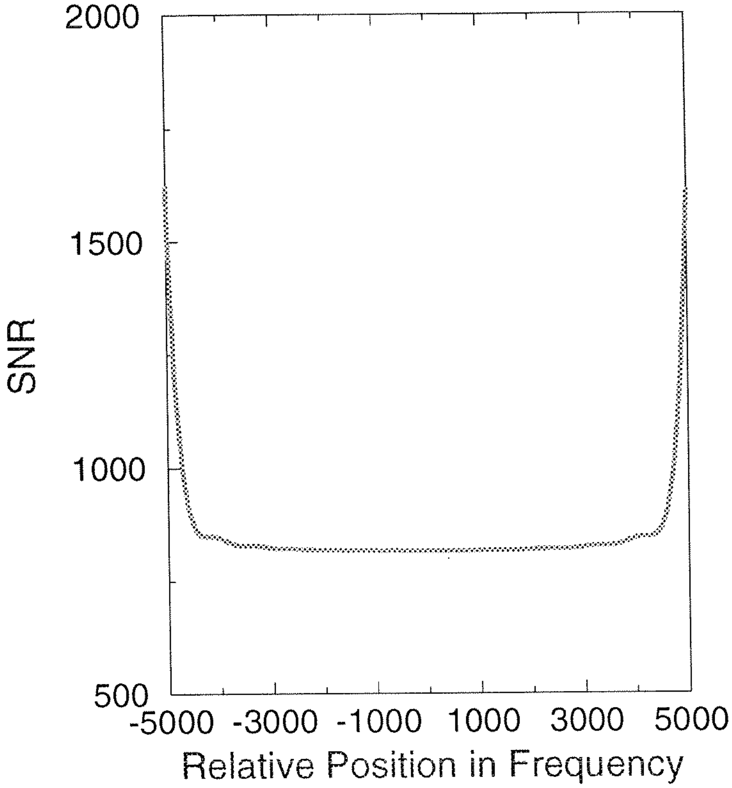

Figure 2.6: The SNR vs hologram number (j) for $N = 10,001$ holograms.

number (j). Figure 2.6 shows the results for $\theta = 0.0°$ with $N = 10{,}001$ holograms. Notice that the last ($j = \pm 5,000$) holograms for both cases has a SNR that is twice as large as the middle ($j = 0$) hologram. This is because the $j = \pm M$ holograms only have holograms on one side. Therefore, the minimum SNR hologram is always the middle hologram in the frequency schedule. However, even this worst case SNR is more than 800 for $\theta = 0.0°$ which is excellent.

From Figure 2.6 we know that the middle ($j = 0$) hologram has the minimum SNR and that the noise is symmetric about this hologram. Therefore, we can set $j = 0$ in Equation 2.10 and use it to find a closed-form solution for the maximum NSR. Let us first define a as follows:

$$a = \frac{(x_2^2 + y_2^2)}{2F^2(1 + \cos\theta)} + \frac{y_2}{F(1 + \cos\theta)} \sin\theta. \tag{2.11}$$

We can drop the last term in the argument of the sinc function in Equation 2.10

since it only becomes comparable to the other terms when m is large. When m is large the sinc function itself adds a negligible contribution to the summation in Equation 2.10. Assuming that $\frac{\nu_o}{m\Delta+\nu_o} \approx 1$ and using the identities $\sin(x+y) = \sin x \cos y + \cos x \sin y$ and $\sin^2 x = \frac{1}{2} - \frac{1}{2}\cos 2x$, Equation 2.10 can be written as

$$\mathrm{NSR}_{\max} = \frac{1}{\pi^2(1+a)^2} \times \left(\sum_{m=1}^{M} \frac{1}{m^2} - \sum_{m=1}^{M} \frac{\cos(2\pi a m)}{m^2} \right). \tag{2.12}$$

These sums can be approximately evaluated for M very large by using the sums:

$$\begin{aligned} \sum_{k=1}^{\infty} \frac{\cos kx}{k^2} &= \frac{\pi^2}{6} - \frac{\pi x}{2} + \frac{x^2}{4} \quad \text{for} \quad 0 \leq x \leq 2\pi, \\ \sum_{k=1}^{\infty} \frac{1}{k^2} &= \zeta(2) = \frac{\pi^2}{6}, \end{aligned} \tag{2.13}$$

from references [184] and [185] respectively. Using these expressions, the $\mathrm{NSR}_{\max}$ goes to

$$\mathrm{NSR}_{\max} = \frac{a}{(1+a)^2} - \frac{a^2}{(1+a)^2} \ . \tag{2.14}$$

This can be further simplified, if $a \ll 1$ (true for typical lens systems), into

$$\mathrm{NSR}_{\max} \approx a \approx \frac{(x_2^2 + y_2^2)}{2F^2(1+\cos\theta)} + \frac{y_2}{F(1+\cos\theta)} \sin\theta, \tag{2.15}$$

as the number of holograms stored becomes very large. Notice that the best SNR is achieved in the $\theta = 0°$ geometry. In this case the SNR becomes

$$\mathrm{SNR}_{\min} \approx \frac{4F^2}{(x_2^2 + y_2^2)}. \tag{2.16}$$

Figure 2.7 is a plot of the SNR at the worst point in the output plane ($x_2 = y_2 = 1.5$cm) vs the total number of holograms stored using the same parameters as given for Figures 2.4 and 2.5. Equation 2.15 above predicts that at $\theta = 0°$ the SNR goes to 800 and at $\theta = 15.0°$ the SNR goes to approximately 127. The plots show that at $N = 4,000$ holograms the SNR is 837 and 131 respectively , showing that the asymptotic expression we derived is in good agreement with the actual values for typical parameters.

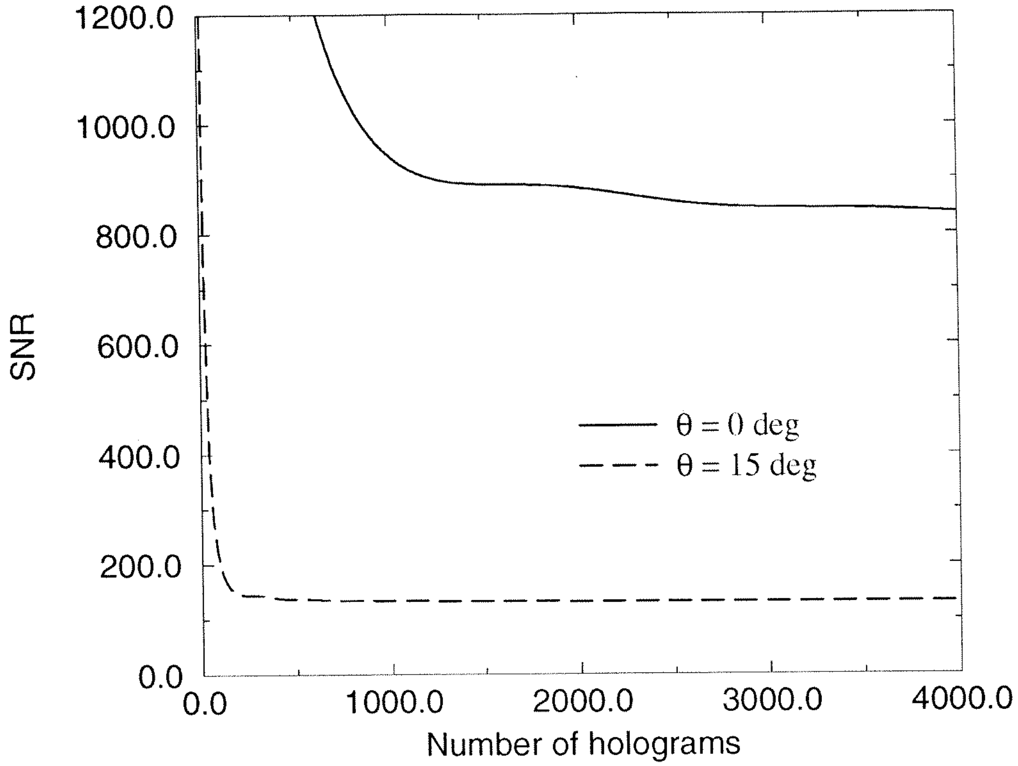

Figure 2.7: The SNR vs the total number of holograms.

2.3 Angle Multiplexing

2.3.1 Introduction

Cross-talk for angle multiplexed Fourier transform holograms is calculated for a recording schedule for which the center of each stored image coincides with the nulls of the selectivity function for the adjacent reference beams. The main result of this section is the closed-form expression that shows that the SNR goes down as one over the total number of holograms stored.

2.3.2 Theory for Angle Multiplexing

Fourier-transform holograms are angle multiplexed in a volume holographic medium using the setup shown in Figure 2.8. A plane wave R_m is generated with wavelength λ and at an angle θ with respect to the z axis by collimating light from a point source. To change the angle the point source is moved in the y_j direction. The angle is only

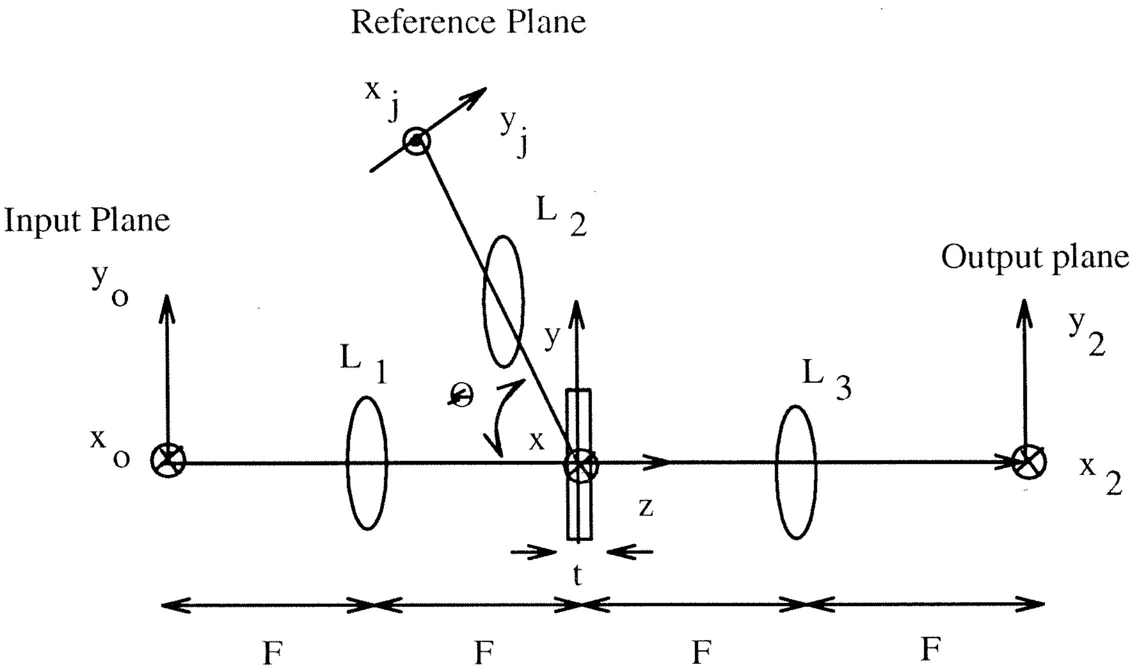

Figure 2.8: Recording and readout geometry for angle multiplexing.

changed in one dimension to eliminate the degenerate grating problem. This plane wave interferes inside the holographic medium with S_m – the Fourier-transform of the mth object image. By labeling the holograms $m = -M, -(M-1), ..., 0, ..., M$, the presence of these $N = 2M + 1$ holograms modulates the permittivity of the material such that the change in the permittivity of the medium can be written as

$$\Delta\epsilon \approx \sum_{m=-M}^{M} R_m^* S_m + c.c. \tag{2.17}$$

where $c.c.$ is the complex conjugate term. The reference wave is given by

$$R_m = e^{ik_m \cdot r}, \tag{2.18}$$

where k_m refers to the wave vector coming from the reference point source at y_m. In addition, using standard Fourier-optics analysis [182], the mth signal beam can be expressed as

$$S_m(r) \approx e^{i\frac{2\pi}{\lambda}z} \iint dx_o\, dy_o f_m(x_o, y_o) e^{-i\frac{2\pi}{\lambda F}(xx_o + yy_o)} e^{-i\frac{\pi z}{\lambda F^2}(x_o^2 + y_o^2)}. \tag{2.19}$$

In the expression above, $f_m(x_o, y_o)$ is the m-th object image, x, y, z are the coordinates at the back focal plane of lens L_1, and F is the focal length of all three lenses L_1, L_2, L_3. By substituting Equations 2.18 and 2.19 into Equation 2.17, $\Delta\epsilon$ can be written out explicitly.

2.3.3 Calculation of Cross-talk

In readout, the recorded medium is illuminated with one of the reference plane waves. Ideally, this would only reconstruct the hologram associated with that particular reference beam. In what follows, we will calculate the deviations of the reconstructed wave from the desired image. The amplitude of the diffracted plane wave components, $E(\vec{k}_d)$, with wave vectors $\vec{k}_d$, can be derived from standard scalar diffraction theory [183]. The following expression assumes that the Born and paraxial approximations are valid.

$$E(\vec{k}_d) \approx \int d\vec{r} e^{-i\vec{K}\cdot\vec{r}} \Delta\epsilon(\vec{r}), \tag{2.20}$$

where $\vec{K} = \vec{k}_d - \vec{k}_j$, $\vec{k}_j$ is the wave vector of the illuminating reference beam.

Lens L_3 maps each diffracted plane wave component with wave vector $\vec{k}_d$ to a point x_2, y_2 at the output plane given by:

$$\vec{k}_d = \left(\frac{2\pi x_2}{\lambda F}, \frac{2\pi y_2}{\lambda F}, \frac{2\pi}{\lambda}(1 - \frac{x_2^2}{2F^2} - \frac{y_2^2}{2F^2})\right), \tag{2.21}$$

assuming the paraxial approximation. Making use of the assumption that the transverse dimensions of the medium are much larger than the spatial bandwidth of the images, substituting relations 2.18, 2.17, 2.19, and 2.21 into Equation 2.20, and carrying out the integration over the volume of the medium, the electric field at the output plane can be written as

$$\begin{aligned} E(x_2, y_2) \approx & \sum_{m=-M}^{M-1} f_m(-x_2 - \frac{F\lambda}{2\pi}\Delta K_{mjx}, -y_2 - \frac{F\lambda}{2\pi}\Delta K_{mjy}) \\ \times \operatorname{sinc}\Bigg(\frac{t}{2\pi}\Bigg(\Delta K_{mjz} & + \frac{1}{F}(\Delta K_{mjx} x_2 + \Delta K_{mjy} y_2) + \frac{\lambda}{4\pi}(\Delta K^2_{mjx} + \Delta K^2_{mjy})\Bigg)\Bigg), \end{aligned} \tag{2.22}$$

where $\Delta\vec{K_{mj}} = \vec{k_m} - \vec{k_j}$ is the difference between the m-th reference wave vector $\vec{k_m}$ and the illuminating beam's wave vector $\vec{k_j}$. Also $\Delta K_{mj\alpha}$ is the component of $\Delta\vec{K_{mj}}$ in the α direction. In Equation 2.22, t is the thickness of the material in the z direction.

If $\Delta K_{mj\alpha} = 0$ for all m, j, α then $E(x_2, y_2) = N f_m(-x_2, -y_2)$ and we get our desired reconstruction. When $\Delta K_{mj\alpha} \neq 0$, cross-talk noise arises from the $m \neq j$ terms in Equation 2.22. We can write the components of $\Delta\vec{K_{mj}}$ in terms of the reference coordinates y_m and y_j:

$$\begin{aligned}
\Delta K_{mjx} &= 0, \\
\Delta K_{mjy} &= \frac{2\pi}{\lambda F}\cos\theta(y_j - y_m) + \frac{\pi}{\lambda F^2}\sin\theta(y_m^2 - y_j^2) \\
\Delta K_{mjz} &= \frac{2\pi}{\lambda F}\sin\theta(y_j - y_m) + \frac{\pi}{\lambda F^2}\cos\theta(y_j^2 - y_m^2),
\end{aligned} \qquad (2.23)$$

where θ is the angle between the normal to the reference plane and the optical axis of the input plane. To estimate the noise-to-signal ratio (NSR), we divide the total average noise power by the magnitude squared of the high signal level. We assume that each pixel of the stored images is an independent random variable taking the values minus one and one with equal probability. This results in

$$\mathrm{NSR} = \sum_m \operatorname{sinc}^2\left(\frac{t}{2\pi}\left(\Delta K_{mjz} + \frac{\Delta K_{mjy} y_2}{F} + \frac{\lambda \Delta K_{mjy}^2}{4\pi}\right)\right). \qquad (2.24)$$

The spacing between the reference pixels is chosen be $\Delta y = \frac{\lambda F}{t \sin\theta} \equiv \Delta$. This makes the sinc function of Equation 2.24 essentially zero at the center pixel ($y_2 = 0$) of each hologram and hence minimizes cross-talk at that location.

2.3.4 SNR Results

In order to calculate the NSR, we assume that $\theta = 90°$ to maximize capacity and that the reference pixels are spaced by Δ. Rewriting Equation 2.24 and keeping terms to

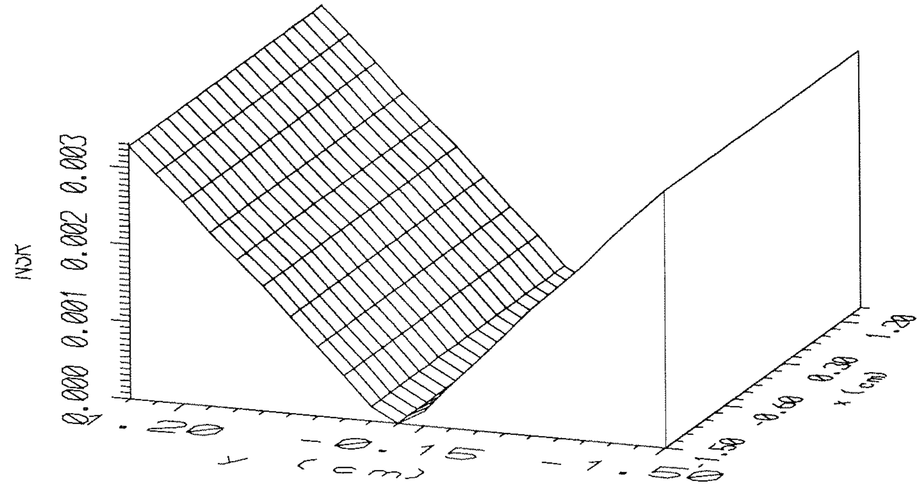

Figure 2.9: NSR at the output plane for the $j = 0$ hologram.

third order in (y/F) results in

$$\text{NSR} = \sum_{m \neq j} \operatorname{sinc}^2\left(\overset{j-m\,?}{\underline{m - j}} + \frac{y_2\lambda}{2Ft}(m^2 - j^2)\right). \tag{2.25}$$

The NSR is a function of the hologram number j (or equivalently the reconstructing angle) and the location at the output plane (x_2, y_2). Given t, λ, F, θ, and N, the above expression can be numerically evaluated . The NSR on the output plane for the hologram stored at the center angle ($j = 0$) was calculated by numerically evaluating Equation 2.25 with $F = 30$ cm, $t = 1$ cm, $x_{2max} = y_{2max} = 1.5$ cm, $\lambda = 500$ nm, and $N = 4{,}001$ holograms, and is shown in Figure 2.9. The maximum NSR is always at the edges of the output plane. Setting x_2 and y_2 to their maximum values, we can plot the worst case SNR vs hologram number (j). Figure 2.10 shows the results for $N = 4{,}001$ holograms. Notice that the last ($j = \pm 2{,}000$) holograms for both cases has a SNR that is twice as large as the worst hologram. This is because the $j = \pm M$ holograms only have holograms on one side. The minimum SNR hologram is close to these $j = \pm M$ holograms in the angular schedule with the middle hologram having

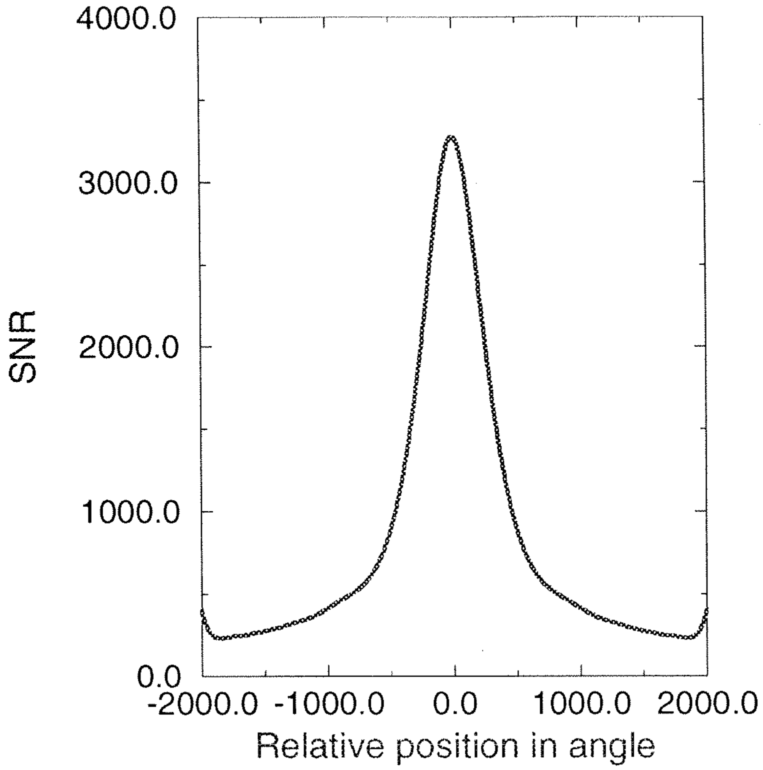

Figure 2.10: The SNR vs hologram position (j) for $N = 4,001$ holograms.

the best SNR. This is because the angular separation between holograms was set for the middle hologram and as the multiplexing angle deviates from this optimum angle the spacing required to put the holograms in the nulls changes. Thus the holograms multiplexed at an angle other than the center are noisier.

From Figure 2.10 we know that the end ($j = \pm M$) holograms have the minimum SNR and that the noise is symmetric about the center hologram. Therefore, we can set $j = M$ in Equation 2.25 (multiply the NSR by 2 make take into account the $j = \pm M$ holograms only have half the neighboring holograms) and use it to find a closed-form solution for the maximum NSR. By defining a as

$$a = \frac{\lambda y_2 M}{tF}, \tag{2.26}$$

rearranging the sum, and dropping one term because it does not contribute significantly to the sum, Equation 2.25 can be written as

$$\mathrm{NSR} = 2\sum_{n=1}^{N} \mathrm{sinc}^2(n + an). \tag{2.27}$$

Using the identities $\sin(x + y) = \sin x \cos y + \cos x \sin y$ and $\sin^2 x = \frac{1}{2} - \frac{1}{2}\cos 2x$, Equation 2.27 can be written as

$$\mathrm{NSR}_{\mathrm{max}} = \frac{1}{\pi^2(1+a)^2} \times \left(\sum_{n=1}^{N} \frac{1}{n^2} - \sum_{n=1}^{N} \frac{\cos(2\pi an)}{n^2}\right). \tag{2.28}$$

These sums can be approximately evaluated for N very large by using the sums:

$$\begin{aligned} \sum_{k=1}^{\infty} \frac{\cos kx}{k^2} &= \frac{\pi^2}{6} - \frac{\pi x}{2} + \frac{x^2}{4} \quad \text{for } 0 \le x \le 2\pi, \\ \sum_{k=1}^{\infty} \frac{1}{k^2} &= \zeta(2) = \frac{\pi^2}{6}, \end{aligned} \tag{2.29}$$

from references [184] and [185] respectively. Using these expressions, the $\mathrm{NSR}_{\mathrm{max}}$ goes to

$$\mathrm{NSR}_{\mathrm{max}} = \frac{a}{(1+a)^2} - \frac{a^2}{(1+a)^2}\ . \tag{2.30}$$

This can be further simplified, if $a \ll 1$ (true for typical lens systems), into

$$\mathrm{NSR}_{\mathrm{max}} \approx a \approx \frac{\lambda y_2 N}{2tF}, \tag{2.31}$$

as the number of holograms stored becomes very large. Thus the worst case SNR goes as

$$\mathrm{SNR}_{\mathrm{min}} \approx \frac{2tF}{\lambda y_2 N}. \tag{2.32}$$

Figure 2.11 is a plot of the SNR at the worst point in the output plane ($y_2 = 1.5$cm) vs the total number of holograms stored using the same parameters as given for Figures 2.9. Notice that the worst case SNR goes down as $1/N$ as predicted.

2.4 Phase Code Multiplexing

2.4.1 Introduction

The cross-talk between holograms multiplexed with Walsh-Hadamard phase codes is analyzed. Each hologram is stored with a reference beam that consists of N phase

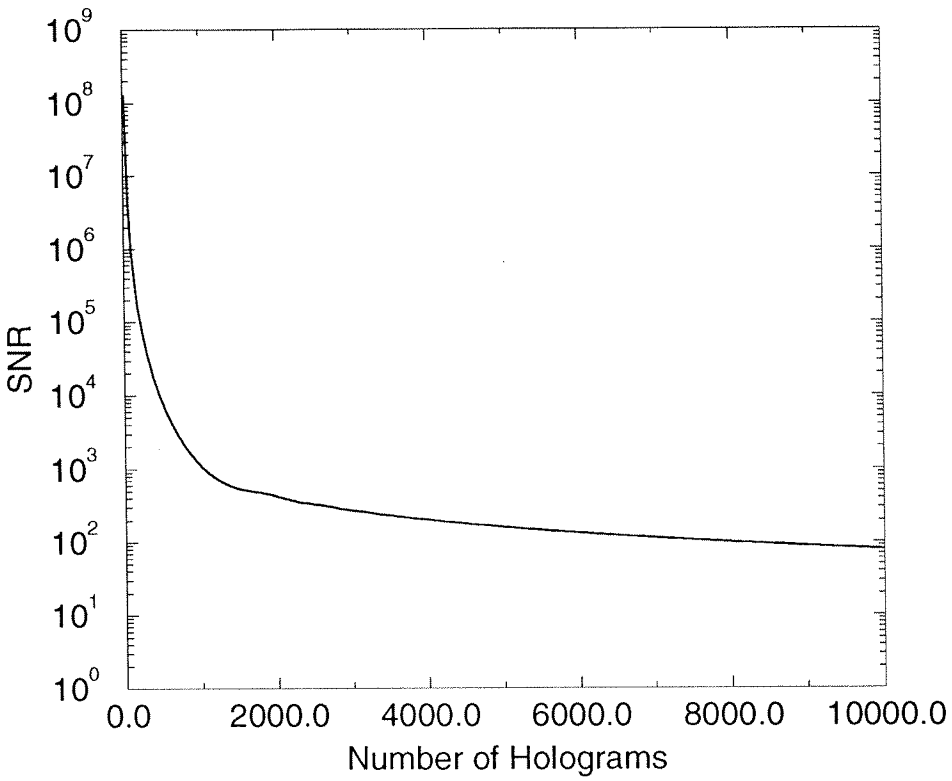

Figure 2.11: The SNR vs the total number of holograms.

coded plane waves. The SNR is calculated for a recording schedule for which the center of each stored image coincides with the nulls of the selectivity function for the adjacent plane wave components of the reference beam. The section contains two main results. First, we show that each phase-coded hologram has almost the same SNR upon reconstruction once we exclude one "bad" code. This is in contrast to θ multiplexing where holograms have much better SNR than the worst hologram depending on their angular position with respect to the other holograms. Second, we show that, the SNR for a given number of holograms is better for ϕ than for θ multiplexing.

2.4.2 Theory for Phase Code Multiplexing

Fourier-transform holograms are multiplexed in a volume holographic medium using the setup shown in Figure 2.12. The m-th hologram is formed by interfering the

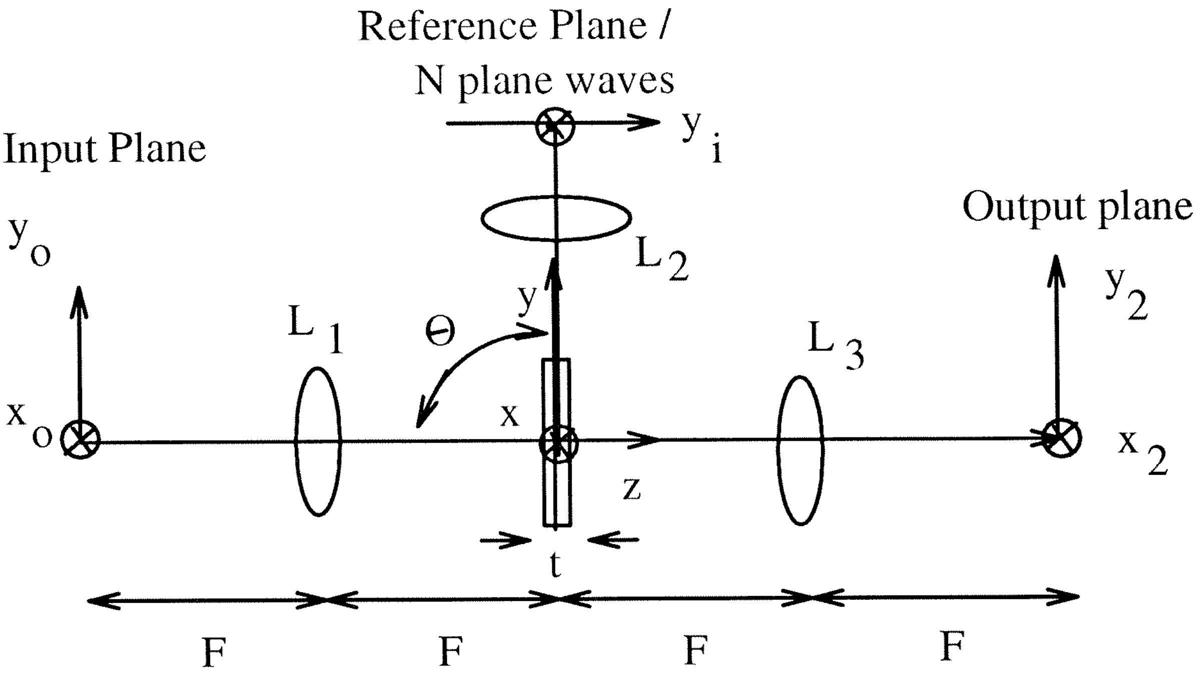

Figure 2.12: Recording and readout geometry for ϕ multiplexing.

signal with a reference beam R_m that consists of N plane wave components, with the phase of the i-th component being modulated by P_i^m:

$$R_m = \sum_{i=-N/2}^{N/2-1} P_i^m e^{ik_i \cdot r}. \tag{2.33}$$

In this section we assume that the P_i^m's are either 1 or -1 and that they are the Walsh-Hadamard codes which are orthogonal and easy to construct. The method used to construct them is given in reference [180]. The codes are constructed using the kernel

$$m = \begin{pmatrix} 1 & 1 \\ 1 & -1 \end{pmatrix}. \tag{2.34}$$

Taking this matrix larger matrices can be constructed by recursively substituting the previous matrix into a new matrix m_{i+1} shown below:

$$m_{i+1} = \begin{pmatrix} m_i & m_i \\ m_i & -m_i \end{pmatrix}. \tag{2.35}$$

This procedure generates orthogonal codes of length $2^{(i+1)}$. Examples of the first 64 codes are shown in Figure 2.13. In the figure above, white stands for a 1 and black

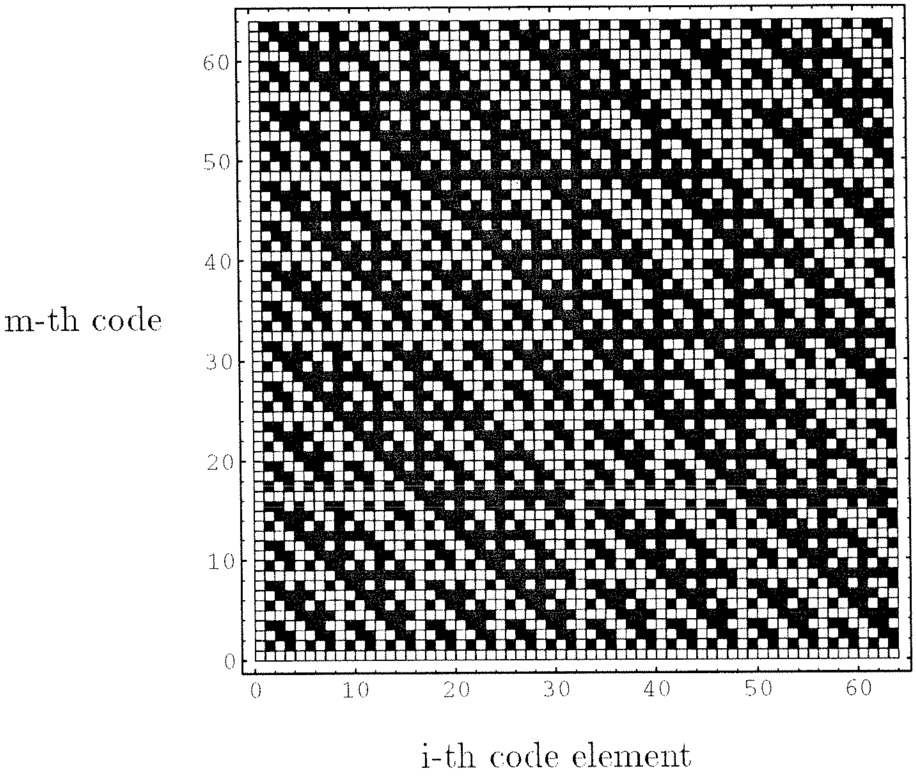

Figure 2.13: First 64 Walsh-Hadamard codes for ϕ multiplexing.

represents a - 1. Notice that the second code has the highest frequency – it alternates 1 and -1. Since Walsh-Hadamard codes are orthogonal and easy to construct they are a logical choice for phase codes for the evaluation of cross-talk in phase coded holographic memory.

This reference beam interferes inside the holographic medium with S_m – the Fourier-transform of the mth object image. The presence of these $N = 2M$ holograms, labeled $m = -M, -(M-1), ..., 0, ..., M-1$, modulates the permittivity of the material such that the change in the permittivity of the medium can be written as

$$\Delta\epsilon \approx \sum_{m=-M}^{M-1} R_m^* S_m + c.c. \tag{2.36}$$

where $c.c.$ represents the complex conjugate term. In addition, using standard Fourier-optics analysis [182], the m-th signal beam can be expressed as

$$S_m(x, y, z) \approx e^{i\frac{2\pi}{\lambda}z} \iint dx_o\, dy_o f_m(x_o, y_o) e^{-i\frac{2\pi}{\lambda F}(xx_o + yy_o)} e^{-i\frac{\pi z}{\lambda F^2}(x_o^2 + y_o^2)}. \tag{2.37}$$

In the expression above, $f_m(x_o, y_o)$ is the m-th object image, x, y, z are the coordinates at the back focal plane of lens L_1, and F is the focal length of all three lenses L_1, L_2, L_3. By substituting Equations 2.33 and 2.37 into Equation 2.36, $\Delta\epsilon$ can be written out explicitly.

2.4.3 Calculation of Cross-talk

In readout, the recorded medium is illuminated with one of the set of phase coded (P_j^n) reference plane waves. Ideally, this would only reconstruct the hologram associated with that particular reference set. In what follows, we will calculate the deviations of the reconstructed wave from the desired image. The amplitude of the diffracted plane wave components, $E(\vec{k_d})$, with wave vectors $\vec{k_d}$, can be derived from standard scalar diffraction theory [183]. The following expression assumes that the Born and paraxial approximations are valid.

$$E(\vec{k_d}) \approx \sum_{j=-M}^{M-1} \int d\vec{r}\; P_j^n e^{-i\vec{K}\cdot\vec{r}} \Delta\epsilon(\vec{r}), \tag{2.38}$$

where $\vec{K} = \vec{k_d} - \vec{k_j}$, $\vec{k_j}$ is the wave vector of one of the plane wave components that make up an illuminating reference beam, j is the read out pixel number corresponding to $\vec{k_j}$, and n is the read out codeword number.

Lens L_3 maps each diffracted plane wave component with wave vector $\vec{k_d}$ to a point x_2, y_2 at the output plane given by:

$$\vec{k_d} = \left(\frac{2\pi x_2}{\lambda F}, \frac{2\pi y_2}{\lambda F}, \frac{2\pi}{\lambda}(1 - \frac{x_2^2}{2F^2} - \frac{y_2^2}{2F^2})\right), \tag{2.39}$$

assuming the paraxial approximation. Making use of the assumption that the transverse dimensions of the medium are much larger than the spatial bandwidth of the images, substituting relations 2.33, 2.36, 2.37, and 2.39 into Equation 2.38, and carrying out the integration over the volume of the medium, the electric field at the output plane can be written as

$$\begin{aligned} E(x_2, y_2) \approx & \sum_{m=-M}^{M-1} \sum_{j=-M}^{M-1} \sum_{i=-M}^{M-1} P_j^n P_i^{*m} f_m(-x_2 - \frac{F\lambda}{2\pi}\Delta K_{ijx}, -y_2 - \frac{F\lambda}{2\pi}\Delta K_{ijy}) \\ & \times \operatorname{sinc}\left(\frac{t}{2\pi}\left(\Delta K_{ijz} + \frac{1}{F}(\Delta K_{ijx}x_2 + \Delta K_{ijy}y_2) + \frac{\lambda}{4\pi}(\Delta K_{ijx}^2 + \Delta K_{ijy}^2)\right)\right), \end{aligned} \tag{2.40}$$

where $\Delta\vec{K_{ij}} = \vec{k_i} - \vec{k_j}$ is the difference between the i-th reference wave vector $\vec{k_i}$ and the illuminating beam's wave vector $\vec{k_j}$. Also $\Delta K_{ij\alpha}$ is the component of $\Delta\vec{K_{ij}}$ in the α direction. In Equation 2.40, t is the thickness of the material in the z direction.

If $\Delta K_{ij\alpha} = 0$ for all i, j, α then $E(x_2, y_2) = N f_m(-x_2, -y_2)$ and we get our desired reconstruction. When $\Delta K_{ij\alpha} \neq 0$, cross-talk noise arises from the $m \neq n$ and the $m = n$ but $i \neq j$ terms in Equation 2.40. We can write the components of $\Delta\vec{K_{ij}}$ in terms of the reference coordinates y_i and y_j:

$$\Delta K_{ijx} \;=\; 0,$$

$$\begin{aligned}\Delta K_{ijy} &= \frac{2\pi}{\lambda F}\cos\theta(y_j - y_i) + \frac{\pi}{\lambda F^2}\sin\theta(y_i^2 - y_j^2)\\ \Delta K_{ijz} &= \frac{2\pi}{\lambda F}\sin\theta(y_j - y_i) + \frac{\pi}{\lambda F^2}\cos\theta(y_j^2 - y_i^2),\end{aligned} \tag{2.41}$$

where θ is the angle between the normal to the reference plane and the optical axis of the input plane. To estimate the noise-to-signal ratio (NSR), we divide the total average noise power by the magnitude squared of the high signal level. We assume that each pixel of the stored images is an independent random variable taking the values minus one and one with equal probability. Using the properties of Hadamard codes, the average NSR is given by

$$\mathrm{NSR} = \frac{1}{N^2}\sum_m \left|\sum_j \sum_{i \neq j} P_j^n P_i^m \operatorname{sinc}\left(\frac{t}{2\pi}\left(\Delta K_{ijz} + \frac{\Delta K_{ijy} y_2}{F} + \frac{\lambda \Delta K_{ijy}^2}{4\pi}\right)\right)\right|^2. \tag{2.42}$$

The spacing between the pixels of the phase code is chosen be $\Delta y = \frac{\lambda F}{t \sin\theta} \equiv \Delta$. This makes the sinc function of Equation 2.42 essentially zero at the center pixel ($y_2 = 0$) of each hologram and hence minimizes cross-talk at that location.

2.4.4 SNR Results

In order to calculate the NSR, we assume that $\theta = 90°$ to maximize capacity and that the reference pixels are spaced by Δ. Rewriting Equation 2.42 results in

$$\mathrm{NSR} = \frac{1}{N^2}\sum_m \left|\sum_j \sum_{i \neq j} P_j^n P_i^m \operatorname{sinc}\left(j - i + \frac{y_2 \lambda}{2Ft}(i^2 - j^2) + \frac{\lambda^3}{8t^3}(i^2 - j^2)^2\right)\right|^2. \tag{2.43}$$

Notice that if the sinc functions are replaced by the Kronecker δ_{ij} then there is no cross-talk. The NSR is a function of the location at the output plane in one dimension (y_2). Given t, λ, F, θ, and N, the above expression can be numerically evaluated. The NSR at the output plane for the n=8 hologram was calculated by numerically evaluating Equation 2.10 with F = 30 cm, t = 1 cm, $x_{2max} = y_{2max} =$

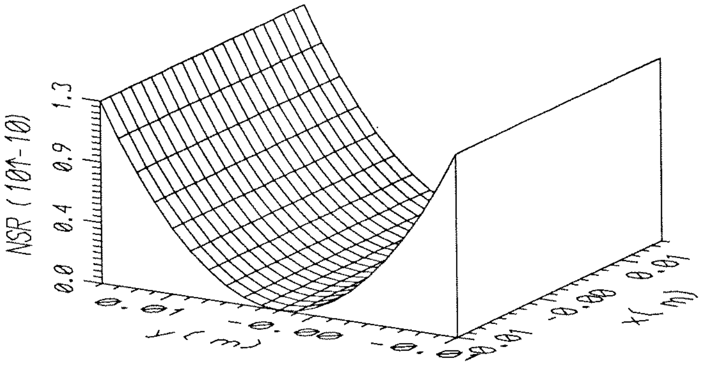

Figure 2.14: NSR vs position (x,y) on the output plane for the $n = 8$ hologram with $N = 16$.

1.5 cm, $\lambda = 500$ nm, and $N = 16$ holograms. Figure 2.14 shows the result plotted as a function of position on the output plane. Notice that the maximum NSR occurs at the y_2 boundary of the output plane.

Setting y_2 to its maximum value, we can plot the worst case SNR vs n, the phase code number. Figure 2.15 shows the result for $N = 64$ holograms. Code word number 2 is the highest frequency codeword (1,-1,1,-1 ...) and its structure complements the sinc function. Therefore when phase code number 2 is multiplied with the sinc function in Equation 2.43 we obtain a consistently positive product which adds up to a large NSR. Figure 2.16 plots the product $P_i^m \operatorname{sinc}\left(j - i + \frac{y_2\lambda}{2Ft}(i^2 - j^2) + \frac{\lambda^3}{8t^3}(i^2 - j^2)^2\right)$ as a function of m and $i' = i - M$ for $n = 6$ and $j = 0$. While this particular codeword has poor SNR, the others average to a much higher SNR. The other codes in Figure 2.15 that have poor SNR are noisy due to cross-talk from code 2. By taking out codeword number 2, it is possible to record holograms that have the same SNR

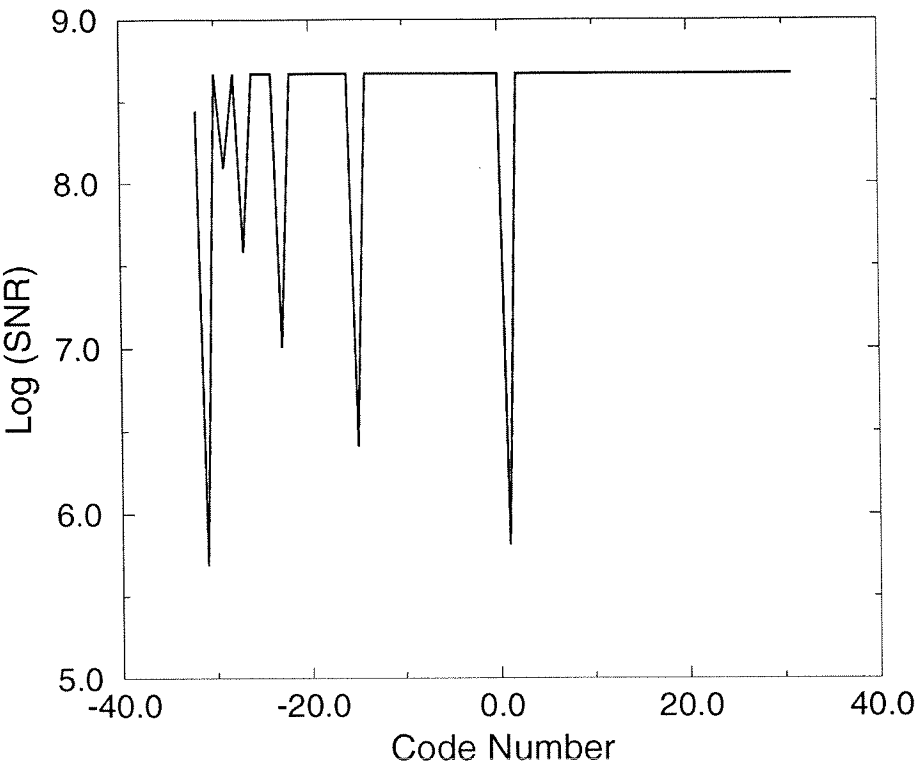

Figure 2.15: The log(SNR) vs hologram code number for $N = 64$ holograms.

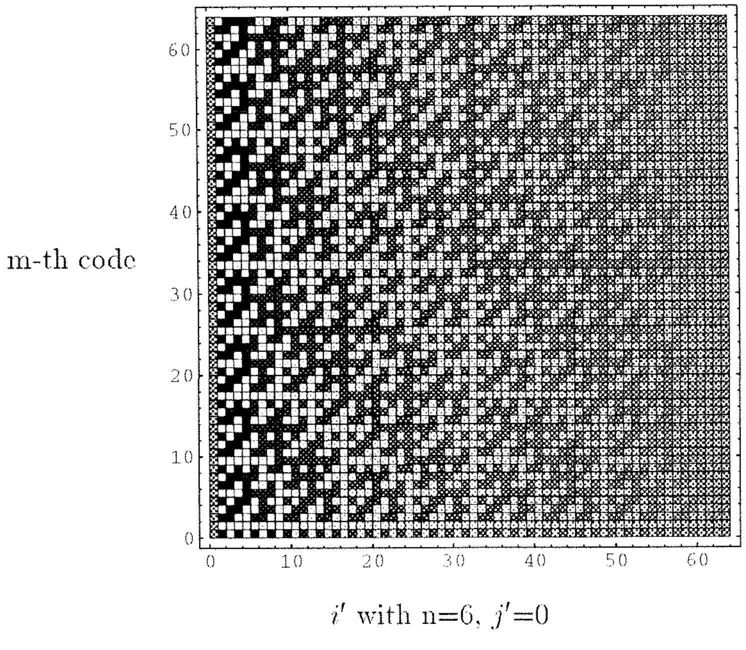

Figure 2.16: Plot of P_i^m sinc$\left(j - i + \frac{y_2\lambda}{2Ft}(i^2 - j^2) + \frac{\lambda^3}{8t^3}(i^2 - j^2)^2\right)$ as a function of m and $i' = i - M$ for $n = 6$ and $j = 0$.

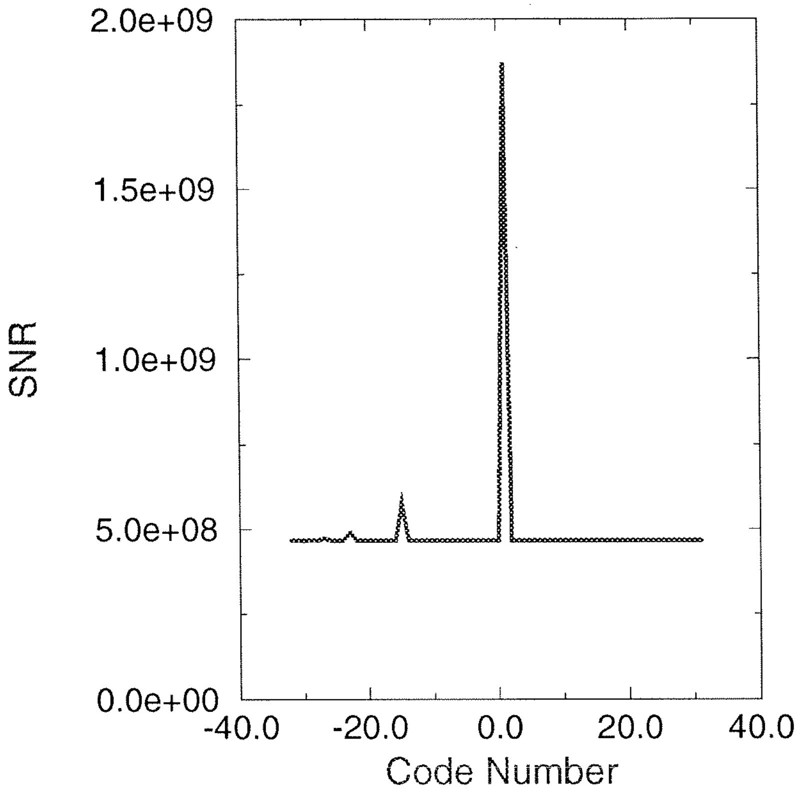

Figure 2.17: The SNR vs hologram code number without code 2.

(to a couple of decimal places) except for a few holograms that have better SNR than the others, as shown in Figure 2.17. This result is different from θ multiplexing [170] where most holograms have better SNR than the worst hologram depending on their angular position with respect to the other holograms.

Figure 2.18 shows the worst case SNR for ϕ and θ multiplexing with the same parameters as listed above. When using codeword number 2, the worst case SNR decreases very quickly for ϕ multiplexing. Taking this codeword out and recording $2^n - 1$ holograms with 2^n plane wave references, results in worst case SNR that is about 3 orders of magnitude better than θ multiplexing. If we take the SNR for θ multiplexing at the maximum y_2, averaged over all holograms, we obtain an average SNR that is still more than two orders of magnitude less than for ϕ multiplexing for large N. Therefore, well chosen phase codes suppress, even on average, the cross-talk. For λ multiplexing, the worst case SNR for 500 holograms, with all other parameters

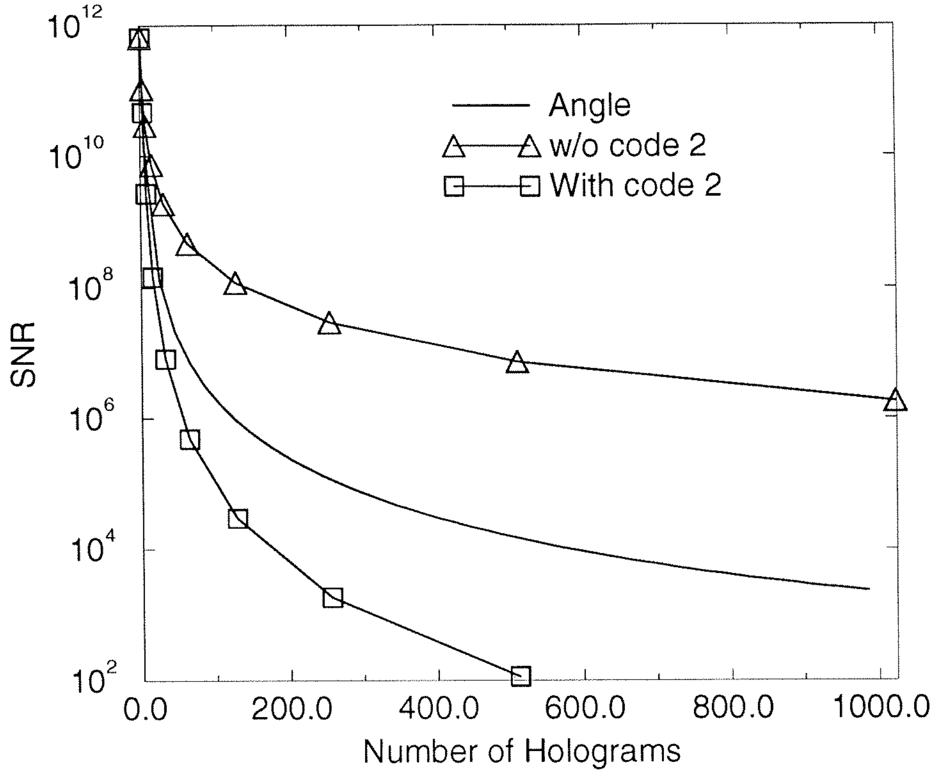

Figure 2.18: The SNR vs the total number of holograms for ϕ (with and w/o code 2) multiplexing, and θ multiplexing.

the same as in Figure 2.18, is 1.4×10^3 [171], compared to 10^7 for ϕ multiplexing and 10^4 for θ multiplexing. We have not calculated the cross-talk for ϕ multiplexing beyond 1024 holograms. Notice that the cross-talk SNR is very high in all cases, indicating that other system imperfections will most likely determine the fidelity of the reconstruction in practice.

2.5 Rotation Multiplexing

2.5.1 Introduction

Cross-talk for holograms multiplexed by rotating the storage media is calculated and compared to the angle multiplexed case. Brady and Psaltis [186] argue that rotation multiplexing can potentially have higher storage capacity than angle multiplexing since more of the grating space is accessible. Assuming that the media is a rectan-

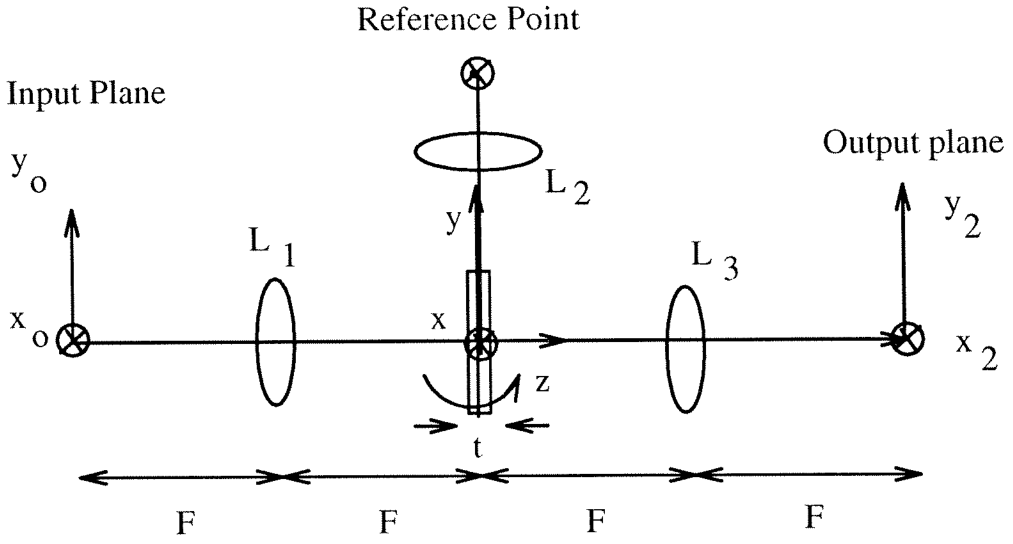

Figure 2.19: Recording and readout geometry for rotation multiplexing.

gular bar, the worst case SNR for rotation multiplexing is shown to have the same dependence on the number of holograms stored as angle multiplexing. For the case of a cylinder, the SNR is shown to saturate as the number of holograms

2.5.2 Storing Rotation Multiplexed Holograms

Fourier-transform holograms are rotation multiplexed in a volume holographic medium using the setup shown in Figure 2.19. A plane wave R_m is generated by collimating light from a reference point source. This interferes inside the holographic medium with S_m – the Fourier-transform of the mth object image and stores a single hologram. Multiple holograms are stored by rotating the medium around the x axis between each new hologram. The holograms are then stored in rotated (x'_m, y'_m) reference systems as shown in Figure 2.20. Notice that positive rotation is shown as counter-clockwise.

We will define the holograms that are currently being reconstructed as the origin of rotation for θ_m, and then label all other holograms with respect to this hologram at rotation θ_i. By labeling the reconstructed holograms as $i = -M, -(M-1), ..., 0, ..., M$,

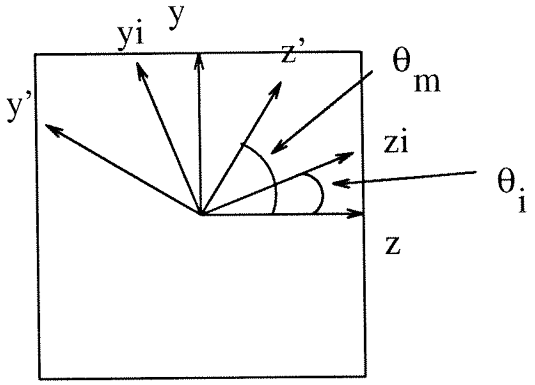

Figure 2.20: Rotated coordinate systems defining θ_m and θ_i.

the presence of these $N = 2M + 1$ holograms modulates the permittivity of the material as

$$\Delta\epsilon \approx \sum_m R_m^* S_m + c.c. \tag{2.44}$$

where *c.c.* is the complex conjugate term. Since we rotate the entire setup instead of the storage media, expressions for the reference and signal beams can easily be expressed. The reference wave coincides with the y_i-axis and is given by

$$R_m = e^{-i\frac{2\pi}{\lambda}y_m}. \tag{2.45}$$

In addition, using standard Fourier-optics analysis [182], the mth signal beam can be expressed as

$$S_m(r) \approx e^{i\frac{2\pi}{\lambda}z'_m} \iint dx_o\, dy_o f_m(x_o, y_o) e^{-i\frac{2\pi}{\lambda F}(xx_o + y'_m y_o)} e^{-i\frac{\pi z'_m}{\lambda F^2}(x_o^2 + y_o^2)}. \tag{2.46}$$

In the expression above, $f_m(x_o, y_o)$ is the m-th object image, and F is the focal length of all three lenses L_1, L_2, L_3. By substituting Equations 2.45 and 2.46 into Equation 2.44, $\Delta\epsilon$ can be written out explicitly.

2.5.3 SNR Calculation for Rotation Multiplexing in Rectangular Media

A rectangular recording medium is illuminated with a reference plane wave in the y_i, z_i coordinate system. Ideally, this reconstructs the i-th hologram associated with that particular rotation. In what follows, we will calculate the deviation of the reconstructed wave from the desired image. The amplitudes $E(\vec{k_d})$ of the diffracted plane wave components with wave vectors $\vec{k_d}$ can be derived from standard scalar diffraction theory [183]. The following expression assumes that the Born and paraxial approximations are valid (small rotations).

$$E(\vec{k_d}) \approx \int d\vec{r}\; e^{-i\vec{K}\cdot\vec{r}} \Delta\epsilon(\vec{r}), \tag{2.47}$$

where $\vec{K}\cdot\vec{r} = \vec{k_d}\cdot\vec{r_m} + \frac{2\pi}{\lambda}y_i$, and $-\frac{2\pi}{\lambda}y_i$ is the wave vector of the illuminating reference beam. Using Equations 2.44 – 2.47, we can solve explictly for the diffracted light due to the presence of the permittivity perturbation. This result can then be related to the detected pattern by using the paraxial approximation to describe how lens L_3 maps k_d to a point x_2, y_2 at the output plane:

$$\vec{k_d} = \left(\frac{2\pi x_2}{\lambda F}, \frac{2\pi y_2}{\lambda F}, \frac{2\pi}{\lambda}(1 - \frac{x_2^2}{2F^2} - \frac{y_2^2}{2F^2})\right). \tag{2.48}$$

Making use of the assumption that the height of the medium in the x direction is much larger than the spatial bandwidth of the images (forces the resulting sinc function to a delta function in x). Transformed back into x, y, z cordinates and integrating over the volume of the media, the electric field at the output plane can be written as

$$\begin{aligned} E(x_2, y_2) \;&\approx\; \sum_m \int dy_o\; f_m(-x_2, yo) \\ \times \frac{\sin(At\cos\theta_i + Bt\sin\theta_i)}{At\cos\theta_i + Bt\sin\theta_i}\; &\frac{\sin(Bt\cos\theta_i - At\sin\theta_i)}{Bt\cos\theta_i - At\sin\theta_i}\;. \end{aligned} \tag{2.49}$$

In Equation 2.49, t is one half of the thickness of the material in the y and z directions, while B is given by

$$B = -\frac{2\pi y_2}{\lambda F}\sin\theta_m - \frac{\pi y_2^2}{\lambda F^2}\cos\theta_m + \frac{2\pi}{\lambda}\sin\theta - \frac{2\pi y_o}{\lambda F}\sin\theta_m + \frac{\pi y_o^2}{\lambda F^2}\cos\theta_m, \tag{2.50}$$

and A by

$$A = \frac{\pi y_o^2}{\lambda F^2}\sin\theta_m + \frac{2\pi y_o}{\lambda F}\cos\theta_m + \frac{2\pi y_2}{\lambda F}\cos\theta_m - \frac{\pi y_2^2}{\lambda F^2}\sin\theta_m + \frac{2\pi}{\lambda}(1-\cos\theta_m). \quad (2.51)$$

Equation 2.49 can be approximated by letting the first sinc function go to a δ function with integration of y_o. Using the condition that the argument of the δ function must be zero, and that the angles are small, results in y_o being given by

$$y_o = -y_2 - \frac{F\theta_m^2}{2} - F\theta_m\theta_i. \quad (2.52)$$

Substituting this expression for y_o into the last sinc and discarding terms that are more than order 3 in θ gives an expression for the scattered electric field. We can estimate the noise-to-signal ratio (NSR) by dividing the total average noise power by the signal's magnitude squared. Assuming that each pixel of the stored images is an independent random variable taking the values minus one and one with equal probability, the NSR is given by

$$\mathrm{NSR} = \sum_{m\neq 0} \mathrm{sinc}^2\left(\frac{L}{\lambda}\theta_m + \frac{Ly_2}{2\lambda F}\theta_m^2 + \frac{Ly_2}{\lambda F}\theta_m\theta_i\right), \quad (2.53)$$

with $L = 2t$ as the thickness of the bar in the y and z directions.

In order to minimize the NSR, the rotational angle between the holograms is chosen to place the center pixel ($y_2 = 0$) of each hologram at the zero of the sinc function of the adjacent holograms. This leads to a rotational angle of $\Delta\theta_m = \frac{\lambda}{L}$. In order to calculate the NSR using this rotational schedule, we assume that the individual rotations are given in terms of $\theta_m = m\frac{\lambda}{L}$. The NSR is a function of the hologram position in the recording sequence i (implicit in the limits of the sum), the location at the output plane (y_2), and the total number of holograms stored (N). Given L, F, λ, and N, the above expression can be numerically evaluated.

The NSR on the output plane for the $i = 100$ hologram was calculated by numerically evaluating Equation 2.53 with $F = 30$ cm, $L = 1$ cm, $x_{2max} = y_{2max} =$

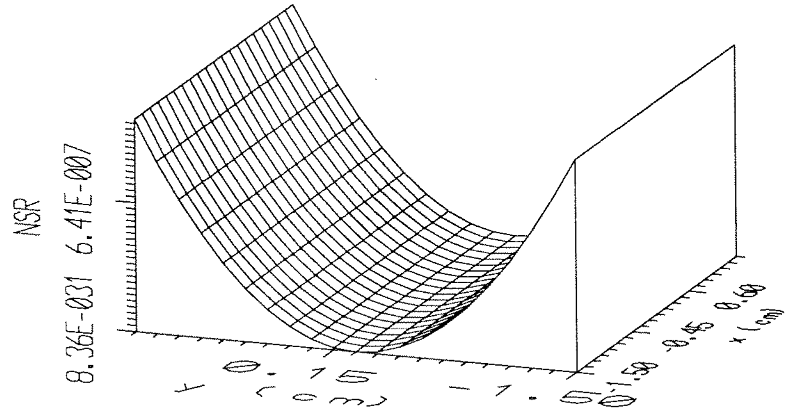

Figure 2.21: NSR vs position on the output plane for rectangular media.

1.5 cm, λ = 500 nm, N = 201 and is shown in Figure 2.21. The $y_2 = -1.5$ side of the reconstruction has slightly more noise than the other side of the image. This is because the gratings on this side of the image are closer to the other holograms' gratings in k-space. The $i = -100$ hologram has an output plane that is similar to Figure 2.21 but the largest NSR is at positive y_2. Figure 2.22 shows the SNR at the worst location on the output plane for 4001 holograms vs i (position in rotation). This is similar to the result given for angle multiplexing where the center holograms – zero rotation – are better than the holograms at large rotation (large angle). Figure 2.23 shows the minimum SNR (worst case in both position on output plane and in hologram number i) vs the total number of holograms stored. This follows exactly the curve for angle multiplexing given in reference [170]. Therefore, for both rotation and angle multiplexing in rectangular media, SNR decreases as $1/N$.

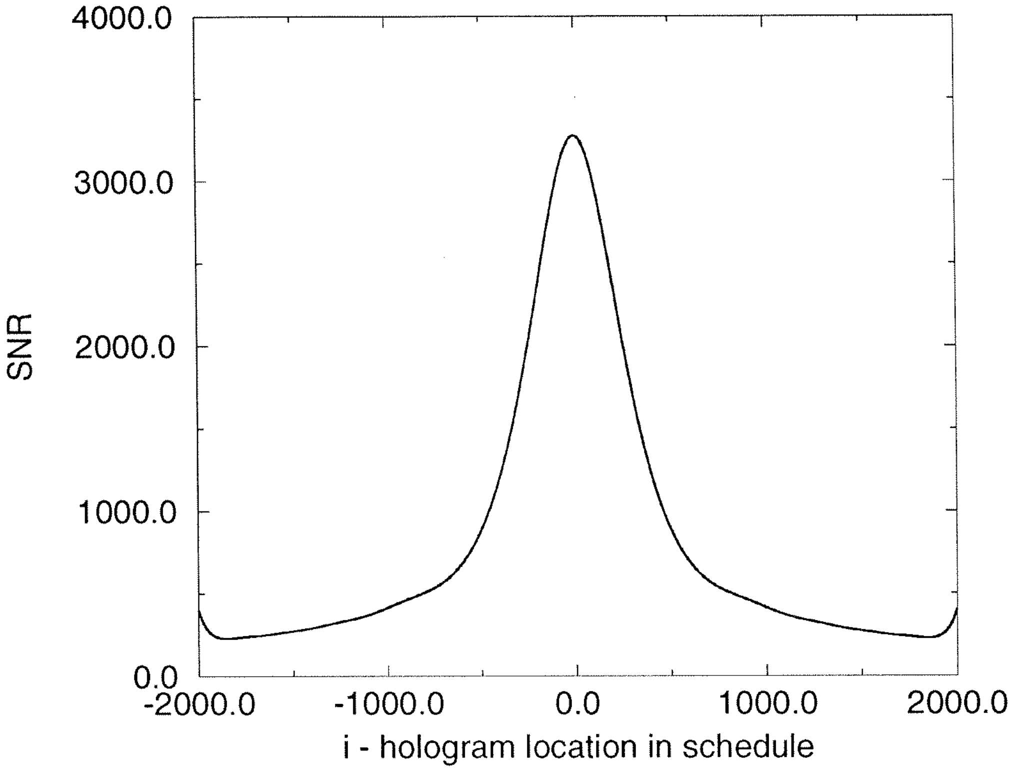

Figure 2.22: SNR vs hologram position in recording schedule.

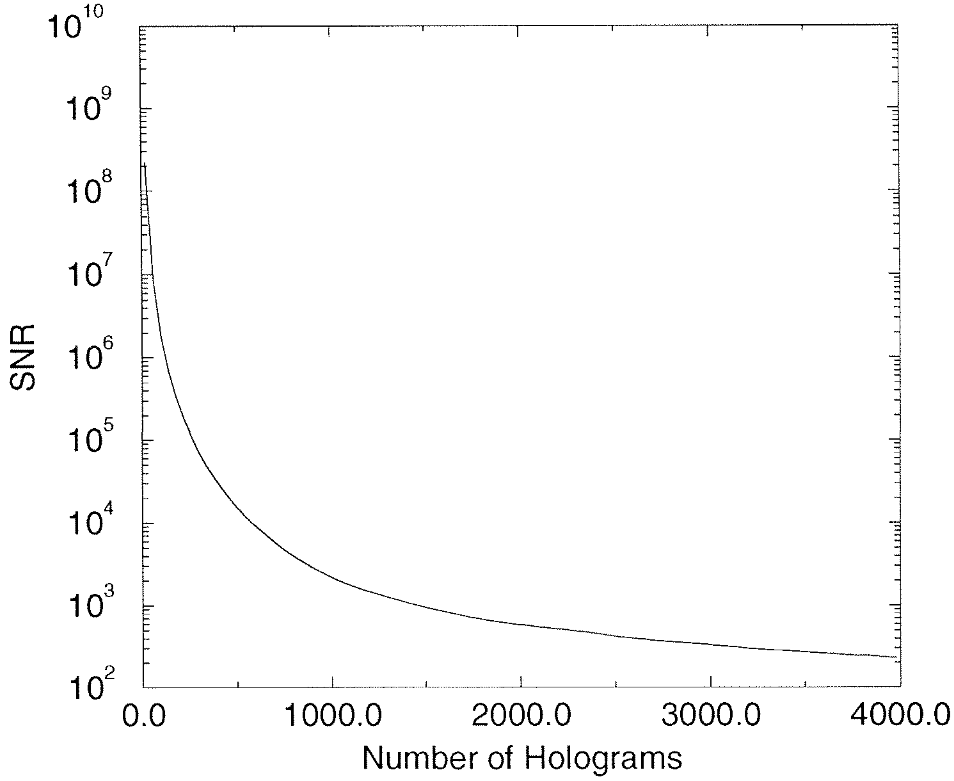

Figure 2.23: SNR vs the number of holograms stored for rectangular media.

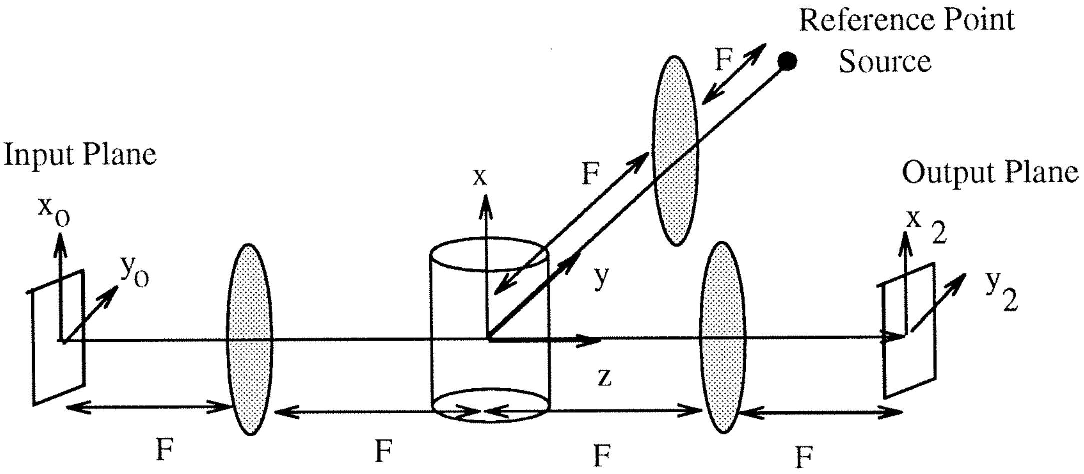

Figure 2.24: Recording and readout geometry for rotation multiplexing in a cylinder.

2.5.4 SNR Calculation for Rotation Multiplexing in a Cylinder

Fourier-transform holograms are recorded in a cylinder using the same setup as in Figure 2.24. The cylinder is situated such that it traces out a circle in the $y-z$ plane with radius r_o, and holograms are multiplexed by rotating the cylinder around the x axis. Ignoring refraction at the surface (the cylinder is surrounded by an index matching material, for instance), Equations 2.44 – 2.48 are identical except that the integral in relation 2.47 is now over the volume of the cylinder. Making use of the assumption that the height of the medium in the x direction is much larger than the spatial bandwidth of the images (again letting the resulting sinc function go to a delta function in x), but before integrating over the volume of the media, transformed into cylindrical coordinates, the electric field at the output plane can be written as

$$E(x_2,y_2) \approx \sum_m \int dy_o \; f_m(-x_2,y_o) \int_0^{r_o} dr \; 2r \int_0^{\pi} d\phi \; e^{-ir\sqrt{A^2+B^2}\cos\phi} \qquad (2.54)$$

where A and B are given in relations 2.50 and 2.51. The resulting integrals can be solved using

$$\int_0^{\pi} e^{i\beta\cos x}\cos(nx)dx = i^n \pi J_n(\beta) \qquad (2.55)$$

[187] and

$$\int_0^1 x^{v+1} J_v(ax)dx = a^{-1} J_{v+1}(a) \tag{2.56}$$

[188]. Using Gegenbauer's formula [189] to simplify gives the electric field as

$$E(x_2, y_2) \approx \sum_m \int dy_o \, f_m(-x_2, yo) \sum_{k=0}^{\infty} \frac{J_1(r_oA)}{r_oA} \frac{J_1(r_oB)}{r_oB} (1+k)C_k^1(0) \tag{2.57}$$

where the $C_k^v()$'s are the Gegenbauer polynomials. Using $J_1(x)/x$ as a δ function, as we did earlier with the sinc functions, leads to the requirement that $r_oA = 0$. Using this requirement to solve for y_o yields

$$y_o = -y_2 - \frac{F\theta_m^2}{2}, \tag{2.58}$$

which is similar to the expression for y_o found before. Substituting this result into our expression for B, and using the properties of $C_k^1(0)J_k(r_oA)/(r_oA)$ as r_oA approaches zero, results in a simplified expression for the electric field. The noise-to-signal ratio is again calculated by dividing the total average noise power by the magnitude squared of the signal. With the same assumptions that each pixel of the stored images is an independent random variable taking the values minus one and one with equal probability, the NSR is given by

$$\text{NSR} = 4 \sum_{m \neq 0} \frac{\left[J_1\left(\frac{\pi D}{\lambda}\theta_m + \frac{\pi D y_2}{2\lambda F}\theta_m^2\right)\right]^2}{\left(\frac{\pi D}{\lambda}\theta_m + \frac{\pi D y_2}{2\lambda F}\theta_m^2\right)^2}, \tag{2.59}$$

where D is the diameter of the cylinder.

SNR Results for Cylinder

In order to minimize the NSR, the spacing between the holograms in rotation is chosen to place the center pixel ($y_2 = 0$) of each adjacent hologram at the zeroes of the $J_1(x)/x$ function. Locating the zeroes was done by numerically evaluating the

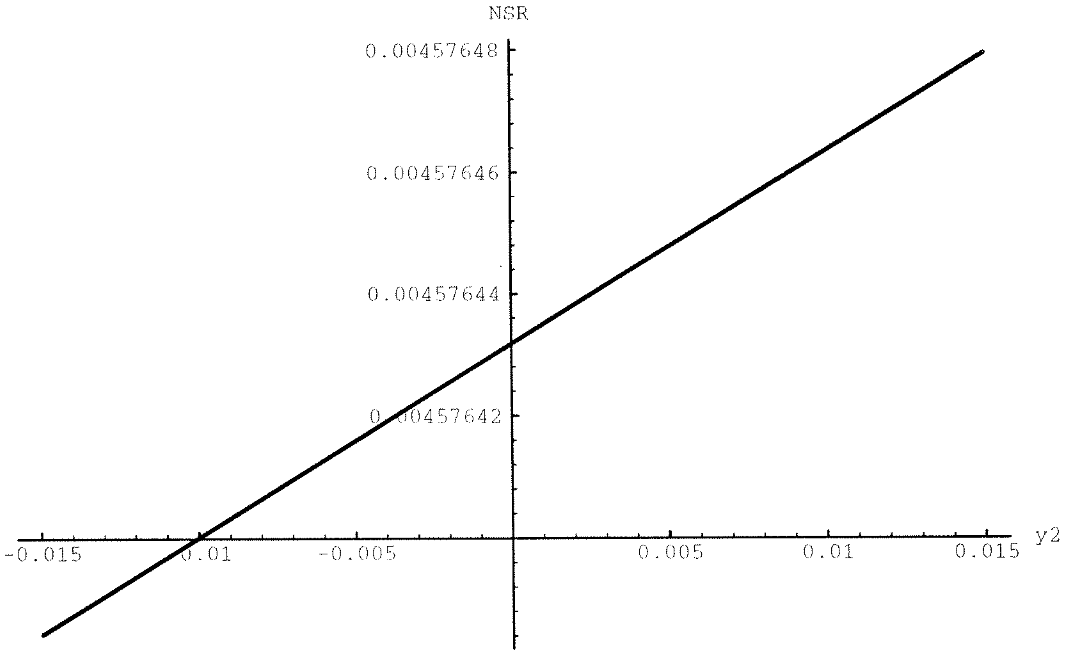

Figure 2.25: NSR vs position on the output plane for cylindrical media for the hologram stored at the furthest clockwise position.

$J_1(x)/x$ function. Compared to the rectangular media spacing ($\frac{\lambda}{L}$) the first zero is approximately 1.22 times larger, the second 2.23 times larger, and the third zero has 3.23 times larger rotation between holograms. This means that the holograms cannot be multiplexed as close together when using cylindrical media.

Using the same parameters as for the rectangular media ($D = L = 1$cm), Equation 2.59 can be numerically evaluated. Figure 2.25 shows the NSR versus y_2 (position on the output plane) for the hologram that is stored at the furthest clockwise position with a total of 21 holograms stored. Again the positive y_2 side is noisier since its grating vectors are closer to the other holograms. The NSR is plotted against position on the output plane for the center hologram in Figure 2.26. In this hologram, the noise is symmetric since there are an equal number of holograms on each side. The worst noise for all holograms occurs at one of the edges of the output plane – the one which is closest to the largest number of holograms. Taking the noise at the worse

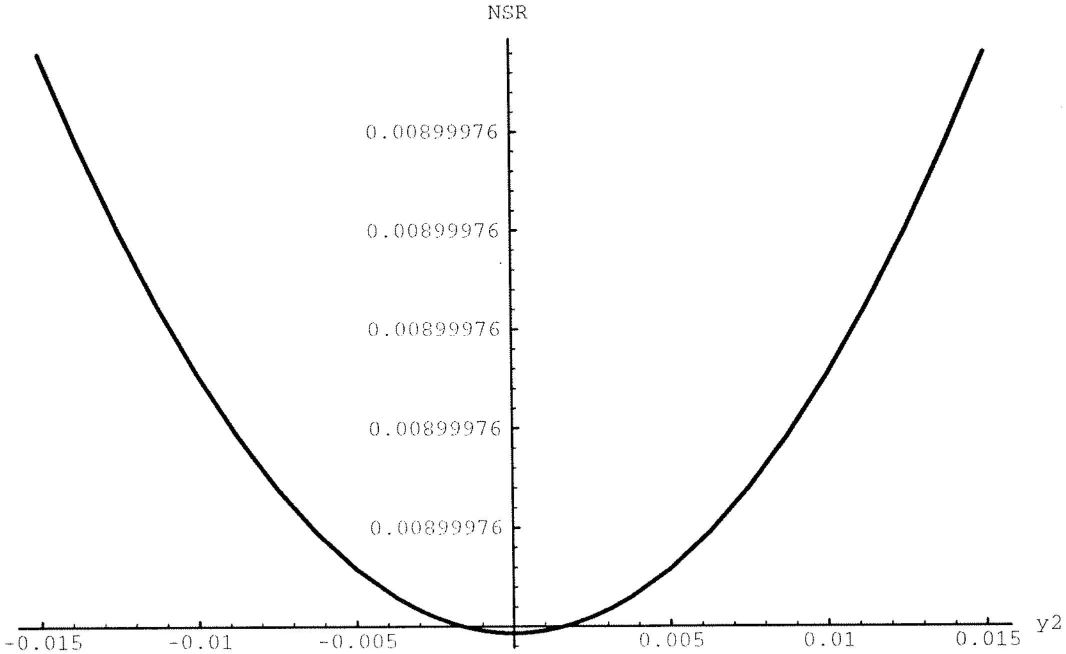

Figure 2.26: NSR vs position on the output plane for cylindrical media for the center hologram.

point in the output plane, we show, in Figure 2.27, SNR as a function of hologram position for 100 holograms. The worse SNR is always the center hologram since it borders the largest number of other holograms. Figure 2.28 shows the worst case SNR versus the total number of holograms stored for the case of multiplexing at the first, second, or third zero of the $J_1(x)/x$ function. Notice that unlike rotation multiplexing or angle multiplexing in a rectangular media, the SNR saturates quickly to a fixed level in a cylindrical media. This is partly due to the fact that as the cylinder is rotated the interaction distance does not change; therefore, the width between nulls of the selectivity function ($J_1(x)/x$) remains identical for all holograms. In addition, rotation tends to further separate gratings from different holograms unlike the case for angle multiplexing. In addition, the noise saturates quickly since $J_1(x)/x$ falls off much faster than the sinc function.

Figure 2.28 shows the SNR for scheduling at the first, second, and third zereos.

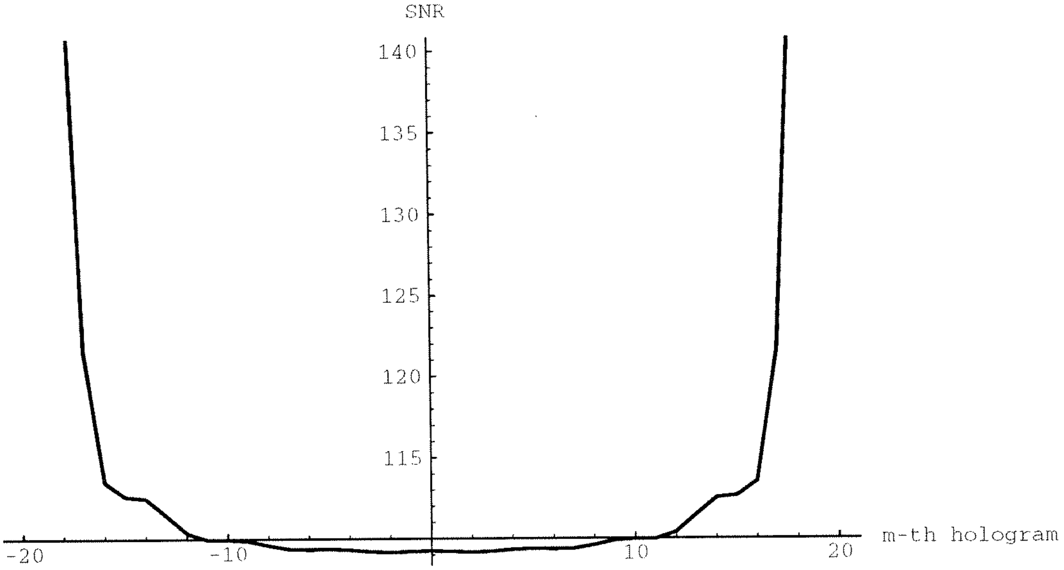

Figure 2.27: SNR vs hologram position in recording schedule for cylindrical media.

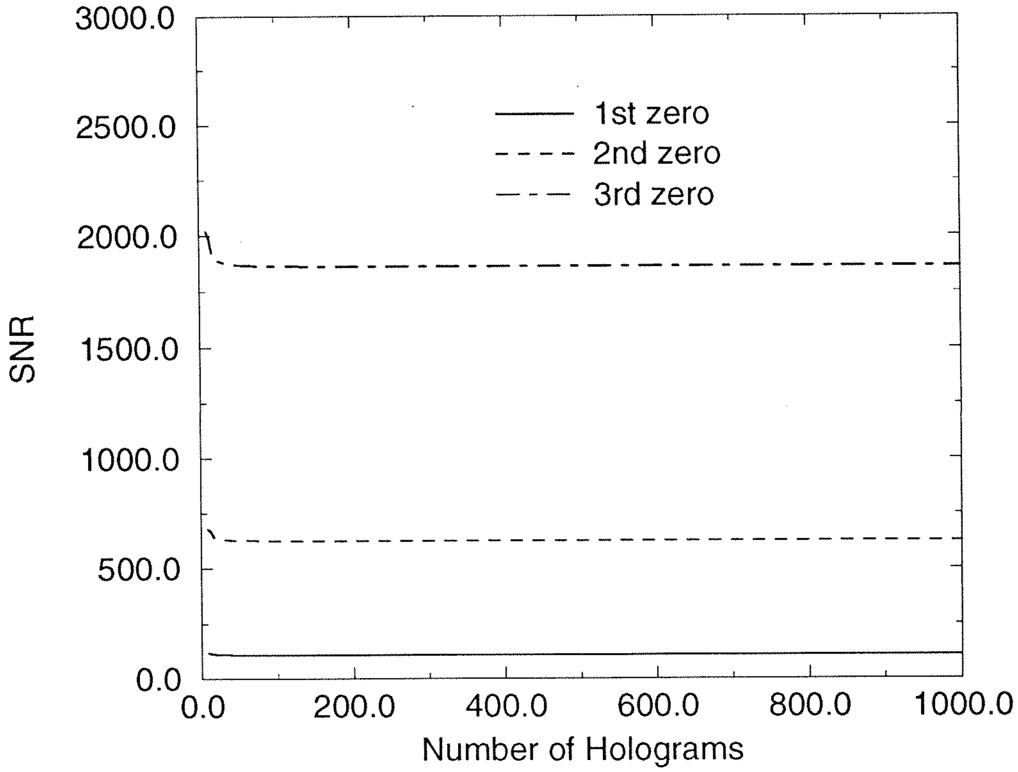

Figure 2.28: SNR vs the number of holograms stored for cylindrical media.

Notice that the SNR can be improved quickly in this way. For comparison, the SNR for the second zero results in saturation at about 640 for the cylindrical media compared to 800 for first zero wavelength multiplexing using the otherwise identical parameters in rectangular media. The SNR for 1,000 holograms for either angle or rotation multiplexing in a rectangular medium is about 2,000 which is comparable to placing the adjacent holograms in the third zero for the cylindrical media. Thus with cylindrical media the holograms cannot be stored as close together as with rectangular media, but since it is possible to access more grating space it is still possible to get comparable SNR. Since the increase in the number of possible angles is around 10 times the number available using angle multiplexing, the factors of 2 – 3 lost because of the wider selectivity function is not significant in terms of storage capacity. Thus different geometries such as cylindrical media may prove to have interesting possibilities for storage.

2.6 Image Plane Angle Multiplexed Holograms

2.6.1 Introduction

The cross-talk for angle multiplexed image plane holograms is derived. The SNR is calculated for a recording schedule that places the center frequency of each image at the null in angle of the adjacent hologram. This section contains two main results. First, we show that for image plane holograms the SNR is independent of the pixel location on the output plane. We also show that the worse case SNR for image plane is better than the worse case SNR for Fourier transformed holograms recorded with typical parameters.

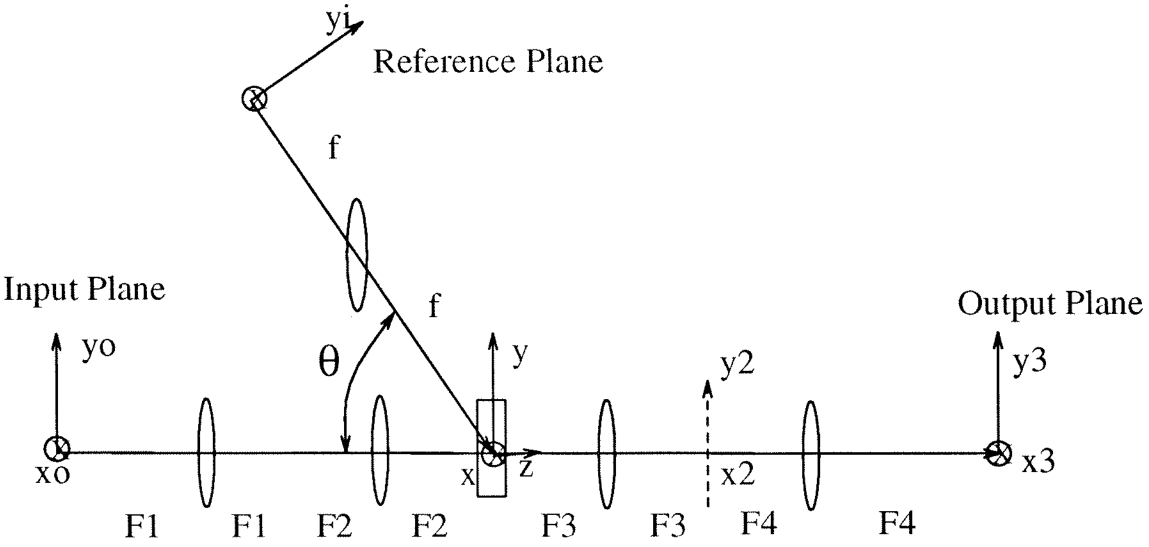

Figure 2.29: Recording and readout geometry for angle multiplexing image plane holograms.

2.6.2 Theory

Image plane holograms are multiplexed in a volume holographic medium using the setup shown in Figure 2.29. A plane wave R_m is generated at the material by collimating light from a point source at the reference plane. This interferes inside the holographic medium with S_m – the magnified image of the m-th object image. By labeling the holograms $m = -M, -(M-1), ..., 0, ..., M$, the presence of these $N = 2M+1$ holograms modulates the permittivity of the material such that the change in the permittivity of the medium can be written as

$$\Delta\epsilon \approx \sum_{m=-M}^{M} R_m^* S_m + c.c. \tag{2.60}$$

where *c.c.* is the complex conjugate term. The reference wave is given by

$$R_m = e^{ik_m \cdot r}, \tag{2.61}$$

where k_m refers to the wave vector coming from the reference point source at y_m. In addition, using standard Fourier-optics analysis [182], the m-th signal beam can be expressed as

$$S_m(r) \approx \iint dx_o\, dy_o \int_{-\infty}^{\infty}\int_{-\infty}^{\infty} du\, dv\, f_m(x_o, y_o) e^{i\frac{2\pi}{\lambda_m}z} e^{-i\pi\lambda z(u^2+v^2)} e^{i2\pi u(x+M_1 x_o)} e^{i2\pi v(y+M_1 y_o)}. \tag{2.62}$$

In the expression above, $f_m(x_o, y_o)$ is the m-th object image, x, y, z are the coordinates at the recording medium, $M_1 = F2/F1$, and u and v are spatial frequencies in the x and y directions respectively. By substituting Equations 2.61 and 2.62 into Equation 2.60, $\Delta\epsilon$ can be written out explicitly.

2.6.3 Cross–talk Calculations

In readout, the recorded medium is illuminated with a reference plane wave from position y_i on the reference plane. Ideally, this would only reconstruct the hologram associated with that particular reference. In what follows, we will calculate the deviations of the reconstructed wave from the desired image. The amplitude of the diffracted plane wave components, $E(\vec{k_d})$, with wave vectors $\vec{k_d}$, can be derived from standard scalar diffraction theory [183]. The following expression assumes that the Born and paraxial approximations are valid.

$$E(\vec{k_d}) \approx \int d\vec{r} e^{-i\vec{K}\cdot\vec{r}} \Delta\epsilon(\vec{r}), \tag{2.63}$$

where $\vec{K} = \vec{k_d} - \vec{k_i}$, $\vec{k_i}$ is the wave vector of the reference plane wave.

Lens with focal length $F3$ maps each diffracted plane wave component with wave vector $\vec{k_d}$ to a point x_2, y_2 at the x_2, y_2 plane given by:

$$\vec{k_d} = \left(\frac{2\pi x_2}{\lambda F_3}, \frac{2\pi y_2}{\lambda F_3}, \frac{2\pi}{\lambda}(1 - \frac{x_2^2}{2F_3^2} - \frac{y_2^2}{2F_3^2})\right), \tag{2.64}$$

assuming the paraxial approximation. Making use of the assumption that the transverse dimensions of the medium are much larger than the spatial bandwidth of the images, substituting relations 2.61, 2.60, 2.62, and 2.64 into Equation 2.63, and carrying out the integration over the volume of the medium and the spatial frequencies, the electric field at the x_2, y_2 plane can be written as

$$E(x_2, y_2) \approx \sum_{m=-M}^{M-1} F_m(-\frac{M_1 x_2}{\lambda F_3} - \frac{M_1}{2\pi}\Delta K_{mix}, (-\frac{M_1 y_2}{\lambda F_3} - \frac{M_1}{2\pi}\Delta K_{miy})$$
$$\times \operatorname{sinc}\left(\frac{t}{2\pi}\left(\Delta K_{miz} + \frac{1}{F}(\Delta K_{mix} x_2 + \Delta K_{miy} y_2) + \frac{\lambda}{4\pi}(\Delta K_{mix}^2 + \Delta K_{miy}^2)\right)\right), \quad (2.65)$$

where $\Delta\vec{K}_{mi} = \vec{k}_m - \vec{k}_i$ is the difference between the m-th reference wave vector $\vec{k}_m$ and the illuminating beam's wave vector $\vec{k}_i$. Also $\Delta K_{mi\alpha}$ is the component of $\Delta\vec{K}_{mi}$ in the α direction and $F_m()$ is the Fourier transform of $f_m()$. The grating vector $\Delta\vec{K}_{ij\alpha}$'s are given by $\Delta K_{ijx} = 0$, $\Delta K_{ijy} = \frac{2\pi}{\lambda f}(y_i - y_m)\cos\theta + \frac{\pi^2}{\lambda f^2}(y_m^2 - y_i^2)\sin\theta$, and $\Delta K_{ijz} = \frac{2\pi}{\lambda f}(y_i - y_m)\sin\theta + \frac{\pi^2}{\lambda f^2}(y_i^2 - y_m^2)\cos\theta$. Also, in Equation 2.65, t is the thickness of the material in the z direction. This is exactly the expression given for Fourier plane holograms.

Setting $\theta = 90°$ in order to maximize the storage capacity, and taking the Fourier transform of equation 2.65 results in an expression for $E_m(x_3, y_3)$. To estimate the noise-to-signal ratio (NSR) we divide the total average noise power by the magnitude squared of the signal. We assume that each pixel of the stored images is an independent random variable taking the values minus one and one with equal probability. In this case, the NSR is given by

$$\mathrm{NSR} = \sum_{m \neq i} \operatorname{sinc}^2\left(\frac{t}{\lambda f}(y_i - y_m) + \frac{\pi t}{4\lambda f^4 M_1}(y_m^2 - y_i^2)^2\right). \quad (2.66)$$

2.6.4 SNR Results

To minimize the noise the reference pixels (y_i's) need to be spaced by $\lambda f/t$ which is exactly the result for Fourier plane holograms. Notice that the NSR is independent of pixel position on the output plane. This means that all pixels in a hologram have the same SNR. Using the spacing described above, the SNR as a function of hologram number (i) was calculated with $N = 513$, $F = 30$ cm, $t = 1$ cm, $M_1 = 1$, and λ =500nm and is shown in Figure 2.30. Notice that the holograms with the worst

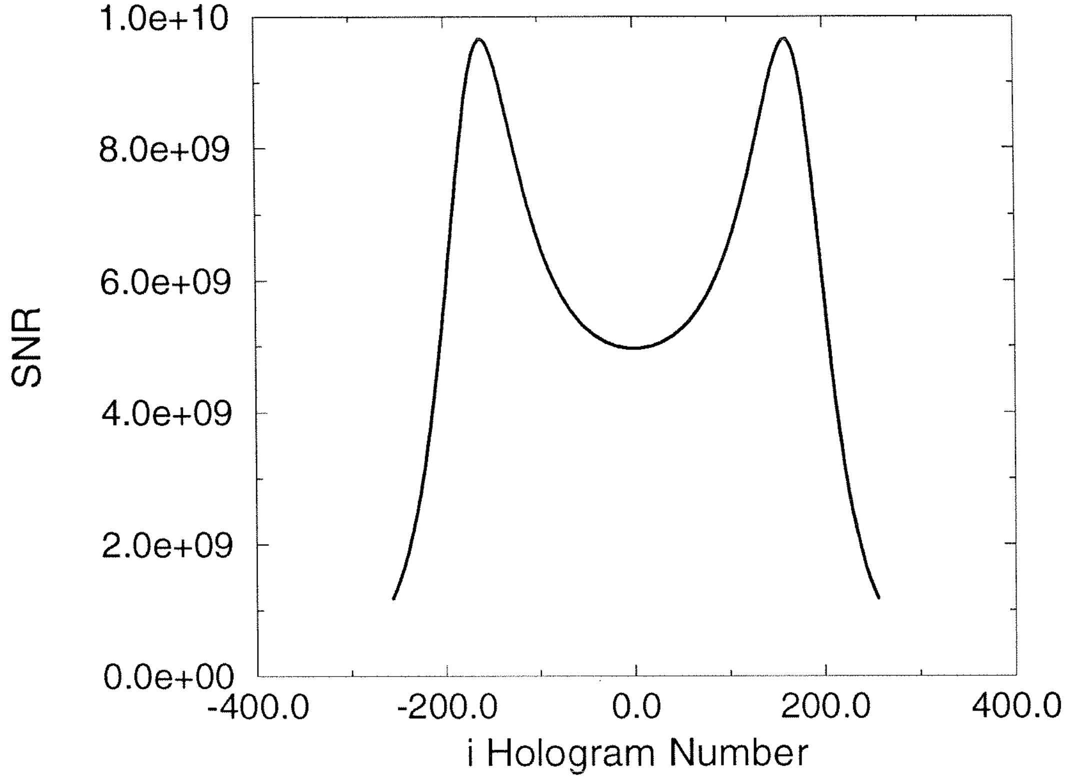

Figure 2.30: SNR vs hologram number – i.

SNR are the holograms that are furthest from 90° ($i = M$, or $i = -M$). Also the holograms stored a little off 90° have better SNR than the hologram stored at 90°.

Figure 2.31 shows worst case SNR for angle multiplexed holograms that are stored in both image plane and Fourier plane formats as a function of the total number of holograms stored. Image plane holograms average out the variations in the noise which results in a higher SNR. Also this higher SNR is the same for every pixel in a given hologram while for Fourier transformed holograms the edges of the image in the y direction have much lower SNR than the middle of the image. Thus, by averaging out variations over the input plane, holograms stored in the image plane have higher SNR than holograms stored in the Fourier plane format.

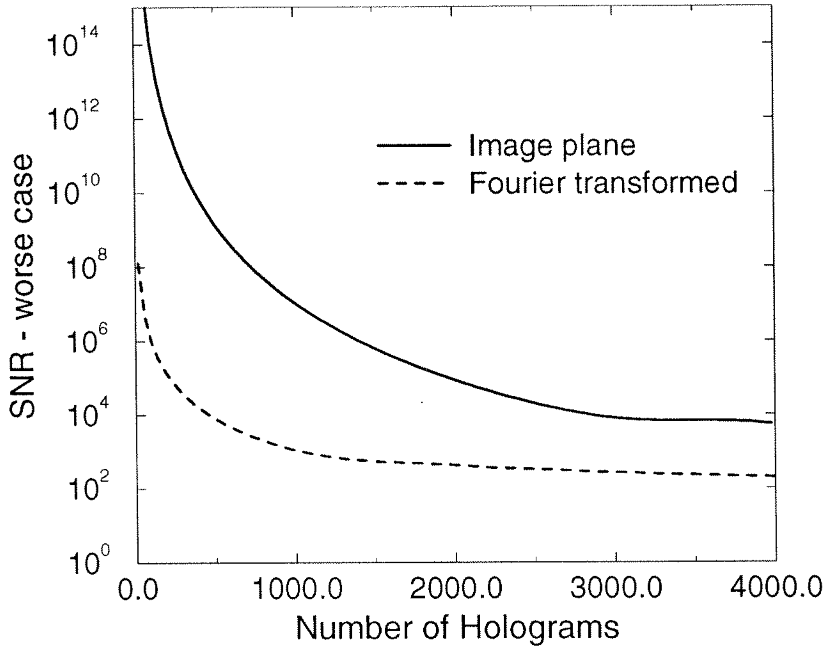

Figure 2.31: Worst case SNR for Fourier transformed and image plane holograms vs number of holograms stored.

2.7 Appendix 2.0: Derivation of Born Approximated Diffraction Equation

All the cross-talk calculations used an equation for diffraction from a volume assuming the both the Born and the paraxial approximations. This equation was derived for both isotropic and anisotropic material in Sidney Li's thesis [215]. The derivation for diffraction in isotropic medium directly follows that derivation and is given here for completeness.

The formula referred to is

$$E(\mathbf{r}) \approx e^{j\mathbf{k}_i \cdot \mathbf{r}} + \frac{k_0^2}{4\pi} \cdot e^{\frac{jkr}{r}} \int_V d\mathbf{r}' \; e^{-j\mathbf{K}' \cdot \mathbf{r}'} \Delta\epsilon(\mathbf{r}') \;, \tag{2.67}$$

where $\Delta\epsilon$ is the change in the dielectric constant (not the permittivity), $\mathbf{k}_i$ is the wave vector of the incident plane wave, $\mathbf{k}'_d$ is the diffracted plane wave, and $\mathbf{K}' = \mathbf{k}'_d - \mathbf{k}_i$.

We begin the derivation with the Born's approximation formula

$$\mathbf{D}(\mathbf{r}) = \mathbf{D}^{(0)}(\mathbf{r}) + \frac{1}{4\pi}\int_V d\mathbf{r}' \frac{e^{jk|\mathbf{r}-\mathbf{r}'|}}{|\mathbf{r}-\mathbf{r}'|} \nabla\times\nabla\times\left[\Delta\epsilon\mathbf{D}^{(0)}(\mathbf{r}')\right] \;, \tag{2.68}$$

where $\mathbf{D}^{(0)}$ is the incident wave. If we assume the region of integration V is finite, take the origin somewhere inside V, and take the observation point far away from V, then we can make the approximation

$$\begin{aligned} |\mathbf{r}-\mathbf{r}'|^2 &= r^2 + r'^2 - 2\mathbf{r}\cdot\mathbf{r}', \\ |\mathbf{r}-\mathbf{r}'| &\approx r - 2\left(\frac{\mathbf{r}}{r}\right)\cdot\mathbf{r}', \end{aligned} \tag{2.69}$$

since $r \gg r'$. Thus we have

$$\frac{e^{jk|\mathbf{r}-\mathbf{r}'|}}{|\mathbf{r}-\mathbf{r}'|} \approx \frac{e^{jkr}}{r}\cdot e^{-j\mathbf{k}\cdot\mathbf{r}'}, \tag{2.70}$$

where we define

$$\mathbf{k} = k\left(\frac{\mathbf{r}}{r}\right), \tag{2.71}$$

and where $r = |\mathbf{r}|$.

We can therefore approximate $\mathbf{D}$ by

$$\mathbf{D}(\mathbf{r}) = \mathbf{D}^{(0)}(\mathbf{r}) + \frac{1}{4\pi}\cdot\frac{e^{jkr}}{r}\int_V d\mathbf{r}'\; e^{-j\mathbf{k}\cdot\mathbf{r}'}\nabla\times\nabla\times\left[\Delta\epsilon\mathbf{D}^{(0)}(\mathbf{r}')\right]. \tag{2.72}$$

Next we assume that $\Delta\epsilon$ is of the form

$$\Delta\epsilon(\mathbf{r}') = \Delta\epsilon_a\; e^{-j\mathbf{K}\cdot\mathbf{r}'}, \tag{2.73}$$

and $\mathbf{D}^{(0)}$ is of the form

$$\mathbf{D}^{(0)}(\mathbf{r}') = D_0\; e^{j\mathbf{k}_i\cdot\mathbf{r}'}\; \mathbf{e}_i, \tag{2.74}$$

where $\mathbf{e}_i$ is the unit vector that gives the polarization of the incident wave $\mathbf{D}^{(0)}$.

We then have

$$\Delta\epsilon\mathbf{D}^{(0)}(\mathbf{r}') = D_0\Delta\epsilon_a\; e^{j\mathbf{k}_d\cdot\mathbf{r}'}\mathbf{e}_i, \tag{2.75}$$

where $\mathbf{k}_d = \mathbf{k}_i - \mathbf{K}$ and

$$\begin{aligned}\nabla\times\nabla\times\left[\Delta\epsilon\,\mathbf{D}^{(0)}(\mathbf{r}')\right] &= -D_0[\mathbf{k}_d\times(\mathbf{k}_d\times\mathbf{e}_i)]\left\{\Delta\epsilon_a\; e^{j\mathbf{k}_d\cdot\mathbf{r}'}\right\},\\ &= -D_0[\mathbf{k}_d\times(\mathbf{k}_d\times\mathbf{e}_i)]\Delta\epsilon\;(\mathbf{r}')e^{j\mathbf{k}_i\cdot\mathbf{r}'} \qquad (2.76)\end{aligned}$$

assuming that $\Delta\epsilon_a$ is a scalar. This then allows us to write $\mathbf{D}$ as

$$\begin{aligned}\mathbf{D}(\mathbf{r}) &= \mathbf{D}^{(0)}(\mathbf{r}) - \frac{\mathbf{k}_d\times(\mathbf{k}_d\times\mathbf{e}_i)}{4\pi}\cdot\frac{e^{jkr}}{r}\int_V d\mathbf{r}'\; e^{-j(\mathbf{k}-\mathbf{k}_i)\cdot\mathbf{r}'}\Delta\epsilon\;(\mathbf{r}')\\ &= \mathbf{D}^{(0)}(\mathbf{r}) - \mathbf{u}\sin(\mathbf{e}_i,\mathbf{k}_d)\cdot\frac{k_0^2}{4\pi}\cdot\frac{e^{jkr}}{r}\int_V d\mathbf{r}'\; e^{-j(\mathbf{k}-\mathbf{k}_i)\cdot\mathbf{r}'}\Delta\epsilon\;(\mathbf{r}'), \qquad (2.77)\end{aligned}$$

where $\mathbf{u}$ is the unit vector in the direction of $\mathbf{k}_d\times(\mathbf{k}_d\times\mathbf{e}_i)$, and $\sin(\mathbf{e}_i,\mathbf{k}_d)$ is the sine of the angle between $\mathbf{e}_i$ and $\mathbf{k}_d$ which is in general not equal to one. Note that $\mathbf{u}$ is perpendicular to $\mathbf{k}_d$. Here we have used the fact that

$$|\mathbf{k}_d\times(\mathbf{k}_d\times\mathbf{e}_i)| = k_0^2\sin(\mathbf{e}_i,\mathbf{k}_d). \qquad (2.78)$$

If we take $\mathbf{k}$ to be $\mathbf{k}_d'$, then the result in Eq. 2.77 agrees with the result in Eq. 2.67. For a general $\Delta\epsilon$, we assume that it can be written as a sum of sinusoidal gratings of the form

$$\Delta\epsilon(\mathbf{r}') = \sum_\alpha \Delta\epsilon_\alpha\; e^{-j\mathbf{K}_\alpha\cdot\mathbf{r}'}. \qquad (2.79)$$

In this case we have

$$\begin{aligned}\mathbf{D}(\mathbf{r}) &= \mathbf{D}^{(0)}(\mathbf{r}) - \frac{1}{4\pi}\cdot\frac{e^{jkr}}{r}\int_V d\mathbf{r}'\; e^{-j\mathbf{k}\cdot\mathbf{r}'}\sum_\alpha \mathbf{k}_\alpha\times(\mathbf{k}_\alpha\times\mathbf{e}_i)\Delta\epsilon_\alpha\; e^{-j\mathbf{k}_\alpha\cdot\mathbf{r}'}\\ &= \mathbf{D}^{(0)}(\mathbf{r}) - \frac{k_0^2}{4\pi}\cdot\frac{e^{jkr}}{r}\int_V d\mathbf{r}'\; e^{-j(\mathbf{k}-\mathbf{k}_i)\cdot\mathbf{r}'}\sum_\alpha \sin(\mathbf{e}_i,\mathbf{k}_\alpha)\Delta\epsilon_\alpha\; e^{-j\mathbf{K}_\alpha\cdot\mathbf{r}'}\;\mathbf{u}_\alpha \qquad (2.80)\end{aligned}$$

where

$$\mathbf{k}_\alpha = \mathbf{k}_i - \mathbf{K}_\alpha, \qquad (2.81)$$

and $\mathbf{u}_\alpha$ is the unit vector in the direction of $\mathbf{k}_\alpha\times(\mathbf{k}_\alpha\times\mathbf{e}_i)$. Assuming that all $\mathbf{u}_\alpha$ are approximately in the same direction, we take

$$\sin(\mathbf{e}_i,\mathbf{k}_\alpha)\mathbf{u}_\alpha \approx \sin(\mathbf{e}_i,\mathbf{k}_{\alpha 0})\mathbf{u}_\alpha \qquad (2.82)$$

to be a constant and move it outside the summation. Eq. 2.80 then becomes

$$\begin{aligned}\mathbf{D}(\mathbf{r}) &= \mathbf{D}^{(0)}(\mathbf{r}) - \left\{\frac{k_0^2}{4\pi}\cdot\frac{e^{jkr}}{r}\int_V d\mathbf{r}'\ e^{-j(\mathbf{k}-\mathbf{k}_i)\cdot\mathbf{r}'}\sum_\alpha \Delta\epsilon_\alpha\ e^{-j\mathbf{K}_\alpha\cdot\mathbf{r}'}\right\}\sin(\mathbf{e}_i,\mathbf{k}_{\alpha 0})\mathbf{u}_{\alpha 0} \\ &= \mathbf{D}^{(0)}(\mathbf{r}) - \left\{\frac{k_0^2}{4\pi}\cdot\frac{e^{jkr}}{r}\int_V d\mathbf{r}'\ e^{-j(\mathbf{k}-\mathbf{k}_i)\cdot\mathbf{r}'}\Delta\epsilon\ (\mathbf{r}')\right\}\sin(\mathbf{e}_i,\mathbf{k}_{\alpha 0})\mathbf{u}_{\alpha 0}. \qquad (2.83)\end{aligned}$$

Except for some constants, this agrees with the expression in Eq 2.67.

2.8 Appendix 2.1: Comments on Input Image Format

2.8.1 Random ± 1's

The input data (a_n) is always assumed to be random plus or minus 1 bits each with equal probability. To calculate the SNR the signal intensity is divided by the average noise intensity. The signal has magnitude one and the average noise intensity depends on the second moment of the random input signal. In the case of random +1 or -1's, the second moment of the random variable is

$$E\{a_n a_m\} = \delta_{mn} \qquad (2.84)$$

where δ_{mn} is a Kronecker delta function. This eliminates one of the sums in the average noise intensity calculation. Since the signal has no zeroes, the holograms consist of the maximum number of gratings.

2.8.2 Random ± 1's or 0

Assuming that the signal (a_n) is either $|1|$ or 0 with equal probability and the 1 bits are equally likely to be -1 or +1, the second moment of a_n becomes

$$E\{a_n a_m\} = \frac{\delta_{mn}}{2} \qquad (2.85)$$

where δ_{mn} is a Kronecker delta function. Thus to convert the SNR calculated in the preceding sections into SNR for a ± 1 or 0 input just multiply by 2. This increase in two is simply due to having 1/2 the number of recorded gratings. Thus the noise intensity due to diffraction off of these gratings is down by a factor of 2.

2.8.3 Random 1 or 0

For the case that the signal consists of random 1 or 0 bits each with equal probability, the second moment of the random variable is

$$E\{a_n a_m\} = \frac{\delta_{mn}}{2} + \frac{1}{4}(n \neq m). \tag{2.86}$$

Since the random variable has a mean the signal is equal the signal plus the noise. The noise is much smaller than one; therefore, the signal intensity is still approximately one. The average noise is now expressed as

$$\text{Ave. Noise} = \frac{1}{2}\sum_{i \neq j} \text{sinc}(i,j) + \frac{1}{4}\sum_{i \neq j} \sum_{i', i \neq i'} \text{sinc}(i,j)\text{sinc}(i',j). \tag{2.87}$$

The second term in the expression can be numerically shown to be much smaller than the first term since it sums over positive and negative values. Thus to convert the SNR calculated in the preceding sections into SNR for a binary 1 or 0 input just multiply by 2. This increase in two is simply due to having half the number of recorded gratings. Thus the noise intensity due to diffraction off of these gratings is down by a factor of two.

2.9 Appendix 2.2: Finite SLM Contrast Ratio

2.9.1 Introduction

Given that the signal is supposed to be a 0 or a ±1 with equal probability, what happens if the SLM has a finite contrast ratio? For instance, what happens to the cross-talk if the signal is $f_m = \epsilon_2 a_m + \epsilon_1$, where a_m is the ideal signal and the contrast ratio is defined as $\epsilon_2^2/\epsilon_1^2$. The signal is given by ϵ_2^2. Using the fact that

$$E\{a_n a_m\} = \frac{\delta_{mn}}{2}$$

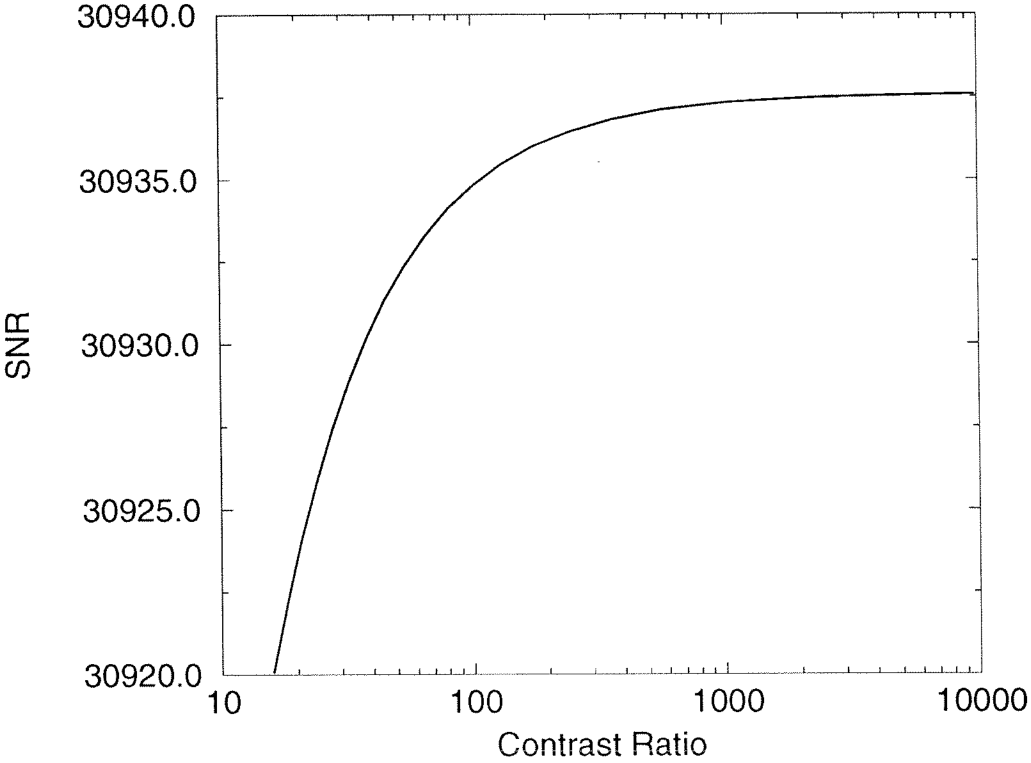

Figure 2.32: Worst case SNR for Fourier transformed holograms vs contrast ratio.

$$E\{a_m\} = 0 , \tag{2.88}$$

the average noise intensity can be written as

$$\text{Ave. Noise} = \frac{1}{2}\sum_{i \neq j} \text{sinc}(i,j) + \epsilon_1^2 \sum_{i \neq j} \sum_{i' \neq j'} \text{sinc}(i,j)\text{sinc}(i',j) \ . \tag{2.89}$$

The SNR is the signal divided by the average noise intensity given in Eq. 2.89.

2.9.2 Contrast Ratio Results

Using the parameters for angle multiplexing given in section 2 of this chapter with N = 501 holograms, the worst case SNR vs contrast ratio is shown in Figure 2.32 For Figure 2.32, we can conclude that as long as the contrast ratio of the SLM is reasonable, the contrast ratio has little effect on the cross-talk noise. For example, looking at Figure 2.32, holograms stored with a 16:1 contrast ratio have SNR that differs by only ~ 0.06% from holograms stored with infinite contrast ratio.

Chapter 3

Comparison of Multiplexing Methods on the Basis of Cross-talk

3.1 Introduction

Multiple holograms can be recorded in a material by changing either the reference beam angle (θ multiplexing), the recording wavelength (λ multiplexing), phase coding the reference beam (ϕ multiplexing) or by rotating the media (rotation multiplexing). In the past, most of the work has concentrated on angle multiplexing, primarily because convenient frequency-tunable light sources and phase modulating SLMs have not been available. With the advent of semiconductor and solid-state tunable lasers and commercial SLMs (spatial light modulators), there has been renewed interest in wavelength and phase code multiplexing.

Recently, Rakuljic et al. [175] argued that λ multiplexed memories have lower cross-talk noise than θ multiplexing. The cross-talk calculations in Chapter 2 indicate that the SNR is independent of the total number of holograms for λ multiplexing, whereas it drops as one over the number of holograms for θ multiplexing, rotation multiplexing, and ϕ multiplexing using Walsh-Hadamard codes. Therefore, for a large enough number of holograms, λ multiplexing has less cross-talk. In this section we

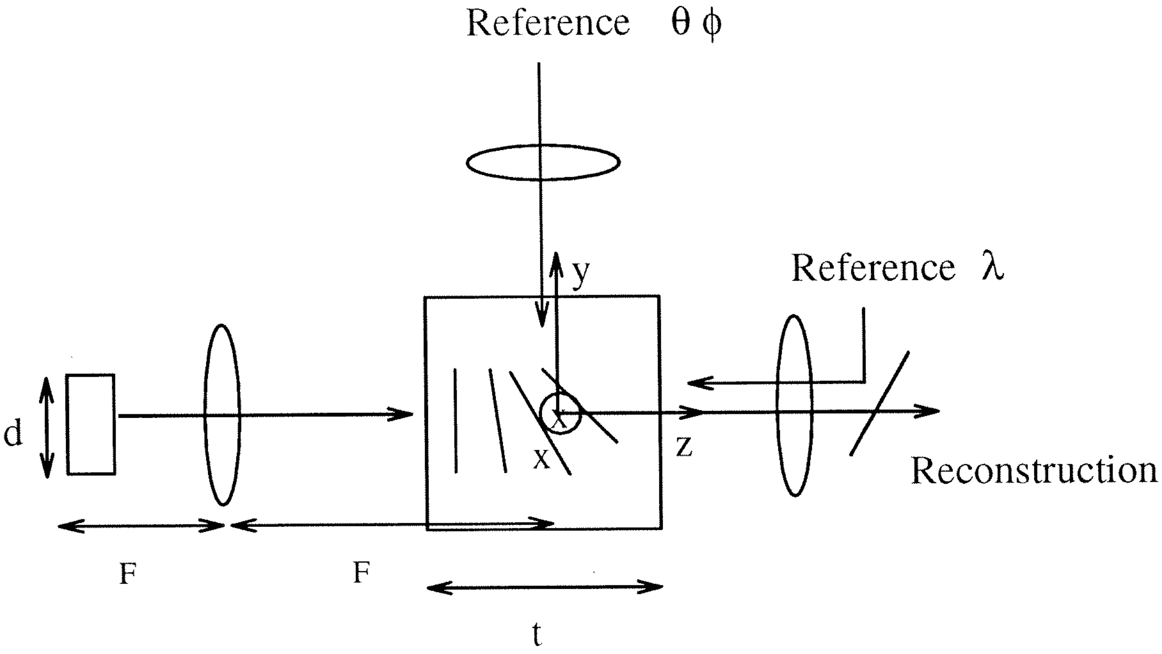

Figure 3.1: Geometry used for recording θ, λ, and ϕ multiplexed Fourier transform holograms.

compare cross-talk results for the three methods and show that, in practice, if the recording geometry is optimal, the maximum number of holograms that can be stored with any of these methods is not limited by cross-talk [190, 191].

3.2 Summary of Cross–talk Results

3.2.1 Comparison of Methods

Gratings are recorded throughout the volume of a material using one of the three methods of multiplexing as shown in Figure 3.1. Since rotation multiplexing is similar to θ multiplexing, only θ, λ, and ϕ results will be summarized in this section. In order to maximize the storage capacity of each of the methods, a 90° geometry was assumed for θ and ϕ multiplexing and a pure reflection geometry for λ multiplexing. When a particular reference beam is incident on the medium, the amount of light diffracted from the gratings can be calculated by assuming the Born and paraxial approximations. When the reference has the correct angle or wavelength, it is Bragg matched to one set of stored gratings, and the stored hologram is reconstructed. Cross-talk noise is due to energy diffracting off non-Bragg matched gratings. The cross-talk for θ, λ, and ϕ multiplexing can be minimized by placing the center pixel of each Fourier transformed hologram at the null of the adjacent hologram's Bragg selectivity function. The calculations of cross-talk noise details are given in Chapter 2.

The noise-to-signal ratio (NSR) at the output plane for each method was numerically evaluated with (focal length) $F = 30$ cm, (material thickness) $t = 1$ cm, (output plane dimensions) $x_{2max} = y_{2max} = 1.5$ cm, and $\lambda = 500$ nm. ϕ multiplexing was done using Walsh-Hadamard codes. Figure 3.2 shows the spatial distribution of the noise at the output plane. As mentioned above, the angular or wavelength separation between adjacent holograms was chosen to minimize the cross-talk of the center pixel for all three methods. Therefore, the center of the image has the lowest amount of noise while the edges of the images are noisier. For ϕ and θ multiplexing, the reference beams can only be scanned in one dimension (y) since there is no Bragg selectivity in the second direction. For this reason, the noise is also a one dimension function at the output plane. For λ multiplexing, the recording geometry is radially symmetric around the z-axis which is reflected in the structure of the noise at the output plane.

Selecting the noisiest pixel on the output plane and plotting this worst case signal-to-noise ratio (SNR) against hologram page number results in Figure 3.3. Here we show the behavior of the SNR for holograms stored at different angles, wavelengths, or phase codes. The plots in Figure 3.3 were made for 4,000, 10,000, and 63 holograms for θ, λ, and ϕ multiplexing respectively. The angular separation was selected to minimize the cross-talk of the central hologram. Therefore, the SNR for θ multiplexing is maximum at $i = 0$ hologram. All λ multiplexed holograms have about the same

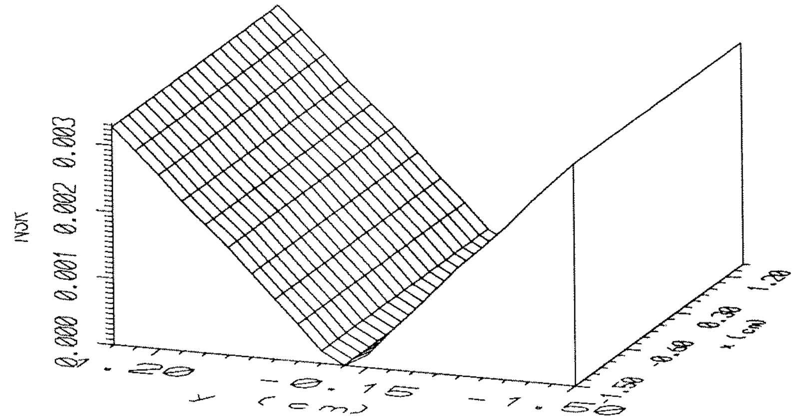

Angle

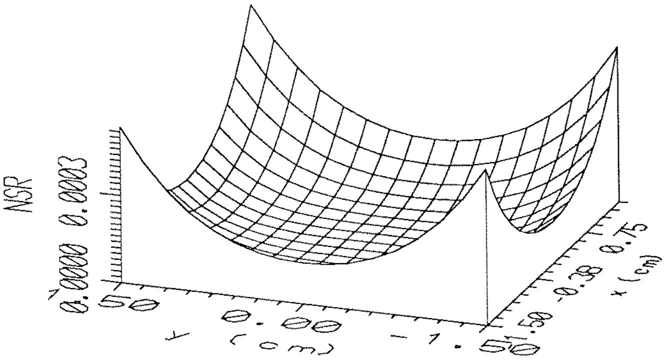

Wavelength

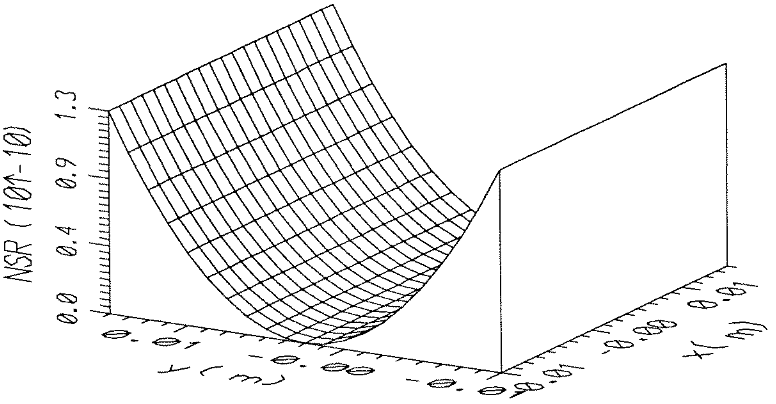

Phase Coded

Figure 3.2: NSR vs. position on the output plane for N =4001, 401, and 15 holograms for θ, λ, and ϕ multiplexing respectively.

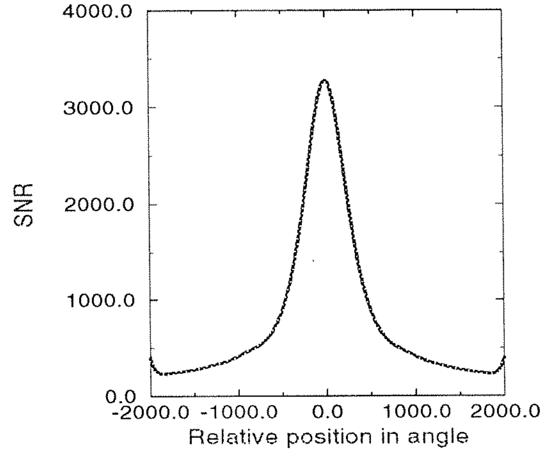

Angle

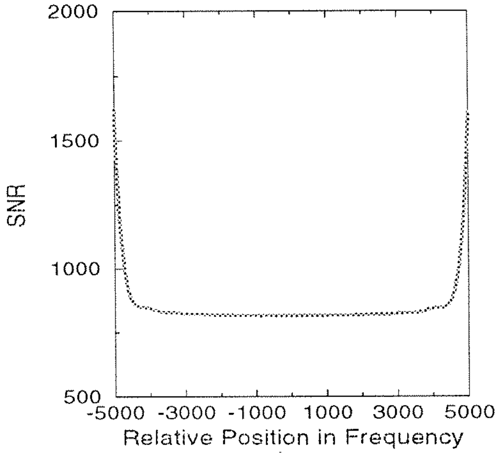

Wavelength

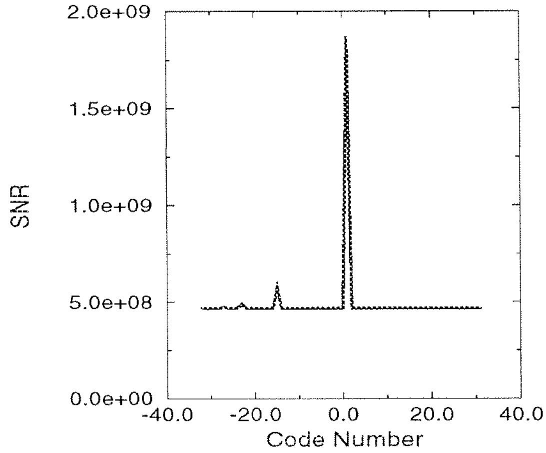

Phase Coded

Figure 3.3: SNR vs. hologram page number in the schedule where zero represents the center angle/wavelength for θ, λ and ϕ multiplexing.

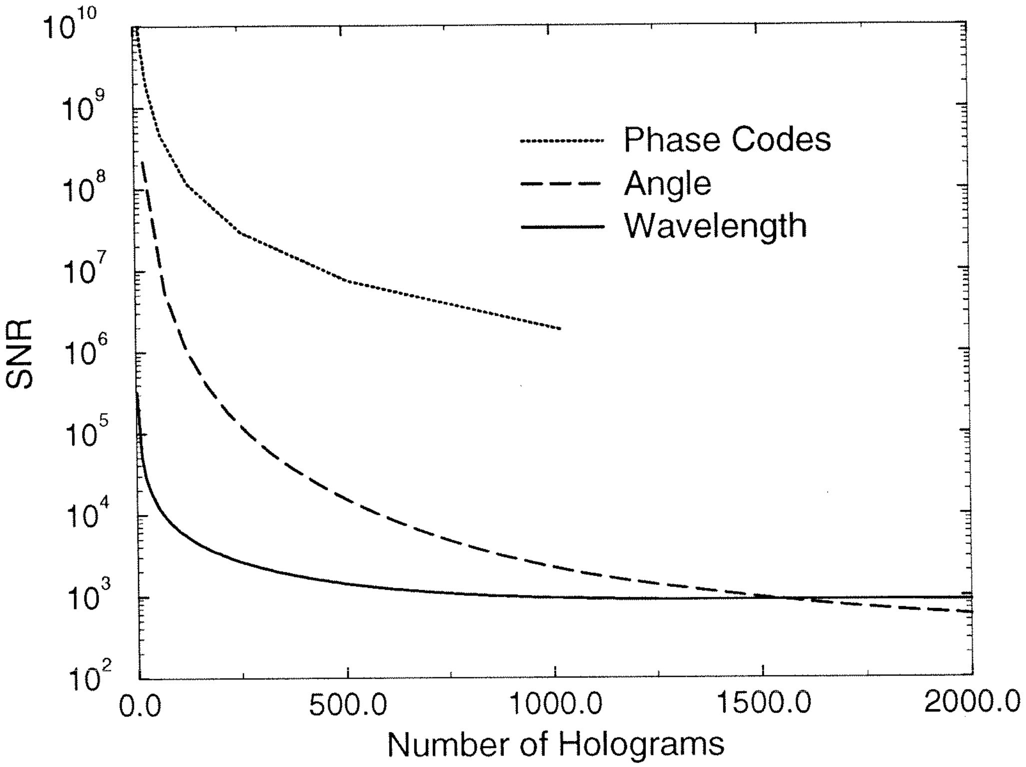

Figure 3.4: Worst case SNR vs. total number of holograms stored.

SNR except for the few holograms stored at the edge of the spectral range of the tunable source. This is due to the fact that cross-talk noise comes mostly from the neighboring holograms and that edge holograms only have neighbors on one side. For ϕ multiplexing, most holograms average to the same SNR since they are recorded with all reference beam angles simultaneously. There is some variation in the SNR from code-word to code-word because they correlate differently with the non-Bragg matched stored holograms.

Figure 3.4 shows the SNR at the noisiest pixel in the output plane for the noisiest hologram stored, as a function of the total number of holograms stored. Notice that as we expected, the SNR decreases as the number of holograms for ϕ and θ multiplexing increases, while for λ multiplexing the SNR decreases rapidly to a saturation value. Also, if we take the SNR for θ multiplexing at the edge of the output plane and average over all holograms, we obtain an average SNR that is still more than two orders of magnitude less than ϕ multiplexing for large N. Therefore, well chosen phase codes suppress, even on average, the cross-talk. The SNR was plotted for up to only 1,023 holograms for ϕ multiplexing since the calculation is computationally intensive. Notice that the crossover point for the worst case SNR between λ and θ is a little more than 1,500 holograms. Therefore, if the number of holograms stored is more than 1,500, λ multiplexing has lower cross-talk noise. For ϕ multiplexing, the crossover point is much larger. The worst case SNR for storage of 1,000 holograms is $\sim 1,000$ for λ multiplexing, compared to $\sim 10^6$ for ϕ multiplexing and $\sim 3,000$ for θ multiplexing. The cross-talk SNR is very high in all cases, which leads us to the conclusion that other system imperfections will determine the fidelity of the reconstruction in practice.

3.2.2 Image Plane vs Fourier Transform Holograms

Figure 3.5 shows worst case SNR for angle multiplexed holograms that are stored in both image plane and Fourier plane formats as a function of the total number of holograms stored. Image plane holograms average out the variations in the noise which results in a higher SNR for image plane holograms than for Fourier plane holograms. Also, this higher SNR is the same for every pixel in a given hologram while for Fourier transform holograms the edges of the image in the y direction(the direction of angle multiplexing) have much lower SNR than the middle of the image. Thus, the higher SNR and equal SNR for each pixel makes image plane holograms a desirable storage format if cross-talk noise is relevant.

3.2.3 Geometrically, When is Cross-talk Important

The conclusion that cross-talk is not the determining noise source was based on θ and ϕ multiplexing at 90°, λ multiplexing in reflection geometry, and the optimum spacing

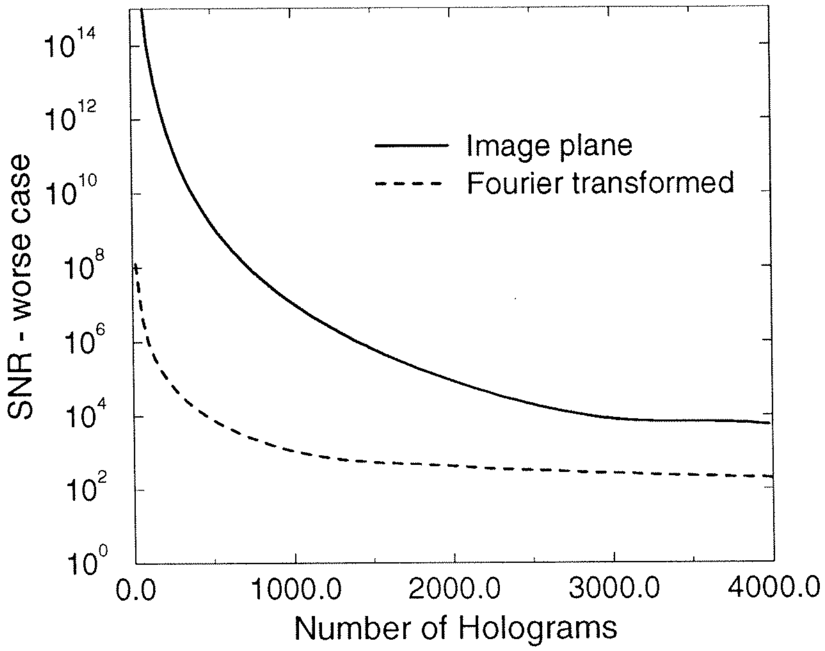

Figure 3.5: Worst case SNR for Fourier transformed and image plane holograms vs number of holograms stored.

of the holograms at the nulls of the Bragg selectivity. When θ and ϕ multiplexing is done at an intersection angle other than 90°, the SNR decreases rapidly. Figure 3.6 shows the worst case SNR for angle multiplexing 101 holograms as the intersection angle between the reference and signal beams is changed from 10° to 90°. Clearly, from a cross-talk point of view, 90° is the best geometry for θ and ϕ multiplexing. This can also be seen in the depth of the minimums of the sinc functions. For one plane wave component of the image using angle multiplexing, the nulls for 90° geometry are zeroes of the sinc function. For other geometries, the minima of the sinc functions are not zeroes due to other geometric terms arising (Figure 3.7). Figure 3.7 shows the diffracted power into the center pixel of the image stored (Fourier hologram) as the reference beam is scanned for different intersection angles. The SNR also decreases rapidly for geometries other than pure reflection for λ multiplexing and reference [171] gives a closed-form asymptotic expression for the SNR. Another

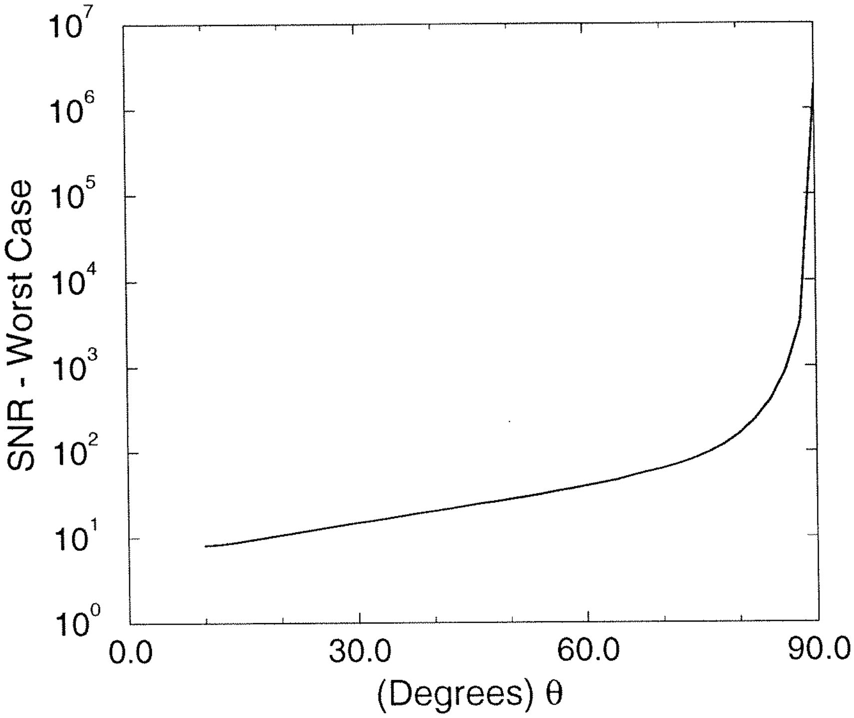

Figure 3.6: Worst case SNR for $N = 101$ holograms as a function of angle between reference and image beams (θ) for **angle** multiplexing.

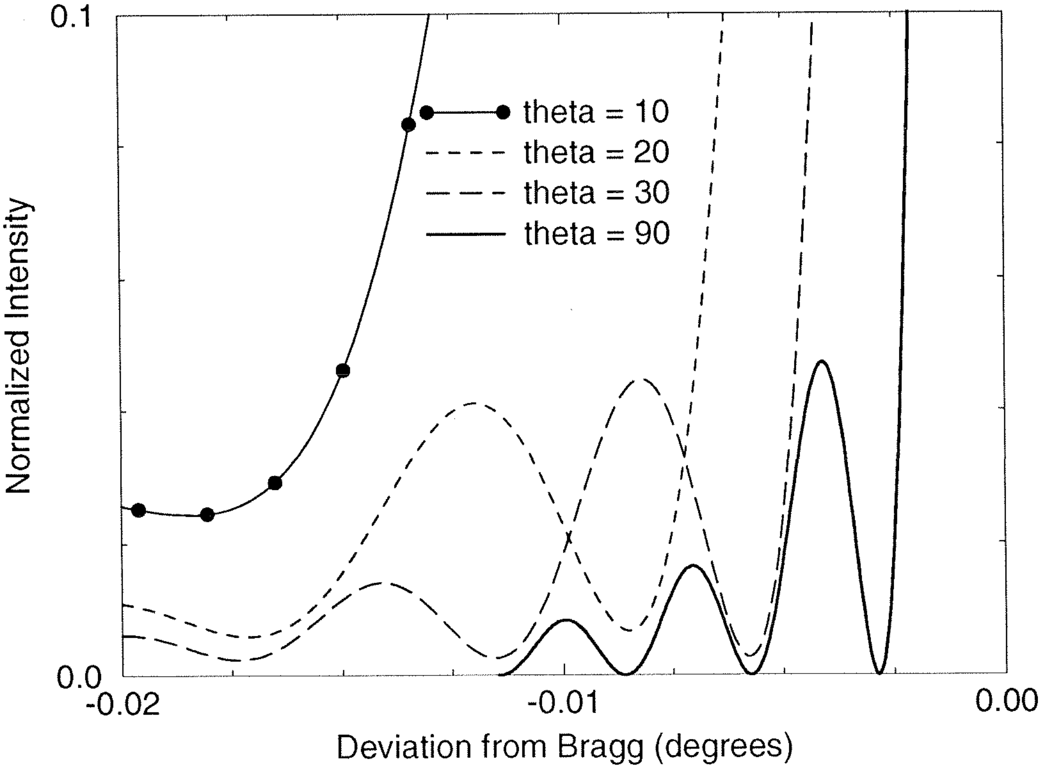

Figure 3.7: Normalized diffraction vs deviation from Bragg for θ (intersection angle) equal to 10, 20, 30, and 90 degrees.

requirement for λ multiplexing is a tunable source with a sufficiently small linewidth to avoid further increases in cross-talk noise [192]. The other important criterion is that the holograms were stored at the minimum of the adjacent hologram's Bragg selectivity function. If the holograms are spaced so as they are not in the nulls, either intentionally or due to experimental error, the SNR will also decrease. Therefore, cross-talk will be irrelevant only when using the best geometry and spacing the holograms correctly in either angle or wavelength.

3.3 Understanding Cross-talk in Wave Vector and Grating Space

3.3.1 k-space Introduction

To better understand the recording of holograms, we consider what happens in wave vector space (**k**-space). Assuming the electric and magnetic fields are plane waves and therefore have the form of

$$\mathbf{E}e^{i(\vec{k}\cdot\vec{r}-\omega t)} \text{ and}$$
$$\mathbf{H}e^{i(\vec{k}\cdot\vec{r}-\omega t)}, \tag{3.1}$$

the wave equation in an anisotropic medium can be written as

$$\vec{k} \times (\vec{k} \times \vec{E}) + \omega^2 \mu\epsilon \vec{E} = 0, \tag{3.2}$$

where $\vec{k}$ is the wave vector, $\vec{E}$ is the electric field, ω is the angular frequency of the wave, μ is the permeability tensor which is assumed to be a constant, and ϵ is the dielectric tensor. Assuming that the coordinate system is chosen such that the dielectric tensor is a diagonal matrix, Equation 3.2 will only have nontrivial solutions if and only if

$$\det \begin{vmatrix} \omega^2\mu\epsilon - k_y^2 - k_z^2 & k_x k_y & k_x k_z \\ k_y k_x & \omega^2\mu\epsilon - k_x^2 - k_z^2 & k_y k_z \\ k_z k_x & k_z k_y & \omega^2\mu\epsilon - k_x^2 - k_y^2 \end{vmatrix} = 0 \ . \tag{3.3}$$

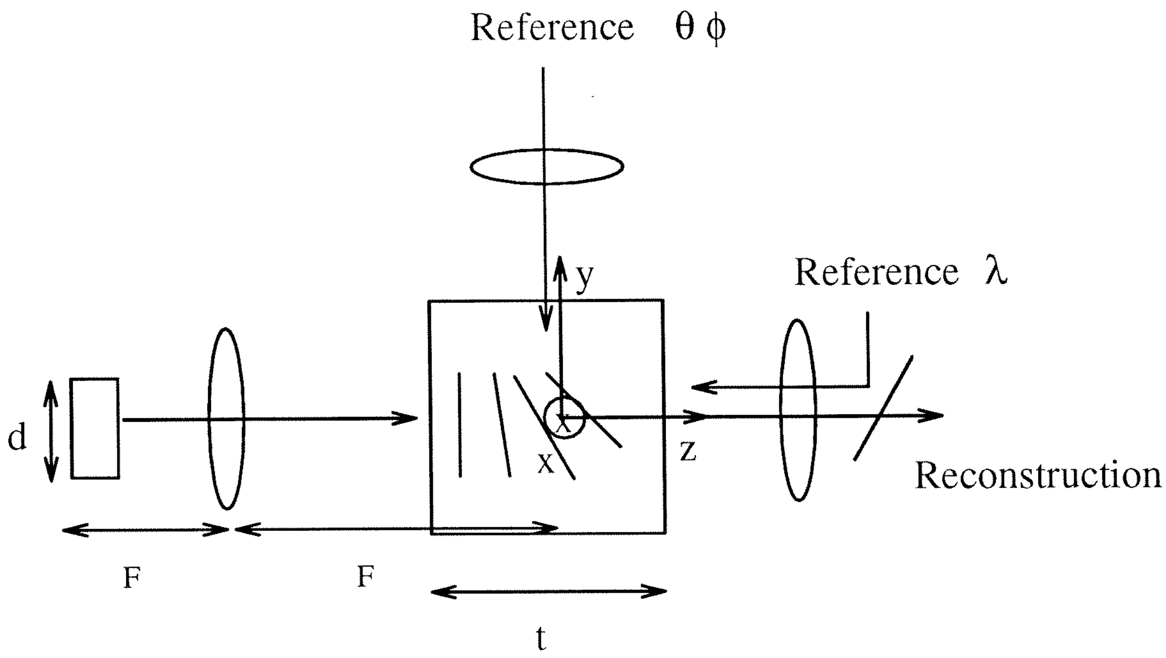

Figure 3.8: Geometry used for recording θ, and λ multiplexed Fourier transform holograms.

Equation 3.3 defines a 3-dimensional **k**-space of all possible wave vectors. In general, each polarization has a 3-dimensional ellipsoid that the tip of the vector is confined to lie on which is called the normal surface. In an isotropic medium, this constrains the vectors to lie on a sphere which can be written as

$$\frac{k_x^2}{n^2} + \frac{k_y^2}{n^2} + \frac{k_z^2}{n^2} = k_o^2 \ . \tag{3.4}$$

3.3.2 k-space for Angle Multiplexing

Angle multiplexing in the 90° geometry is shown in Figure 3.8. To construct the **k**-space picture for the geometry in Figure 3.8, we center the normal surface on the material and represent each plane wave by a vector that starts in the middle and extends to the surface. The **k**-space picture corresponding to the geometry in Figure 3.8 is shown in Figure 3.9. Since images are composed of a spectrum of plane waves, they are shown with several vectors. The plane wave reference beam records

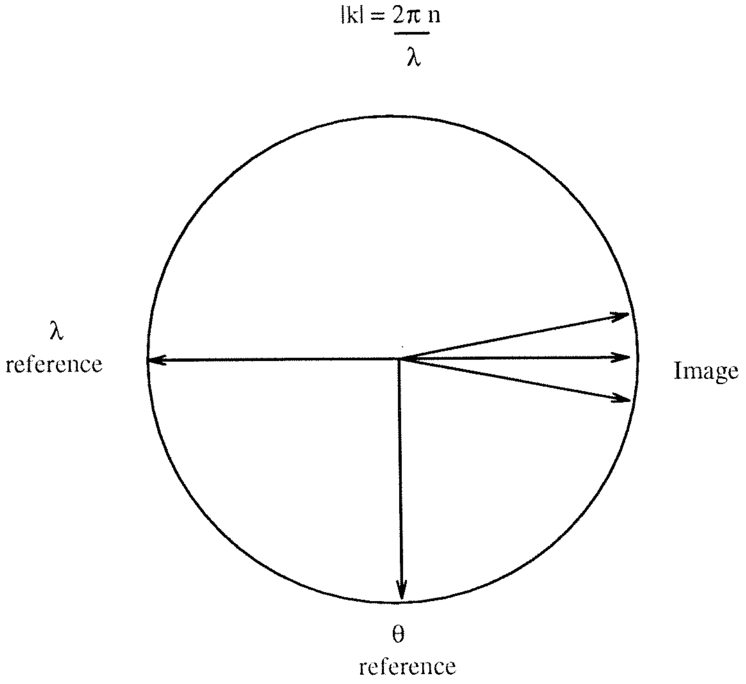

Figure 3.9: k-space diagram for θ and λ multiplexing.

a grating with each plane wave component of the image.

A single grating is recorded by two plane waves interfering inside the material as shown in Figure 3.10 part (a). The grating vector is the thicker vector that connects the reference and signal plane waves and is defined as $\vec{K} = \vec{k_s} - \vec{k_r}$. To reconstruct the hologram, the reference beam is input, diffracts off the grating, and reconstructs the original signal, since $\vec{K} + \vec{k_r} = \vec{k_s}$. Since the material is of finite thickness, you can imagine that instead of a single grating the actual recording is a spectrum of gratings that have an amplitude distribution of a sinc function as shown in Figure 3.10 part (a). To angle multiplex another grating, the reference angle is changed and a new grating is recorded as in part (b). To find the cross-talk between the gratings, simply place the second grating vector at the beginning of the first vector and see where the resultant vector's sinc function crosses the normal surface. Notice that for two plane waves recorded at 90° it is possible to place this second resultant grating in the zero of the sinc function. Thus, it is possible to record two plane waves with zero

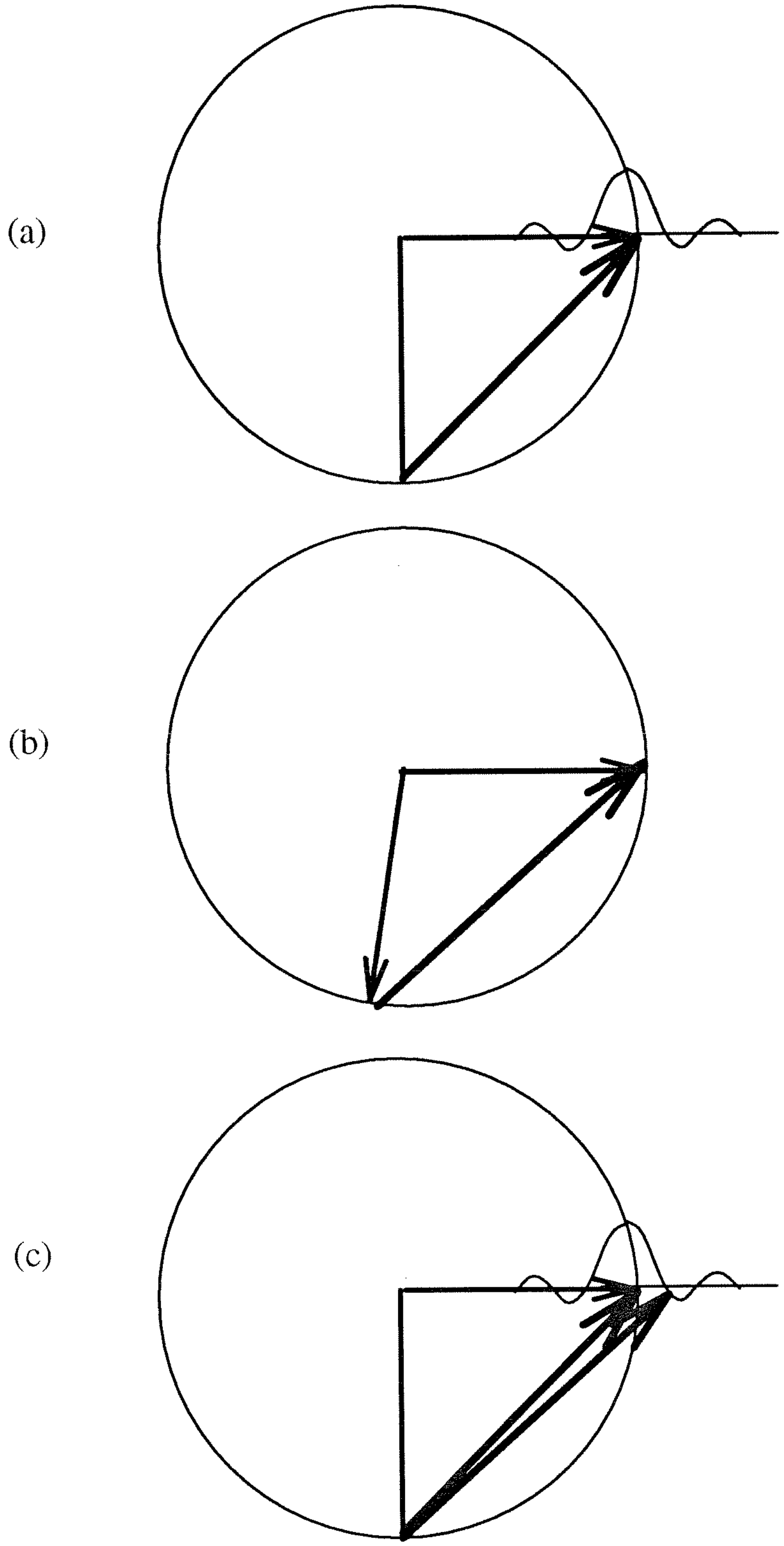

Figure 3.10: **k**-space diagram for reconstruction (a) single grating selectivity, (b) another grating angle multiplexing, (c) placing in nulls of first grating.

cross-talk. Unfortunately, since images are made up of many plane wave components it is **not** possible to make all of the components fall in the nulls. To better see what factors influence the cross-talk, it is advantageous to look at the grating relationships in "grating space."

3.3.3 K-space for Angle Multiplexing

Grating space (or **K**-space) is simply the volume traced out by all the grating vectors after the ends are superimposed. This creates a space that is filled by the gratings and allows the distance between gratings to be easily visualized. Since only one particular value of separation in the z direction allows the sinc function to cross the normal surface at the minimum of the sinc function, any change in the distance between gratings results in cross-talk noise. Thus, **K**-space allows sources of cross-talk to be visualized.

K-space for angle multiplexing is made by first drawing the **k**-space pictures for the various holograms as shown in Figure 3.11. The spectrum of plane wave vectors that make up the image lie in the shaded regions of Figure 3.11. For simplicity, only the grating to the center plane wave of the image is drawn. To form **K**-space, the ends of the gratings are placed together. This results in Figure 3.12 which shows the **K**-space picture for three angle multiplexed holograms. Notice that as the angular spread of the images are increased the distance between the gratings is changed. If $d/2$ is the maximum extent of the image plane and F is the focal length of the Fourier transforming lens, the maximum angular bandwidth of the image can be written as $\Delta\theta_i = d/2F$. Also notice that the outer holograms tend to rotate down on their normal surfaces relative to the center hologram. This rotation also changes the distance between the gratings and therefore introduces cross-talk. The maximum rotation is directly related to the maximum angular bandwidth of the reference beams. This spread of reference beams depends on the number of holograms and the spacing

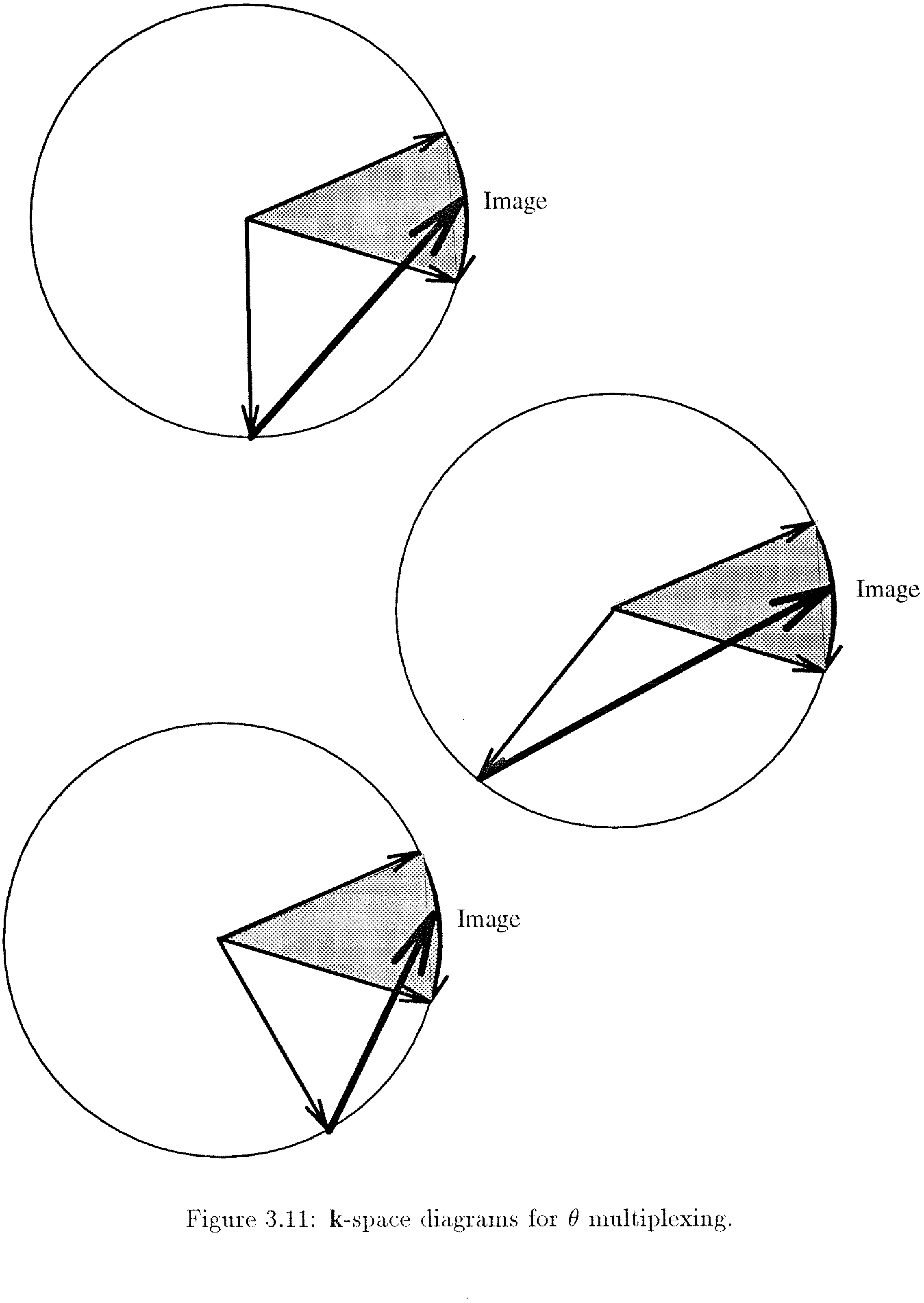

Figure 3.11: **k**-space diagrams for θ multiplexing.

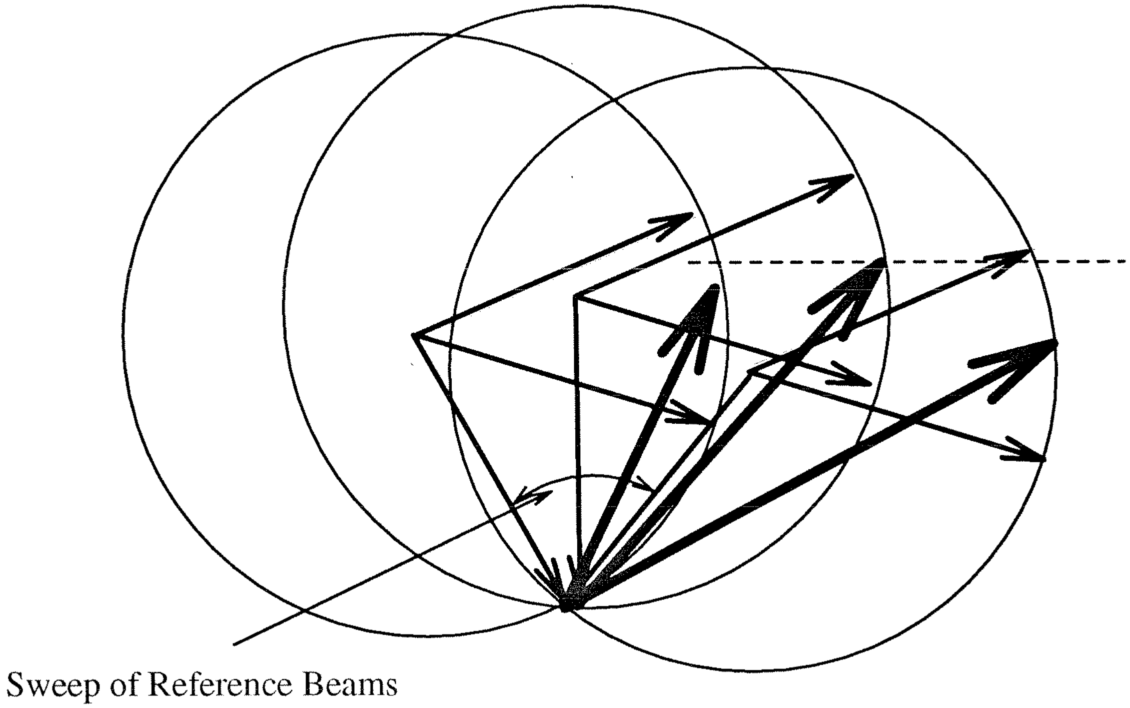

Figure 3.12: **K**-space diagrams for θ multiplexing.

of the reference angles. In the 90° geometry, the bandwidth of the reference beams is equal to $\Delta\theta_r = \lambda N_\theta / t$, where N_θ is the number of holograms stored, and t is the thickness of the recording medium in the z direction.

The closed form solution for SNR of θ multiplexed holograms in the 90° geometry was given in Chapter 2 as

$$\mathrm{SNR} = \frac{2tF}{\lambda d N_\theta} = (\frac{1}{\Delta\theta_i})(\frac{1}{\Delta\theta_r}). \tag{3.5}$$

We see that the SNR for angle multiplexing goes as one over bandwidth of the reference beams and one over the bandwidth of the image beam.

Rotation and phase code have geometries similar to the geometry for angle multiplexing. Phase code multiplexing has exactly the same geometry except that the noise does not add up coherently. For rotation multiplexing, the grating space picture is shown in Figure 3.13. Notice that again the two factors are image bandwidth and rotation of image away from the center. Because of this, for small rotations, the SNR result for rotation multiplexing is approximately the same as for θ multiplexing.

3.3.4 k-space for Wavelength Multiplexing

Wavelength multiplexing in the pure reflection geometry is shown in Figure 3.8. A single grating is recorded by two plane waves of a given wavelength interfering inside the material as shown in Figure 3.14 part (a). Again, the grating vector is the thicker vector that connects the reference and signal plane waves and is defined as $\vec{K} = \vec{k}_s - \vec{k}_r$. To reconstruct the hologram, the reference beam with the original wavelength is input, diffracts off the grating, and reconstructs the original signal, since $\vec{K} + \vec{k}_r = \vec{k}_s$.

Just like in θ multiplexing, since the material is of finite thickness one can imagine that instead of a single grating the actual recording is a spectrum of gratings that have an amplitude distribution of a sinc function as shown in Figure 3.14 part (a).

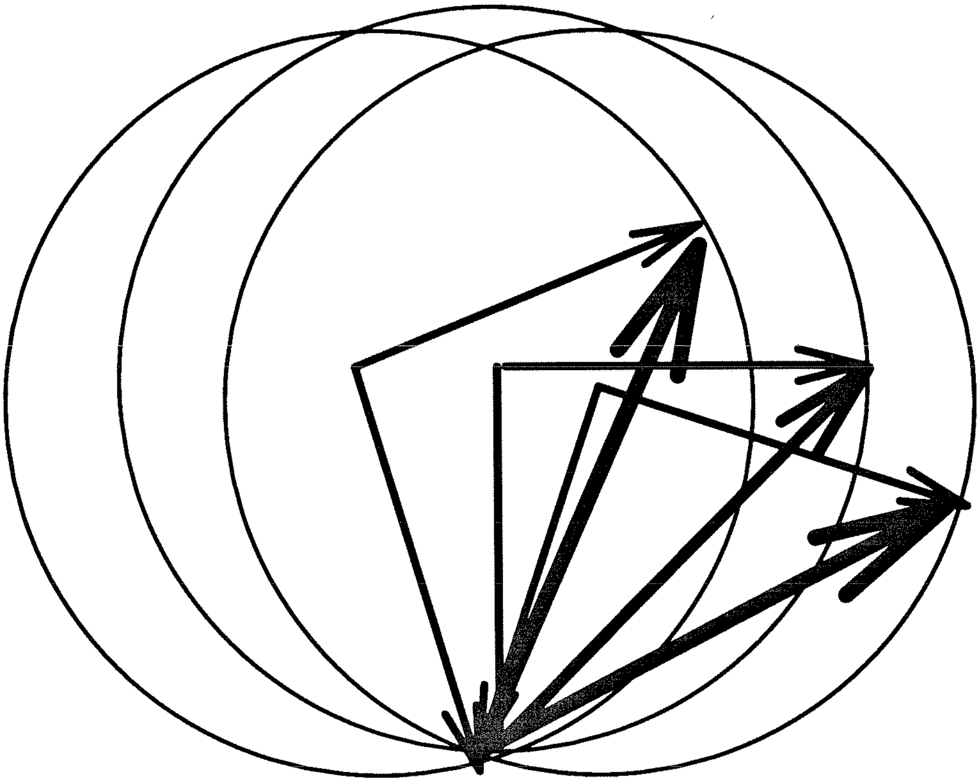

Figure 3.13: K-space diagrams for rotation multiplexing.

To λ multiplex another grating, both the reference and signal beam wavelengths are changed and a new grating is recorded on a different normal surface, since the radius of the normal surface depends in the wavelength of the light as in part (b). To find the cross-talk between the gratings, simply place the second grating vector at the tip of the first vector and see where the resultant vector's sinc function crosses the normal surface. Notice that for two plane waves it again is possible to place the resultant in the minimum of the sinc function. In other words, it is possible to record two plane waves with minimal cross-talk. Unfortunately, as in the angle multiplexing case, images are composed of many plane wave components and it is **not** possible to make all of these components fall in the minima of the sinc functions. To better see what factors influence the cross-talk for wavelength multiplexing, it is again advantageous to look at the grating relationships in grating space.

3.3.5 K-space for Wavelength Multiplexing

The same procedure of placing the ends of the gratings together is used to construct the **K**-space picture for λ multiplexing. Figure 3.15 shows the grating space picture for three λ multiplexed holograms. For clarity, the grating vectors are not shown. Again, notice that as the angular spread of the images ($\Delta\theta_i = d/2F$) is increased the distance between the gratings is changed. Unlike in the θ multiplexing case, the images do not rotate or move relative to each other as more holograms are stored. This explains why the SNR saturates to a fixed value for a large number of λ multiplexed holograms.

The closed form solution for the SNR for λ multiplexing holograms in a pure reflection geometry was given in Chapter 2 as

$$\mathrm{SNR} = \frac{8F^2}{d^2} = 4(\frac{1}{\Delta\theta_i})(\frac{1}{\Delta\theta_i}). \tag{3.6}$$

We see that for λ multiplexing, the SNR goes as one over the bandwidth of the image

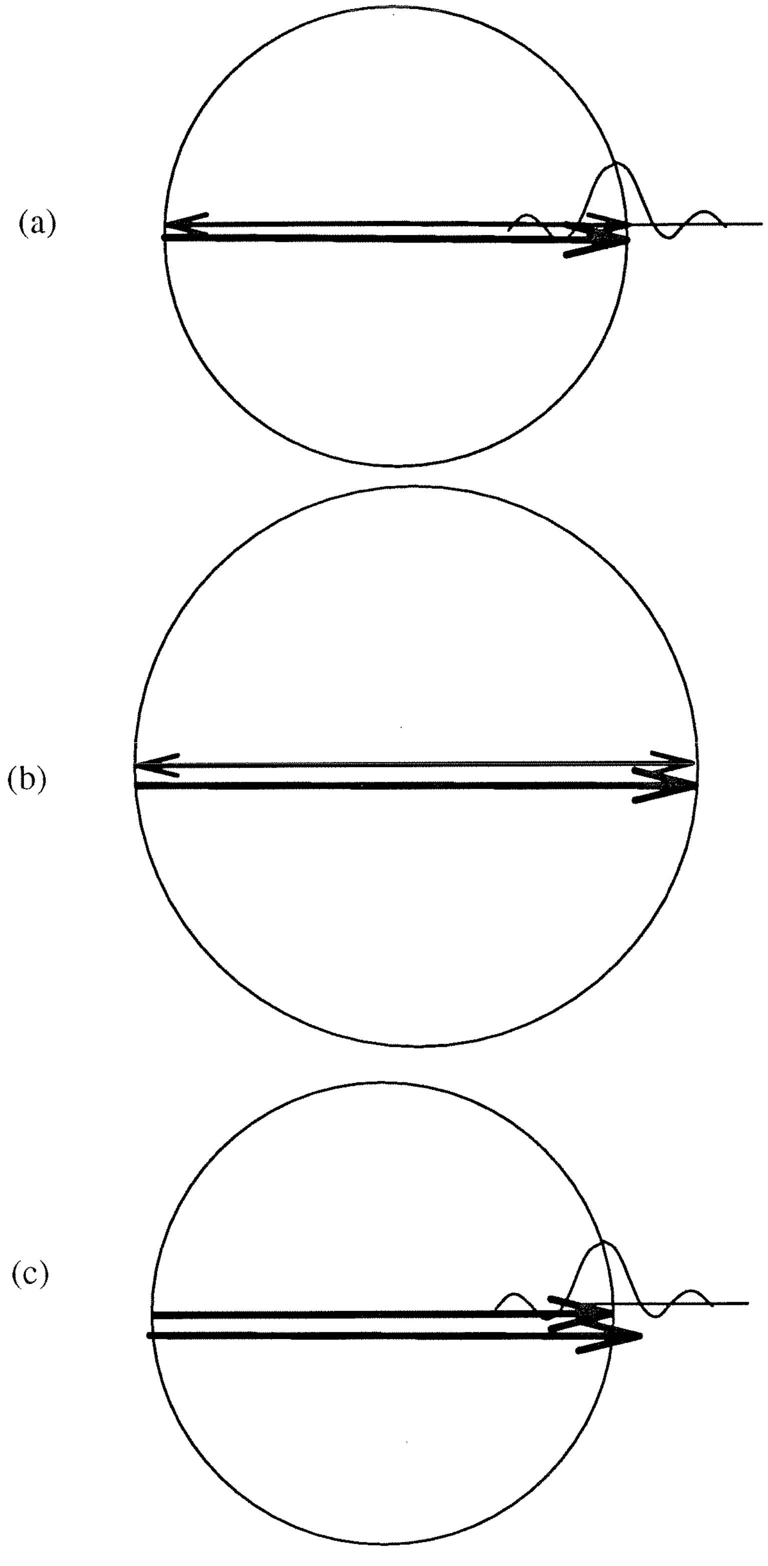

Figure 3.14: **k**-space diagram for reconstruction (a) single grating selectivity, (b) another grating angle multiplexing, (c) placing subsequent gratings in nulls of first grating.

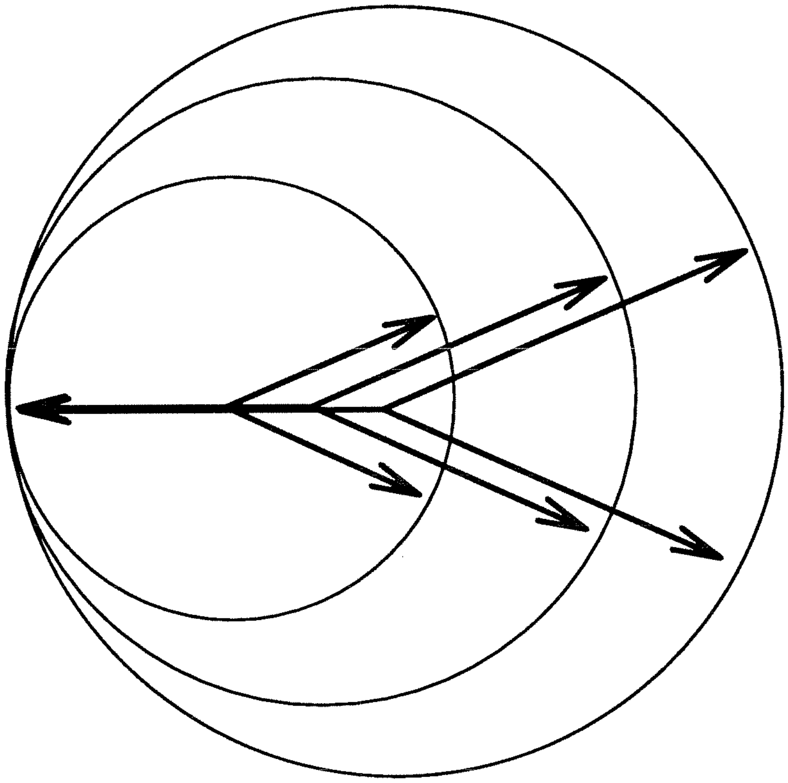

Figure 3.15: K-space diagrams for wavelength multiplexing.

beam squared.

3.3.6 Comparison of Methods

For angle multiplexed Fourier transform holograms in a 90° configuration the minimum SNR is given by

$$SNR_\theta = \frac{2tf}{\lambda d N}, \tag{3.7}$$

where t is the interaction length, f is focal length, λ is the wavelength, d is the full length of the output/image plane, and N is the number of holograms. For wavelength multiplexed Fourier-transform holograms in a 180° configuration, the minimum SNR is given by

$$SNR_\lambda = \frac{8f^2}{d^2}, \tag{3.8}$$

where f is focal length, and d is the full length of the output/image plane. Therefore, for λ multiplexing, the SNR (for $N >$ a few holograms) is independent of the number of holograms.

The SNR expressions can be compared to derive some general trends of how to best use each multiplexing method. Looking at the closed form solution we can see that the SNR depends on the bandwidth of the image beam or the reference beams. Looking at the functional behavior, the SNRs can be written as

$$\begin{aligned} \mathrm{SNR}_\theta &\sim \frac{1}{dN_\theta} \\ \mathrm{SNR}_\lambda &\sim \frac{1}{d^2} \end{aligned} . \tag{3.9}$$

Therefore, when θ multiplexing one wants to store large images and fewer holograms. When λ multiplexing one should store many small images. Thus, increasing the page size favors θ multiplexing, but increasing the number of holograms favors λ multiplexing.

We can divide Equation 3.8 by Equation 3.7 and get the ratio of the two SNR's. The number of holograms that can be stored is proportional to $\frac{t}{\delta}$, where δ is the resolution of the material. This fact follows from a degrees of freedom argument and is relatively easy to prove for θ multiplexing. We will briefly show how it is also true for λ multiplexing. The largest optical frequency that we can use is $2c/\delta$ and the smallest is $2c/t$. The selectivity of the λ multiplexed holograms to a change in the optical frequency is $\delta\nu = c/t$. The number of holograms that can be λ multiplexed is therefore $c(\frac{1}{\delta} - \frac{1}{t})/(c/t) \approx \frac{t}{\delta}$. Using this upper bound for N, the ratio of SNRs becomes

$$\frac{SNR_\lambda}{SNR_\theta} = \frac{4\lambda f N}{dt} \approx \frac{4\lambda f}{d\delta}. \tag{3.10}$$

Using typical experimental parameters of $f/d = 5$ and $\lambda \approx \delta$ results in an SNR ratio ~ 10 when storing the maximum possible (geometrically limited) number of holograms. Notice that for thicker holograms, θ multiplexing becomes more favorable since for a given number of holograms the needed $\Delta\theta_r$ is smaller which reduces the rotation of the images in **K**-space for the case for angle multiplexing.

Another way to compare the two methods is by solving Equation 3.7 for N, and then using the SNR$_\lambda$ from Equation 3.8 to obtain an expression for the number of holograms that can be θ multiplexed with the same SNR as that obtained by λ multiplexing. This results in an expression for the number of holograms that can be angle multiplexing as

$$N_\theta = \frac{td}{4\lambda f}. \tag{3.11}$$

Using typical parameters ($t \approx 1$cm) results in $N_\theta \sim 10^3$. Let $\Delta\nu$ be the spectral width of the light source and/or the spectral sensitivity of the material. Then the number of holograms that can be stored with λ multiplexing is

$$N_\lambda = \frac{\Delta\nu}{\delta\nu} = \frac{\Delta\nu t}{c}\ . \tag{3.12}$$

We can now obtain an expression for the ratio of the number of holograms that can be stored with the same SNR for λ and θ multiplexing due to system constraints:

$$R = \frac{N_\theta}{N_\lambda} = \frac{1}{8}\frac{\frac{d}{f}}{\frac{\Delta\nu}{\nu}} = \frac{1}{4}\frac{\Delta\theta_i}{\frac{\Delta\nu}{\nu}} \ . \tag{3.13}$$

Therefore, it is the **fractional spectral bandwidth of the tunable laser versus the bandwidth of the optical system that carries the stored images** that determines which method can store more holograms in the same volume and with the same SNR. Using $\Delta\theta_i \sim 1/5$ and $\frac{\Delta\nu}{\nu} \sim 1/10$ results in a ratio on the order of one. Thus, the number of holograms that can be stored with the same SNR and in the same volume using either method is roughly equivalent.

3.4 Dynamic Range – When Does Crosstalk Dominate?

There are many sources of noise in a practical holographic memory system such as scattering, fanning, spatial light modulator uniformity, mechanical instabilities, and detector noise. To answer how these noise sources compare to cross-talk, we must consider how the grating strengths change as more holograms are recorded. Given that we want the diffraction efficiencies of the individual holograms to be the same, we know that the individual grating amplitudes varying as $1/M$ where M is the number of holograms multiplexed in the same volume [155]. Therefore, the individual diffraction efficiency goes as $1/M^2$. The total NSR can now be written as

$$NSR = \frac{\alpha N_{ct}/M^2 + N_o}{\alpha/M^2}, \tag{3.14}$$

where N_{ct} is the normalized cross-talk noise, α is the reconstructed intensity in W/cm^2 that is obtained when a single hologram is recalled, and N_o is the noise from all sources that are independent of the number of holograms stored.

The crossover between cross-talk dominated noise and domination by other noise sources can be found by setting the two terms equal and solving for M. This results in

$$M = \sqrt{\frac{NSR_x \ \alpha}{N_o}}, \tag{3.15}$$

where NSR$_x$ is the cross-talk NSR. Using the closed-form asymptotic expressions for NSR$_x$ with typical experimental parameters that we see in the lab, such as $\alpha =$ .1 W/cm^2, N_o = 1nW/cm^2 and the parameters mentioned previously, we find the crossover points to be $M_\lambda \sim 350$ and $M_\theta \sim 700$. This means that if we λ multiplex more than 350 holograms, N_o will dominate since its contribution increases relative to the cross-talk noise. The crossover number for ϕ multiplexing is even smaller than for θ multiplexing, since ϕ multiplexing has significantly better SNR. The exact value of the crossover depends on the parameters used; however, we can still conclude that for all three multiplexing methods in the optimal geometries **cross-talk is only important for a small number of holograms**, and SNR will be dominated by other noise sources in any holographic memory that multiplexes a large number of holograms in the same volume. Moreover, if the total number of holograms is small then the SNR is large and cross-talk is not the limiting factor in performance.

Chapter 4

Holographic Storage Using DuPont Photopolymer

4.1 Introduction to Photopolymers

4.1.1 Background

In the early 1970's, while photorefractives were initially being developed, photopolymers were also being pursued for the purpose of holographic storage [100]–[110]. These photopolymers consist of monomers and a light sensitive dye inside a polymer matrix. Two plane waves interfere inside the material and sets up a sinusoidal intensity pattern as shown in Figure 4.1(a). The light excites the dye and initiates a free radical reaction. This locally polymerizes the monomers in the illuminated regions and sets up gradients in monomer concentration inside the polymer as in Figure 4.1(b). The monomers then diffuse into these regions and are polymerized, which increases the density of the film in the illuminated regions. This density change directly relates to a change in the index of refraction as in Figure 4.1(c). Thus, like photorefractives, these polymers record phase gratings. Unlike photorefractives, these films inherently record permanent gratings since the polymerization reaction is irreversible. Figure 4.1(d) diagrams the entire process with monomer diffusion and local polymerization. After the holograms are stored, the film is uniformly exposed to complete polymerization

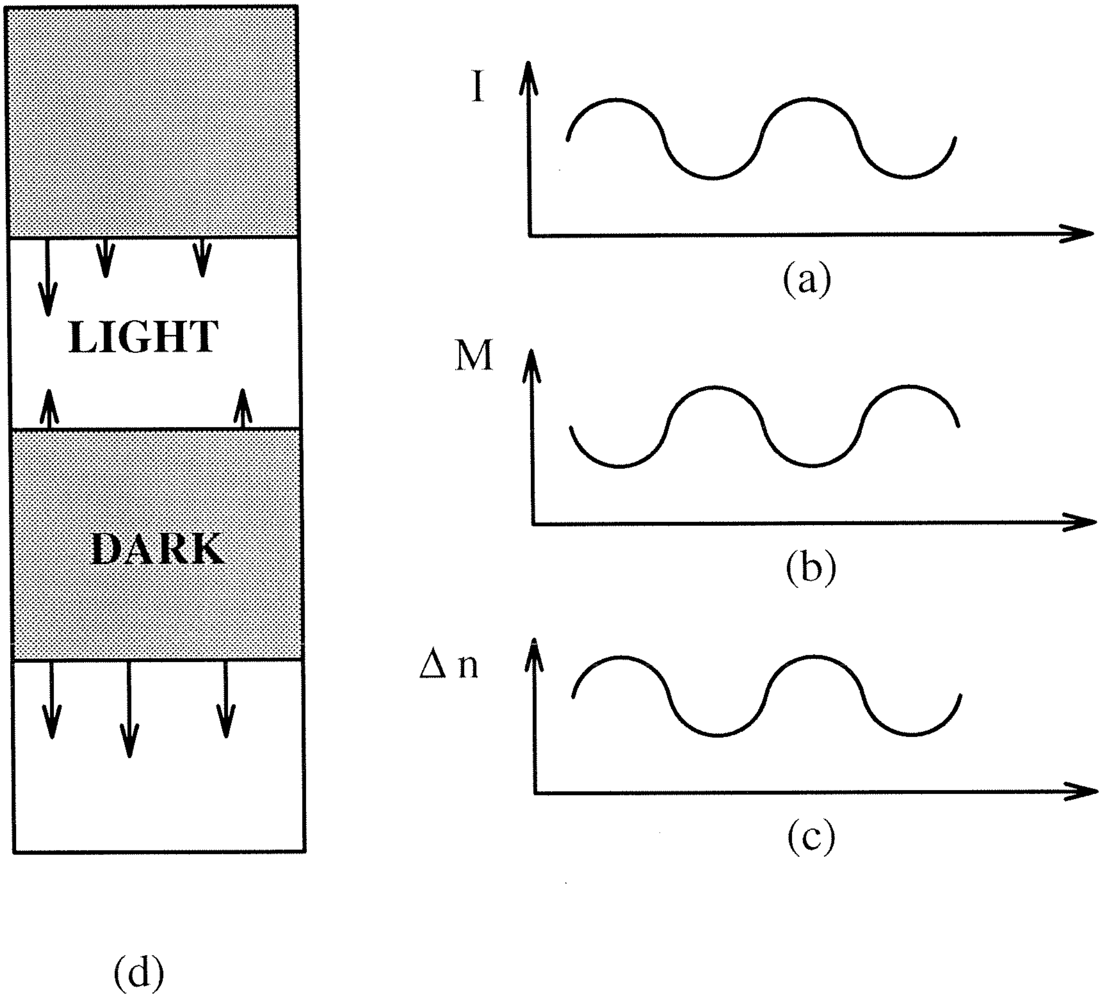

Figure 4.1: Light induced polymerization: (a) light intensity (b) monomer concentration after local polymerization (c) resulting index grating (d) diagram of the entire grating formation process.

and ensures the stability of the gratings and the film.

In 1976, Bartolini et al. [111] angle multiplexed 550 holograms in one centimeter thick photopolymer film. Using similar material, DuPont marketed a commercial holographic photopolymer product in the 1970's. Recently, DuPont, Polaroid, and others have photopolymer films [112]- [117] that have good sensitivity, resolution, and relatively large index changes. These films have been used for filters [118, 119, 120], holographic storage [121, 122], and the verification of drivers licenses and credit cards (although, the holograms on these cards are mechanically, not holographically reproduced). In addition, the theory of polymerization and monomer diffusion in photopolymer films has been investigated [123, 124].

4.2 Characterization of the DuPont Photopolymer for Holographic Storage

4.2.1 Introduction

DuPont's HRF-150 photopolymer film is investigated for use in 3-D holographic memories. Measurements of sensitivity, hologram persistence, the lateral spread of the photo-initiated reaction, and the variation of diffraction efficiency with modulation depth, spatial frequency/tilt angle, and intensity are reported. 3-D holographic disk systems can be used as memories and correlation devices with very high storage density and correlation rates [196, 120]. DuPont's photopolymer HRF-150 has excellent sensitivity and good resolution for transmission holograms recorded with blue-green light [112, 194, 195]. Thus it is a likely candidate for use as a holographic storage material. This section presents results on sensitivity, hologram persistence, the lateral spread of the photo-initiated reaction, and the variation of the diffraction efficiency with modulation depth, spatial frequency/tilt angle and intensity. These are all important characteristics for evaluating these photopolymer films as media for

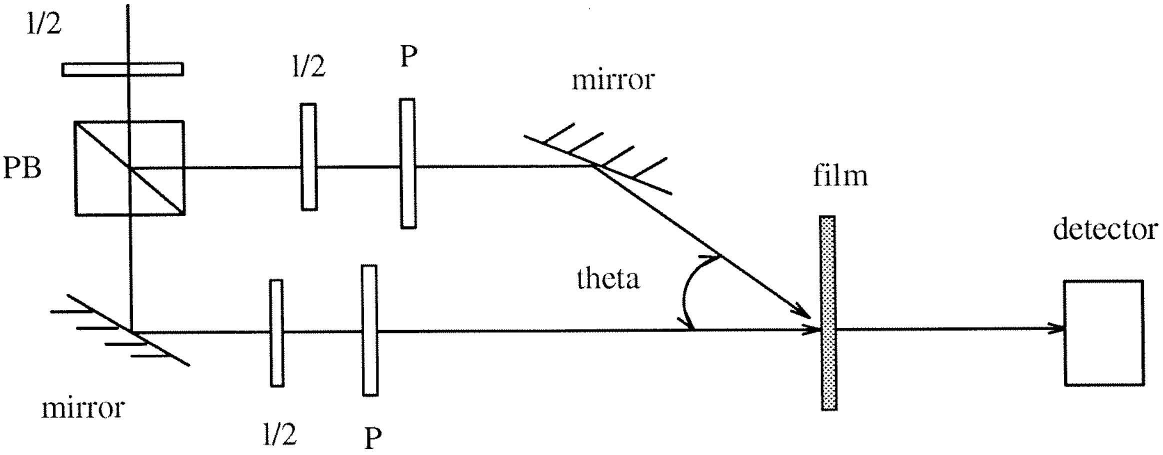

Figure 4.2: Recording geometry used for measurements with the elements given as: P – polarizer, 1/2 – half-wave plate, PB – polarizing beam splitter.

holographic storage applications.

4.2.2 Recording Characteristics

HRF-150 photopolymer films consist of 38μm thick photopolymer film sandwiched between two thin sheets of mylar. Hologram storage was performed using the setup shown in Figure 4.2. The object beam is incident normal to the surface, while the reference beam is incident at an angle θ. Both beams are plane waves at 488 nm and the film is mounted on a glass substrate. After recording, the hologram is fixed by exposing the film to uniform UV light for 45 seconds. We define diffraction efficiency as incident intensity divided by diffracted intensity after the reference beam is re-Bragg matched to adjust for film shrinkage [122].

The sensitivity curve of the material is shown in Figure 4.3 where the diffraction efficiency of the first diffracted order is plotted against the total exposure energy. The intensity of each beam was kept constant at 2 mW/cm^2 with $\theta \approx 18°$ and the exposure time varied to obtain the data in Figure 2. When the diffraction efficiency exceeded 20%, a considerable amount of energy was diffracted into the 2 and -1 orders. Notice

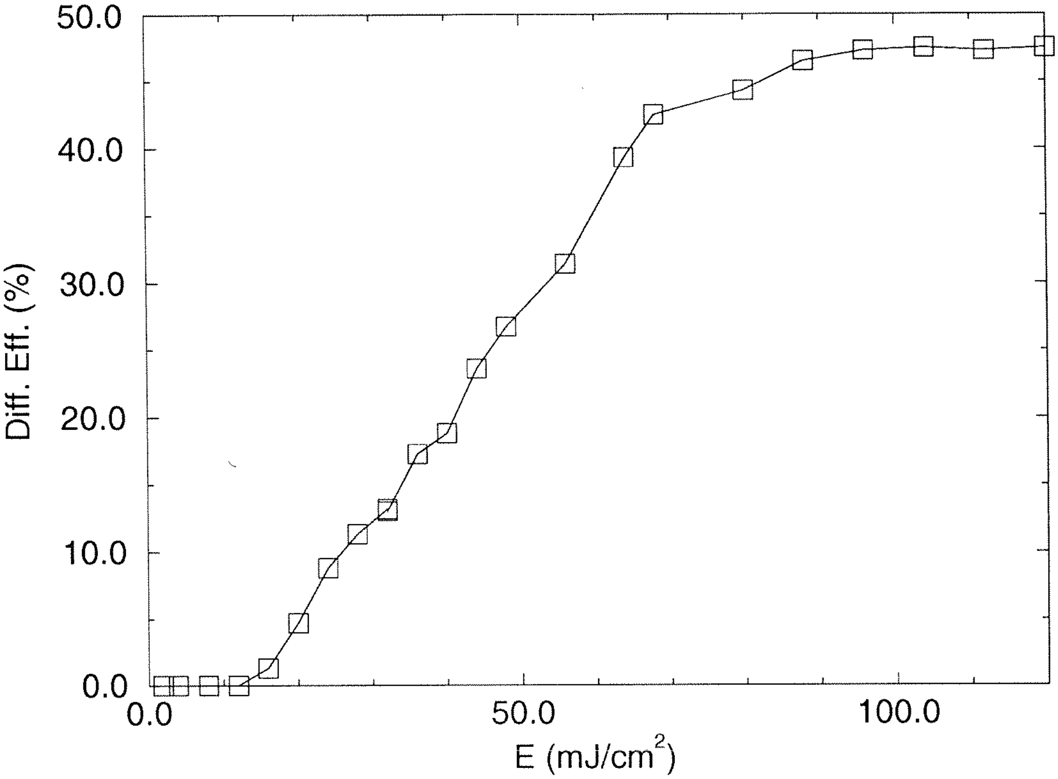

Figure 4.3: Diffraction efficiency vs exposure energy.

that the saturation exposure was approximately 80 mJ/cm^2.

We also measured the effect of the intensity on the photopolymer's sensitivity. Keeping the intensities of the two beams equal, $\theta \sim 20°$, and the total exposure of 20 mJ/cm^2, the diffraction efficiency was measured as the total intensity of the two beams was changed. Figure 4.4 shows that as the intensity is increased, the film becomes less effective. Since the photo-initiated reaction is a free radical reaction, it can be slowed or stopped by inhibitors. Free radicals themselves are very efficient inhibitors, therefore, increasing intensity, which generates more free radicals, can inhibit the reaction.

The modulation depth is defined as $m = 2RS/(R^2 + S^2)$ where R and S are the amplitudes of the reference and the signal beams. Figure 4.5 shows the diffraction efficiency versus m for $\theta \sim 20°$ with the total exposure kept constant at 20 mJ/cm^2. The curve shows that if $m < 0.2$, the diffraction efficiency is small. This is probably

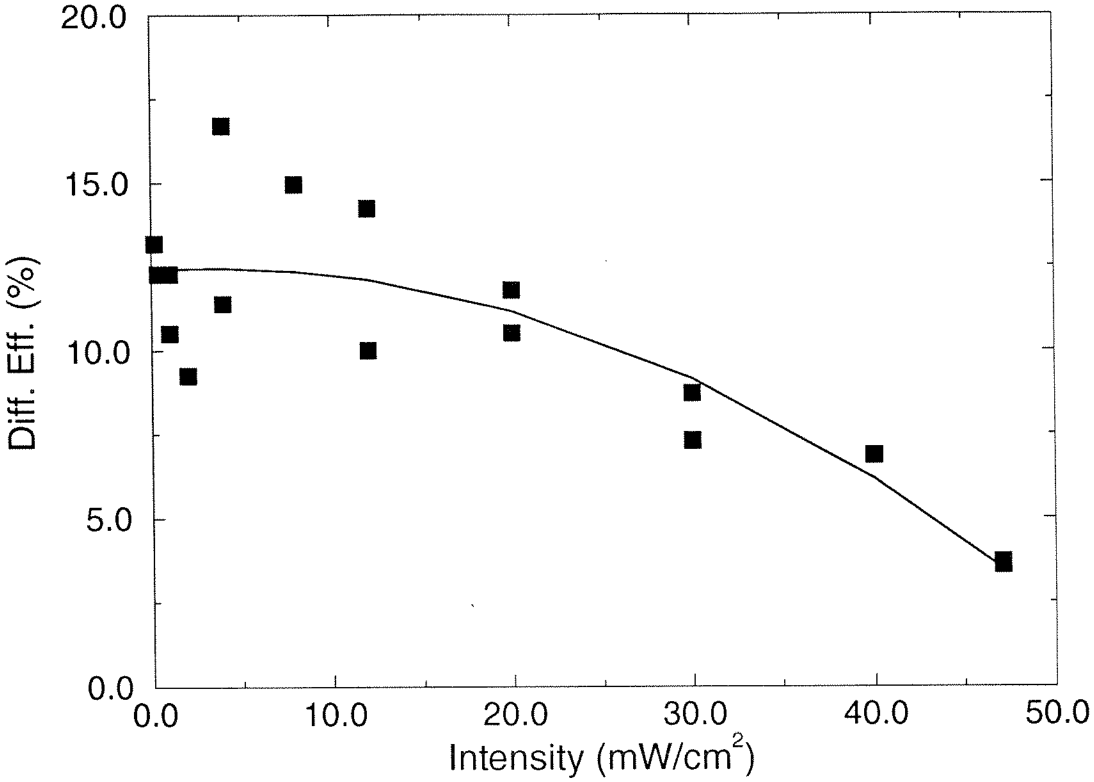

Figure 4.4: Diffraction efficiency vs intensity for E = 20 mJ/cm^2.

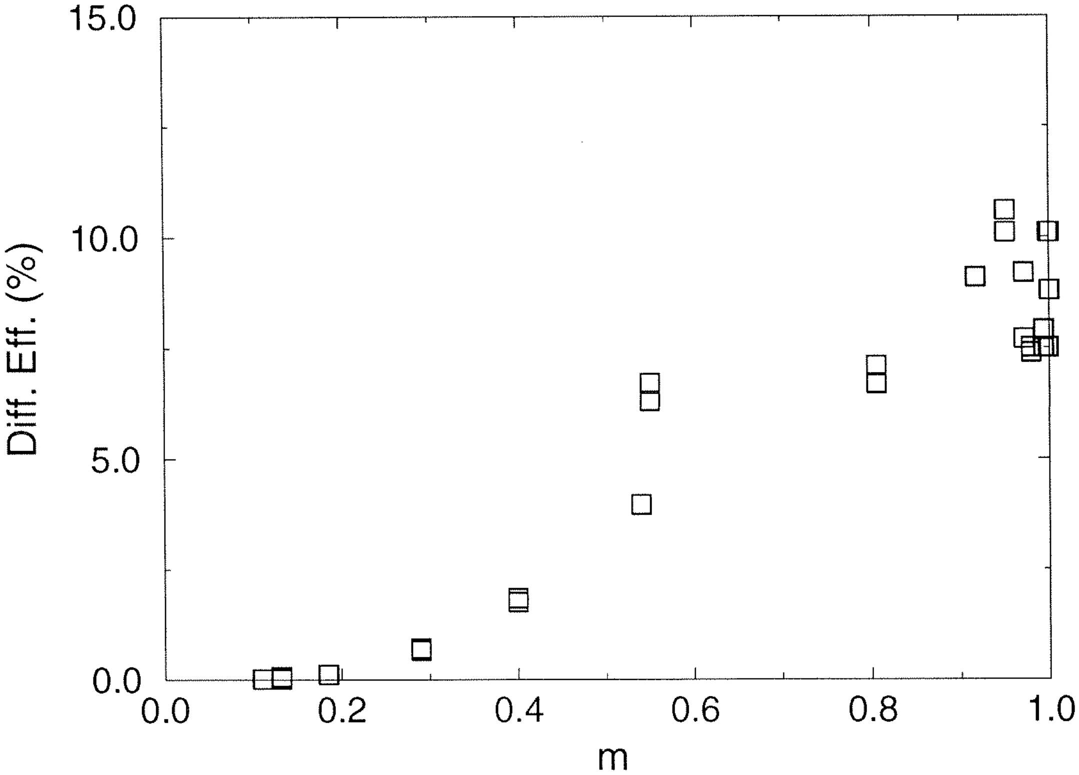

Figure 4.5: Diffraction efficiency vs modulation depth.

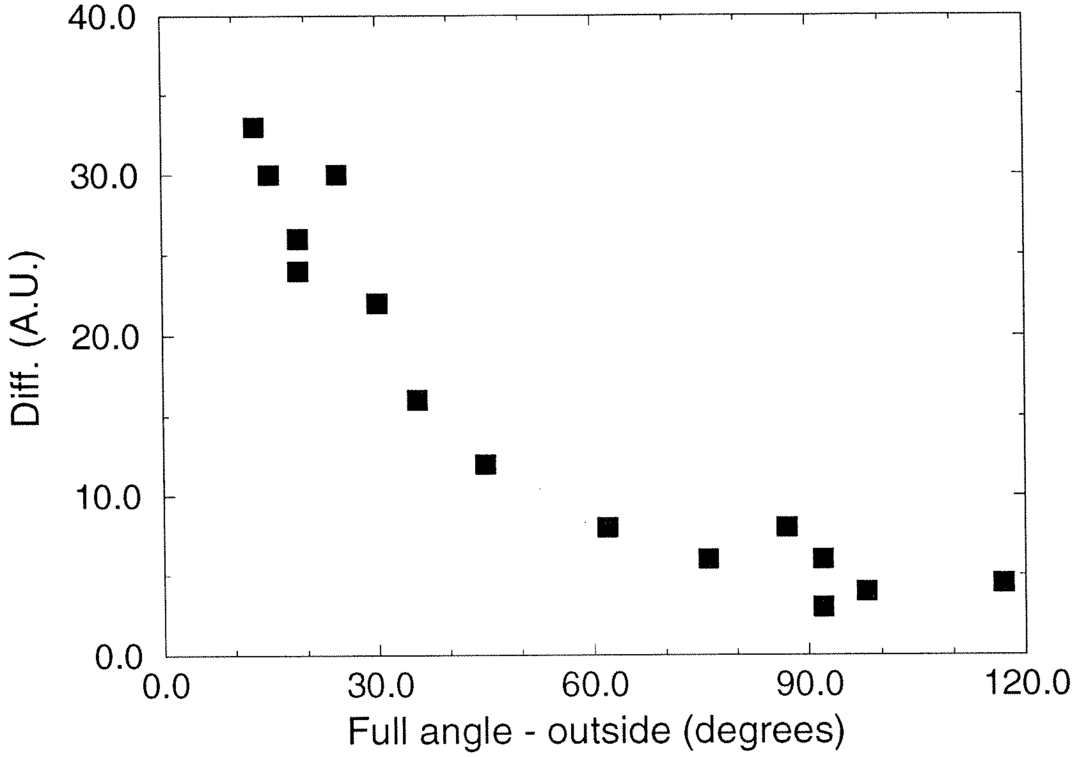

Figure 4.6: Diffraction efficiency vs full angle between the beams outside the material for E = 20 mJ/cm^2 and no grating tilt.

due to the fact that at low modulation the large background intensity polymerizes the material uniformly which impedes monomer diffusion. The curve also shows a saturation behavior around $m = 1$. This saturation is not due to the normal diffraction from a strong grating because we have a relatively weak modulation ($\frac{2\pi\Delta nL}{\lambda n} < .33$). Therefore, we attribute this saturation to the monomer diffusion mechanism in the film.

The film's response to grating frequency is measured by recording the diffraction efficiency as a function of the angle between the beams while keeping the bisector of the angle perpendicular to the film's surface. This geometry ensures that the fringes are always perpendicular to the film surface. Figure 4.6 shows the result for $E = 20$ mJ/cm^2. The efficiency is plotted against the full angle between the beams to make it

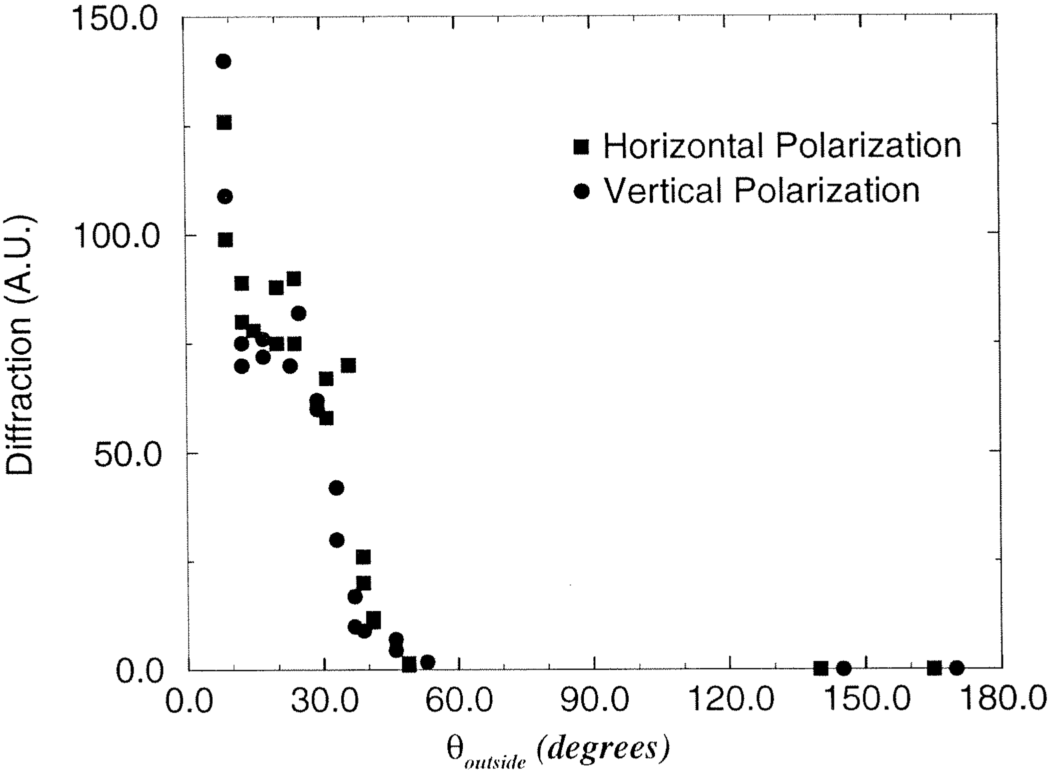

Figure 4.7: Diffraction efficiency vs angle outside the material for E = 20 mJ/cm^2 image beam incident normal to the surface.

easier to understand the next two results. Notice that the film prefers lower frequency gratings but the curve becomes flatter around 90° between the beams. The 3db point of the frequency response is at approximately 30°, corresponding to approximately 1,000 cycles/mm.

Figure 4.7 shows the diffraction efficiency for a total exposure of 20 mJ/cm^2 as a function of the reference angle θ for both polarizations with the signal beam incident normal to the surface. The intensity of each beam is 2.2 mW/cm^2. The results for each polarization are similar. HRF-150 is designed by DuPont as a transmission film and, as Figure 4.6 shows, it does not effectively record reflection holograms. Comparing this result with Figure 4.6, we see that the drop in efficiency for angles larger than 30° is not due entirely to the change in spatial frequency. It appears that the film does not effectively record gratings that have a large tilt angle inside the material. This is probably due to the film's thickness being only 38μm.

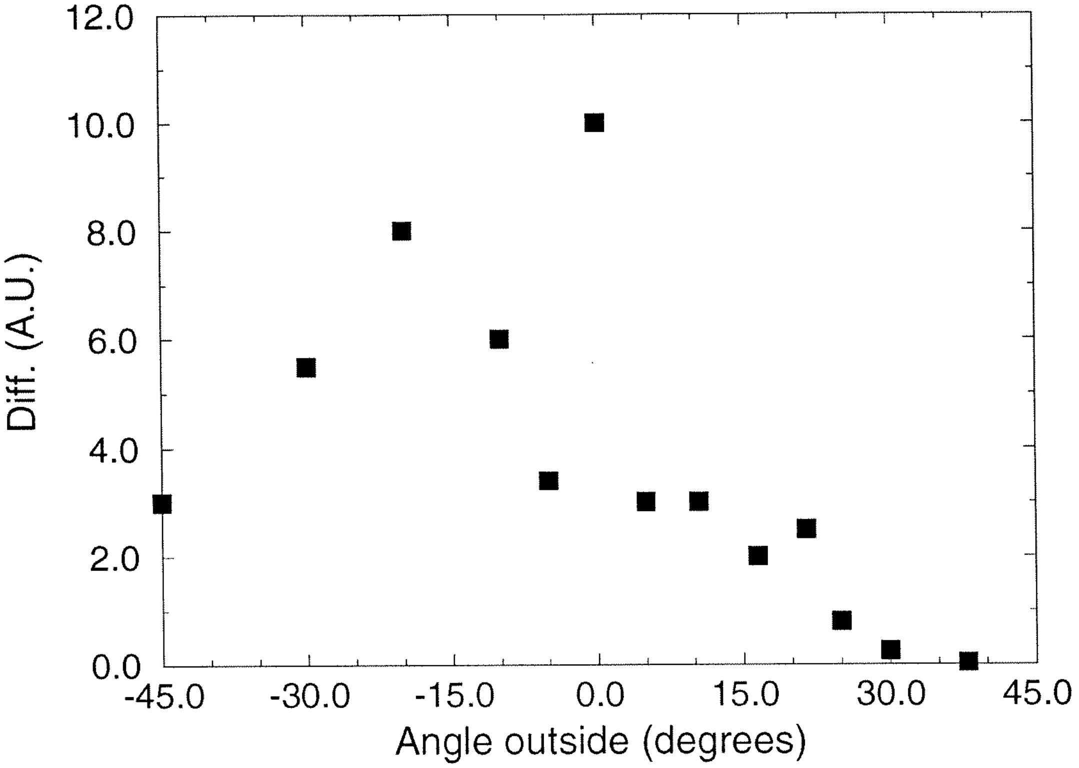

Figure 4.8: Diffraction efficiency vs angle outside the material for E = 20 mJ/cm^2 with 90° degrees between the 0° reference beam and the signal.

To evaluate this effect further, we again measured the film's response as the reference angle is changed, but this time with the center angle between the beams being 90° where we know (from Figure 4.6) that the film's frequency response is relatively flat. Figure 4.8 plots diffraction efficiency for a total exposure of 20 mJ/cm^2 as a function of the reference angle θ. In this plot, an angle of 0° refers to 90° angle between the beams with no tilt in the gratings. Notice that at -45° the diffraction is less than at -20° even though we know that the spatial frequency at -45° is preferred by the film when the grating is not tilted. This loss in sensitivity is attributed to the grating tilt. The maximum fringe tilt that the film can tolerate is approximately 10°.

If the material is going to be used as a storage element, the holograms must be able to be recalled nondestructively after they are fixed with UV light. Figure 4.9 shows the continuous readout of a hologram for 100 hours. The reference intensity was $\sim$ 3mW/cm^2 with a diffraction efficiency of about 1.5%. The initial increase,

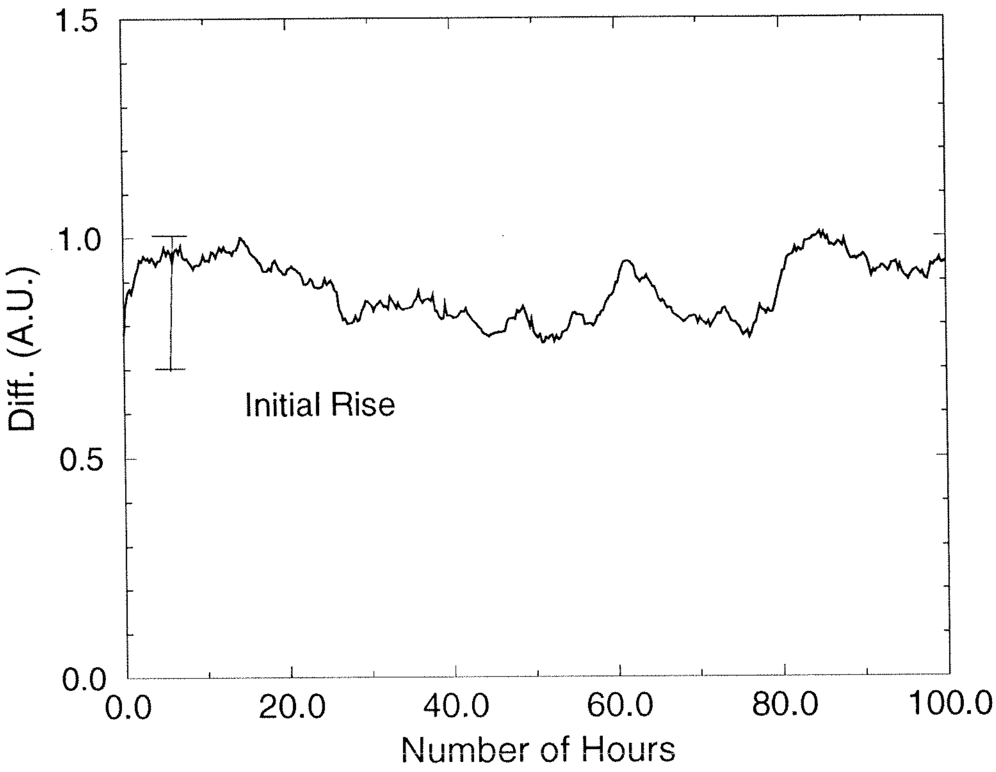

Figure 4.9: Diffraction vs readout time demonstrating nondestructive recall.

shown on the graph, is due to the bleaching of the material with light exposure. The grating was recorded with the object beam incident at -45° and the reference beam incident at 45° from surface normal. Multiplexed image plane holograms recorded more than a year ago and stored at room temperature can still be recalled.

Whether or not the reaction spreads laterally (in the plane of the film) is important if spatial multiplexing is desired. To test if the reaction spreads, a slit about 1mm across and 1cm long was cut in tin-foil to create a mask. The photopolymer was exposed with a single normal incident beam through this mask (E$\approx$ 300mJ/cm^2). The sample was then left in the dark, giving the reaction time to polymerize the material in the exposed region and possibly laterally spread to beyond the illuminated area. The mask was then removed and a hologram recorded in a large area around the slit's location on the film. The reconstructed hologram consists of bright areas where the film was unaffected by the first exposure, and dark areas where the film had already

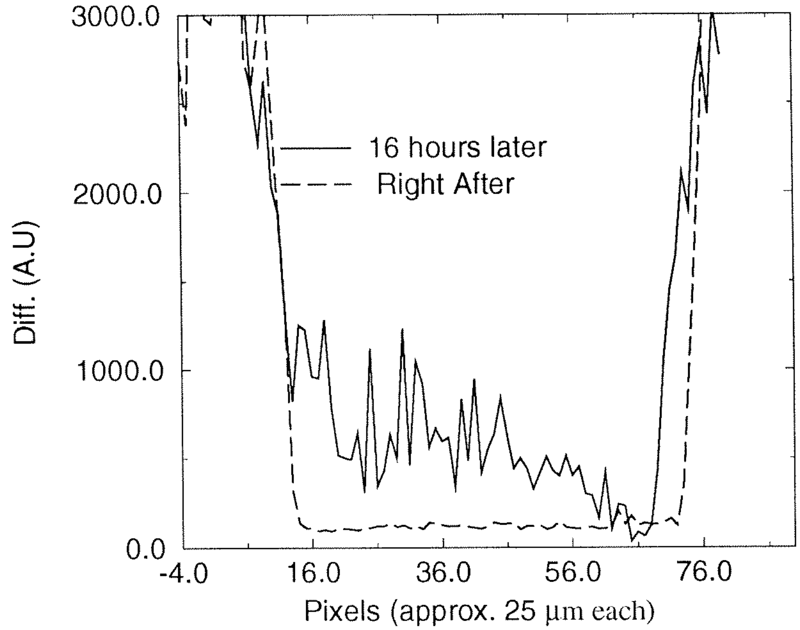

Figure 4.10: Cross sections of two reconstructed holograms across pre-exposed areas.

been exposed. Any lateral spreading of the reaction would cause a gradual loss of efficiency as the reaction spreads out and uses up the film's dynamic range. When the second exposure immediately followed the first, no appreciable lateral spread was observed, as shown in Figure 4.10 . The curve marked "Right After" shows a cross section of the intensity of the reconstruction across the dark area. The experiment was repeated, except this time the sample was left in the dark for 16 hours before the holographic exposure was done. Again, a dark slit was seen in the hologram, and a cross section marked "16 hours later" is shown in Figure 4.10. Notice that at the transition from dark to light the slope of the two curves is approximately the same. Therefore, within a measurement error of $\sim 100\mu m$, the reaction does not laterally spread. The 16 hour curve is slightly narrower width because it was taken at a different place along the slit.

In summary, we have observed that the sensitivity of the HRF-150 photopolymer decreases with increases in intensity and grating tilt angle. The holograms can be nondestructively reconstructed for long periods of time at room temperature. The photo-initiated reaction was seen to spread less than 100μm over periods of many hours. Overall, the HRF-150 has many of the desirable characteristics needed for a practical holographic storage material. The major improvement that is needed is an increase in film thickness to 200 μm or more. This would allow more holograms to be multiplexed at a single location and also it would probably alleviate the problem with tilted gratings that is reported in this paper.

4.3 Phase Grating Profiles in Photopolymers

4.3.1 Introduction

Thick volume gratings have been investigated since the beginning of the century in connection with X-ray diffraction, light diffraction by acoustic waves, and holography. The simplest theory [26] takes into account two waves (the diffracted wave and the transmitted wave) diffracting off a pure sinusoidal phase grating. Considerable work has been done on calculating the effect of higher order modes for arbitrary grating shapes at on-Bragg angle incidence [28, 197, 198, 199]. This was expanded for pure sinusoidal gratings to off-Bragg angles of incidence by B. Benlarbi et al. [200]. Recently, for photorefractives, Kukhtarev's equations have been solved for higher modes at on and off-Bragg angles of incidence [201, 202]. In addition to photorefractives, there is reason to believe that photopolymers form gratings that are nonsinusoidal [124]. Solutions to the nonlinear diffusion equation that governs photopolymer polymerization are given in reference [124], and they demonstrate that nonsinusoidal gratings are possible.

The criteria for the validity of the two mode theory is related to two quantities F and Q' [27], where F and Q' are defined as

$$\begin{aligned} F &= \frac{16n^2 \sin^2\theta}{\epsilon_{r1}} \\ Q' &= \frac{2\pi\lambda L}{\Lambda^2 \cos\theta} \,. \end{aligned} \tag{4.1}$$

In the above equations λ is the wavelength of the radiation, L is the interaction length, θ is the interior angle of incidence measured from the perpendicular, ϵ_{r1} is the relative permittivity of the perturbation, n is the index of refraction of the material, and Λ is the grating period. For sinusoidal gratings at on and off-Bragg angles of incidence, $Q' \gg 1$ and $F \gg 1$ is a sufficient condition for two mode theory to be adequate. By recording holograms in a geometry such that either Q' or F is small, the angular selectivity and diffraction efficiencies of the modes are determined by the grating profile.

Analyzing the grating profile and its effect on diffraction efficiency and angular selectivity is important for the effective use of photopolymers in optical systems that operate in the small F or small Q' regimes. For example, using thermoplastic plates, a system that uses the second-order mode instead of the first-order mode has been demonstrated [203]. In addition, if the gratings are similar to what is predicted by the nonlinear diffusion equation, this would indicate that diffusion is the dominant process in photopolymer grating formation. For these reasons, determination of the grating profile is the subject of this section.

4.3.2 Theoretical Model

We shall consider a one-dimensional, lossless, unslanted phase grating with the setup shown in Figure 4.11. Because the grating formation conditions are symmetrical around the peak of the sinusoidal intensity, we will look for symmetrical solutions

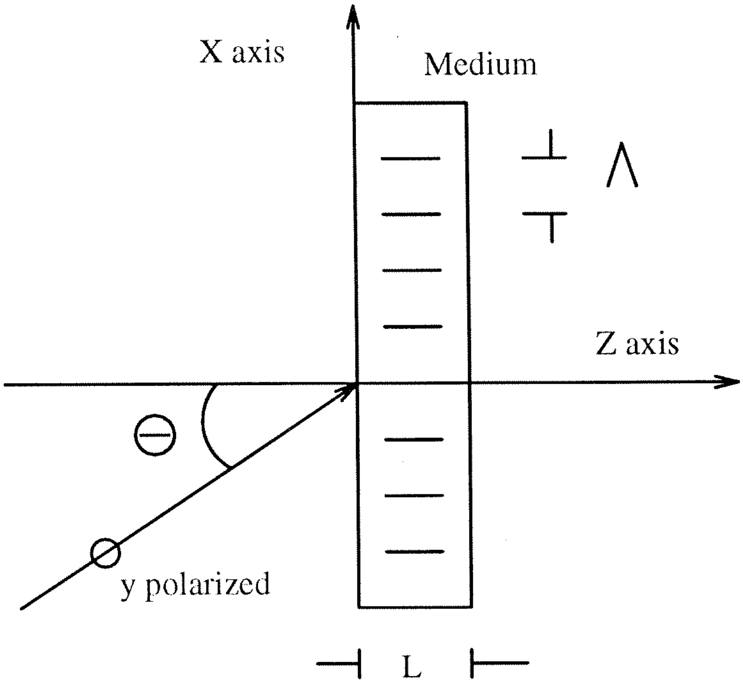

Figure 4.11: Geometry for diffraction from unslanted gratings.

without a phase shift. Therefore the relative permittivity is defined as

$$\epsilon_r(x) = \epsilon_{r0} + \sum_{i=1}^{\infty} \epsilon_{ri} \cos(iK_h x) \tag{4.2}$$

where $K_h = 2\pi/\Lambda$, and Λ is the grating period. Note that Δn_i is approximately equal to $\epsilon_{ri}/2n$. Using this information and the quantities defined in Figures 4.11 and 4.12, the problem is reduced to solving the scalar wave equation for E_y.

$$\frac{\partial^2}{\partial x^2}E_y + \frac{\partial^2}{\partial z^2}E_y - \mu_0\epsilon_0\epsilon_r(x)\frac{\partial^2}{\partial t^2}E_y = 0 \tag{4.3}$$

Now we assume a solution of the form of:

$$E_y(x,z) = e^{j\omega t} \sum_{m=-\infty}^{\infty} A_m(z)e^{j\phi_m} \tag{4.4}$$

where

$$\phi_m = \frac{2\pi n}{\lambda}(\sin(\theta)x + \cos(\theta)z) + mK_h x. \tag{4.5}$$

Plugging equation 4.4 into equation 4.3 and assuming the interchange of energy between modes is slow with respect to a wavelength (so that the second order derivatives can be neglected) results in a series of coupled differential equations for the mode amplitudes $A_m(z)$,

$$\sum_{m=-\infty}^{\infty} \frac{\partial}{\partial z} A_m(z) + j\frac{m\beta}{L}(m + \frac{2n\sin\theta\Lambda}{\lambda})A_m(z) - j\sum_{i=1}^{\infty} \alpha_i(A_{m+i}(z) + A_{m-i}(z)) = 0 \quad (4.6)$$

where m is the number of the mode, and β and α_i are defined as

$$\beta \equiv \frac{\pi\lambda L}{n\cos\theta\Lambda^2} \quad (4.7)$$

$$\alpha_i \equiv \frac{\pi\epsilon_{ri}}{2n\cos\theta\lambda} \ . \quad (4.8)$$

The initial conditions for the modes are

$$A_0(0) = 1 \qquad A_m(0) = 0 \quad \text{for } m \neq 0 \ . \quad (4.9)$$

These coupled differential equations were solved numerically by using a fourth order Runge-Kutta algorithm [204] to numerically integrate the equations. Seven modes were used (-3 to +3). When converting from exterior to interior angles, Snell's Law was used with n = 1.525 as the index of refraction of the material. The plots were graphed using

$$\gamma = |\frac{A_{-1}(\theta)}{A_{-1}(\theta_{Bragg})}|^2, \quad (4.10)$$

where $A_{-1}(\theta_{Bragg})$ is the amplitude of the -1 mode at Bragg incidence.

4.3.3 Experimental Results

To record a hologram that has low F and Q' values requires a very small angle between the recording beams. The geometry used is shown in Figure 4.12. The thickness of the sample was measured with a second hologram, recorded in the regime that Kogelnik's theory is valid (large F and Q'). The two plane wave holograms were sequentially recorded in HRF-150 photopolymer using 488 nm light. Both holograms

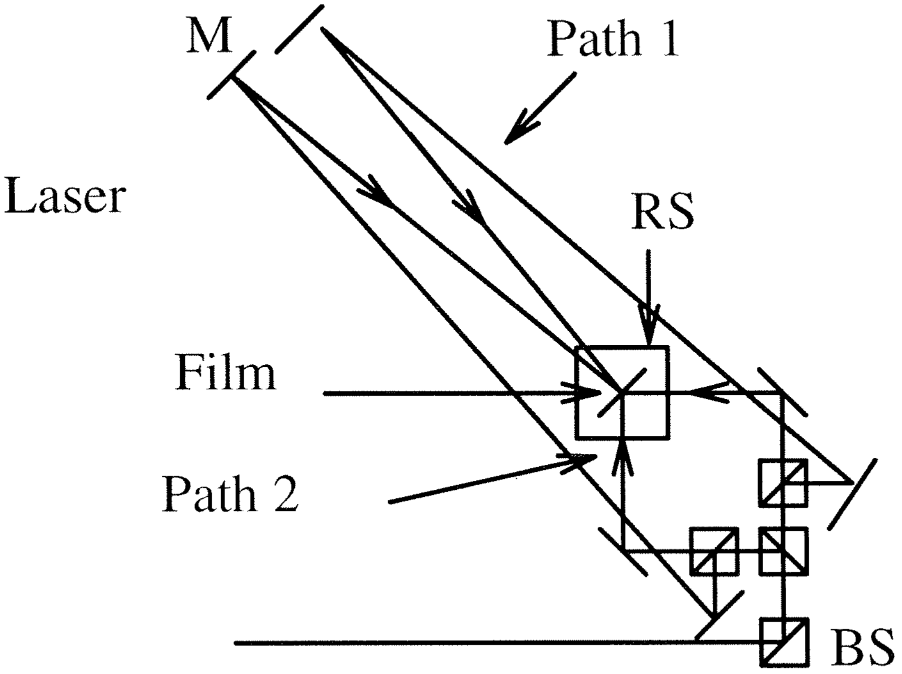

Figure 4.12: Experimental Setup. BS - beam splitter, RS - rotation stage, M - mirror, BE - beam expander, L - lens.

record unslanted gratings by aligning the reflections of a HeNe laser before making exposures with the blue light (equal and opposite angles from material's normal). First the hologram of interest (low spatial frequency) was recorded using Path 1 on Figure 4.12. Path 2 was blocked during this time. The exposure time for the first hologram was 50 seconds with a reference beam's intensity of 104 μW/cm^2 and an object beam's intensity of 73 μW/cm^2. The -1 mode's diffraction efficiency was 9.17%. This was measured by taking the diffracted intensity of the -1 mode and dividing by the sum of the diffracted intensities of all modes plus the undiffracted light. The second hologram was recorded with 90 degrees between the beams using Path 2 while Path 1 was blocked. The exposure time was 30 seconds with a reference beam intensity of 77 μW/cm^2 and an object beam intensity of 77μW/cm^2. Its diffraction efficiency was 10.1%. The sample was then fixed by exposure to UV light.

The thickness of the sample was given by DuPont as nominally 38 μm. By mea-

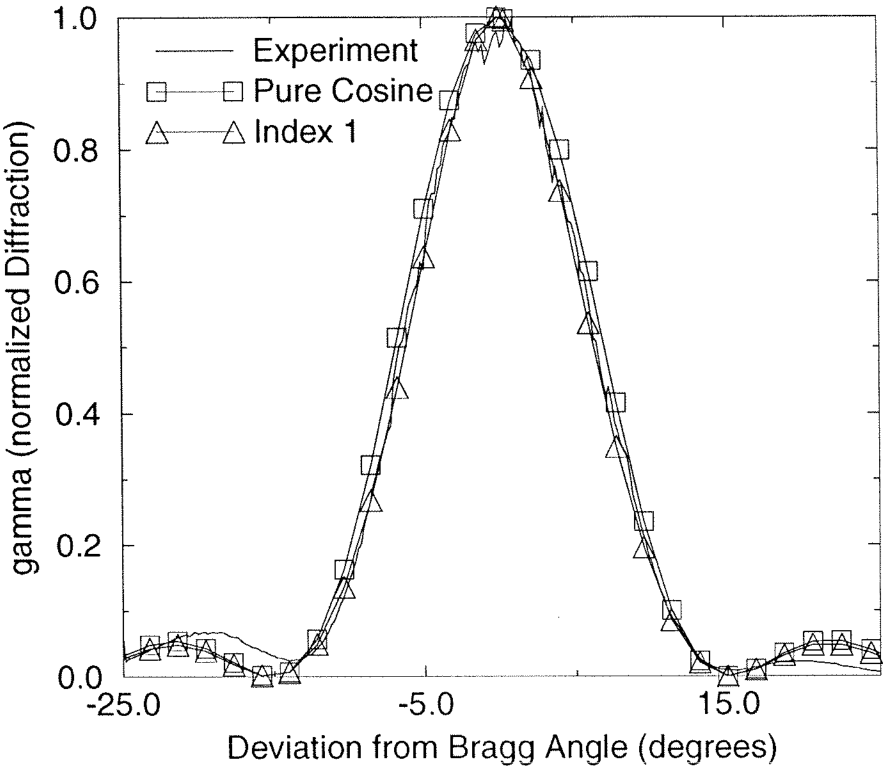

Figure 4.13: Theoretical and experimental -1 order mode angular selectivity.

suring the angular selectivity of the second hologram the thickness can be accurately measured. Angular selectivity was determined by measuring the diffracted intensity while rotating the sample and dividing by the diffracted intensity at Bragg incidence giving a γ vs angle curve. In this way the thickness of the sample was measured to be 38.4 um. The angular selectivity of the first hologram was measured in the same way and produced the experimental curve in Figure 4.13. The first hologram was recorded with a half angle between the beams of 2.1 degrees. This was measured by replacing the sample with a mirror normal to one beam and using the rotation stage to rotate the mirror to reflect the beam back along the other beam. The experimental diffraction efficiencies of the various modes measured at the -1 mode's Bragg angle are: $\eta_{-1} = 9.17\%$, $\eta_1 = 6.80\%$, and $\eta_{-2} = 1.0\%$.

4.3.4 Comparison

The pure cosine curve in Figure 4.13 was generated using the parameters of n = 1.525, $\Delta n = 1.281x10^{-3}$, thickness L = 38.4 um, external wavelength $\lambda = 488$ nm, and $\Lambda = 6.6587x10^{-6}$ meters. This corresponds to F = 5.5 and $Q' = 1.74$. The Δn was found by matching diffraction efficiency of the -1 mode at the Bragg angle. Notice that the curve is wider than the experimental curve. The predicted diffraction efficiencies at the -1 mode's Bragg angle are $\eta_{-1} = 9.17\%$, $\eta_1 = 7.17\%$, and $\eta_{-2} = 0.20\%$. This also differs from the experimental results.

By adding another coefficient in the cosine expansion of the perturbation, the angular selectivity could be dramatically and apparently uniquely altered. By varying this parameter to find a good fit, a second order correction term to the grating profile can be determined. The "Index1" curve on Figure 4.13 is a better match to the experimental data. It was calculated using the same parameters but with $\Delta n_1 = 1.21x10^{-3}$ and $\Delta n_2 = 4.423x10^{-4}$. The predicted diffraction efficiencies of $\eta_{-1} = 9.16\%$, $\eta_1 = 6.59\%$, and $\eta_{-2} = 0.74\%$ also agree better with the experimental results. "Index1" is compared to a pure cosine in Figure 4.14. It also is similar to the predicted solutions to the nonlinear diffusion equation given in Reference [124].

4.3.5 Conclusions

The angular selectivity of the -1 mode, and the diffraction efficiencies of the modes depend on the grating profile when F and/or Q' are small. By measuring these quantities and comparing to theory, a second order correction term was determined. Since experimentally both F and Q' were small, a small change in the second order coefficient produced noticeable changes in the predicted angular selectivity curve. The relatively small second order coefficient and small changes in the angular selectivity means that the material in this geometry records fairly linearly. The postulated in-

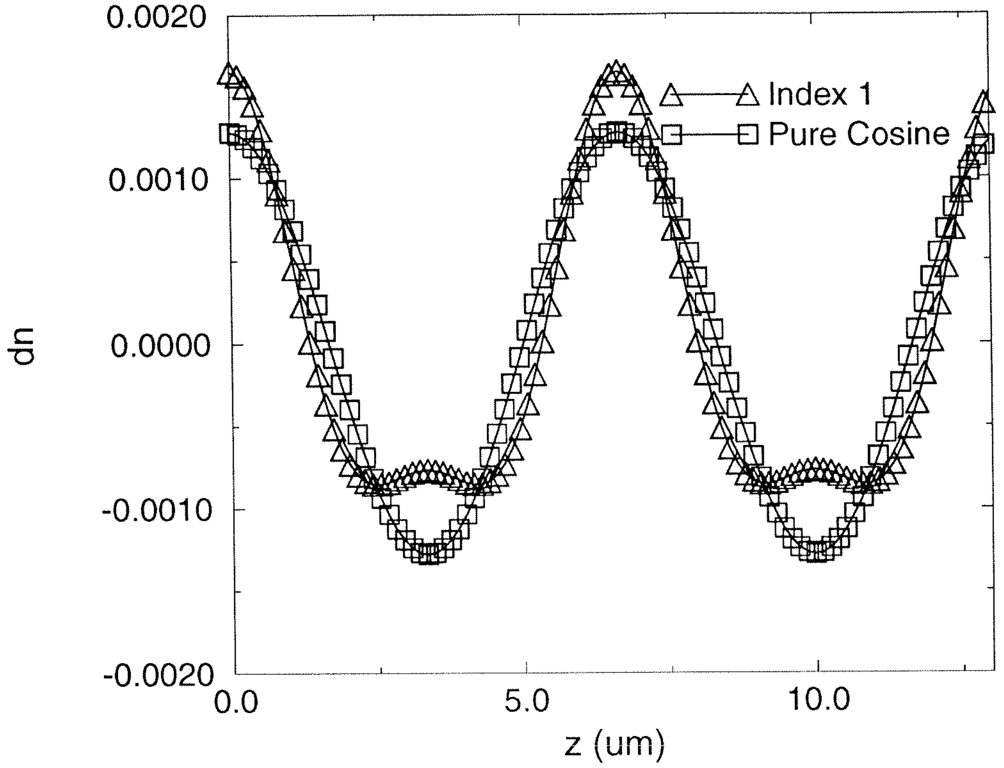

Figure 4.14: Index profiles.

dex profile from these measurements resembles the possible solutions of the diffusion model for photopolymer grating formation given in reference [124]. This agreement indicates that diffusion could be an important factor in grating formation as opposed to local effects. Since the grating profile determines the angular selectivity and diffraction efficiencies of the modes, it is an important parameter if systems that use these other modes are to be implemented using photopolymers.

4.4 Recording of Multiple Holograms in Photopolymer Films

4.4.1 Introduction

Angle multiplexed holograms have potential applications as optical memories, information processors, and interconnections. Important considerations include sensitivity, resolution, and the ability to record permanent holograms. DuPont's photopolymer

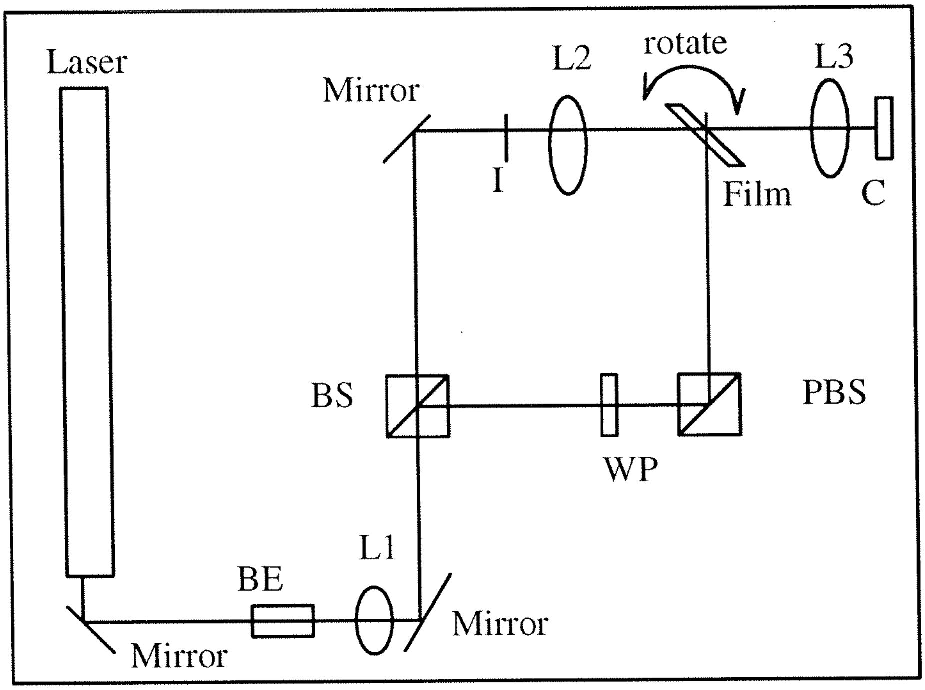

Figure 4.15: Geometry: BE - beam expander, L1 - lens, BS - beam splitter, L2,L3 - imaging lenses, WP - 1/2 waveplate, PBS - polarizing BS, I - image, C - camera.

HRF-150 has already been shown to have excellent sensitivity and resolution for transmission holograms recorded with blue-green light. With this in mind, HRF-150 is a good candidate for a practical, optical storage medium in which multiple holograms can be recorded. In this section we report the experimental demonstration of multiple holograms recorded in HRF-150.

4.4.2 Experiment

Ten images were recorded using the geometry shown in Figure 4.15. A sheet of DuPont HRF-150 photopolymer was taped to a glass plate with a centered window cut out of it and mounted on a rotation stage. The holograms were recorded with visible light($\lambda = 488nm$) with 90 degrees between the writing beams and then fixed with UV light. First the angular selectivity of the material was determined at 488 nm. The material was approximately 38 microns thick, and had angular selectivity

(half width, measured at the first minimum) of one degree in very good agreement with Kogelnik's two wave theory [26] for diffraction from thick phase gratings. The equation for the diffraction efficiency from an unslanted, lossless grating is

$$\eta = \frac{\sin^2(\nu^2+\xi^2)^{1/2}}{(1+\xi^2/\nu^2)}, \tag{4.11}$$

where

$$\nu = \pi \Delta n d/\lambda \cos\theta, \tag{4.12}$$

and

$$\xi = (K\cos(\pi/2-\theta) - K^2\lambda/4\pi n)d/2\cos\theta. \tag{4.13}$$

In the above equations, η is the diffraction efficiency, Δn is the index perturbation, n is the index of the material, λ is the wavelength, θ is the angle inside the material measured from the normal to the surface, K is the grating vector's magnitude, and d is the interaction length. Good agreement between experiment and theory for a single plane wave hologram recorded with 90 degrees separation between beams outside the material (± 45 deg from the normal to the film surface) is shown in Figure 4.16. The theoretical plot was calculated using d= 39 microns, n = 1.525, K = 1.82x10^7 rad/m, $\Delta n = 1.51x10^{-3}$, $\theta_{Bragg} = 27.62$ degrees, and $\lambda = 488$ nm. The angles were adjusted according to account for refraction at the surfaces. The agreement of the experiment and theory, indicates two things. First, it indicates that the gratings are not due to surface deformations which has been observed in similar materials [102] for low spatial frequency holograms. Also it indicates that the recorded hologram is most likely a phase grating rather than an absorption grating since the diffraction efficiency of 17.1 percent would be too large for an absorption grating.

Figure 4.17 shows the diffraction efficiency for 10 holograms of the same image stored at 10 different angular setting of the recording medium while keeping the angles between the recording beams the same. The holograms were recorded at

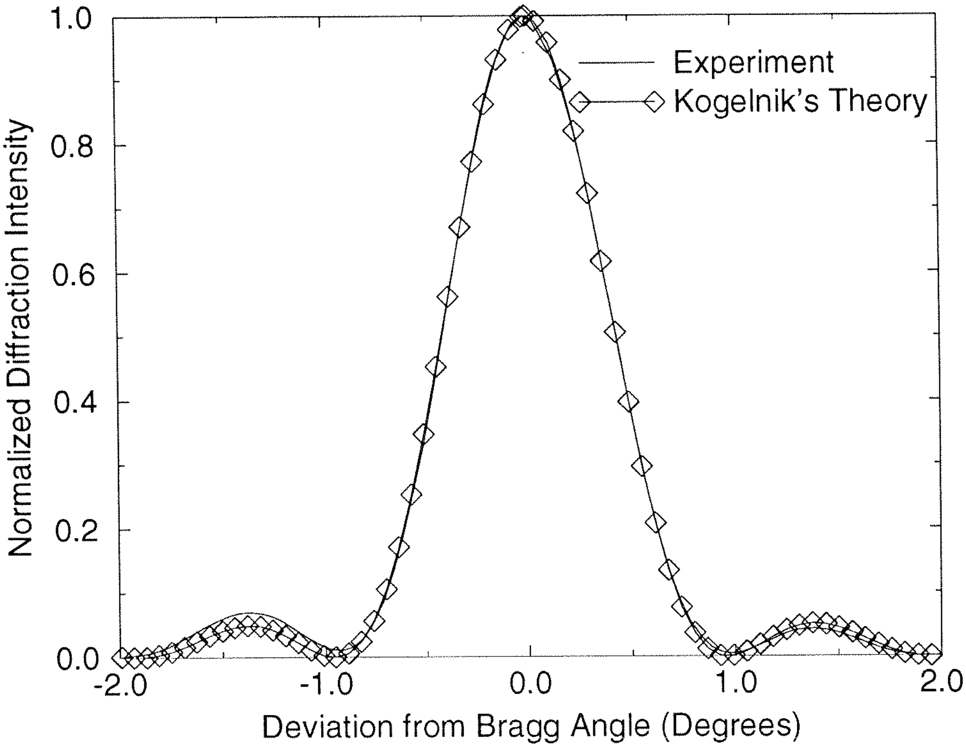

Figure 4.16: Angular selectivity of plane wave hologram.

intervals of two degrees or at the second minima of the angular selectivity curve of the adjacent holograms. The holograms were read out by blocking the object beam and detecting the reconstructed image while rotating the sample. Notice that the first two holograms (at $-10°$ and $-8°$) are weaker than the others, which indicates that exposure to light enhances the sensitivity. Figure 4.18 shows 10 image holograms of roughly equal strength that were recorded with a five second pre-illumination pulse with 1.85 mW/cm^2 intensity ten seconds before the first hologram was recorded. Both Figure 4.17 and 4.18 holograms were recorded using the setup in Figure 4.15, and, except for the pre-illumination pulse, identical recording parameters were used. The total recording energy per hologram was 1.88 mJ/cm^2 (one second exposure per hologram) with an object-to-reference beam ratio of approximately 1/4.6. The time between holograms is 10 seconds for a total experiment run time of 120 seconds. The diffraction efficiency shown is calculated by dividing the diffracted light by the incident

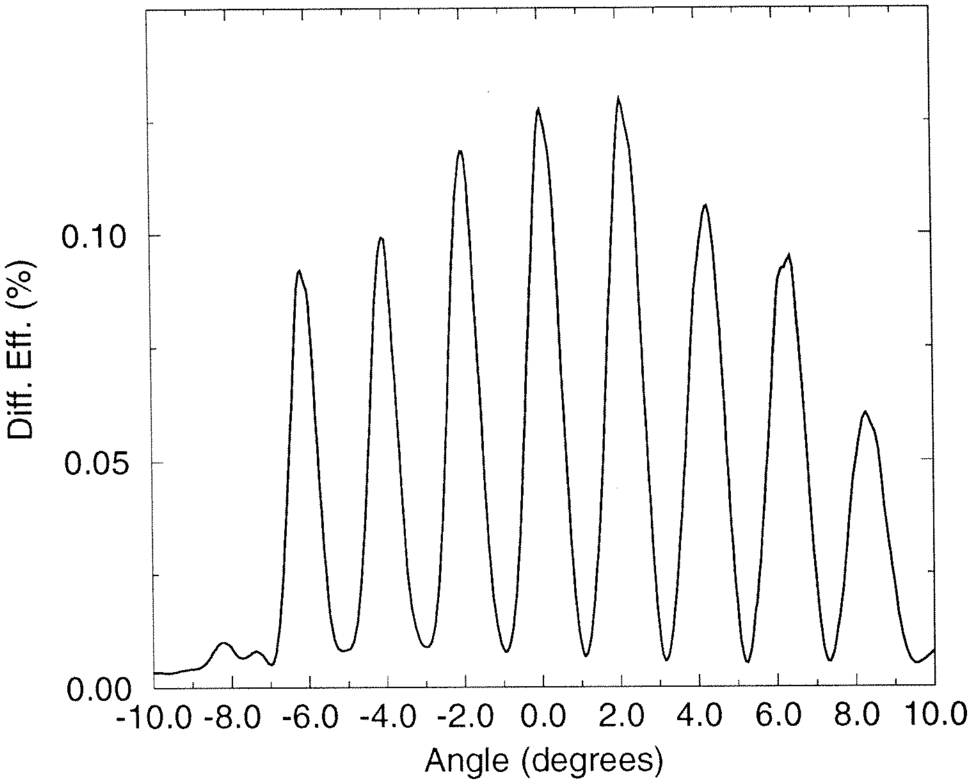

Figure 4.17: 10 holograms, no pre-exposure.

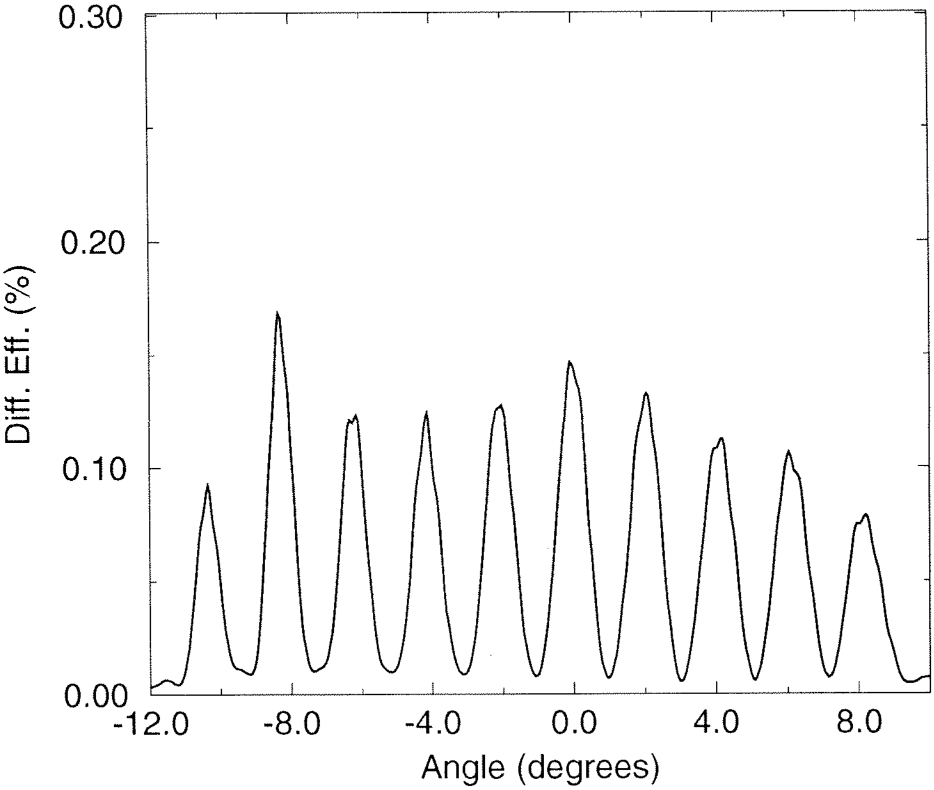

Figure 4.18: 10 image plane holograms.

Figure 4.19: Reconstructed image.

minus reflected light intensities, and multiplied by 100 to convert to a percentage. The pre-illumination pulse sensitizes the material and is necessary if the first hologram is to be recorded effectively. Since the material has a finite dynamic range, too long of a pre-illumination pulse wastes dynamic range causing the later holograms to be weaker than previous ones. Too short of a pre-illumination pulse fails to sensitize the material and the first few holograms are lost as shown in Figure 4.17.

The optical quality of the material is good, and Figure 4.19 shows a reconstructed image (hologram number 6 in Figure 4.18- at 0°) with no noticeable distortion. Figure 4.20 shows the index perturbation vs exposure and demonstrates that the pre-illumination pulse does use up dynamic range and increases the sensitivity for small exposures. The index perturbation was calculated by measuring the Bragg matched diffraction efficiency ($\xi = 0$) and solving for Δn in equation 4.11. In this case the diffraction efficiency used for η is diffracted light divided by transmitted light intensity

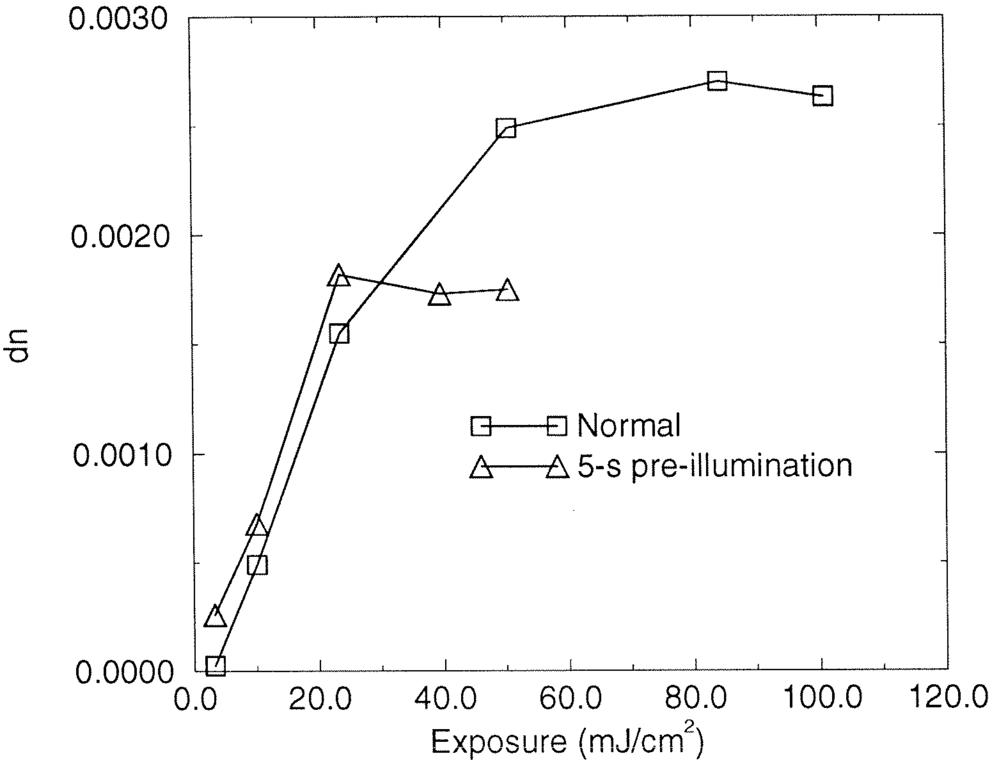

Figure 4.20: Index perturbation vs exposure.

to eliminate the effects of reflection from the surface and absorption. Notice also that the saturation exposure was about 20 mJ/cm^2; therefore, each of the ten holograms should be given about 2 mJ/cm^2. This is close to the actual value of 1.88 mJ/cm^2 per hologram used. Without the pre-illumination pulse the maximum Δn obtained was $\Delta n \approx .0028$. The Δn we measured is lower than what is reported in reference [112] ($\Delta n \approx .008$), most likely because of the much higher spatial frequency recorded in out experiment (2897 cycles/mm versus 1007 cycles/mm). With the pre-illumination pulse, the saturation exposure for this material is 20 mJ/cm^2 for a $\Delta n_{max} = 1.7x10^{-3}$. In comparison, for a thick sample of BaTiO$_3$ [205] the experimentally measured saturation exposure is approximately 100 mJ/cm^2. Recent experiments with thin samples of BaTiO$_3$ [206] and doped SBN [207] indicate sensitivities and Δn's roughly equivalent to the photopolymer.

Figure 4.21 shows the effect of extending the total run time by increasing the

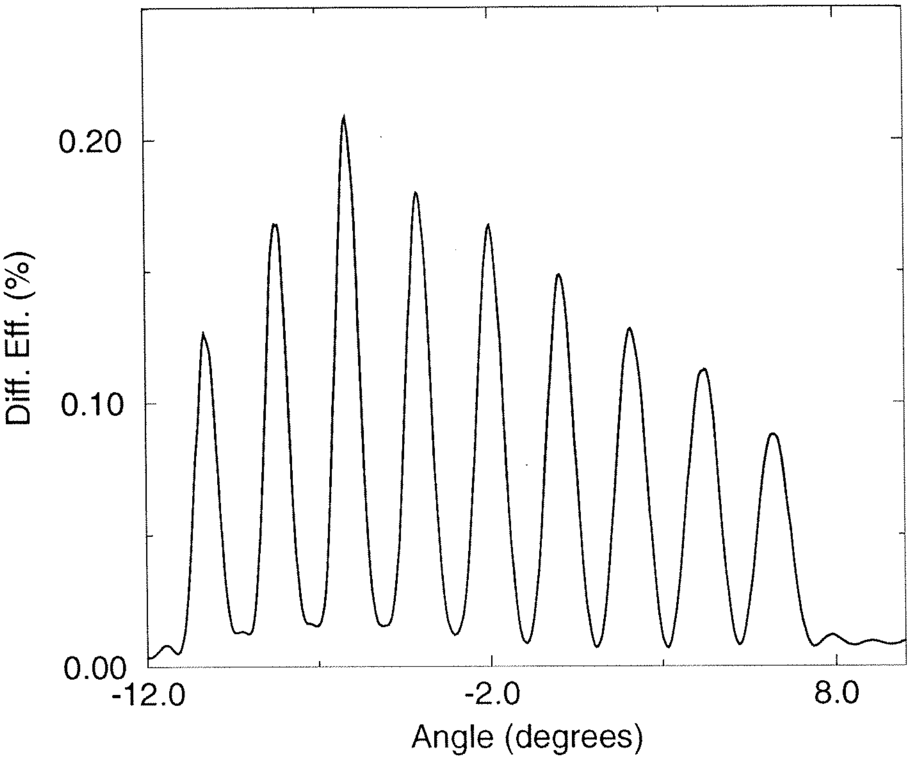

Figure 4.21: 10 image plane holograms, 1 minute apart.

time between holograms from 10 seconds as in Figure 4.18 to one minute. As the exposure time increases the dynamic range of the material is also used up as the residual monomer is polymerized. The decrease in hologram strength due to loss of dynamic range is evident in Figure 4.21. Therefore, not only is angular selectivity and exposure time important parameters for recording, but total run time is also. In order to maximize the number of holograms that can be stored, the total run time (T_{run}) should be minimized. T_{run} depends on t_{setup} (the time to present an image to the system and change the angle) and t_e (the exposure time) which varies as t_o/N where t_o is the single hologram saturation time and N the number of holograms. T_{run} can be written as

$$T_{run} = t_{setup} \times N + t_e \times N = t_{setup} \times N + t_o. \tag{4.14}$$

Using N=1000, t_{setup} = .1 seconds, and t_o = 10 seconds results in a total run time of 110 seconds. For a large number of holograms , the setup time dominates t_o.

However since t_{setup} can be equal to .1 seconds or less, the total run time even for 1000 holograms is below the 120 seconds that was experimentally demonstrated. Therefore, in practice the total run time is not the limiting factor in the number of holograms that can be stored.

The factor that does limit the number of holograms that can be stored is the thickness of the current samples. Increasing the thickness of the material, increases the angular selectivity and hence the storage capacity of the material. Scattering may eventually limit the maximum useful thickness of the material. As an example, let us assume that we can fabricate material that is 4 mm thick with sufficiently low scatter level. Then using the method presented in Reference [208] and with a maximum index perturbation of $1x10^{-3}$, we predict that around 2,800 holograms each with .01 percent diffraction efficiency can be superimposed in this material. However fabricating thick samples with good optical quality is not going to be trivial.

4.4.3 Conclusions

High quality, multiple holographic storage has been demonstrated in DuPont's HRF-150 photopolymer. Angular multiplexing qualities have been shown to be predictable using Kogelnik's two wave diffraction theory. In addition, a pre-illumination pulse can be used to record equal strength holograms with the same exposure energy per hologram. Uniform diffraction efficiency for multiple holograms over a long run time can be obtained at the expense of hologram strength due to the finite dynamic range of the material. Therefore, total run time, for sequential exposures, is an important recording parameter and needs to be minimized. The thickness of the material is currently the limiting factor in the number of holograms that can be stored. With a large dynamic range, if it is possible to increase the thickness of the material without significantly degrading the optical quality, it might be possible for thousands of permanent holograms to be recorded with adequate diffraction efficiency.

4.5 Thick Samples of DuPont Photopolymer

4.5.1 Why Thickness is Important?

The number of holograms that can be angularly multiplexed in a given holographic system is primarily a function of two parameters – the system's angular bandwidth and the material's dynamic range. From the section above, we were able to conclude that the photopolymer had sufficient dynamic range for more holograms than could be recorded due to angular bandwidth restrictions. Making the photopolymer films thicker can help both the dynamic range and the required bandwidth resulting in an increased system capacity.

The angular selectivity ($\Delta\theta(L)$) of the holograms goes linearly with the material's thickness. The total number of holograms that can be stored due to bandwidth restrictions is given by

$$\text{Number of Holograms} = \left(\frac{\theta_r}{\Delta\theta(L)}\right), \tag{4.15}$$

where θ_r is the total bandwidth of system (total angle that the reference beam can be changed, and $\Delta\theta(L)$ is the individual holograms selectivity (how much the reference angle must be changed before another hologram can be recorded). The total system bandwidth can also be increased by using fractal sampling grids [43]. By doubling the thickness of the material, the number of holograms that can be stored is doubled.

In addition to increasing the bandwidth limited number of holograms, increasing the thickness will increase the dynamic range of the material which allows more holograms to be stored. For transmission holograms the diffraction efficiency scales as the thickness squared. Thus increasing the thickness of the film allows for a larger number of holograms to be stored with the same diffraction efficiency. The practical demonstration of this idea is given by Burr et al. [50] in their long interaction length architecture (LILA). Using this increased interaction length idea, they demonstrated

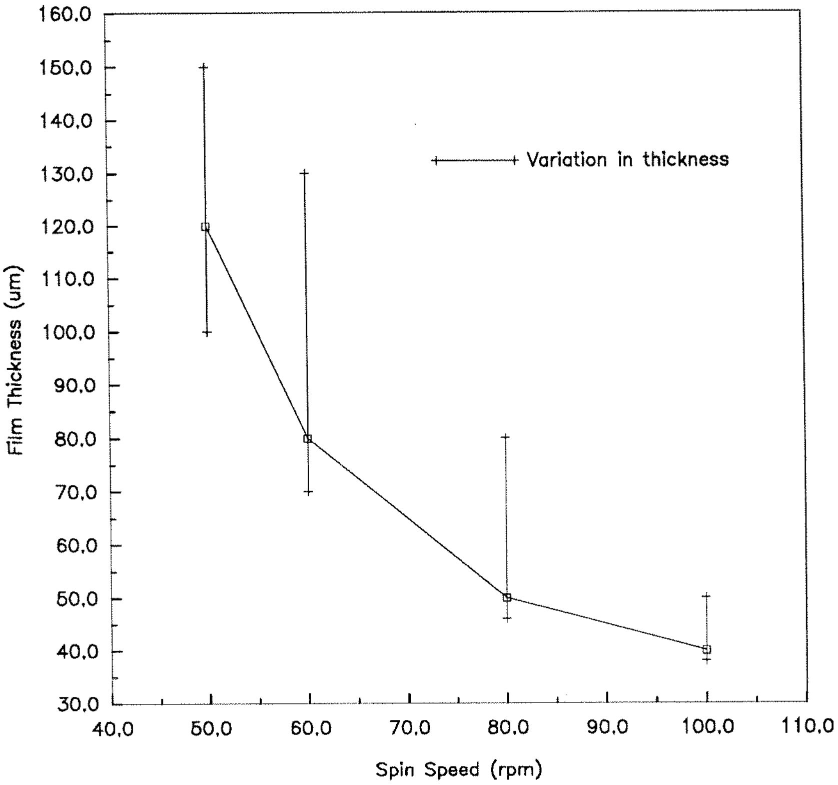

Figure 4.22: Film thickness in μms vs spin speed in rpms.

the storage of 10,000 holograms in a single iron doped LiNbO$_3$ crystal. The trade off for this increase in capacity is a less sensitive material (if the overall absorption is kept relatively low) resulting in slower recording times. Eventually other qualities of the recording material such as absorption or trap/dye density will prevent the capacity of the material from being raised arbitrarily high. Still, increasing the thickness of film from its present 38μm thickness should increase both the film's dynamic range and, of particular interest, its angular selectivity.

4.5.2 Spin Coating and Casting Photopolymer Films

An obvious way to make thicker films is to spin coat glass substrates with the photopolymer. Figure 4.22 shows the film thickness vs revolutions per minute for HRF-150 photopolymer with a 50% solid solution. The solution is mixed with the sensi-

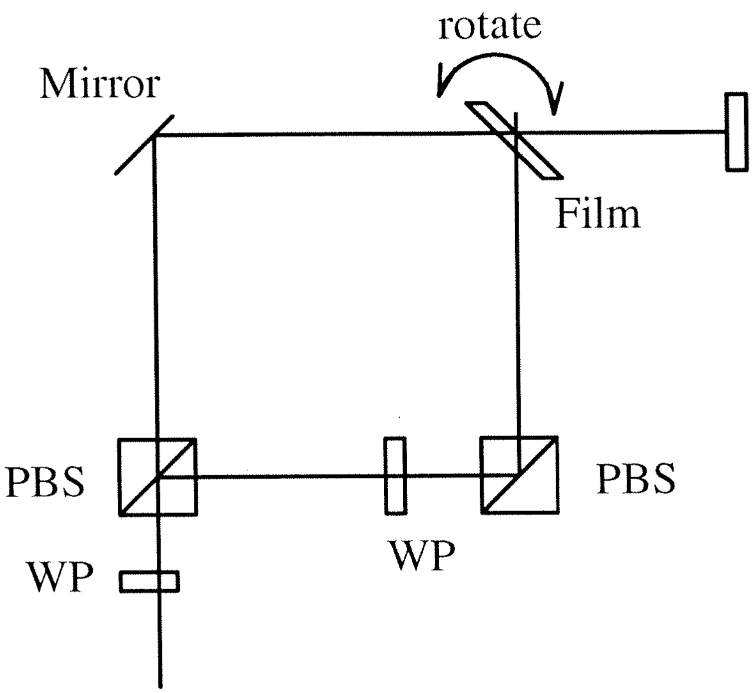

Figure 4.23: Setup for testing films: PBS – polarizing beam splitter, WP – 1/2 waveplate.

tizing dye and allowed to sit in the dark in order to get the bubbles out. Then the material is spun at the desired rpm for several minutes to coat the glass evenly and to dry the film. The coated film is left in the dark overnight. The long spin and waiting period is necessary to evaporate the solvents in the polymer solution. Exposing "wet" film results in either a white non-transparent plastic being formed during recording or, if the film is just slightly "wet," the angular selectivity of the film is less than what it should be for its given thickness. Films have been made up to 200-250 μm thick with either single or double coating. Coating the film more than twice was not possible because the effects of surface imperfections or dust accummulating with each layer.

The films were tested using the setup shown in Figure 4.23 with plane waves incident on the film. Figure 4.24 show the angular selectivity function of a 120 μm thick film that was spun at 50 rpm for one hour and then dried over night.

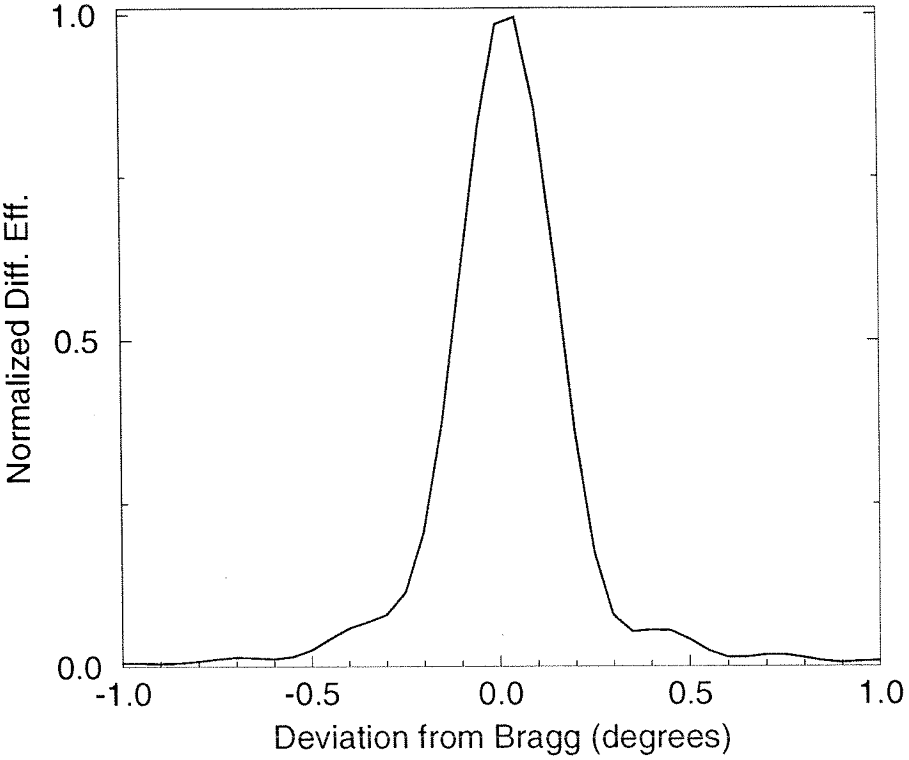

Figure 4.24: Angular selectivity for 120 μm thick film.

The diffraction efficiency of this film was 92.8%. The biggest problems with spin coating were thickness variations and optical quality. Two films using the exact same procedure and processed one after another would result in films of different thickness. Some of this variation in the thickness is due to evaporation of the solution over time which change the film viscosity. The change in thickness is important because the film's angular selectivity and sensitivity can change which makes experiments difficult to repeat. The optical quality got worse with increasing thickness. If the films have good optical quality, such as the standard films that are purchased directly from DuPont, they can be stuck together to double the thickness. Figure 4.25 shows a plot of diffraction efficiency for 50 holograms multiplexed in an approximately 200 μm thick sample prepared by spin coating two layers at 60 rpms. The separation between holograms is 0.4 degrees. The first couple are not present due to the fact that the pre-illumination was not sufficient to get the film into the linear region of its

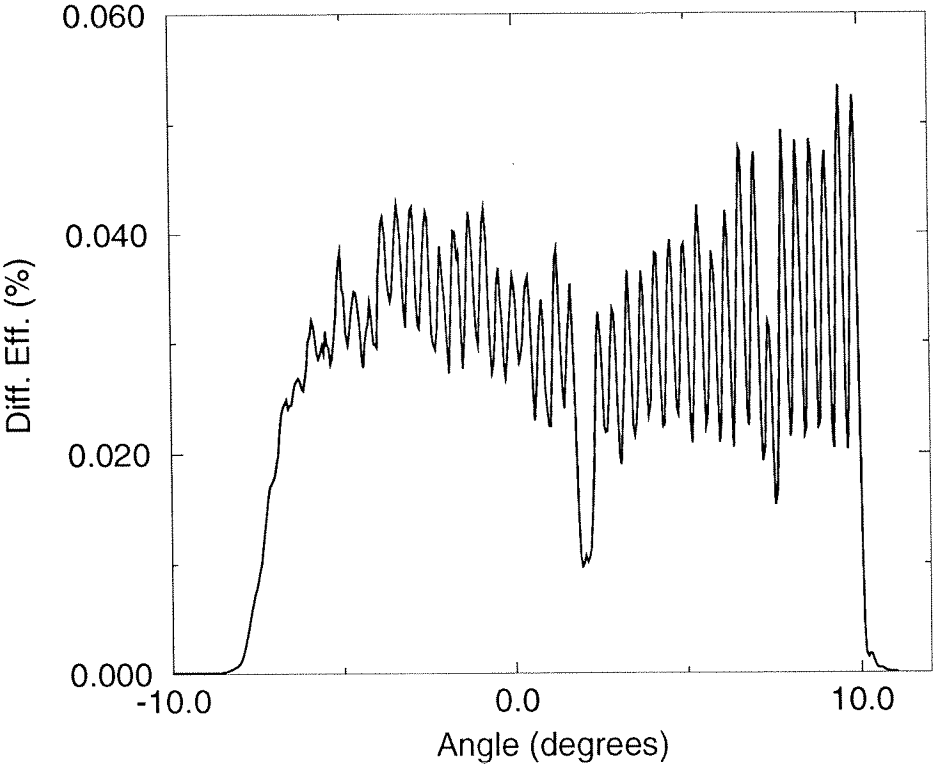

Figure 4.25: 50 holograms in a ~ 200 μm thick film.

exposure curve.

The other method developed for manufacturing thick films is called casting. The solution is prepared as before, but this time it is poured onto a glass plate with an o-ring glued to it to prevent the solution from spreading. The film is then left in the dark to dry. The samples can be periodically weighed to estimate when they are dry. The center of such samples will have good optical quality on both sides. This technique was developed here and later DuPont was persuaded to experiment with it. DuPont produced a 200 μm film that looked prefect. Unfortunately, after a uniform UV exposure DuPont measured 12% scattering in the film. The scattering (DuPont calls it haze) in the standard HRF-150 films is less than 0.1%.

Figure 4.26 show the real-time development of the grating in the 200 μm thick film that DuPont produced. Notice that the film is less sensitive since it takes more than 30 mJ/cm^2 to get to the linear region on the curve compared to about 15 mJ/cm^2

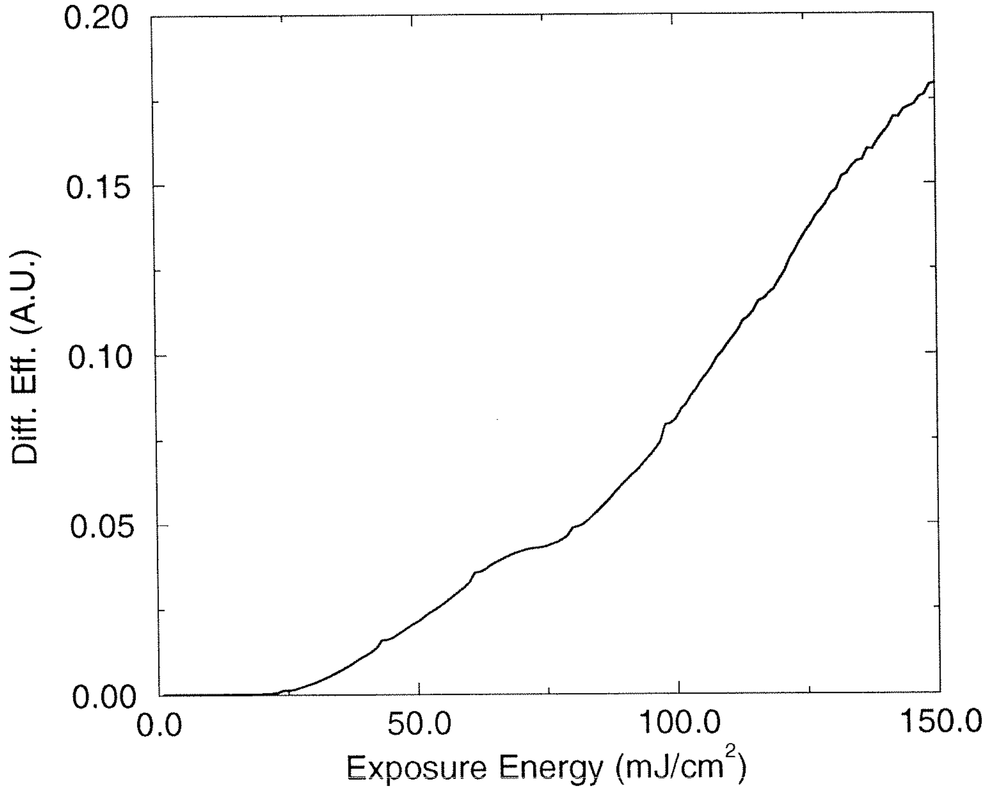

Figure 4.26: Diffraction vs exposure energy for 200 μm thick film.

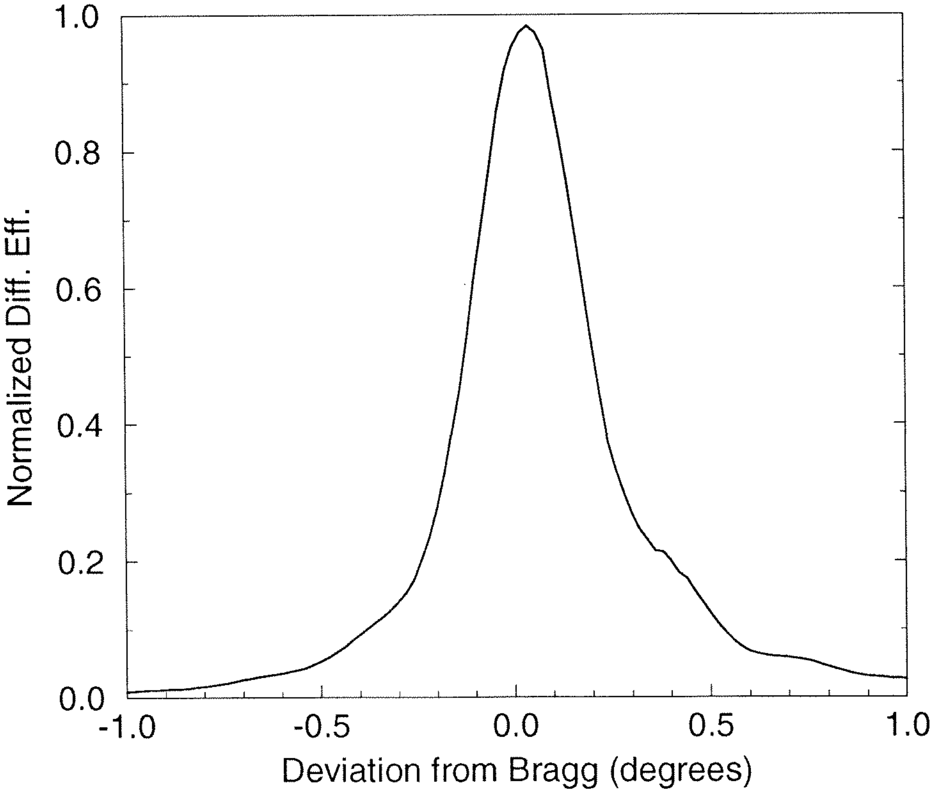

Figure 4.27: Angular selectivity for 200 μm thick cast film.

for the standard films. Figure 4.27 shows the angular selectivity for the 200 μm thick film. Notice that the angular selectivity is about equivalent to a sample that is about 100 μm thick. The really bad news is scattering makes this film unusable.

Using any method, the optical quality of thick samples of HRF-150 is not satisfactory. At most, about 150 μm thick films can be made with acceptable optical quality. It appears that it will require some work on DuPont's part to change the chemical composition of the films to made solution based photopolymers thick. Other polymer work has been done with thick materials – Bartolini et al. [111]. These use materials that have already undergone a free radical reaction to form the thick solid matrix. The photopolymer reaction then uses the residual monomers. This method results in thick material at a significant loss in sensitivity, dynamic range, and repeatability. Thus, the solution based polymers have substantially better recording characteristics.

4.5.3 Stratified Media

Another method of making thick materials from thin layers is to make a stratified medium. In such a medium, the thin layers are surrounded by buffer material which does not interact with the light. These thin layers of material and buffer are then stacked up to make a thick medium – sort of like a sandwich. This has been proposed before [209, 210, 211, 212], and the theory of diffraction from these stacks of material has been worked out. This particular photopolymer was used to make a stratified medium and compared to theory by Nordin et al. [213]. We also made stratified media out of the photopolymer to evaluate its potential.

Figure 4.28 shows two films stuck together with a thin mylar sheet in between. Figure 4.29 shows two films stuck together with a thick ($\sim 50\mu$m) mylar sheet in between. In both cases, the overall selectivity is the same as the thin layer, but the

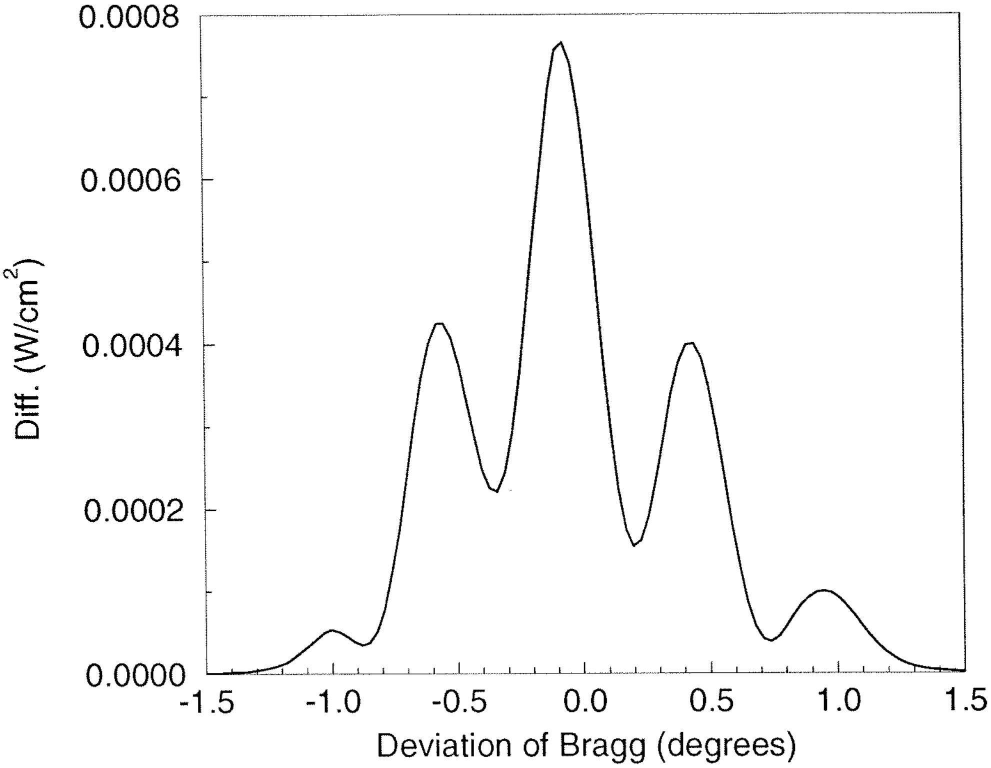

Figure 4.28: Angular selectivity 2 films stuck together with a thin mylar sheet in between.

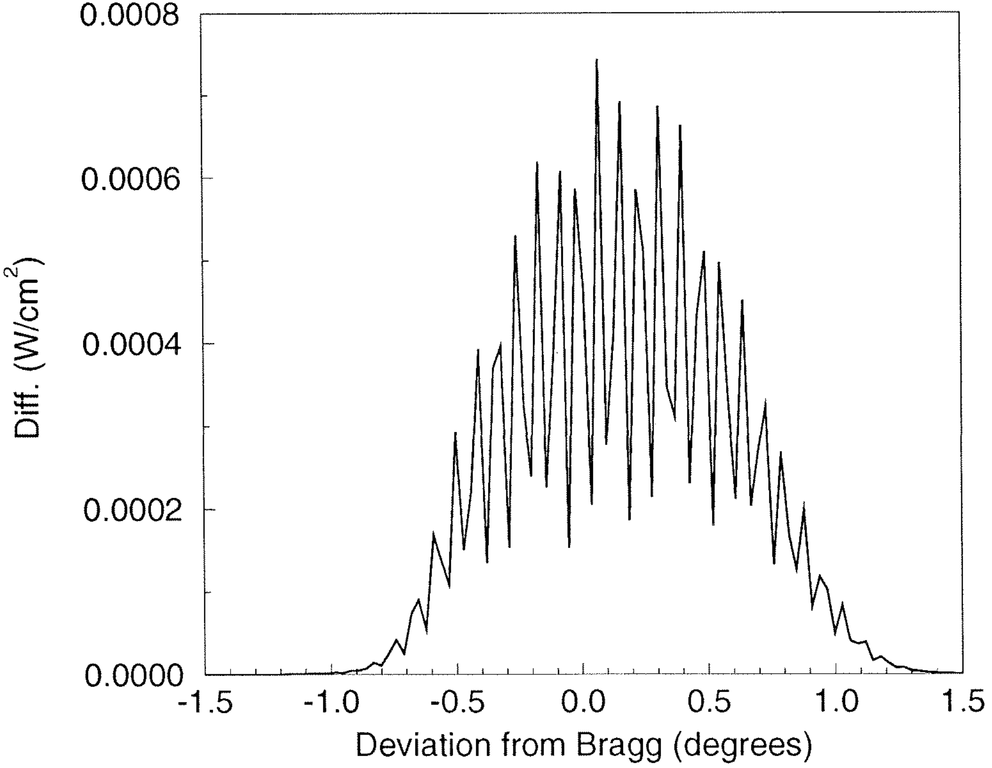

Figure 4.29: Angular selectivity 2 films stuck together with a thick mylar sheet in between.

main and sidelobes of this sinc function have nulls in them. The spacing of these nulls is very dependent on the buffer layer thickness. To try to multiplex holograms in a nulls is possible, but it is very difficult. The spacing must be maintained carefully since the other holograms also have this same selectivity function. Also the cross-talk for holograms spaced in the inner minimums of the main lope will be much greater. Basically, stratified medium is useful for increasing the dynamic range or the material, but it probably is not a practical solution to the angular bandwidth limited problem.

4.6 A Method for Holographic Storage Using Peristrophic Multiplexing

4.6.1 Introduction

In a previous section we reported 10 angle multiplexed holograms in a $38\mu m$ thick film [121] with diffraction efficiency of 10^{-3}. Since we can typically work with holographic diffraction efficiencies on the order of 10^{-6}, we have sufficient dynamic range to record significantly more than 10 holograms. The angular bandwidth limitation can be alleviated by making the film thicker [113] but scattering increases rapidly with thickness in these materials. Another method that has been previously used to increase the utilization of the available bandwidth of the system is fractal sampling grids [214, 43].

In this section we describe peristrophic (Greek for rotation) multiplexing as a solution to the bandwidth limited capacity problem. With this method the hologram is physically rotated with the axis of rotation being perpendicular to the film's surface every time a new hologram is stored. The rotation does two things. It shifts the reconstructed image away from the detector allowing a new hologram to be stored and viewed without interference, and it can also cause the stored hologram to become non-Bragg matched. In addition, peristrophic multiplexing can be combined with

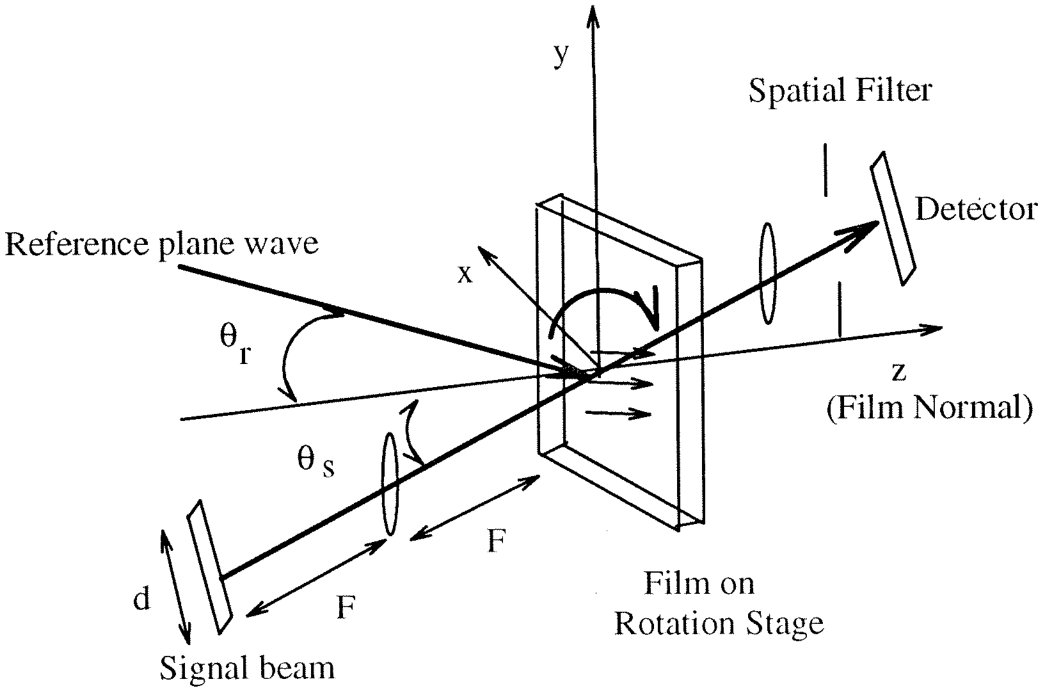

Figure 4.30: Setup for peristrophic multiplexing.

other multiplexing techniques such as angle or wavelength multiplexing to increase the storage density and with spatial multiplexing to increase the storage capacity of the system.

4.6.2 Theory

The setup for peristrophic multiplexing is shown in Figure 4.30. The reference plane wave (R) is incident at an angle θ_r and the signal beam (S) is incident at an angle θ_s, both angles measured with respect to the film's normal. Taking the center pixel of the image as the signal and neglecting any effects due to hologram thickness, the hologram transmittance can be written as

$$R^* S = e^{-i2\pi\frac{\sin\theta_r}{\lambda}x} e^{-i2\pi\frac{\sin\theta_s}{\lambda}x} \; . \tag{4.16}$$

The hologram is then rotated by $d\theta$ about the center of the x-y plane as shown in Figure 4.30. Assuming the rotation is small, this results in the coordinates being transformed according to: $x' \approx x - y d\theta$, and $y' \approx y + x d\theta$. Substituting these relations into Eq. 4.16, the hologram be expressed in terms of the unrotated coordinates (x, y)

$$R^* S = e^{-i\frac{2\pi \sin\theta_r x}{\lambda}} e^{-i\frac{2\pi \sin\theta_s x}{\lambda}} e^{-i\frac{2\pi(\sin\theta_s + \sin\theta_r) d\theta y}{\lambda}} . \tag{4.17}$$

After multiplying by R and Fourier transforming, the last term in Eq. 4.17 results a shift in the image. The rotation required to translate the image out of the detector aperture is approximately given by,

$$d\theta \geq \frac{\frac{d}{F}}{\sin\theta_s + \sin\theta_r}, \tag{4.18}$$

where d is the size of the image at the detector plane and F is the focal length of the lens used. For image plane holograms, the expression is

$$d\theta \geq \frac{\frac{2\lambda}{\delta}}{\sin\theta_s + \sin\theta_r}, \tag{4.19}$$

where $1/\delta$ is the highest spatial frequency in the image. For image plane holograms the filtering must be done at the Fourier plane of the system. Similar expressions can be found for Fresnel holograms [215]. Notice that this method can be combined with other volumetric multiplexing methods to further increase the storage capacity.

The Bragg selectivity, assuming the reference is given by $R = e^{-i(\frac{2\pi \sin\theta_r}{\lambda} x + \frac{2\pi \cos\theta_r}{\lambda} z)}$ and the signal given by $S = e^{i(\frac{2\pi \sin\theta_r}{\lambda} x + \frac{2\pi \cos\theta_r}{\lambda} z)}$, can be calculated using the Born and paraxial approximations and integrating over the volume of the hologram. Assuming that the transverse (x, y) dimensions of the film are much larger than the bandwidth of the images, the Bragg selectivity can be shown to be

$$d\theta = \sqrt{\frac{2\lambda}{t}\left(\frac{\cos\theta_s}{\sin\theta_r(\sin\theta_s + \sin\theta_r)}\right)}, \tag{4.20}$$

where t is the thickness of the material. Using $\lambda = 488\text{nm}$, $t = 38\mu\text{m}$, and $\theta_s = \theta_r = 30°$ results in a selectivity of about $10°$. The Bragg matching requirement is the dominant effect if $\frac{d}{F} > \sqrt{2\lambda \cos\theta_s(\sin\theta_s + \sin\theta_r)/t \sin\theta_r}$. For most material thicknesses,

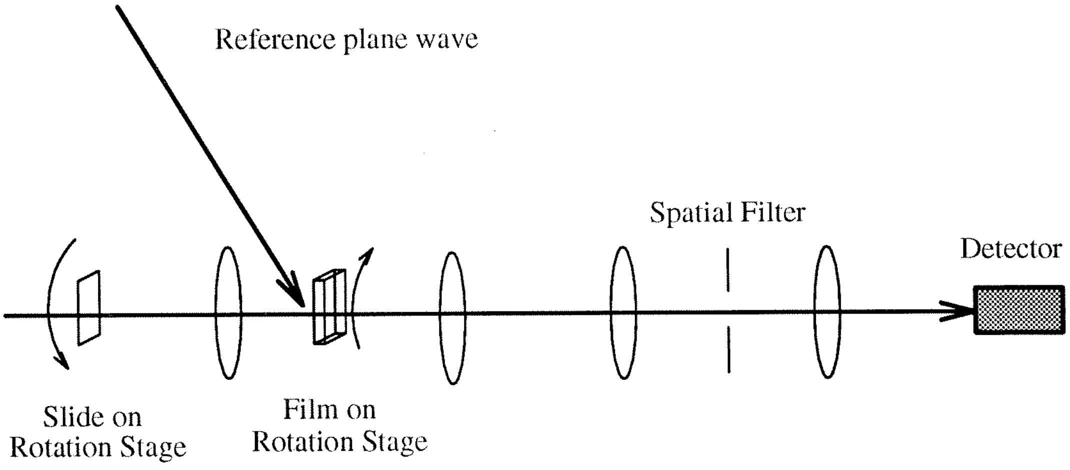

Figure 4.31: Experimental setup for peristrophic multiplexing.

the Bragg matching criterion determines the required rotation for peristrophic multiplexing. In our experiments, because the thickness of the film is only 38μm, the image could be filtered out before the gratings become non-Bragg matched.

4.6.3 Experimental Results

Peristrophic multiplexing was demonstrated using DuPont's HRF-150 photopolymer. The setup in Figure 4.31 was used to record 100 holograms in the 38μm thick film. The image stored was a random black and white pattern on a slide. The slide was placed on a rotation stage and rotated in the opposite direction that the film was rotated to distinguish individual images from each other. The reference plane wave was incident at 32° from normal and the signal at 29° from the normal. The reference beam intensity was 3.76 mW/cm^2 and the signal beam had 449 μmW in it. The film was rotated by 1.7° degrees between holograms to enable the other holograms to be filtered out. The image was rotated by -2° for each hologram. The exposure time per hologram was 0.12 seconds and there was a two second delay between holograms to allow the rotation stages to rotate to a complete stop. Figure 4.32 shows some of the reconstructed holograms, and Figure 4.33 shows their diffraction efficiency. The variations in diffraction efficiency are due in part to exposing the material through a mylar cover sheet. The mylar is weakly birefringent and therefore slightly depolarizes the beams by an amount that depends on orientation of the film.

The experimental setup shown in Figure 4.34 was used to demonstrate both peristrophic and angle multiplexing. Notice that a second rotation stage was added to rotate the film around a vertical axis as well as around the film's normal. This makes it possible to combine peristrophic and angle multiplexing. The film was located a significant distance from the Fourier plane so that the signal beam was approximately uniform. For each peristrophic position, multiple holograms are stored using standard angle multiplexing by rotating the medium. A spatial light modulator (SLM) was used to present images (cartoons) to the system. Each frame is numbered according to the sequence in which they were stored. The reference and signal beams were initially incident at ±30° from the film's normal. The reference beam intensity was 1.1 mW/cm^2 and the signal beam had 300 μW in about a 1 cm by 0.5 cm area. The film was rotated in-plane by 3° between each set of angle multiplexed holograms to enable the other holograms to be filtered out. Eq. 4.18 predicts a required rotation of about 9° for Fourier plane hologram while Eq. 4.19 predicts about 1.7° rotation for image plane. The 3° was experimentally observed for the in-between (Fresnel) case we used. Each angle multiplexed hologram was also separated by 3°. The initial exposure time was 0.11 seconds, but starting at hologram number 26, each hologram was exposed for 0.005 seconds longer than the previous hologram to correct for the lost sensitivity due to run time [2]. There was a 1.5 second delay between holograms to allow the rotation stages to completely stop. Figure 4.35 shows five of the 295 holograms stored in the polymer by peristrophic multiplexing 59 times and storing 5 angle multiplexed holograms with each peristrophic position. The diffraction efficiency of the 295 holograms is plotted in Fig. 4.36. The average efficiency was $\sim 4 \times 10^{-6}$ and

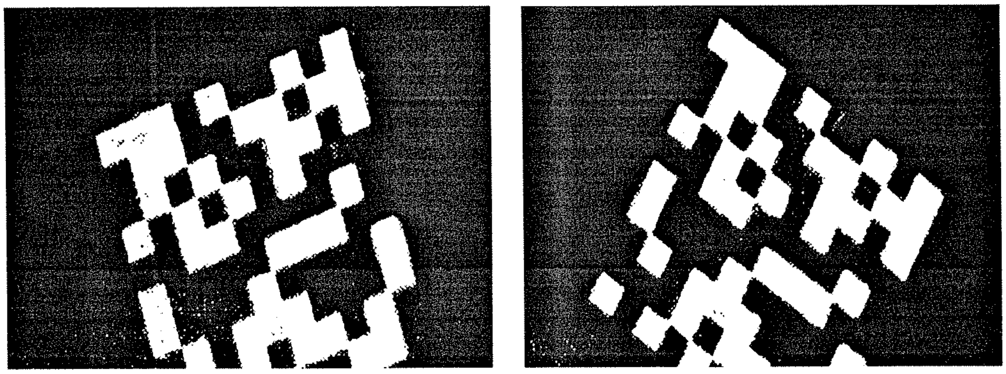

1st Hologram

25th Hologram

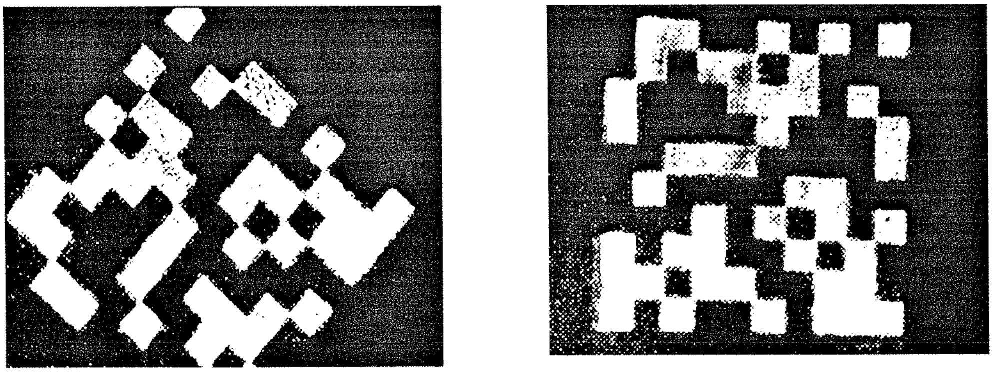

75 th Hologram

100th

Figure 4.32: Some of the 100 reconstructed holograms.

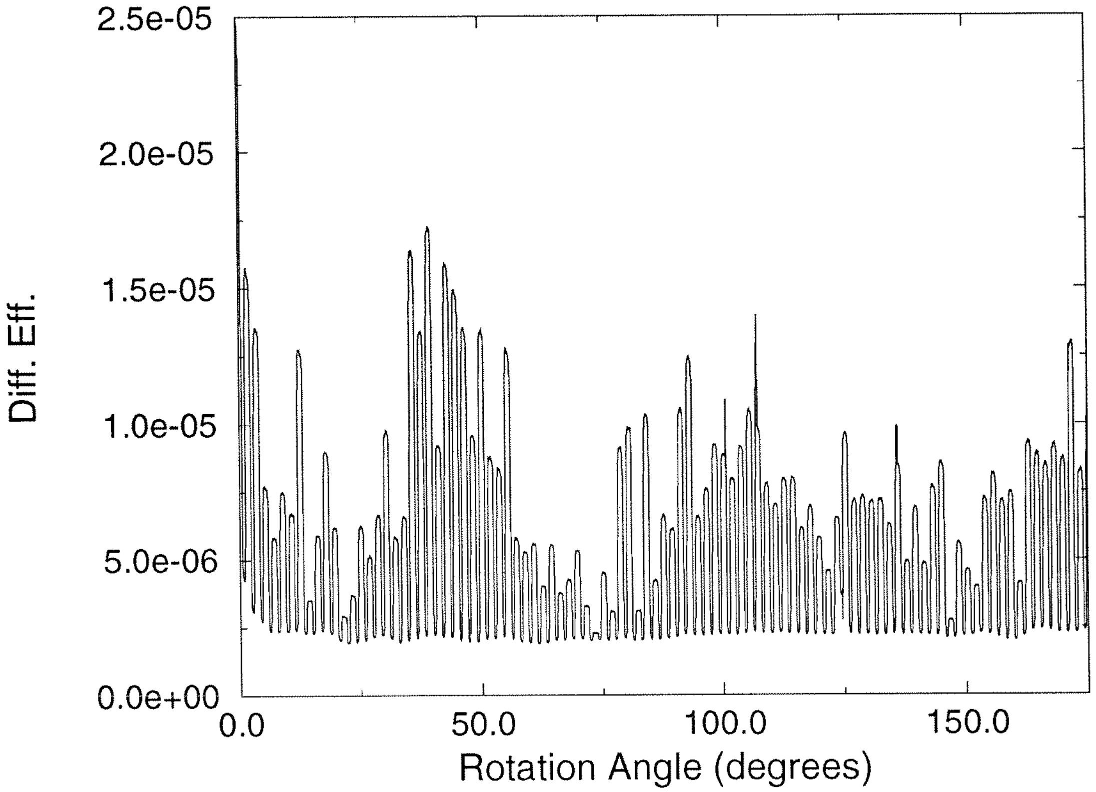

Figure 4.33: Diffraction efficiency of 100 holograms stored in 38μm thick film.

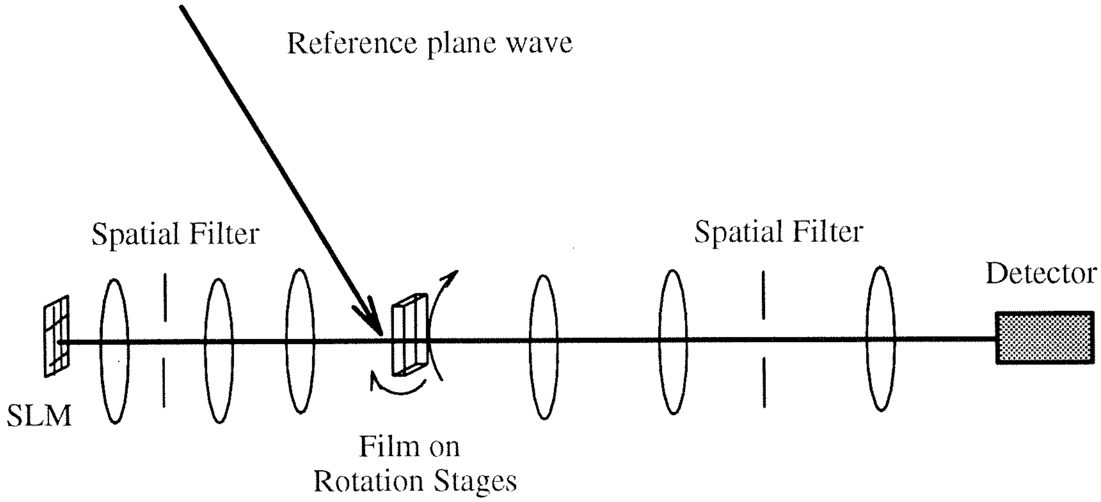

Figure 4.34: Setup for both peristrophic and angle multiplexing.

the variations are primarily due to variation in the average intensity of the frames. In separate experiment, we stored equal amplitude plane wave holograms and observed a decrease in diffraction efficiency proportional to $1/M^2$ [216].

Previously we stored M =10 holograms with roughly 10^{-3} diffraction efficiency [121] limited by the angular bandwidth of the optical system. Peristrophic multiplexing made it possible to store M =295 holograms with a diffraction efficiency of $\sim 4 \times 10^{-6}$. Assuming one bit per pixel, the above experiment results in a storage density of roughly 1 bit/μm^2. Thus, peristrophic multiplexing allowed for almost two orders of magnitude increase in the storage capacity of the DuPont photopolymer and changed the limiting factor from the angular bandwidth of the optical system to the dynamic range of the material.

1st Hologram

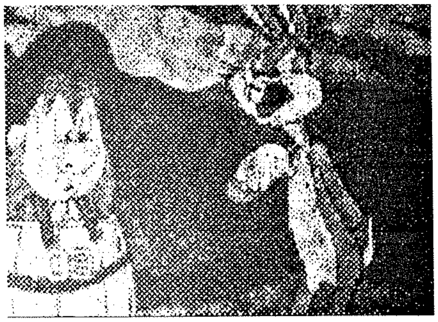

103th Hologram

160th Hologram

219th Hologram

295th

Figure 4.35: Some of the 295 reconstructed holograms.

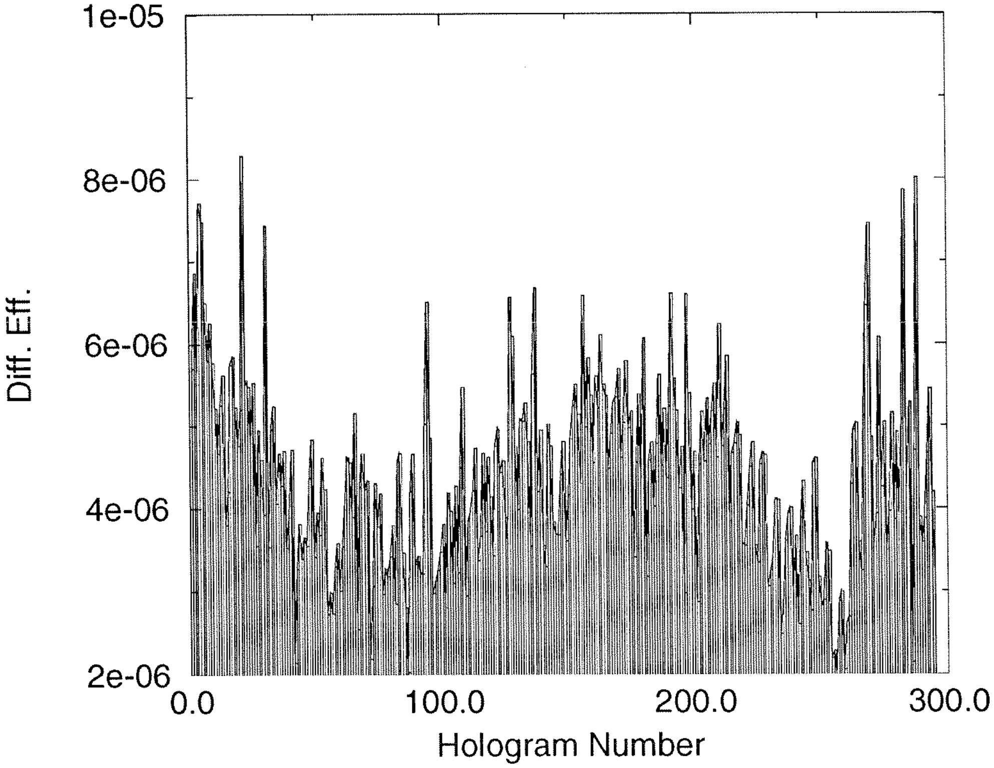

Figure 4.36: Diffraction efficiency of 295 holograms stored in 38μm thick film.

Chapter 5

3-D Photopolymer Disks for Correlation and Data Storage

5.1 Correlator

5.1.1 Introduction

In recent years we have seen the implementation of several pattern recognition systems that use arrays of optical correlators to realize a variety of algorithms (e.g., template matching, radial basis functions, and neural networks). An array of correlators can be implemented by spatially multiplexing different filters on a 2-D medium, typically in a disk configuration [217, 218, 219, 220]. Alternatively, 3-D holographic storage can be used by superimposing multiple holograms utilizing either wavelength [176] or angular [221, 222] multiplexing to form the correlation between the input and any stored reference. Finally, spectral and time domains can be used to store multiple filters in 2-D spectral hole burning media [223]. In this chapter we present a method that combines angularly multiplexed storage in 3-D media with spatial multiplexing to form a 3-D disk [196]. The 3-D disk allows us to store a very large number of gray scale templates (in excess of 100,000) whereas the disk rotation proves convenient for implementing the necessary shift in one of the two dimensions for the calculation of the image correlation function. The architecture we describe can be implemented with any holographic storage medium that can be fabricated into a thick slab (to allow volume holography) with sufficient area (to make a sizable disk). For instance, photorefractive crystals can be used. The 3-D disk used in the experimental demonstration in this paper, is constructed with the HRF-150 Dupont photopolymer [112].

5.1.2 Theory of Operation

When a thick hologram is used to store the Fourier transform filter in a VanderLugt correlator, the shift invariance is destroyed in one of the two dimensions [224]. As a result, the output of such a system is simply one line of the 2-D correlation function. We can use angularly multiplexed holograms in a 3-D volume to store multiple templates and use the second dimension of the output plane to display in parallel one line of each of the 2-D correlation patterns between the input and the stored templates. By translating the input image, the 2-D correlation patterns are generated line by line with time [218, 221, 222]. Here we describe an alternative solution in which we translate the holographic medium instead. The reference holograms are stored by Fourier transforming in one direction and imaging in the other. Since the input is imaged onto the hologram in one dimension, translating the hologram produces the desired relative shift between input and reference that is necessary to compute the correlation function in 2-D. If the holographic medium is a 3-D disk, then this translation is provided by the disk rotation. Moreover, in this architecture, we can increase the number of templates by storing multiple sets of angle multiplexed holograms at different locations on the disk. Disk rotation can also be conveniently used to access the different locations in sequence.

The optical setup is shown in Figure 5.1. The image f(x,y) to be stored is presented to the system on a SLM (an Epson LCTV). The first lens takes the Fourier transform of the image presented on the SLM. At the Fourier plane the image is filtered both

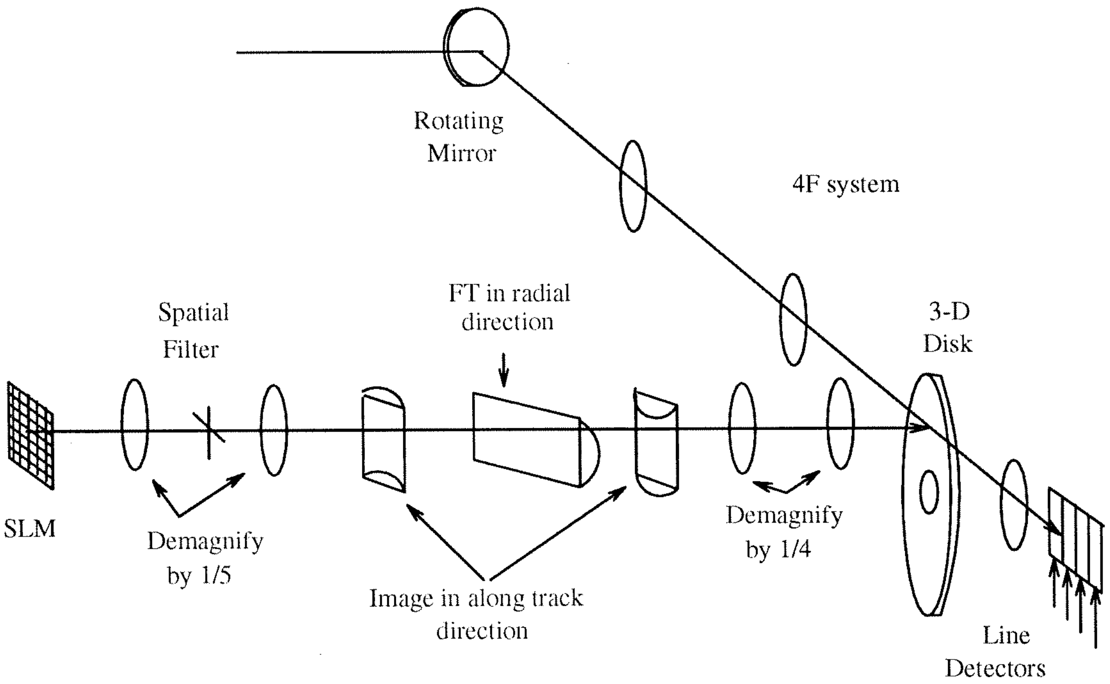

Figure 5.1: Optical setup for 3-D disk-based correlator.

to edge enhance and to remove the diffraction orders of the SLM. The second lens transforms this filtered signal back into a filtered and demagnified version of the original image. Using three cylindrical lenses, the image is imaged in the along "track" (x) direction and Fourier transformed in the radial (y) direction. The spherical lens, after the cylindrical lenses, demagnify the 1-D Fourier transform and 1-D image further. This pattern is then interfered with a plane wave with spatial frequency μ and stored in a optically thick photopolymer film on a glass optical disk. This results in the image of f in the x direction and complex conjugate of Fourier transform of f in the y direction ($f^*(M_1x', M_2v)$) being stored, where v is the spatial frequency in the y direction. More holograms can be multiplexed at this location on the disk by changing μ using the rotating mirror and a 4F system of lenses to change the incident angle of the reference beam without changing the beam location. The hologram can be written as

$$T(x', y') \approx f^*(M_1x', M_2v)e^{j2\pi\mu x'}, \tag{5.1}$$

where the M's are magnification factors.

To generate the correlation function between f and another function g, input $g(x, y)$ on the SLM. After going through the same optics before the disk, $g(x, y)$ is mapped into $g(M_1x', M_2v)$. The signal after the disk is given by

$$g(M_1x', M_2v)f^*(M_1x', M_2v)e^{j2\pi\mu x'}. \tag{5.2}$$

This signal is then Fourier transformed by a spherical lens, with focal length F, and detected a distance 2F away from the disk. Ignoring the reconstructed plane wave that ends up uniquely shifting (for each angle multiplexed hologram) the result on the detector plane, the signal - to within angular selectivity limits - is given by

$$S(x_d, y_d) = \int_{-\infty}^{\infty}\int_{-\infty}^{\infty} g(M_1x', M_2v)f^*(M_1x', M_2v)e^{-j\frac{2\pi}{\lambda F}(x'x_d+y'y_d)}dx'dy'. \tag{5.3}$$

Detecting the signal at $x_d = 0$ and taking the Fourier transform in the y direction results in the signal becoming:

$$S(O, y_d) \approx \int_{-\infty}^{\infty}\int_{-\infty}^{\infty} g(M_1x', y'')f^*(M_1x', y'' - \frac{y_d}{M_2})dx'dy''. \tag{5.4}$$

This is an inner product in the x direction and a correlation in the y direction or one line of the full 2-D correlation function of f and g.

Using disk rotation as approximately a linear shift ($\theta(t)$) in x direction generates the full 2D correlation function with time.

$$S(O, y_d, t) \approx \int_{-\infty}^{\infty}\int_{-\infty}^{\infty} g(M_1x', y'')f^*(M_1x' + \theta(t), y'' - \frac{y_d}{M_2})dx'dy''. \tag{5.5}$$

Since intensity at detector is $I(0, y_d, t) = SS^*$, the intensity detected is equal to the square of the correlation function. With a thick medium, multiple holograms can be recorded at a single spot on the disk using angle multiplexing. Therefore, different

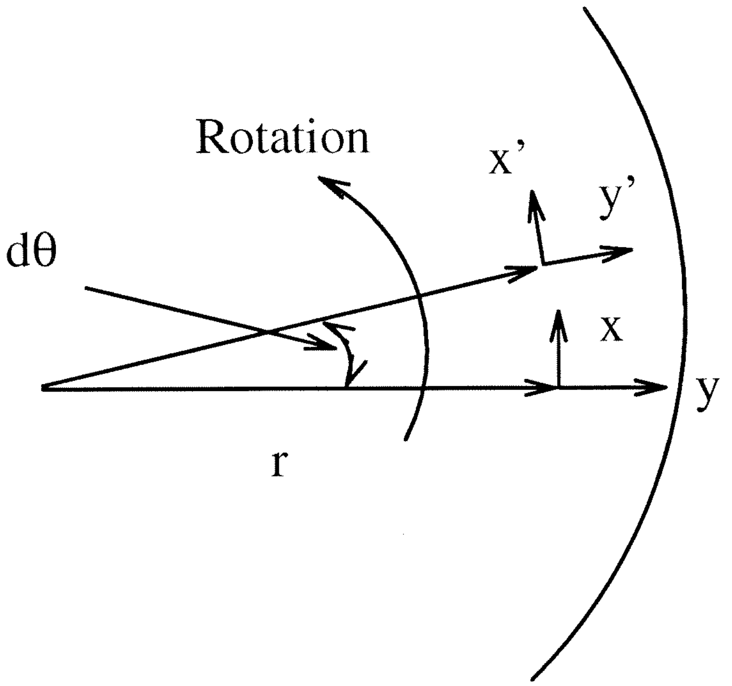

Figure 5.2: Coordinates for disk rotation by $d\theta$ in counterclockwise direction.

2-D correlation functions for each hologram multiplexed at a spot can be generated one line at a time and detected in parallel.

5.1.3 Disk Rotation Effects

Hologram rotation during reconstruction results in a shift at the correlation detection plane. To analyze this effect, a cylindrical wave with origin at $z = 0$ and x_o is the signal beam. The coordinates for disk rotation are shown in Figure 5.2. This signal beam is further simplified to a plane wave $S \sim e^{-j2\pi\beta y}$ with spatial frequency $\beta = \frac{\sin\theta_s}{\lambda}$, since the cylindrical wave in the x direction is a point on the film that forms the inner product ignoring the effects of thickness. This signal beam is stored with a plane wave $R = e^{j2\pi\alpha x}$ with spatial frequency of $\alpha = \frac{\sin\theta}{\lambda}$) in the x direction. In the expressions above, θ is the angle between the normal to the disk and the reference beam, and x, y are the coordinates at the disk (x along "track" direction, y radial direction). The recorded hologram is

$$RS^* = e^{j2\pi\alpha x}e^{j2\pi\beta y}. \tag{5.6}$$

The hologram is then rotated by $d\theta$ about a center of rotation in the x-y plane a distance r away from the center of the x, y coordinates as shown in Figure 5.2. This rotation results in the coordinates being transformed according to the formulas:

$$\begin{aligned} x' &\doteq x - (y + r)d\theta, \\ y' &\doteq y + xd\theta. \end{aligned} \tag{5.7}$$

Substituting these into equation 5.6, the hologram can now be written as

$$RS^* = e^{j2\pi\alpha(x-(y+r)d\theta)}e^{j2\pi\beta y}e^{j2\pi\beta d\theta x}. \tag{5.8}$$

Multiplying by S to generate the 1-D inner product and 1-D correlation, expand and simplify, results in

$$SRS^* = e^{j2\pi\alpha x}e^{-j2\pi\alpha d\theta y}e^{j2\pi\beta d\theta x}. \tag{5.9}$$

In the above expression after the Fourier transforming lens, the factors are:
$e^{j2\pi\alpha x}$ is the reconstructed plane wave without rotation – the desired signal.
$e^{-j2\pi\alpha d\theta y}$ corresponds to a shift in y direction on the correlation plane.
$e^{j2\pi\beta d\theta x}$ corresponds to a shift in x direction on the correlation plane.

Since in the experimental setup $\alpha \gg \beta$, we expect the correlation to shift in the y direction on the detector as the disk is rotated.

5.1.4 Experimental Correlation

Using the system shown in Figure 5.1, 300 transmission holograms were stored on one 5 cm radius "ring" of a holographic (6 cm radius) 3D disk. Using DuPont's HRF-150 film and exposing with 488 nm light, three holograms (image plane in the

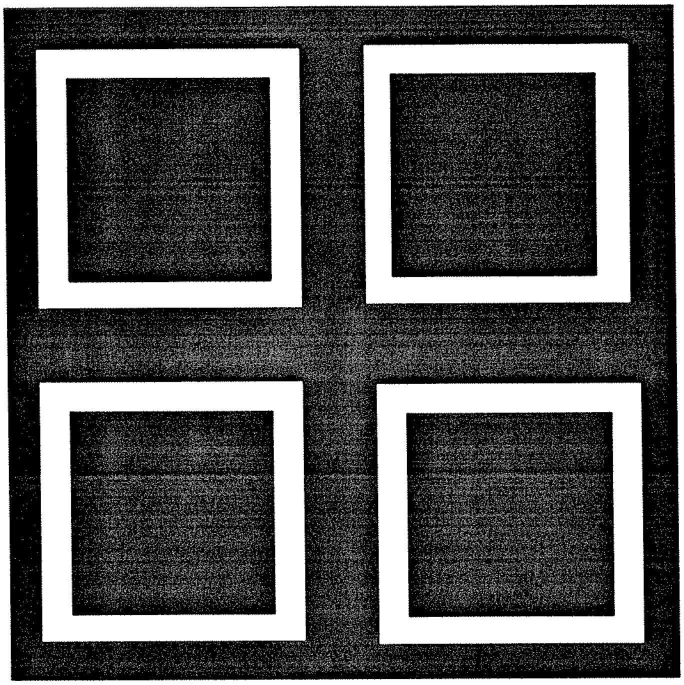

Figure 5.3: Image of four boxes that were used to test the correlator.

along "track" direction and Fourier transformed in the radial direction) were angle multiplexed at a given spot on the disk using the methods presented in Chapter 4. The disk was then rotated to expose a total of 100 different spots; at each spot, three holograms were recorded for a total of 300 holograms stored. The object size was approximately .9x.6 mm with 13 μW intensity recorded with a 1 cm x 1.5 mm plane wave reference beam with 300 μW intensity. After each spot had been sensitized with pre-illumination with the reference beam for 25 seconds, each hologram was exposed for 10 seconds. Disk rotation between spots was 3.5° and the angular separation of the three multiplexed holograms was 1.5°. The holograms were made with an image of four boxes as shown in Figure 5.3. The peak diffraction efficiency for the three hundred holograms is shown in Figure 5.4.The 3-D disk was made by pressing (laminating) the 38 μm thick photopolymer film onto the glass disk. In addition, spin coating the photopolymer onto the disk is possible.

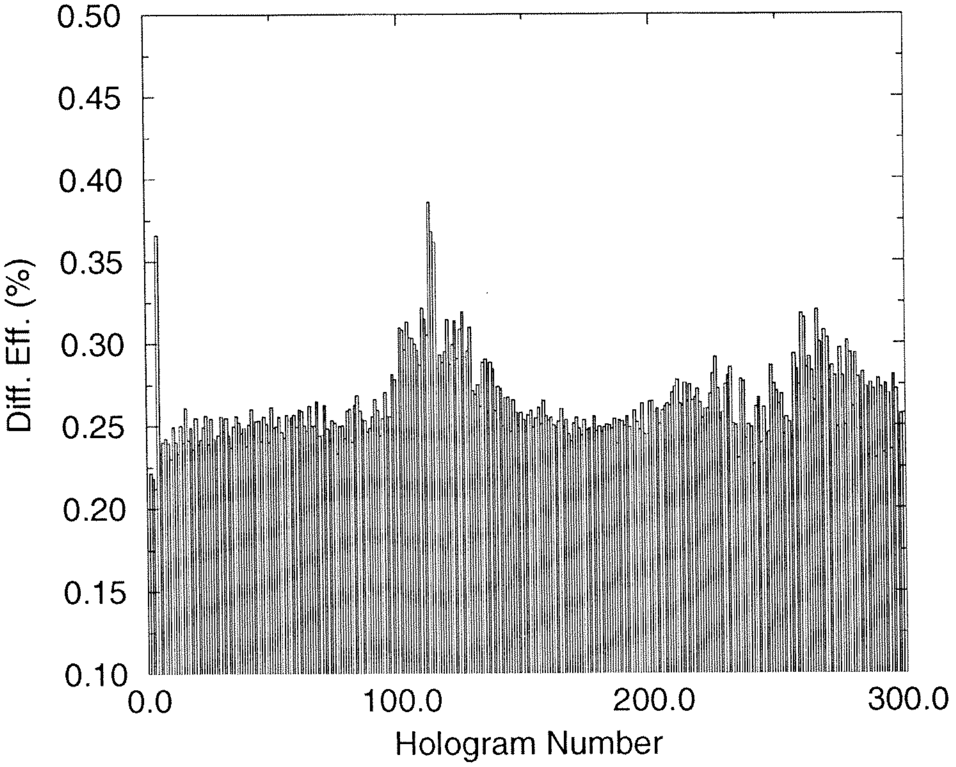

Figure 5.4: Peak diffraction efficiency of 300 holograms – 3 holograms at a spot with 100 spots on a ring of the 3-D disk.

To test the correlator, an experimental autocorrelation squared of the four boxes was measured using the correlator setup in Figure 5.1. Figure 5.5 is an experimental plot of the autocorrelation function squared of the four boxes of Figure 5.3 and roughly agrees with the theoretical autocorrelation of this image shown in Figure 5.6 (both plots are linear).

Figure 5.5 was generated by storing the image on the disk as explained above, and then presenting the image to the system. The correlation plane was sampled by a line detector. The detector was read out, the disk was rotated, and the detector was read out again. This procedure was repeated until the entire 2-D autocorrelation function squared was generated. Since the boxes occupy a large portion of the input plane (SLM), Figure 5.5 demonstrates that the correlation ability exists across most of the input plane. In addition, Figure 5.7, is the gray scale image looking straight down from the top of Figure 5.5. Notice the shift in peak location due to disk/hologram

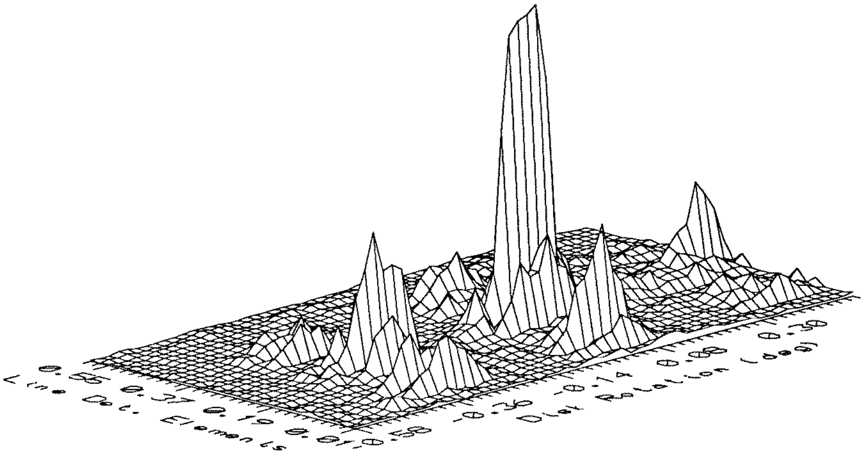

Figure 5.5: Experimental autocorrelation squared of the test image generated using the optical disk-based correlator.

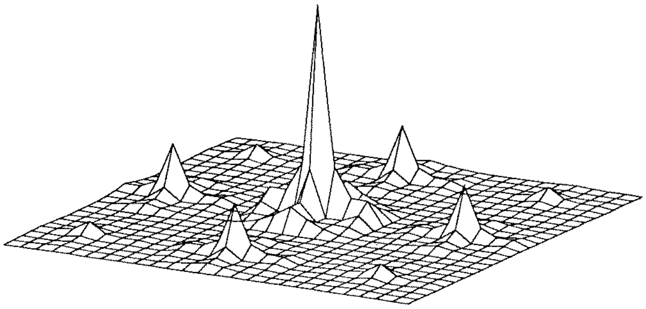

Figure 5.6: Theoretical autocorrelation squared of the test image.

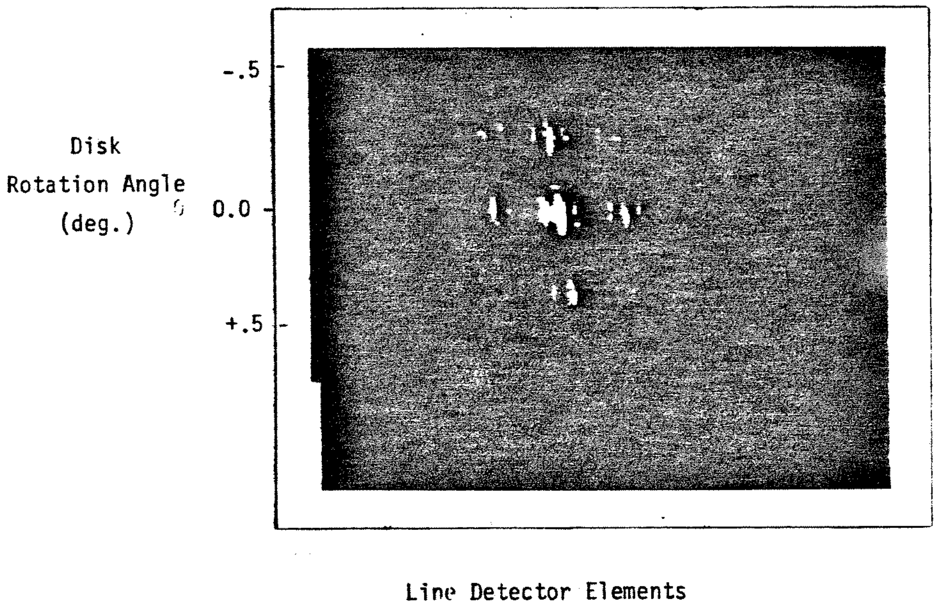

Figure 5.7: Experimental gray scale representation of autocorrelation squared.

rotation. The shift produced by the experimental setup was in the y direction as predicted.

The correlator described above eliminates the need for fast SLM's; instead, the processing bottle neck is shifted to the detectors. The detectors need to read out the correlation peaks. The largest peak then needs to be found and the address associated with it (pixel and line detector location) reported out. This means that a tremendous amount of information must be quickly read out and moved off chip. To alleviate this problem, we have tested prototype chips that do winner-take-all over multiple line detectors and report out the winner's address and magnitude. Figure 5.8 shows a picture of a chip that consists of a row of eight pixels on the left that go to a winner-take-all circuit (in the center of the picture) and then to a static encoder (far right) to report out the winning pixel address and magnitude. This chip was built through a $2um$ p-well MOSIS process and implements the desired functions for

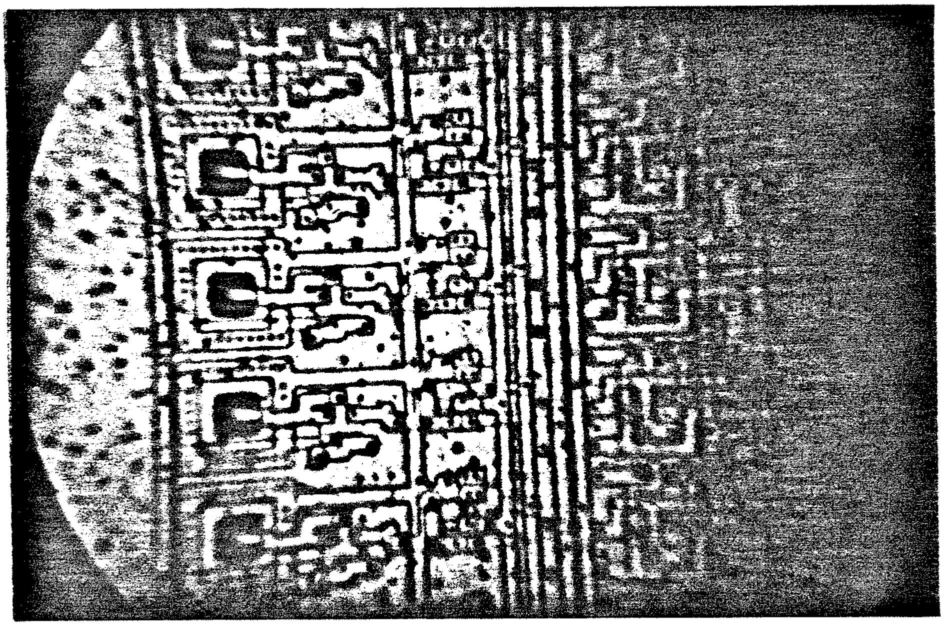

Figure 5.8: Picture of detector chip for correlator.

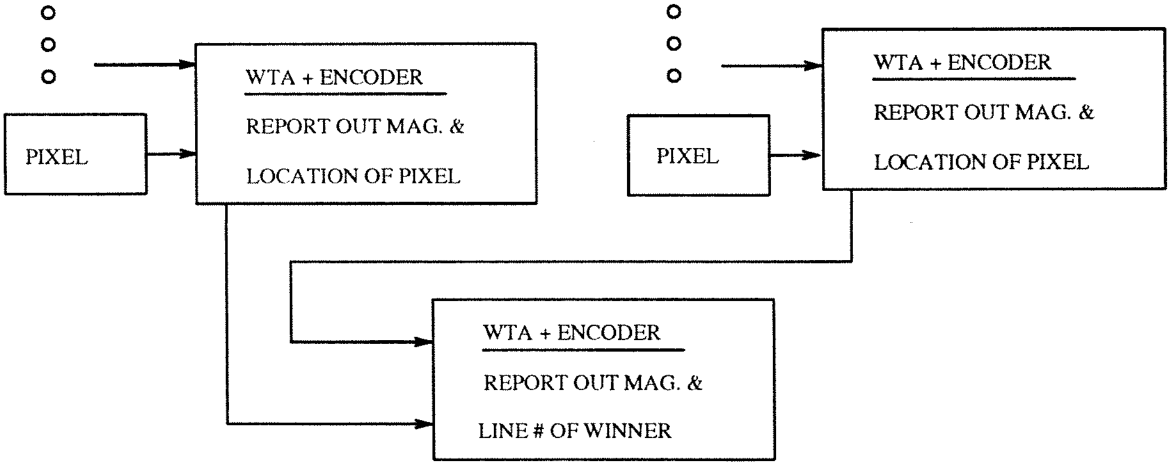

Figure 5.9: Box diagram of detector chip for correlator.

a single line of pixels. Figure 5.9 shows a box diagram of the detector circuit used for peak detection. A chip that does both pixel and multiple line WTA and then reports out the address and the magnitude of the winner was also built. These chips have the potential to increase the correlation rate by an order of magnitude.

5.1.5 Correlator Summary

We have demonstrated a multi-channel disk-based optical correlator using both angular and spatial multiplexing of volume holograms. The full 2-D correlation function of a presented image against stored images is generated by using disk rotation to shift one image over the other, thus reading out one line of each correlation function in parallel. 300 holograms, in the required 1-D image and 1-D Fourier transformed format, were stored on a single ring of an optical disk. The correlation generation was experimentally verified and compared to theory. Also, custom detector arrays were built and tested that find the peak on chip and report out its location which dramatically reduces how fast information is required to be read off chip.

The current system stores three holograms at a single spot and uses most of one ring around the disk resulting in 300 holograms stored. The effective thickness of the material was about 38 μm. Using the spin coating technique, a photopolymer film thick enough ($\approx$ 350 μm) to store more than 50 holograms in one spot has been made. Using the whole area of the disk and leaving enough blank space between spots, approximately 3000 spots can be stored on a 5 cm radius disk. This results in a $\sim$ 150,000 hologram storage capacity. The speed of the current correlator is limited by the speed of the linear detectors. A line detector is needed for each angularly multiplexed hologram position. For example, if 50 holograms are multiplexed at each spot then 50 line detectors are needed. Table 5.1 shows the capacity and speed of a disk that can be realized with off the shelf technology. For example, small parallel detector arrays, SLMs, and photopolymer films that can use existing red light sources,

Characteristic	Value	Limiting Factor
Pixels (N)	500 x 500	SLM
# Holograms/spot	60	Thickness (L)
Total stored images	$\sim 3 \times 10^5$	12cm diameter & L
Correlation Rate (R)	$\sim 10^4$	30 MHz detectors & L
Integer Ops/sec ($N^2 \times R$)	$10^{14} - 10^{15}$	detectors & L

Table 5.1: Disk-based Correlator Parameters

are all currently available. Using the custom detector arrays similar to what has already been demonstrated, the correlation rate could be increased by an order of magnitude.

5.2 Data Storage

5.2.1 Introduction

Holographic storage of data in 3-D materials such as photorefractives or photopolymers can provide large capacities and fast parallel readout of the stored information. These memories were investigated in the 1960's and 1970's, but they never found commercial applications. Recently, with improvements in materials, light sources, detectors, and the invention of spatial light modulators, holographic storage has again arisen as a possible mass storage candidate. The theoretical upper limit on the storage density is V/λ^3, where V is the volume of the media and λ is the wavelength of the light used. This limit suggests that densities of $\sim 10^{12}$ bits per cm^3 are possible. Unfortunately, due to the finite numerical aperture or the finite dynamic range of the material, practical systems are limited to approximately 10^9–10^{10} bits per cm^3. For example, 10^3 holograms each with 10^6 pixels has a total capacity of 10^9 bits. With the increase in storage densities of both magnetic and RAM memories, storage technologies that are limited to these capacities are not of commercial interest. In order to increase the capacity to useful levels it is necessary to spatially multiplex the

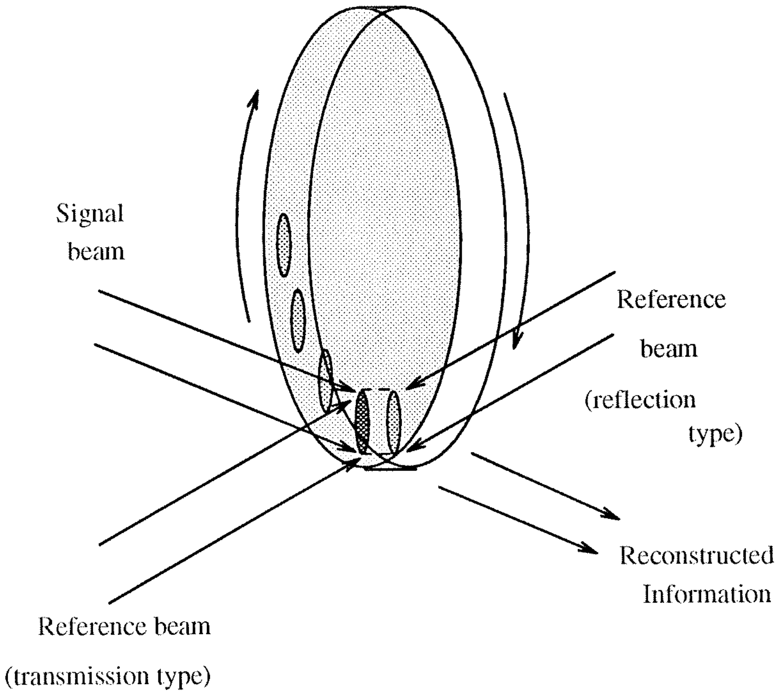

Figure 5.10: Using the disk as a storage device by presenting the reference plane wave for reconstruction of the stored data.

holograms as well as volumetrically multiplexing them. Spatial multiplexing simply means to use new, "unexposed" material to record more holograms.

The storage architectures presented here accomplishes the spatial multiplexing by shaping the medium in the form of a disk and rotating the disk or moving the location of the beams. At each spot on the holographic disk (HD), holograms are multiplexed by angle, wavelength, phase code, or in-plane rotation. The disk/head motion is used to access new spots to record the information just like in the correlator in the preceding section. To get the data out, the correct plane wave reference illuminates the correct spot on the disk. Figure 5.10 shows a disk system where holograms are multiplexed in either transmission or reflection geomerties. In this section, we will calculate the geometrically limited storage capacity of such a system for angle, wavelength, and peristrophic plus angle multiplexing schemes. The derivation for angle and wavelength follows the derivation presented in reference [225] where the signal beam is incident normal to the disk surface.

5.2.2 Angle Multiplexed Holographic Disk

The capacity of the angle multiplexed HD is

$$N = N_p^2 N_\theta N_s, \tag{5.10}$$

where N_p^2 is the total number of pixels per hologram, N_θ is the number of multiplexed holograms, and N_s is the number of spatial locations used. The number of angularly multiplexed holograms per location that one can store if the holograms are stored in the second minimum of the adjacent holograms sinc function is given by

$$N_\theta = 1 + \left(\frac{nL}{2\lambda}\right)|\cos\theta_1 - \cos\theta_2|. \tag{5.11}$$

In relation 5.11, n is the index of the material, L is the thickness of the material, $\cos\theta_1$ is the smallest reference angle inside the material, and $\cos\theta_2$ is the largest reference angle inside the material.

To calculate the number of unique locations in a given area A, we need to find the area of the individual spots. Figure 5.11 shows the geometry of the recording areas. For angle multiplexing there are two widths. One due to angular spread of the image, and one due to the angular spread of the reference beams. Using geometrical optics the highest frequency component of the image is traveling at an angle $\theta = \sin^{-1}(\lambda/n\delta)$, where δ is the resolution or pixel spacing of the focused image on the disk. δ in terms of system parameter is given by

$$\delta = \lambda\sqrt{4F\# + 1}, \tag{5.12}$$

where $F\#$ is the F-number of the optical system. The width of the image inside the material is then

$$w = N_p\delta + L\tan\theta = N_p\delta + \frac{L}{\sqrt{(n\delta/\lambda)^2 - 1}}. \tag{5.13}$$

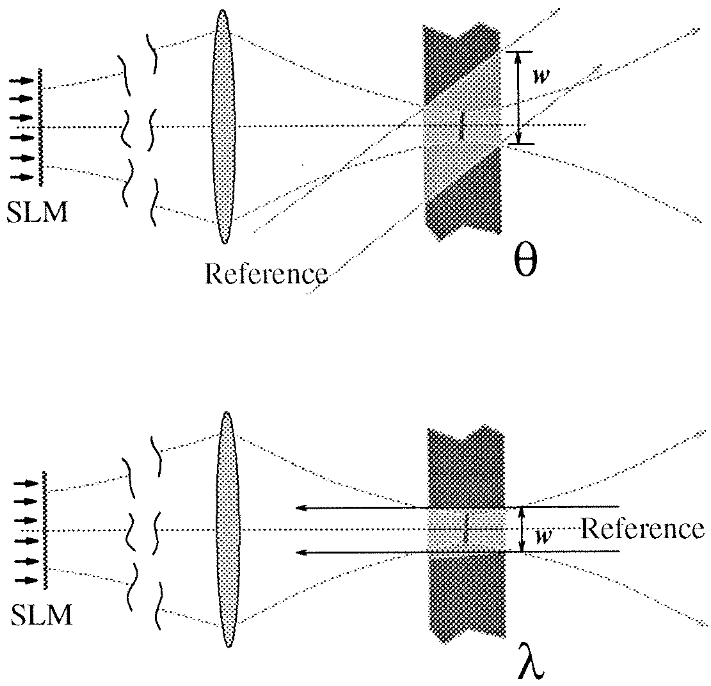

Figure 5.11: Area considerations for density calculation for both θ and λ multiplexing.

As shown at the top of Figure 5.11, the reference beams occupy more area so the width in the direction of reference and signal intersection is given by

$$w' = w + L \tan \theta_2. \tag{5.14}$$

Therefore, the number of spots available is $N_s = A/ww'$.

The density of the information is given by dividing out the area from the total capacity. The expression is shown below.

$$N/A = N_p^2 \frac{1 + \left(\frac{nL}{2\lambda}\right) |\cos\theta_1 - \cos\theta_2|}{\left(N_p\delta + \frac{L}{\sqrt{(n\delta/\lambda)^2 - 1}}\right)\left(N_p\delta + \frac{L}{\sqrt{(n\delta/\lambda)^2 - 1}} + L\tan\theta_2\right)} \tag{5.15}$$

This equation has two optimal regions depending on L. Figure 5.12 shows the theoretical data storage limit for a photopolymer disk calculated using the Eq 5.15 in the thin regime. Also plotted is the number of holograms that have to be stored at a given location on the disk to get the density shown. Figure 5.12 was calculated with

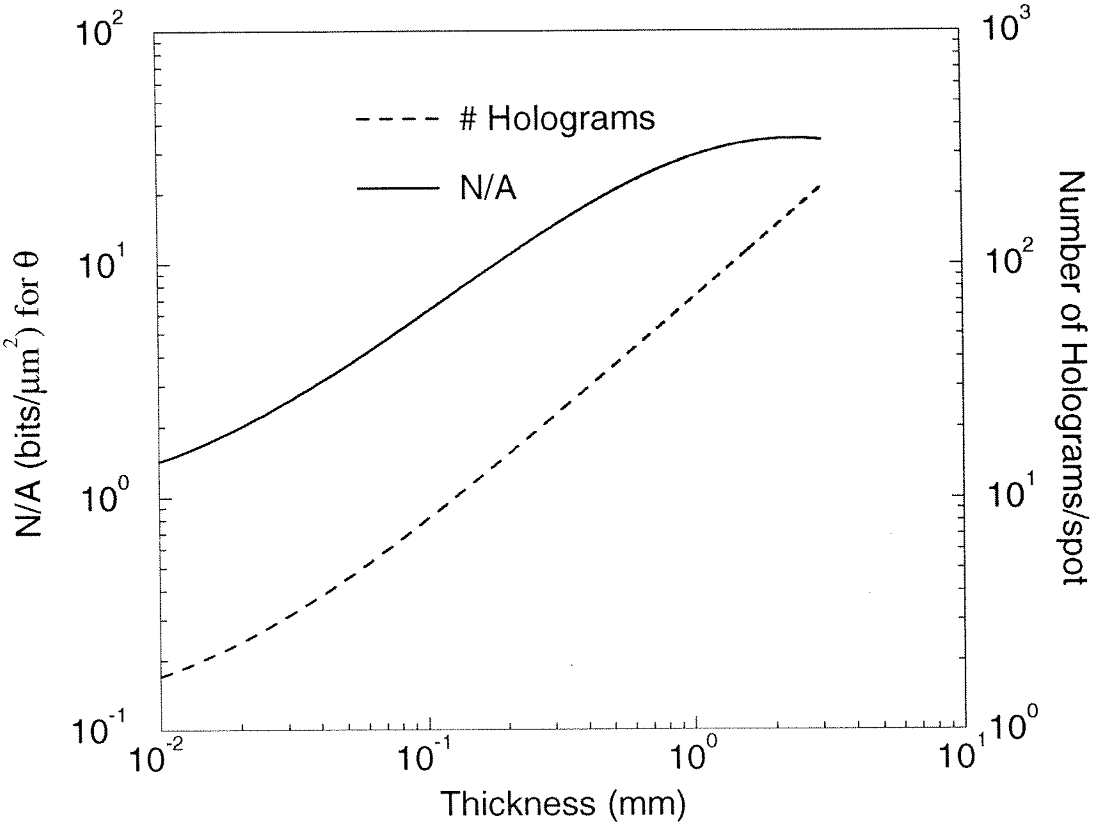

Figure 5.12: Geometrical storage limit of angle multiplexed HD.

λ=488nm, $\theta_1 = 10°$, $\theta_2 = 20°$, $N_p = 1000$, $n = 1.525$ and $F^{\#} = 1$. Notice that for a 40μm thick film the optimal number of holograms is about 20 holograms/spot. Therefore, our demonstrated 10 angle multiplexed holograms would work out to about 6 bits/μm^2. In addition, angle multiplexing can be done on the other side of the signal beam and in reflection geometry which increases the storage density by a factor of four. Since current 2-D disks have densities on the order of 1 bit/μm^2, 3-D photopolymer disks can have densities that are about 100 times that of current disks depending on the film thickness. The density for Fourier multiplexed holograms is equivalent to the density for image plane holograms calculated here given the systems' bandwidths are equal.

5.2.3 Wavelength Multiplexed Holographic Disk

The capacity of a wavelength multiplexed HD is

$$N = N_p^2 N_\lambda N_s, \tag{5.16}$$

where N_p^2 is the total number of pixels per hologram, N_λ is the number of multiplexed holograms, and N_s is the number of spatial locations used. The number of wavelength multiplexed holograms per location that one can store if the holograms are stored in the fourth minimum of the adjacent holograms sinc function is given by

$$N_\lambda = 1 + \frac{nL}{2}\left(\frac{1}{\lambda_1} - \frac{1}{\lambda_2}\right), \tag{5.17}$$

where the wavelength was swept from λ_1 to λ_2 to multiplex the holograms.

As the bottom of Figure 5.11 shows, wavelength multiplexing's area per location is smaller since the reference beam is interfered in reflection geometry. The maximum area is just the signal beam area with $\lambda = \lambda_2$. The number of spots on the disk for lambda becomes

$$w = N_p\delta + \frac{L}{\sqrt{(n\delta/\lambda_2)^2 - 1}}\ . \tag{5.18}$$

Thus the density for wavelength multiplexed HD can be written as

$$N/A = N_p^2 \frac{1 + \frac{nL}{2}\left(\frac{1}{\lambda_1} - \frac{1}{\lambda_2}\right)}{\left(N_p\delta + \frac{L}{\sqrt{(n\delta/\lambda_2)^2-1}}\right)^2}\ . \tag{5.19}$$

Figure 5.13 shows the theoretical data storage limit for a photopolymer disk calculated using the Eq 5.15 in the thin regime. Also plotted is the number of holograms that have to be stored at a given location on the disk to get the density shown. Figure 5.13 was calculated with $\lambda_1 = 500$nm, $\lambda_2 = 550$nm, $N_p = 1000$, $n = 1.525$ and $F^\# = 1$. Notice that the density for wavelength multiplexing is higher than the transmission angle multiplexed HD since the spot area is less for wavelength.

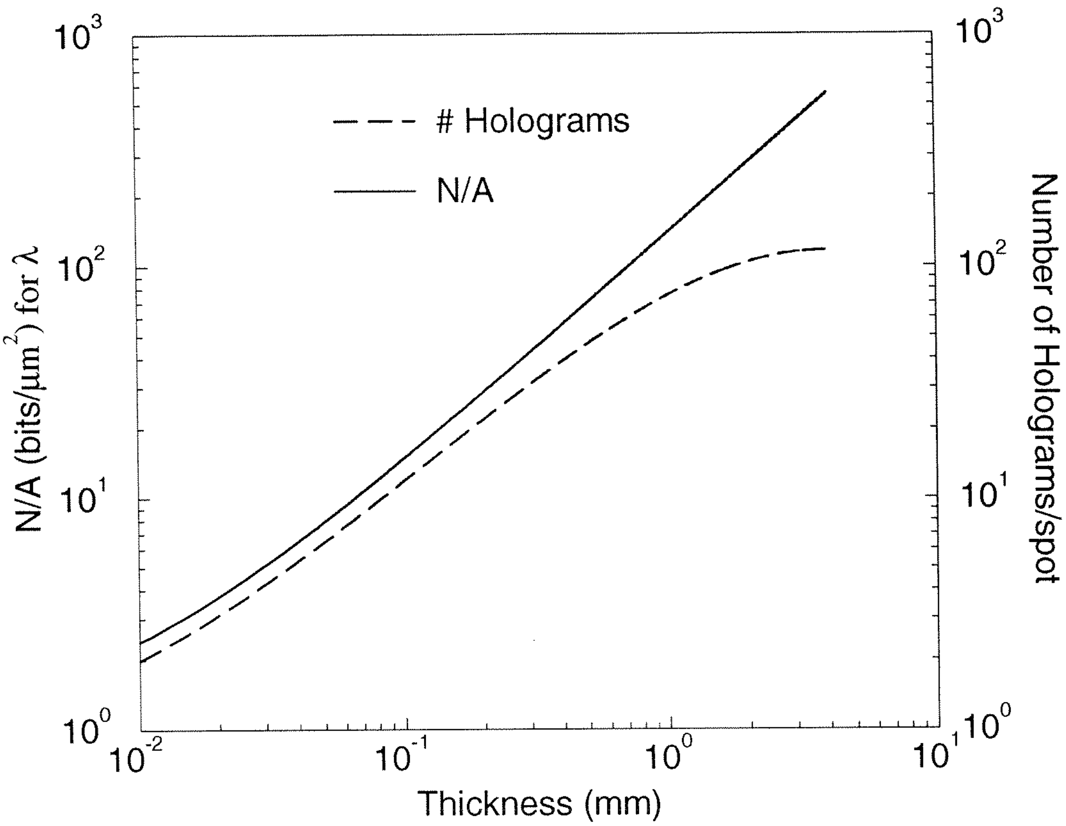

Figure 5.13: Geometrical storage limit of wavelength multiplexed HD.

5.2.4 Peristrophic and Angle Multiplexed Holographic Disk

The capacity of the peristrophic and the angle multiplexed HD is

$$N = N_p^2 N_\theta N_r N_s, \tag{5.20}$$

where N_p^2 is the total number of pixels per hologram, N_θ is the number of multiplexed holograms, N_r is the number of peristrophic multiplexed holograms possible, and N_s is the number of spatial locations used. For each peristrophic position, a new set of holograms can be angle multiplexed which makes the total number of holograms multiplexed at a given spot approximately equal to $N_r \times N_\theta$. The number of angularly multiplexed holograms per location that one can store if the holograms are stored in the second minimum of the adjacent holograms sinc function is again given by

$$N_\theta = 1 + \left(\frac{nL}{2\lambda}\right) |\cos\theta_1 - \cos\theta_2|. \tag{5.21}$$

In relation 5.21, n is the index of the material, L is the thickness of the material, $\cos\theta_1$ is the smallest reference angle inside the material, and $\cos\theta_2$ is the largest reference angle inside the material. To calculate the number of unique locations in a given area A, we need to find the area of the individual spots. For peristrophic and angle multiplexing the area of recording is a circle, and the number of spots available is given by

$$N_s = \frac{A}{\sqrt{3}}\,\frac{1}{[N_p\delta + \frac{L}{\sqrt{(\delta n/L)^2-1}} + 2L\tan\theta_2]^2}. \tag{5.22}$$

With peristrophic multiplexing, the number of holograms can depend on the bandwidth of the signal or the thickness of the film. I will use the Bragg condition worked out in the previous chapter with $\theta_2 = 0°$. The amount of rotation required to place the holograms in the second minimum is

$$d\theta = \frac{2}{\sin\theta_1}\sqrt{\frac{2\lambda}{Ln}}\ . \tag{5.23}$$

The total rotation possible is π, since greater than π rotation results in grating degeneracy. Thus the number of holograms that can be rotation multiplexed is

$$N_r = \frac{\pi}{d\theta} = \frac{\pi\sin\theta_1}{2}\sqrt{\frac{Ln}{2\lambda}}\ . \tag{5.24}$$

The storage density of the information is given by dividing out the area from the total capacity. The expression is shown below.

$$N/A = N_p^2\frac{\pi\sin\theta_1}{2\sqrt{3}}\sqrt{\frac{Ln}{2\lambda}}\ \frac{(1+\left(\frac{nL}{2\lambda}\right)|\cos\theta_1-\cos\theta_2|)}{[N_p\delta + \frac{L}{\sqrt{(\delta n/L)^2-1}} + 2L\tan\theta_2]^2}\ . \tag{5.25}$$

Figure 5.14 shows the theoretical data storage limit for a photopolymer disk calculated using the Eq 5.25. Also plotted is the number of holograms that have to be stored at a given location on the disk to get the density shown and the density for just angle multiplexing without peristrophic. Figure 5.14 was calculated with λ=488nm, $\theta_1 = 20°$, $\theta_2 = 30°$, $N_p = 1000$, $n = 1.525$, and $F^{\#} = 1$. In addition, angle multiplexing

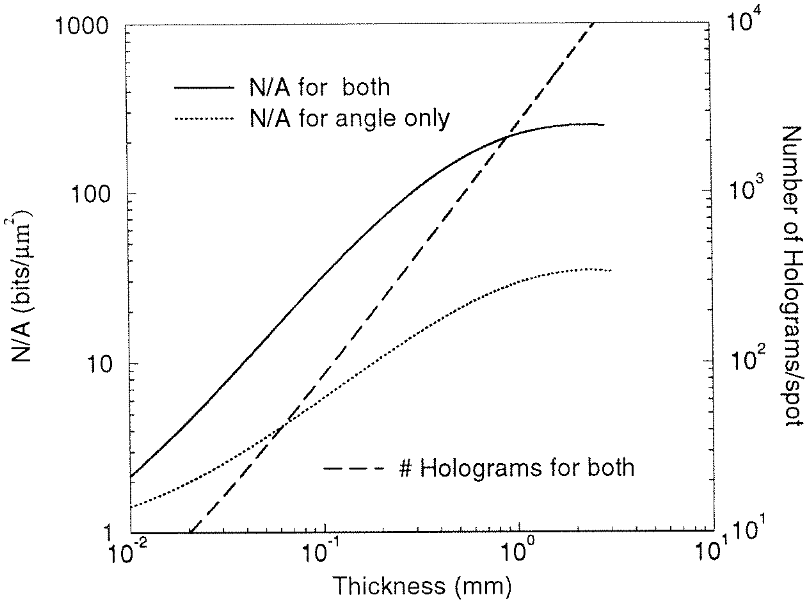

Figure 5.14: Geometrical storage limit of peristrophic and angle multiplexed HD.

can be done on the other side of the signal beam and in reflection geometry which adds another factor of four to the storage densities. Peristrophic multiplexing can help alleviate the bandwidth limitation inherent in multiplexing holograms in thin films and increase the density. N_r may also be further increased by making the signal beam incident at an angle. Thus, the density of 3-D disks using these techniques is not geometry limited but is limited by the dynamic range of the material used to fabricate the disk.

5.2.5 Read-out Rates

Data read-out rates are determined by the power of the light source, diffraction efficiency of the holograms, the size of the SLM, noise sources in the system, and the required signal-to-noise ratio. Li [226] has shown that with Fourier transformed holograms and a disk rotation rate of 3,600 rpm for a 6cm radius disk the maximum

M_e	η	I_{inc}	τ (μsec)	Read-out Rate
1,000	10^{-5}	20 W	2	500 Gbits/sec
100	10^{-5}	2 W	2	500 Gbits/sec
100	10^{-4}	200 mW	2	500 Gbits/sec
100	10^{-4}	400 mW	1	1 Tbits/sec

Table 5.2: Read-out Rate Parameters

alignment limited integration time is about 2μsec. Thus, the transfer rate for a 1,000 × 1,000 pixel SLM, assuming binary value for the pixels, is $\sim 5 \times 10^{11}$ bits/second. Unfortunately, pixel registration is not the only factor that must be considered. A sufficient number of photons must be incident on the detector to ensure a reasonable SNR. The required incident intensity for a given number of electrons is expressed as

$$I_{inc} = \frac{N_p^2 M hc}{\tau \lambda \eta}, \tag{5.26}$$

where M is the number of required photons, η is the diffraction efficiency, N_p^2 is the total number of pixels per hologram, τ is the integration time, h is Plank's constant, c is the speed of light, and λ is the wavelength of the light. In order to get a feeling for the read-out rates and the required power for these devices. Table 5.2 shows read-out rates calculated with various diffraction efficiencies and photo-electrons with $N_p^2 = 10^6$, and $\lambda = 500$nm. The diffraction efficiency scales as one of the total number of holograms stored per spot squared. Thus, the capacity can be traded off for an increase in the data rate or for a lower power requirement as shown in the last two lines of Table 5.2. Since detector noise is typically between 20 to 60 photons for commercial detectors, M_e equal to 1,000 is probably too high while 100 is too low for a practical system. Clearly, with their inherent parallel read-out, 3-D memories can have fast read-out rate but requires relatively large light powers to achieve these rates.

Bibliography

[1] D. Gabor, "A new microscope principle," *Nature*, 161:777, 1948.

[2] D. Gabor, "Microscopy by reconstructed wavefronts," *Proceedings of the Royal Society*, A454, 1949.

[3] D. Gabor, "Microscopy by reconstructed wavefronts II," *Proceedings of the Royal Society*, B64:449, 1951.

[4] G. L. Rogers, "Gabor diffraction microscopy: The hologram as a generalized zone plate," *Nature*, 166:237, 1950.

[5] H. M. A. El-Sum, "Reconstructed wavefront microscope," Thesis, Stanford Univerisity, 1952.

[6] A. Lohmann, "Optical single-sideband transmission applied to the Gabor microscope," *Optica Acta*, 3:97–103, 1956.

[7] E. N. Leith, and J. Upatnieks, "Reconstructed wavefront and communication theory," *Journal of the Optical Society of America*, 52:1123, 1962.

[8] E. N. Leith, and J. Upatnieks, "Wavefront reconstruction with diffused illumination and three-dimensional objects," *Journal of the Optical Society of America*, 54:1295–1301, 1964.

[9] P. J. van Heerden, "Theory of optical information storage in solids," *Applied Optics*, 2(4):393–400, 1963.

[10] F. M. Smits and L. E. Gallaher, "Design considerations for a semipermanent optical memory," *The Bell System Technical Journal*, pages 1267–1278, July–August 1967.

[11] E. N. Leith, A. Kozma, J. Upatnieks, J. Marks, and N. Massey, "Holographic data storage in three–dimensional media," *Applied Optics*, 5(8):1303–1311, 1966.

[12] E. G. Ramberg, "Holographic information storage," *RCA Review*, 33:5–53, 1972.

[13] A. Vander Lugt, "Design relationships for holographic memories," *Applied Optics*, 12(7):1675–1685, 1973.

[14] A. Vander Lugt, "Signal detection by complex spatial filtering," *IEEE Transactions on Information Theory*, pages 139–145, April 1964.

[15] J. W. Goodman, "Temporal filtering properties of holograms," *Applied Optics*, 6:857–862, 1967.

[16] J. Upatnieks, A. Vander Lugt, and E. Leith, "Correction of lens aberrations by means of holograms," *Applied Optics*, 5:589–593, 1966.

[17] J. W. Goodman, "Wavefront-reconstruction imaging through random media," *Applied Physics Letters*, 8:311–315, 1966.

[18] L. J. Cutrona, et al., "On the application of coherent optical processing techniques to synthetic-aperture radar," *Proceedings of the IEEE*, 54:1026, 1966.

[19] P. L. Jackson, "Diffractive processing of geophysical data," *Applied Optics*, 4:419–425, 1965.

[20] W. H. Lee, "Effect of film–grain noise on the performance of holographic memory," *Journal of the Optical Society of America*, 62(6):797–801, 1972.

[21] R. F. van Ligten, "Influence of photographic film on wavefront reconstruction. I: Plane wavefronts," *Journal of the Optical Society of America*, 56:1–7, 1966.

[22] J. T. LaMacchia and C. J. Vincelette, "Comparison of the diffraction efficiency of multiple exposure and single exposure holograms," *Applied Optics*, 7(9):1857–1858, 1968.

[23] O. Bryngdahl and A. Lohmann, "Nonlinear effects in holography," *Journal of the Optical Society of America*, 58(10):1325–1334, 1968.

[24] J. W. Goodman, "Effects of film nonlinearitites in holography," *Journal of the Optical Society of America*, 57:560–564, 1967.

[25] W. L. Bragg, "The X-ray microscope," *Nature*, 149:470–475, 1942.

[26] H. Kogelnik, "Coupled wave theory for thick hologram gratings," *The Bell System Technical Journal*, 48(9):2909–2947, 1969.

[27] B. Benlarbi, D. J. Cooke, and L. Solymar, "Higher order modes in thick phase gratings," *Optica Acta*, 27(7):885–895, 1980.

[28] B. Benlarbi and L. Solymar, "Higher order modes in non–sinusoidal volume phase holograms," *International Journal of Electronics*, 48(4):351–359, 1980.

[29] M. G. Moharam, T. K. Gaylord, and R. Magnusson, "Criteria for Bragg regime diffraction by phase gratings," *Optics Communication*, 32(1):14–18, 1980.

[30] M. G. Moharam, T. K. Gaylord, and R. Magnusson, "Diffraction characteristics of three–dimensional crossed–beam volume gratings," *Journal of the Optical Society of America*, 70(4):437–442, 1980.

[31] J. J. Amodei, "Analysis of transport processes during holographic recording in insulators," *RCA Review*, 32:185–197, 1972.

[32] D. L. Staebler and J. J. Amodei, "Coupled–wave analysis of holographic storage in $LiNbO_3$," *Journal of Applied Physics*, 43(3):1042–1049, 1972.

[33] A. M. Glass and D. von der Linde, "Photovoltaic, photoconductive and excited state dipole mechanisms for optical storage in pyroelectrics," *Ferroelectrics*, 10:163–166, 1976.

[34] K. Blotekjaer, "Theory of hologram formation in photorefractive media," *Journal of Applied Physics*, 48(6):2495–2501, 1977.

[35] N. V. Kukhtarev, "Kinetics of hologram recording and erasure in electrooptic crystals," *Soviet Technical Physics Letters*, 2(12):438–440, 1977.

[36] N. V. Kukhtarev, V. B. Markov, S. G. Odulov, M. S. Soskin, and V. L. Vinetskii, "Holographic storage in electrooptic crystals I. Steady state," *Ferroelectrics*, 22:949–960, 1979.

[37] N. V. Kukhtarev, V. B. Markov, S. G. Odulov, M. S. Soskin, and V. L. Vinetskii, "Holographic storage in electrooptic crystals II. Beam coupling–light amplification," *Ferroelectrics*, 22:961–964, 1979.

[38] F. S. Chen, J. T. LaMacchia, and D. B. Fraser, "Holographic storage in lithium niobate," *Applied Physics Letters*, 13(7):223–225, 1968,"

[39] J. J. Amodei and D. L. Staebler, "Holographic recording in lithium niobate," *RCA Review*, 33:71–93, 1972.

[40] J. Bordogna, S. A. Keneman, and J. J. Amodei, "Recyclable holographic storage media," *RCA Review*, 33:227–247, 1972.

[41] D. L. Staebler, J. J. Amodei, and W. Phillips, "Multiple storage of thick phase holograms in $LiNbO_3$," *IEEE Journal of Quantum Electronics*, QE–8:611, 1972.

[42] D. L. Staebler, W. J. Burke, W. Phillips, and J. J. Amodei, "Multiple storage and erasure of fixed holograms in Fe–doped $LiNbO_3$," *Applied Physics Letters*, 26(4):182–184, 1975.

[43] F. H. Mok, "Angle–multiplexed storage of 5000 holograms in lithium niobate," *Optics Letters*, 18(11):915–917, 1993.

[44] F. H. Mok, D. Psaltis, and G. Burr, "Spatially- and Angle-multiplexed holographic random access memory," *SPIE Conference on Photonic Neural Networks*, 1773:334–345, 1992.

[45] J. J. Amodei and D. L. Staebler, "Holographic pattern fixing in electro–optic crystals," *Applied Physics Letters*, 18(12):540–542, 1971.

[46] J. J. Amodei, W. Phillips, and D. L. Staebler, "Improved electrooptic materials and fixing techniques for holographic recording," *Applied Optics*, 11(2):390–396, 1972.

[47] D. Kirillov and J. Feinberg, "Fixable complementary gratings in photorefractive $BaTiO_3$," *Optics Letters*, 16(19):1520–1522, 1991.

[48] G. Montemezzani, and P. Gunter, "Thermal fixing inpure and doped $KNbO_3$ crystals," *Journal of the Optical Society of America B.*, 7(12):2323–2328, 1990

[49] A. Kewitsch, M. Segev, A. Yariv, and R. Neurgaonkar, "Selective page-addressable fixing of volume holograms in $Sr_{.75}Ba_{.25}Nb_2O_6$ crystals," *Optics Letters*, 18(15):1262–1264, 1993.

[50] G. Burr, F. Mok, and D. Psaltis, "Long interaction length architecture (LILA)," *OSA Annual Meeting*, Vol 16 of 1993 OSA Technical Digest Series (OSA, Washington D.C., 1993), paper TuH6, p. 79.

[51] F. Micheron and G. Bismuth, "Electrical control of fixation and erasure of holographic patterns in ferroelectric materials," *Applied Physics Letters*, 20(2):79–81, 1972.

[52] F. Micheron and G. Bismuth, "Field and time thresholds for the electrical fixation of holograms recorded in $(Sr_{0.75}Ba_{0.25})Nb_2O_6$ crystals," *Applied Physics Letters*, 23(2):71–72, 1973.

[53] J. P. Herriau and J. P. Huignard, "Hologram fixing process at room temperature in photorefractive $Bi_{12}SiO_{20}$ crystals," *Applied Physics Letters*, 49(18):1140–1142, 1986.

[54] S. W. McCahon adn D. Rytz, G. C. Valley, M. B. Klein, and B. A. Wechsler, "Hologram fixing in $Bi_{12}TiO_{20}$ using heating and an ac electric field," *Applied Optics*, 28(11):1967–1969, 1989.

[55] Y. Qiao, S. Orlov, and D. Psaltis, "Electrical fixing of photorefractive holograms in $Sr_{0.75}Ba_{0.25}Nb_2O_6$," *Optics Letters*, 18(12):1004–1006, 1993.

[56] M. Horowitz, A. Bekker, and B. Fischer, "Image and hologram fixing method with $Sr_xBa_{1-x}Nb_2O_6$ crystals," *Optics Letters*, 18(22):1964–1966, 1993.

[57] Y. Qiao, D. Psaltis, and C. Gu. "Phase-locked sustainment of photorefractive holograms using phase conjugation," *Journal of Applied Physics*, 70(8):4646-4648 1991.

[58] Y. Qiao and D. Psaltis, "Sampled dynamic holographic memory," *Optics Letters*, 17(19):1376–1378, 1992.

[59] H. Tajbenbach, S. Bann, and J. P. Huignard, "Long–term readout of photorefractive memories by using a storage/amplification two–crystal configuration," *Optics Letters*, 17(23):1712–1714, 1992.

[60] S. Li, F. Mok, and D. Psaltis, "Non-volatile holographic memory in photorefractive crystals using two wavelengths," *submitted to Applied Optics*, 1993.

[61] D. von der Linde, A. M. Glass, and K.F. Rodgers, "Multiphoton photorefractive processes for optical storage in LiNbO3," *Applied Physics Letters*, 25:155-7 (1974).

[62] D. von der Linde, A. M. Glass, and K.F. Rodgers, "Optical storage using refractive index changes induced by two-step excitation," *Journal of Applied Physics*, 47:217-220 (1976).

[63] V.E. Wood, R.C. Sherman, N.F. Hartman, and C. M. Verber, "Optical erasure of one- and two-photon holograms in Fe-doped LiNbO3," *Ferroelectrics*, 34:175-178 (1981).

[64] C. Chen, and D.M. Kim, " Efficient hologram recording in LiNbO3 :Fe using optical pulses," *Applied Physics Letters*, 34:321-324 (1979).

[65] D. A. Parthenopoulos and P. M. Rentzepis, "Three–dimensional optical storage memory," *Science*, 245:843–845, 1989.

[66] S. Hunter, F. Kiamilev, S. Esener, D. A. Parthenopoulos, and P. M. Rentzepis, "Potentials of two–photon based 3–D optical memories for high performance computing," *Applied Optics*, 29(14):2058–2066, 1990.

[67] D. A. Parthenopoulos and P. M. Rentzepis, "Two–photon volume information storage in doped polymer systems," *Journal of Applied Physics*, 68(11):5814–5818, 1990.

[68] S. Jutamulia, G. M. Storti, J. Lindmayer, and W. Selderman, "Use of electron trapping materials in optical signal processing. 2: two–dimensional associative memory," *Applied Optics*, 30(20):2879–2884, 1991.

[69] S. Jutamulia, G. M. Storti, W. Seiderman, J. Lindmayer, and D. A. Gregory, "Use of electron–trapping materials in optical signal processing. iv: Parallel incoherent image subtraction," *Applied Optics*, 32(5):743–745, 1993.

[70] T. W. Mossberg, "Time–domain frequency–selective optical data storage," *Optics Letters*, 7(2):77–79, 1982.

[71] N. W. Carolson, L. J. Rothberg, A. G. Yodh, W. R. Babbit, and T. W. Mossberg, "Storage and time reversal of light pulses using photon echoes," *Optics Letters*, 8(9):483–485, 1983.

[72] U. P. Wild, S. E. Bucher, and F. A. Burkhalter, "Hole burning, stark effect, and data storage," *Applied Optics*, 24(10):1526–1530, 1985.

[73] P. Saari, R. Kaarli, and A. Rebane, "Picosecond time– and space–domain holography by photochemical hole burning," *Journal of the Optical Society of America* **B**, 3(4):527–533, 1986.

[74] G. S. Chen and D. J. Brady, "Liquid crystal doped polymers as volume holographic elements," *SPIE, Devices for Optical Processing*, 1562:128–135, 1991.

[75] C. Bowry and P. Bonnett, "Liquid crystal polymer optical memories: analogue, digital and holographic," *Optical Computing and Processing*, 1(1):13–21, 1991.

[76] S. Hvilsted, F. Andruzzi, and P. S. Ramanujam, " Side-chain liquid-crystalline polyesters for optical information storage," *Optics Letters*, 17(17):1234–1236, 1992.

[77] G. S. Chen and D. J. Brady, "Surface–stabilized holography in an azo–dye–doped liquid crystal," *Optics Letters*, 17(17):1231–1233, 1992.

[78] J. Zhang and M. B. Sponsler, "Switchable liquid crystalline photopolymer media for holography," *Journal of the American Chemical Society*, 114:1506–1506, 1992.

[79] L. Domash, C. Gozewski, A. Nelson, and J. Schwartz, "Programable beamlet generator, dynamic lens, and optical memory using electrically switchable holographic devices," *SPIE, Very Large Optical Memories*, 2026c , 1993.

[80] S. Ducharme, J. C. Scott, R. J. Tweig, and W. E. Moerner, "Observation of the photorefractive effect in a polymer," *Physical Review Letters*, 66(14):1846–1849, 1991.

[81] K. Sutter and P. Gunter, "Photorefractive gratings in the organic crystal 2-cycloctylamino-5-nitropyridine doped with 7,7,8,8-tetracyanoquinodimethane," *Journal of the Optical Society of America B.*, 7(12):2274–2278, 1990.

[82] J. S. Schildkraut, "Photoconducting electrooptic polymer films," *Applied Physics Letters*, 58(4):340–342, 1991.

[83] S. G. Anderson, "Photorefractive polymer may function as computer memory," *Laser Focus World*, 29(8):18–19, 1993.

[84] B. Kippelen, K. Tamura, N. Peyghambarian, A. B. Padias, H.K. Hall, "Photorefractive effect in a poled polymer containing the tricyanovinylcarbazole group," *Journal of Applied Physics*,74(5):3617–3619, 1993.

[85] M. J. Sansone, C. C. Teng, A. J. East, M. S. Kwiatek, "Observation of the photorefractive effect in a dialkylaminonitrostilbene copolymer," *Optics Letters*, 18(17):1400–1402, 1993.

[86] M.C.J.M. Donckers, S.M. Silence, C.A. Walsh, F. Hache, D.M. Burland, et al., "Net 2-beam-coupling gain in a polymeric photorefractive material," *Optics Letters*, 18(13):1044–1046, 1993.

[87] L.P. Yu, W.K. Chan, Z.N. Bao, S.X.F. Cao, "Photorefractive polymers .2. structure design and property characterization," *Macromolecules*, 26(9):2216–2221, 1993.

[88] C.A. Walsh, W.E. Moerner, "2-beam coupling measurements of grating phase in a photorefractive polymer," *Journal of the Optical Society of America B-Optical Physics*, 10(4):753–753, 1993.

[89] J. C. Scott, L. T. Pautmeier, W. E. Moerner, "Photoconduction and photorefraction in molecularly doped polymers," *Synthetic Metals*, 54(1-3):9–19, 1993.

[90] Y. T. Mazurenko, V. S. Udaltsov, A. V. Veniaminov, E. Dopel, P. Kuhmstedt, "Recording and reconstruction of femtosecond light-pulses using volume holograms," *Optics Communications*, 96(4-6):202–207, 1993.

[91] K.A. Verkhovskaya, V.M. Fridkin, A.V. Bune, J.F. Legrand, "Photoconducting ferroelectric polymers," *Ferroelectrics*, 134(1-4):7–15, 1992.

[92] S. Ducharme, B. Jones, J.M. Takacs, Z. Lei, "Electric-field stabilization and competition of gratings in a photorefractive polymer," *Optics Letters*, 18(2):152–154, 1992.

[93] S.M. Silence, C.A. Walsh, J. C. Scott, W. E. Moerner, "C-60 sensitization of a photorefractive polymer," *Applied Physics Letters*, 61(25):2967–2969, 1992.

[94] L. P. Yu, W. K. Chan, Z. N. Bao, S. X. F. Cao, "Synthesis and physical measurements of a photorefractive polymer," *Journal of the Chemical Society-Chemical Communications*, (23):1735–1737, 1992.

[95] Y. P. Cui, Y. Zhang, P. N. Prasad, J. S. Schildkraut, D. J. Williams, "Photorefractive effect in a new organic-system of doped nonlinear polymer," *Applied Physics Letters*, 61(18):2132–2134, 1992.

[96] Y. Zhang, Y. P. Cui, P. N. Prasad, "Observation of photorefractivity in a fullerene-doped polymer composite," *Physical Review B-Condensed Matter*, 46(15):9900–9902, 1992.

[97] L. P. Yu, W. K. Chan, Z. N. Bao, "Pure photorefractive polymer-synthesis and physical measurements," *Abstracts of papers of the American Chemical Society*, 204(AUG):198–POLY, 1992.

[98] S. M. Silence,C. A. Walsh, J. C. Scott,T. J. Matray, R. J. Tweig, "Subsecond grating growth in a photorefractive polymer," *Optics Letters*, 17(16):1107-1109, 1992.

[99] K. Tamura, A. B. Padias, H. K. Hall, N. Peyghambarian, "New polymeric material containing the tricyanovinylcarbazole group for photorefractive applications," *Applied Physics Letters*, 60(15):1803–1805, 1992.

[100] J. A. Jenny, "Holographic recording with photopolymers," Journal of the Optical Society of America, 60(9):1155–1161, 1970.

[101] F. P. Laming, "Holographic grating formation in photopolymers – polymethylmethacrylate," *Polymer Engineering and Science*, 11(5):421–425, 1971.

[102] W. S. Colburn and K. A. Haines, "Volume hologram formation in photopolymer materials," *Applied Optics*, 10:1636–1641, 1971.

[103] J. M. Moran and I. P. Kaminow, "Properties of holographic grating photoinduced in polymethyl methacrylate," *Applied Optics*, 12(8):1964–1970, 1973.

[104] A. Bloom, R. A. Bartolini, and D. L. Ross, "Organic recording medium for volume-phase holography," *Applied Physics Letters*, 24(12):612–614, 1974.

[105] A. Bloom, R. A. Bartolini, H. A. Weakliem, and P. L. K. Hung, "A volume phase holographic recording medium," *Coatings and Plastic Preprints*, 35(2):319–323, 1975.

[106] R. A. Bartolini, A. Bloom, and H. A. Weakliem, "Volume holographic recording characteristics of an organic medium," *Applied Optics*, 15(5):1261–1265, 1976.

[107] R. A Bartolini, A. Bloom, and D. J. Channin, "Organic medium for integrated optics," *Applied Optics*, 15(11):2628–2629, 1976.

[108] A. Bloom, R. A. Bartolini, P. L. K. Hung, and D. L. Ross, "Nonpolymeric organic host for recording volume phase holograms," *Applied Physics Letters*, 29(8):483–484, 1976.

[109] R. A. Bartolini, H. A. Weakliem and B. F. Williams, "Review and analysis of optical recording media," *Optical Engineering*, 15(2):99–107, 1976.

[110] A. Bloom, R. A. Bartolini, and H. A. Weakliem, "Organic materials for optical devices," *Optical Engineering*, 17(5):446–452, 1978.

[111] R. A. Bartolini, A. Bloom, and J. S. Escher, "Multiple storage of holograms in an organic medium," *Applied Physics Letters*, 28(9):506–507, 1976.

[112] W. K. Smothers, T. J. Trout, A. M. Weber, and D. J. Mickish, " Hologram recording in DuPont's new photopolymer material," 2^{nd} *Int. Conf. on Holographic Systems*, Bath, UK (1989).

[113] K. Curtis and D. Psaltis, "Holographic recording in photopolymer films," *OSA Annual Meeting*, Vol. 23 of 1992 OSA Technical Digest Series (OSA, Washington D.C., 1992), paper ThX3, p. 145.

[114] K. Curtis, "Phase grating profiles in photopolymers," *Optics Communications*, 95(13):113–116, 1993.

[115] K. Curtis and D. Psaltis, "Characterization of the DuPont photopolymer films for 3-D holographic memories," *submitted to Applied Optics.*

[116] W. C. Hay and B. D. Guenther, "Characterization of Polaroid's DMP-128 holographic recording photopolymer," *SPIE, Holographic Optics: Design and Applications*, 883:102–105, 1988.

[117] V. Weiss, A. A. Friesem, and V. A. Krongauz, "Holographic recording and all-optical modulation in photochromic polymers," *Optics Letters*, 18(13):1089–1091, 1993.

[118] D. J. Lanteigne, T. D. Hudson, and D. A. Gregory, "Matched spatial filtering using a new photopolymer," *Applied Optics*, 26(2):184–185, 1987.

[119] J. C. Kirsch, D. A. Gregory, T. D. Hudson, and D. J. Lanteigne, "Design of photopolymer holograms for optical interconnect applications," *Optical Engineering*, 27(4):301–308, 1988.

[120] K. Curtis and D. Psaltis, "Multi-channel disk-based optical correlator," *SPIE Conference on Information Processing*, July 1993.

[121] K. Curtis and D. Psaltis, "Recording of multiple holograms in photopolymer films," *Applied Optics*, 31(35):7425–7428, 1992.

[122] U. Rhee, H. J. Caulfield, J. Shamir, C. S. Vikram, and M. M. Mirsalehi, "Characteristics of the DuPont photopolymer for angularly multiplexed page-oriented holographic memories," *Optical Engineering*, 32(8):1839–1847, 1993.

[123] E. S. Gyulnazarov, V. V. Obukhovskii, and T. N. Smirnov, "Theory of holographic recording on a photopolymerized material," *Optical Spectroscopy, USSR*, 69(1):109–111, 1990.

[124] R. R. Adhami, D. J. Lanteigne, and D. A. Gregory, "Photopolymer hologram formation theory," *Microwave and Optical Technology Letters*, 4(3):106–109, 1991.

[125] I. Abdulhalim, G. Moddel, and K. M. Johnson, "High–speed analog spatial light modulator using a hydrogenated amorphous silicon photosensor and an electroclinic liquid crystal," *Applied Physics Letters*, 55(16):1603–1605, 1989.

[126] D. R. Collins, J. B. Sampsell, L. J. Hornbeck, J. M. Florence, P. A. Penz, and M. T. Gately, "Deformable mirror device spatial light modulators and their applicability to optical neural networks," *Applied Optics*, 28(22):4900–4907, 1989.

[127] K. M. Johnson and G. Moddel, "Motivations for using ferroelectric liquid crystal spatial light modulators in neurocomputing," *Applied Optics*, 28(22):4888–4899, 1989.

[128] W. Li, R. A. Rice, G. Moddel, L. A. Pagano-Stauffer, and M. A. Handschy, "Hydrogenated amorphous–silicon photosensor for optically addressed high–speed spatial light modulator," *IEEE Transactions on Electron Devices*, 36(12):2959–2964, 1989.

[129] H.-K. Liu and T.-H. Chao, "Liquid crystal television spatial light modulators," *Applied Optics*, 28(22):4772–4780, 1989.

[130] G. Moddel, K. M. Johnson, W. Li, and R. A. Rice, "High–speed binary optically addressed spatial light modulator," *Applied Physics Letters*, 55(6):537–539, 1989.

[131] J. Aiken, B. Bates, M. G. Catney, and P. C. Miller, "Programmable liquid–crystal TV spatial light modulator: modified drive electronics to improve device performance for spatial–light–modulation operation," *Applied Optics*, 30(32):4605–4609, 1991.

[132] J. L. de Bougrenet de la Tocnaye and J. R. Brocklehurst, "Parallel access read/write memory using an optically addressed ferroelectric spatial light modulator," *Applied Optics*, 30(2):179–180, 1991.

[133] D. Armitage and D. K. Kinell, "Liquid–crystal integrated silicon spatial light modulator," *Applied Optics*, 31(20):3945–3949, 1992.

[134] M. Killinger, J. L. de Bougrenet de la Tocnaye, P. Cambon, R. C. Chittick, and W. A. Crossland, "Bistability and nonlinearity in optically addressed ferroelectric liquid–crystal spatial light modulators: applications to neurocomputing," *Applied Optics*, 31(20):3930–3936, 1992.

[135] M. G. Robinson, "Analog nonvolatile data storage and update in an optically addressed spatial light modulator," *Optics Letters*, 17(12):895–897, 1992.

[136] T. M. Slagle and K. Wagner, "Winner–take–all spatial light modulator," *Optics Letters*, 17(16):1164–1166, 1992.

[137] A. M. Gabor, B. Landreth, and G. Moddrel, "Integrating mode for an optically addressed spatial light modulator," *Applied Optics*, 32(17):3064–3067, 1993.

[138] D. A. Scribner, M. R. Kruer, J. M. Killiany, "Infrared focal plane array technology," *Proceedings of the IEEE*,79(1):66–85, 1991.

[139] E. G. Stevens, B. C. Burkey, D. N. Nichols, Y. S. Yee, D. L. Losee, et al., "A 1-megapixel, progressive-scan image sensor with antiblooming control and lag-free operation," *IEEE Transactions on Electron Devices*, 38(5):981–988, 1991.

[140] S. Manabe and N. Harada, "High-definition television (HDTV) solid-state image sensors," *IEICE Transactions on Electronics*, E76C(1):78–85, 1993.

[141] D. J. Burt, "CCD performance limitations - theory and practice," *Nuclear Instruments and Methods in Physics Research Section A–Accelerators Spectrometers Detectors and Associated Equipment*, 305(3):564-573, 1991.

[142] J. J. Kasinski, W. Hughes, D. Dibiase, P. Bournes, R. Burnham, "One joule output from a diode-array-pumped Nd-YAG laser with side-pumped rod geometry," *IEEE Journal of Quantum Electronics*, 28(4):977–985, 1992.

[143] H. Hemmati, J. R. Lesh, "High repetition-rate Q-switched and intracavity doubled diode- pumped Nd-Yag laser," *IEEE Journal of Quantum Electronics*, 28(4):1018–1020, 1992.

[144] T.V. Higgins, " Diode-pumped Nd-YAG laser-light doubled with 71-percent efficiency," *Laser Focus World*, 27(12):35–38, 1991.

[145] T. R. Steele, D. C. Gerstenberger, A. Drobshoff, R. W. Wallace, "Broadly tunable high-power operation of an all-solid-state titanium- doped sapphire laser system," *Optics Letters*, 16(6):399–401, 1991.

[146] Z. Yu, J. Ren, J. W. Cook, J. F. Schetzina, "Blue-green laser-diodes and light-emitting-diodes," *Physica B*, 191(1-2):119–123, 1993.

[147] N. Nakayama, S. Itoh, T. Ohata, K. Nakano, H. Okuyama, et al., "Room-temperature continuous operation of blue-green laser-diodes," *Electronics Letters*, 29(16):1488–1489, 1993.

[148] Z. Yu, J. Ren, B. Sneed, K. Bowers, J. W. Cook, et al., "Blue laser-diodes and LEDS based on II-VI semiconductor heterostructures," *IEEE Transactions on Electron Devices*, 39(11):2653–2653, 1992.

[149] H. Jaeckel, G. L. Bona, P. Buchmann, H. P. Meier, P. Vettiger, et al., "Very high-power (425 mw) ALGaAs Sqw-Grinsch ridge laser with frequency-doubled output (41 mw at 428 nm)," *IEEE Journal of Quantum Electronics*, 27(6):1560–1567, 1991.

[150] W. J. Burke and P. Sheng, "Crosstalk noise from multiple thick–phase holograms," *Journal of Applied Physics*, 48(2):681–685, 1977.

[151] E. G. Ramberg, "Holographic information storage," *RCA Review*, 33:5–53, 1972.

[152] P. St. J. Russell and L. Solymar, "The properties of holographic overlap gratings," *Optica Acta*, 26(3):329–347, 1979.

[153] P. Varga, and G. Kiss, "Crosstalk and loss of information in holography," *Kvantovaya Elektronika*, 10(1):111-119, 1983.

[154] H. Lee, "Cross–talk effects in multiplexed volume holograms," *Optics Letters*, 13(10):874–876, 1988.

[155] D. Psaltis, X.-G. Gu, and D. Brady, "Fractal sampling grids for holographic interconnections," In *Proceedings of the SPIE*. SPIE, 1988.

[156] H. Lee, X.-G. Gu, and D. Psaltis, "Volume holographic interconnections with maximal capacity and minimal cross-talk," *Journal of Applied Physics*, 65(6):2191–2194, 1989.

[157] H. Lee, "Volume holographic global and local interconnecting patterns with maximal capacity and minimal first–order cross-talk," *Applied Optics*, 28(24):5312–5316, 1989.

[158] C. W. Slinger and L. Solymar, "Grating interactions in holograms recorded with two object waves," *Applied Optics*, 25(18):3283–3287, 1986.

[159] M. G. Moharam, "Cross–talk and cross–coupling in multiplexed holographic gratings," In *Practical Holography III—SPIE Vol 1051*, pages 143–147. SPIE, 1989.

[160] E. N. Glytsis and T. K. Gaylord, "Rigorous 3–D coupled wave diffraction analysis of multiple superposed gratings in anisotropic media," *Applied Optics*, 28(12):2401–2421, 1989.

[161] C. Gu, J. Hong, and P. Yeh, "Diffraction properties of momentum-mismatched gratings in photorefractive media," *Journal of the Optical Society of America* **B**, 9(8):1478–1479, 1992.

[162] C. Gu, A. Chiou, and J. Hong, "Cross-talk noise in photorefractive interconnections," *Applied Optics*, 32(8):1437–1440, 1993.

[163] K.-Y. Tu, T. Tamir, and H. Lee, "Multiple–scattering theory of wave diffraction by superposed volume gratings," *Journal of the Optical Society of America* **A**, 7(8):1421–1435, 1990.

[164] K. Y. Tu, H. Lee, and T. Tamir, "Analysis of cross talk in volume holographic interconnections," *Applied Optics*, 31(11):1717–1729, 1992.

[165] H. Lee, "Perturbative integral expansion method of analyzing cross-talk in volume holographic interconnections," *Journal of Applied Physics*, 73(5):2103–2113, 1993.

[166] K. Rastani, "Storage capacity and cross talk in angularly multiplexed holograms: two case studies," *Applied Optics*, 32(20):3772–3778, 1993.

[167] K.-Y. Tu and T. Tamir, "Wave diffraction by many superposed volume gratings," *Applied Optics*, 32(20):3654–3660, 1993.

[168] P. Asthana, G. P. Nordin, A. R. Tanguay, Jr., and B. K. Jenkins, "Analysis of weighted fan–out/fan–in volume holographic optical interconnections," *Applied Optics*, 32(8):1441–1469, 1993.

[169] G. P. Nordin, P. Asthana, "Effects of cross-talk on fidelity in page-oriented volume holographic optical-data storage," *Optics Letters*, 18(18):1553–1557, 1993.

[170] C. Gu, J. Hong, I. McMichael, R. Saxena, and F. Mok, "Cross–talk–limited storage capacity of volume holographic memory," *Journal of the Optical Society of America* **A**, 9(11):1–6, 1992.

[171] K. Curtis, D. Psaltis, and C. Gu, "Crosstalk in wavelength multiplexed holographic memories," *Optics Letters*, 18(12):1001–1003, 1993.

[172] K. Curtis, and D. Psaltis, "Cross-talk in phased coded holographic memories," *Journal of the Optical Society of America* **A**, 10(12):2547–2550, 1993.

[173] K. Curtis, and D. Psaltis, "Cross-talk in rotating media holographic memories," *submitted to Journal of the Optical Society of America A*, 1993.

[174] K. Curtis, and D. Psaltis, "Cross-talk in image plane angle multiplexed holographic memories," *submitted to Optics Letters*, 1993.

[175] G. A. Rakuljic, V. Leyva, and A. Yariv, "Optical-data storage by using orthogonal wavelength-multiplexed volume holograms," *Optics Letters*, 17(20):1471–1473, 1992.

[176] F. T. S. Yu, S. Wu, A. W. Mayers, and S. Rajan, "Wavelength multiplexed reflection matched spatial filters using $LiNbO_3$," *Optics Communications*, 81:343-345, 1991.

[177] C. Denz, G. Pauliat, and G. Roosen, "Volume hologram multiplexing using a deterministic phase encoding method," *Optics Communications*, 85:171-176, 1991.

[178] J. Trisnadi, and S. Redfield, "Practical verification of hologram multiplexing without beam movement," *Photonic Neural Networks, SPIE*, 1773:362-371, 1992.

[179] J. E. Ford, Y. Fainman, and S. H. Lee, "Array interconnection by phase-coded optical correlation," *Optics Letters*, 15(19):1088-1090, 1990.

[180] C. Denz, G. Pauliat, G. Roosen, and T. Tschudi, "Potentialities and limitations of hologram multiplexing by using the phase-encoding technique," *Applied Optics*, 31(26):5700-5705, 1992.

[181] C. Gu, and J. Hong, "Cross-talk in wavelength multiplexed memories," *OSA Annual Meeting*, Vol 23 of 1992 OSA Technical Digest Series (OSA, Washington D.C., 1992), paper WT2, p. 111.

[182] J. W. Goodman, *Introduction to Fourier Optics*, (McGraw-Hill, New York, 1968), p. 57-96.

[183] J. D. Jackson, *Classical Electrodynamics*, (Wiley, New York, 1975), p. 427-432.

[184] I. S. Gradshteyn, and I. M. Ryzhik, *Table of Integrals, Series, and Products*, (Academic Press Inc., London, 1980), p.39.

[185] M. Abramowitz, and I. E. Stegun, *Handbook of Mathematical Fuctions with Formulas, Graphs, and Mathematical Tables*, (National Bureau of Standards, Washington, D.C., 1972) p. 807.

[186] D. Brady and D. Psaltis, "Information Capacity of 3-D Holographic Data Storage," *Optical and Quantum Electronics*, 25:S597–S610, 1993.

[187] I. S. Gradshteyn, and I. M. Ryzhik, *Table of Integrals, Series, and Products* (Academic Press Inc., London, 1980), p.482.

[188] I. S. Gradshteyn, and I. M. Ryzhik, *Table of Integrals, Series, and Products* (Academic Press Inc., London, 1980), p.683.

[189] M. Abramowitz, and I. E. Stegun, *Handbook of Mathematical Functions with Formulas, Graphs, and Mathematical Tables* (National Bureau of Standards, Washington, D.C., 1972) p. 363.

[190] K. Curtis, G. Burr, and D. Psaltis, "Comparison of wavelength and angle multiplexed holographic memories," *OSA Topical Meeting on Optical Computing*, Vol. 7 of 1993 OSA Technical Digest Series (OSA, Washington D.C., 1993), paper OWB4,p. 87.

[191] K. Curtis, S. Li, and D. Psaltis, "Comparison of Wavelength, Phase Coded, and Angle Multiplexed Holographic Memories," *OSA Annual Meeting*, Vol 16 of 1993 OSA Technical Digest Series (OSA, Washington D.C., 1993), paper TuH3, p. 78.

[192] F. T. S. Yu, F. Zhao, H. Zhou, and S. Yin, "Cross-talk noise in a wavelength-multiplexed reflection-type photorefractive fiber hologram," *Optics Letters*, 18(21):1849-1851, 1993.

[193] D. Psaltis, D. Brady, and K. Wagner, "Adaptive optical networks using photorefractive crystals," *Applied Optics*, 27(9):1752-59, 1988.

[194] A. M. Weber, W. K. Smothers, T. J. Trout, and D. J. Mickish, " Hologram recording in DuPont's new photopolymer materials," *SPIE Conference on Practical Holography IV*, Vol. 1212:30–39, 1990.

[195] W. J. Gambogi, W. A. Gerstadt, S. R. Mackara, and A. M. Weber, " Holographic transmission elements using improved photopolymer films," *SPIE Conference on Computer and Optical Generated Holographic Optics*, Vol. 1555:256–267, 1991.

[196] D. Psaltis, "Parallel optical memories," *Byte*, 17(9):179–182, 1992.

[197] R. Magnusson and T. K. Gaylord, " Analysis of multiwave diffraction," *Journal of the Optical Society of America*, 67(9):1165–1170, 1977.

[198] R. Magnusson and T. K. Gaylord, "Diffraction efficiencies of thin phase gratings with arbitrary grating shape," *Journal of the Optical Society of America*, 68(6):806–809, 1976.

[199] R. Magnusson and T. K. Gaylord, "Diffraction efficiencies of thin absorption and transmittance gratings," *Optics Communications*, 28(1):1–3, 1979.

[200] B. Benlarbi and L. Solymar, "Higher order modes at off-Bragg angle incidence in thick phase gratings," *International Journal of Electronics*, 52(2):95–100, 1982).

[201] L.-B. Au and L. Solymar. "Higher diffraction orders in photorefractive material," *IEEE Journal of Quantum Electronics*, 24(2):162–168, 1988.

[202] L. B. Au and L. Solymar. "Higher harmonic gratings in photorefractive materials at large modulation with moving fringes," *Journal of the Optical Society of America* **A**, 7(8):1554–1561, 1990.

[203] E. G. Paek, and E. C. Jung, "Simplified holographic associative memory using enhanced nonlinear processing with a thermoplastic plate," *Optics Letters*, 16(13):1034–36, 1991.

[204] W. Press, B. Flannery, S. Teukolsky, and W. Vetterling, Numerical Recipes in C (Cambridge Univ. Press, New York, 1988) pp. 569-73.

[205] J. Feinberg, D. Heiman, A. R. Tanguay, Jr., and R. W. Hellwarth, "Photorefractive effects and light-induced charge migration in barium titanate," *Journal of Applied Physics*, 51(3):1297-1305, 1980.

[206] M. H. Garrett, J. Y. Chang, H. P. Jenssen, and C. Warde, "High photorefractive sensitivity in an n-type 45deg -cut $BaTiO_3$ crystal," *Optics Letters*, 17(2):103-5, 1992.

[207] R. A. Vazquez, F. R. Vachss, R. R. Neurgaonkar, and M. D. Ewbank, "Large photorefractive coupling coefficient in a thin cerium-doped strontium barium niobate crystal," *Journal of the Optical Society of America B*, 8(9):1932-41, 1991.

[208] J. Hong, P. Yeh, D. Psaltis, and D. Brady, "Diffraction efficiency of strong volume holograms," *Optics Letters*, 15(6):344-346, 1990.

[209] G. P. Nordin, R. V. Johnson, and A. R. Tanguay, Jr., "Diffraction properties of stratified volume holographic optical-elements," *Journal of the Optical Society of America A*, 9(12):2206-2217, 1992.

[210] R. V. Johnson, and A. R. Tanguay, Jr., "Stratified volume holographic optical-elements," *Optics Letters*, 13(3):189-191, 1988.

[211] A. Granger, L. Song, and R. A. Lessard, "Multiple beam generation using a stratified volume holographic grating," *Applied Optics*, 32(14):2534-2537, 1993.

[212] D. Brady, "Photorefractive volume holography in artificial neural networks," *Thesis* California Institute of Technology, 1990.

[213] G. P. Nordin and A. R. Tanguay, Jr., "Photopolymer-based stratified volume holographic optical elements," *Optics Letters*, 17(23):1709–1711, 1992.

[214] D. Psaltis, D. Brady, X. G. Gu, S. Lin, "Holography in artificial neural networks," *Nature*, 343(6256):325-330, 1990.

[215] H. Y. S. Li, "Photorefractive 3–D disks for optical data storage and artificial neural networks," *Thesis* California Institute of Technology, 1994.

[216] D. Brady and D. Psaltis, "Control of volume holograms," *Journal of the Optical Society of America A*, 9(7):1167–1182, 1992.

[217] D. Psaltis, M. A. Neifeld, and A. Yamamura, "Image correlators using optical memory disks," *Optics Letters*, 14(9):429–432, 1989.

[218] D. Psaltis, M. A. Neifeld, A. Yamamura, and S. Kobayashi, "Optical memory disks in optical information processing," *Applied Optics*, 29(14):2038–2057, 1990.

[219] A. Kutanov, B. Abdrisaev and S. Dordoev, "Holographic disked-based optical neural network," *Optics Letters*, 17(13):952–955, 1992.

[220] E′ Kh. Gulanyan, A. L. Mikaelyan, L. V. Molchanova, V. A. Sidorov, and I. V. Fedorov, "Use of a photothermoplastic disk in memories based on one-dimensional holograms," *Soviet Journal Quantum Electronics*, 19(8):1124-26, 1989.

[221] F. H. Mok, M. C. Tackett, and H. M. Stoll, "Massively parallel optical template matcher/ correlator," *OSA Annual Meeting* ThI14, Boston, Massachusetts, 1990.

[222] C. Gu, J. Hong and S. Campbell, "2-D shift-invariant volume holographic correlator," *Optics Communications*, 88:309–311, 1992.

[223] X. A. Shen and R. Kachru, "High speed pattern recognition by using stimulated echoes," *Optics Letters*, 17(7):520–523, 1992.

[224] J. Yu, F. Mok, and D. Psaltis, "Capacity of optical correlators," *SPIE Annual Meeting*, p. 825-32, San Diego, CA, 1987.

[225] H. Y. S. Li, and D. Psaltis, "Storage capacity of 3-D holographic optical disks," submitted to *Applied Optics*.

[226] H. Y. S. Li, K. Curtis, Y. Qiao, and D. Psaltis, "3-D holographic disks," *Joint International Symposium on Optical Memory and Optical Data Storage*, July 1993, Maui, Hawaii.